Studie en optimalisatie van gemagnetiseerde ICRF-ontladingen voor wandconditionering in tokamaks en beoordeling van de toepasbaarheid op ITER

Study and Optimization of Magnetized ICRF Discharges for Tokamak Wall Conditioning and Assessment of the Applicability to ITER

Tom Wauters

Promotoren: prof. dr. ir. G. Van Oost, prof. dr. ir. M. Van Schoor
Proefschrift ingediend tot het behalen van de graden van
Doctor in de Ingenieurswetenschappen: Toegepaste Natuurkunde (UGent) en
Doctor in de Ingenieurswetenschappen (KMS)

Vakgroep Toegepaste Fysica
Voorzitter: prof. dr. ir. C. Leys
Faculteit Ingenieurswetenschappen en Architectuur

UNIVERSITEIT GENT

Departement Fysica
Departementshoofd: prof. dr. ir. M. Van Schoor
Faculteit Polytechniek

Academiejaar 2011 - 2012

ISBN 978-90-8578-458-6
NUR 926
Wettelijk depot: D/2011/10.500/62

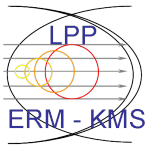

This work was carried out as a collaboration between the Institute for Magnetic Fusion Research (IRFM, CEA Cadarache, France) and the Laboratory for Plasma Physics of the Royal Military Academy (LPP-ERM/KMS Brussels, Belgium). The work was supported by EURATOM and frames within the European Fusion Development Agreement. The views and opinions expressed herein do not necessarily reflect those of the European Commission.

Members of the examining board

Prof. Guido Van Oost Promotor
Ghent University, Department of Applied Physics

Prof. Michael Van Schoor Promotor
Royal Military Academy of Belgium, Head Department of Physics

Dr. David Douai Supervisor
CEA, Institute for Magnetic Fusion Research

Dr. Anatoli Lyssoivan Supervisor
Royal Military Academy of Belgium

Prof. Daniël De Zutter Chairman
Ghent University, Former Dean of the Faculty of Engineering

Prof. Christophe Leys Secretary
Ghent University, Department of Applied Physics

Prof. Raymond Koch
Royal Military Academy of Belgium

Prof. Jean-Marie Noterdaeme
Ghent University, Department of Electrical Energy, Systems & Automation

Dr. Volker Philipps
FZJ, Institute for Energy and Climate Research, Head of Plasma Wall Interaction group

Dr. Michiya Shimada
ITER Organization, Chief Scientific Officer of Fusion Science & Technology Department

Acknowledgements

First of all I would like to thank my supervisors David Douai[1] and Anatoli Lyssoivan[2], with whom I've enjoyed working with. The progress that I've made over the past three years is largely thanks to them. The efforts they have dedicated to my work and my personal development deserve my gratitude and respect. I would also like to thank Prof. Van Oost[3] and Prof. Van Schoor[2] for accepting the co-tutorship of this PhD, for establishing the collaboration between IRFM-CEA[1] and LPP-ERM/KMS[2], for their availability and for the constant interest they have shown in my work.

In the course of this PhD I had the opportunity to work in four European research institutions. Approximately two years of the work are carried out at IRFM-CEA[1] and one year at IPP-Jülich[4] with occasional visits to IPP-Garching[5] and CCFE-Culham[6]. For these excellent collaborations I would like to thank specifically S. Brémond, A. Argouarch, J. Bucalossi, L. Colas, E. Gauthier, E. Joffrin, G. Lombard, P. Mollard, P. Monier-Garbet, B. Pégourié and the TORE SUPRA Team from IRFM-CEA[1], R. Koch, S. Jachmich, E. Lerche, J. Ongena, M.K. Paul, D. Van Eester, M. Vervier and G. Van Wassenhove from LPP-ERM/KMS[2], V. Philipps, M. Freisinger, A. Kreter, O. Marchuk, H. Reimer, G. Sergienko, S. Brezinsek and the TEXTOR Team from IPP-Jülich[4], V. Rohde, D. Wünderlich, V. Bobkov, J.-M. Noterdaeme, A. Scarabosio, W. Suttrop and the ASDEX Upgrade Team from IPP-Garching[5], V. Plyusnin from IST-Lisboa[7], E. de la Cal from CIEMAT-Madrid[8], T. Blackman, T. Coyne, M. Graham, M. Maslov, M.-L. Mayoral, A. Miller and I. Monakhov from CCFE-Culham[6], and P. Lamalle, F.C. Schüller, M. Shimada and R. Pitts from ITER[9].

Cadarache, September 2011
Tom Wauters

[1]IRFM-CEA, Association Euratom-CEA, St Paul lez Durance, France.
[2]LPP-ERM/KMS, Association Euratom-Belgian State, Brussels, Belgium.
[3]Ghent University, Department of Applied Physics, Ghent, Belgium
[4]IEK-Plasmaphysik, FZ-Jülich, Euratom Association, Jülich, Germany.
[5]Max-Planck Institut für Plasmaphysik, Euratom Association, Garching, Germany.
[6]CCFE, Culham Science Centre, Abingdon, UK.
[7]Centro de FNIST, Association Euratom-IST, Lisboa, Portugal.
[8]Laboratorio Nacional de Fusión, Association Euratom-CIEMAT, Madrid, Spain.
[9]ITER International Organization, St Paul lez Durance, France.

Table of Contents

List of Acronyms

0-9

0D	Zero Dimensional
1D	One Dimensional

A

ALT	Advanced Limiter Test (toroidal limiter on TEXTOR)
Ar	Argon
AUG	ASDEX Upgrade (Axially Symmetric Divertor EXperiment), Garching, Germany

B

B	Boron
Be	Beryllium

C

C	Carbon
CCD	Charge-Coupled Device
CFC	Carbon Fibre Composites
CS	Central Solenoid
CX	Charge exchange

D

D	Deuterium
D-IIID	Doublet III-Divertor experiment, San Diego, USA
DC-GDC	Direct Current GDC
DCN	Molecule used to produce laser light in the far infrared
DEMO	Demonstration Fusion Power Plant

E

EAST	Experimental Advanced Superconducting Tokamak (also called HT-7U), Hefei, China
ECE	Electron Cyclotron Emission
ECR	Electron Cyclotron Resonance
ECRF	Electron Cyclotron Range of Frequencies
ECRH	Electron Cyclotron Resonance Heating
ECWC	Electron Cyclotron Wall Conditioning
EFDA	European Fusion Development Agreement
EM	Electromagnetic

F

FS	Faraday screen
FW	Fast Wave

G

GDC	Glow Discharge Conditioning

H

H	Hydrogen

HCN	Molecule used to produce laser light in the far infrared
He	Helium
HFS	High Field Side
HT-7	Hefei Tokamak-7, Hefei, China

I

IBW	Ion Bernstein Wave
ICRF	Ion Cyclotron Range of Frequencies
ICRH	Ion Cyclotron Resonance Heating
ICWC	Ion Cyclotron Wall Conditioning
IO	ITER Organization
IR	Infrared
ITER	International Thermonuclear Experimental Reactor, Cadarache, France

J

JAERI	Japan Atomic Energy Research Institute
JET	Joint European Torus, Culham, UK
JFT-2	JAERI Fusion Torus-2, Japan
JT-60SA	JAERI Tokamak - 60 Super Advanced, Naka, Japan
JT-60U	JAERI Tokamak - 60 Upgrade (Currently upgraded to JT-60SA), Naka, Japan

K

KSTAR	Korea Superconducting Tokamak Advanced Research, Daejon, Korea

L

LCFS	Last Closed Flux Surface
LFS	Low Field Side

LH	Lower Hybrid (heating)
LHD	Large Helical Device, Toki, Japan

M

MC	Mode Conversion

N

N	Nitrogen
NPA	Neutral Particle Analyzer

O

O	Oxygen

P

P-GDC	Pulsed GDC
PFC	Plasma Facing Components
PL	Pulse Length, RF discharge pulse length
PSI	Plasma Surface Interactions
PT	Pumping Time, time between two RF discharge pulses
PWI	Plasma Wall Interactions

Q

QMS	Quadrupole Mass Spectrometer

R

RC	Radiative-collisional
RF	Radio Frequency
RFA	Retarding Field Analyzer
rhs	right hand side
RMS	Root Mean Square

S

Si	Silicium
SOL	Scrape Off Layer
SW	Slow Wave

T

T	Tritium
TDC	Taylor Discharge Cleaning
TEXTOR	Tokamak Experiment for Technology Oriented Research in the field of plasma wall interaction, Jülich, Germany
TF	Toroidal Field
TOMAS	TOroidal MAgnetic field System, Jülich, Germany
TORE SUPRA	Superconducting tokamak, in operation since 1988 in Cadarache, France
TRIAM-1M	Tokamak of Research Institute for Applied Mechanics, Kyushu University, Japan

V

VSWR	Voltage Standing Wave Ratio

W

W	Tungsten
W7-AS	Wendelstein 7 - Advanced Stellarator (currently upgrading to W7-X), Greifswald, Germany

W7-X	Wendelstein 7X, under construction, Greifswald, Germany

Nederlandse samenvatting
–Summary in Dutch–

Inleiding

Energie uit magnetische fusie is een veelbelovend alternatief voor huidige broeikasgas-uitstotende energietechnologieën. Fusie is inherent veel veiliger dan de energieproductie uit kernsplijting, en in tegenstelling tot de genoemde technologieën is de brandstof voor fusie overvloedig beschikbaar. Het ambitieuze wereldwijde ITER-project is momenteel het toonaangevende onderwerp in het onderzoek naar magnetische fusie. Het doel van het project is aantonen dat commerciele energieproductie uit fusie mogelijk is. ITER is namelijk ontworpen om vijf tot tien maal het ingangsvermogen te produceren voor een duur van maximaal 1000 seconden. In geval van succes, zal het ITER-project worden opgevolgd door een industrieel demonstratiereactorproject: DEMO (anno 2030-2040).

Energie uit kernfusie wordt geproduceerd door het samensmelten van lichte atoomkernen in zwaardere kernen. Deze samensmelting is het gevolg van de nucleaire aantrekkingskracht en wordt bereikt door het zeer dicht bij elkaar brengen van positief geladen kernen, zodat de aantrekkende kernkracht groter wordt dan de afstotende elektrostatische Coulombkracht. Om de Coulomb-barrière te overbruggen zijn er hoge energiën in de orde van miljoenen Kelvin vereist. Het huidige onderzoek naar fusieenergie baseert zich op de deuterium-tritium (D-T) reactie, beide isotopen van waterstof, waarbij een (niet radioactieve) heliumkern en een neutron geproduceerd worden met een gecombineerde energie van 17.6 MeV: $\mathrm{D} + \mathrm{T} \rightarrow {}^4\mathrm{He}\ (3.5\,\mathrm{MeV}) + \mathrm{n}\ (14.1\,\mathrm{MeV})$. Bij de vereiste temperaturen zullen de deuterium en tritium 'brandstof'-moleculen opgesplitst zijn in hun samenstellende atomen. De atomen op hun beurt zullen worden geïoniseerd, hetgeen van brandstof een gas van geladen deeltjes maakt, namelijk een plasma met positieve ionen (kernen) en negatieve elektronen. Het plasma van een energie-efficiënte fusiereactor moet een voldoende aantal fusiereacties voortbrengen (1 GW fusie-energie is gelijk aan $3.5 \cdot 10^{20}$ D-T reacties per seconde), en de vrijgekomen energie moet hoger zijn dan de externe energie die nodig is om het plasma op te warmen. De toestand waarin het plasma zichzelf verwarmt door fusiereacties zodat externe verwarming kan worden

uitgeschakeld heet 'ontsteking'. Het criterium om ontsteking te bekomen wordt uitgedrukt door het 'drievoudige product': $n_e T \tau_E \geq 3 \cdot 10^{21}\,\mathrm{m}^{-3}\mathrm{keVs}$, waarbij n_e de plasma-elektron dichtheid is, T de plasma temperatuur en τ_E de energie-opsluitingstijd, een maat voor de snelheid waarmee het systeem energie verliest aan zijn omgeving. Het magnetische fusieonderzoek richt zich op het benaderen van de ontstekingsconditie door het opsluiten van het plasma ($n_e = 10^{20}\,\mathrm{m}^{-3}$) in een torusvormige fles gevormd door magnetische velden hetgeen een hoge energie-opsluitingstijd ($\tau_E = 3\,\mathrm{s}$) voorziet en het plasma op zeer hoge temperatuur kan vasthouden ($T = 10\,\mathrm{keV} \approx 10^8\,\mathrm{K}$).

De tokamak magnetische opsluitingsconfiguratie is reeds met succes gebruikt om fusiereacties te produceren en is op dit moment de methode die het meest bestudeerd wordt. De magnetische configuratie van een tokamak bestaat uit schroefvormige magnetische veldlijnen die samen een torus beschrijven bestaande uit concentrische magnetische oppervlakken. De toroidale veldcomponent van de configuratie wordt gegenereerd door een reeks poloïdale spoelen die de plasmatorus omhullen. Een eerste poloïdaal magnetisch veldcomponent wordt geproduceerd door een intense axiale stroom in het torusvormige plasma zelf, opgewekt door inductie zoals in een transformator. Een tweede poloïdale veldcomponent, gebruikt om een stabiel plasma evenwicht te verkrijgen en om de vorm van de magnetische oppervlakken te optimaliseren, wordt geproduceerd door toroïdale spoelen. De experimenten die in dit proefschrift gepresenteerd worden zijn uitgevoerd op de Europese tokamaks TORE SUPRA (IRFM, CEA/Cadarache, Frankrijk), TEXTOR (IPP-Jülich, Duitsland), ASDEX Upgrade (IPP-Garching, Duitsland) en JET (CCFE, Verenigd Koninkrijk), en kaderen in de voorbereiding van de ITER-tokamak ingebruikname.

Voor het opvangen en het onttrekken van de plasma-warmtebelasting op onvermijdelijke snijpunten van de buitenste magnetische veldlijnen en de wand zijn er speciale objecten geplaatst op de wand van bovenstaande tokamaks. In een limiter-tokamak (TORE SUPRA, TEXTOR) wordt de rand van het opgesloten plasma (waar de magnetische oppervlakken gesloten zijn) bepaald door een toroidaal oppervlak dat het eerste vaste materiaaloppervlak is die de veldlijnen onderschept, gezien vanuit het plasma-centrum. Een fusiereactor kan geen beroep doen op deze configuratie omdat de warmtebelasting op dit begrenzend oppervlak en de productiesnelheid van onzuiverheden ontoelaatbaar hoog zou zijn. In de divertor configuratie (ASDEX Upgrade, JET), is het laatste gesloten magnetisch oppervlak uitsluitend bepaald door de magnetische veldlijnen zelf. De eerste vaste materiaalcomponent, de divertortarget, bevindt zich op enige afstand van het laatste gesloten magnetisch oppervlak, zodat onzuiverheden moeilijker tot in het plasmacentrum kunnen doordringen. ITER is ontworpen met de divertor configuratie.

De prestatie van het centrale tokamakplasma is sterk afhankelijk van zijn interactie met de plasmarand en met de plasma-blootgestelde componenten (PFC's). Fundamentele plasma-wandinteractieprocessen zoals erosie

(sputteren en chemische erosie), implantatie, trapping, depositie, adsorptie en desorptie kunnen het vrijkomen van wandmateriaal veroorzaken en dus onzuiverheden introduceren in het plasma (desorptie van onzuiverheden), netto brandstof retentie of vrijgave door de wand veroorzaken (brandstof recycling), en degradaties van de wandmaterialen induceren. Productie van plasma-onzuiverheden dient te worden vermeden omdat dit het plasma afkoelt door straling, het plasma verdunt met als gevolg een vermindering van de fusie-energie, de stabiliteit van het plasma verlaagt, de totale energie-opsluitingstijd vermindert en verdere productie van onzuiverheden versnelt. Sterke brandstofvrijgave door de wanden dient te worden vermeden omdat dit plasmaproductie en de controle van de plasmadichtheid onmogelijk kan maken. Hoge retentie van brandstof is ook problematisch omdat wordt geschat dat door deze opname de administratieve toelaatbare grens toegeschreven aan de retentie van tritium in ITER, ingesteld op 640 g, kan worden bereikt in minder dan één ITER-DT-exploitatie jaar. Om de ITER 'levensduur' te verlengen dient de tritium inventarisopbouw, te wijten aan retentie van brandstof door implantatie en codepositie, dus beperkt te worden.

Om de beschreven plasmawandinteracties en de tritium inventarisopbouw te controleren zijn er drie actoren: (1) optimale keuze van de wandmaterialen, (2) optimale selectie van de tokamak magnetische configuratie, zoals divertor, limiters, en de exploitatieregimes en (3) de controle van de staat van de wandoppervlakken. Dit proefschrift richt zich op de derde actor, namelijk wandconditionering. In de huidige tokamaks worden er een reeks wandconditioneringstechnieken gebruikt om de wanden in de gewenste toestand te brengen. De ITER-relevante technieken zijn (a) verwarming van de wandmaterialen (Baking) om thermische desorptie van deeltjes te induceren. Baking is een efficiënte maar tijdrovende procedure (orde van dagen). Om de tritiuminventaris in ITER te verminderen wordt de benodigde baking-frequentie geschat op 2 tot 8 keer per jaar. (b) Glimontladingsconditionering (GDC), is een routine-conditioneringstechniek op vrijwel alle fusie-apparaten. Het is aangetoond dat GDC inefficiënt is in aanwezigheid van het toroïdaal magnetisch veld. In supergeleidende tokamaks zoals ITER, waar het toroïdale magnetisch veld steeds aanwezig zal zijn gedurende de operationele cycli (periodes van de orde van weken), zal de toepassing van GDC dus beperkt zijn tot shut-down periodes. (c) Het gebruik van tokamak plasma-ontladingen voor conditioneren (scannen van de separatrix en gecontroleerde plasmadisrupties), hetgeen apparte ontladingen zou kunnen vereisen aangezien de controle van de ontladingsbeëindiging in ITER DT-plasma's als subtiel en fragiel wordt beschouwd. (d) Ion-cyclotron wandconditionering (ICWC), het hoofdonderwerp van dit proefschrift, en momenteel de meest belovende techniek om te worden ingezet op ITER tijdens de operationele cycli (dus in aanwezigheid van het magnetisch veld). (e) Electron-cyclotron wandconditioneringsontladingen (ECWC), geproduceerd in aanwezigheid van het toroïdale magnetische veld door het koppelen van RF-golven in het elektron-cyclotron frequentiebereik, met behulp

van de standaard tokamak elektron-cyclotron verwarmingssystemen. De techniek blijkt minder efficiënt te zijn dan ICWC en GDC, en bovendien is de poloïdale ontladingshomogeniteit onvoldoende. (f) Gepulseerde glimontladingsconditionering (P-GDC), waarbij de ontladingen geproduceerd worden door gebruik te maken van de conventionele GDC elektroden gekoppeld aan een hoge frequentie voedingsbron. Deze recente techniek vereist verdere onderzoeks- en ontwikkelingsinspanningen op meerdere machines, om de homogeniteit te optimaliseren, de efficiëntie te demonstreren, en de toepasbaarheid voor ITER te beoordelen.

De kwalificatie van wandconditioneringsontladingen toepasbaar in aanwezigheid van het toroïdale magnetisch veld voor inter-shot conditioning en conditionering gedurende de nachten tijdens de ITER-operationale cycli, wordt beschouwd als een prioriteitsonderwerp in de voorbereiding van de expoitatie van ITER. De conditioneringsontladingen zijn noodzakelijk om de tritium-inventarisopbouw verminderen, om de vereiste lage brandstofrecycling te voorzien tijdens de plasmaopstartfase en om onzuiverheden (en brandstof) te verwijderen na plasmadisrupties. Omdat ICWC met succes getest is op verschillende tokamaks en gunstige kenmerken vertoont in vergelijking met ECWC, is het opgenomen in de functionele projectvereisten. Dit proefschrift kadert in het R&D-programma rond ICWC dat als doel heeft de ICWC-techniek te consolideren en de toepasselijkheid ervan op ITER, en mogelijk andere toekomstige machines, te kwalificeren.

ICWC principe

ICWC, toegepast in aanwezigheid van het toroïdale magnetisch veld, maakt gebruik van vier voorname tokamaksystemen: de ICRF antennes om de conditioneringsontlading te initiëren en te ondersteunen, de gasinjectieventielen om het ontladingsgas te voorzien, de vacuümsystemen om gedesorbeerde deeltjes van de wand uit de machine te pompen, en het poloïdaal magnetisch veld-systeem om de ontladingshomogeniteit te optimaliseren. Daarnaast zijn er ook gas- en plasmadiagnostieken nodig om de plasmaontlading en de conditioneringsefficiëntie te diagnosticeren.

ICRF ontladingproductie kan worden onderverdeeld in de pre-golf fase en de plasmagolf fase. De ontladingsintiatiefase komt overeen met de pregolffase. De plasmadichtheidsopbouw in de ontladingsintiatiefase is het gevolg van botsingsionisatiereacties door elektronen versneld in het parallel elektrisch veld in nabijheid van de antennes. In de golffase breidt het elektromagnetische veld zich uit in het vacuümvat waardoor meer ruimte-ionisatie mogelijk wordt. In deze fase wordt het RF-vermogen voornamelijk collisioneel geabsorbeerd door elektronen. Antenne-operatiescenarios zijn geïdentificeerd die de plasma-doorbreek tijd, de RF-vermogenkoppelingsefficiëntie en de plasmahomogeniteit verbeteren. Deze bestaan ofwel uit het verlagen van de cut-off dichtheid voor snelle golf (FW) propagatie, namelijk de

werking dichtbij monopoolfasering van de antennestraps en/of werking bij hoge harmonische cyclotronnummers (bijv. bij sterk gereduceerde toroïdaal magnetische veldwaarden), of zijn gebaseerd op mode-conversiescenario's van de exponentieel dalende FW in de langzame golf of ion-Bernsteingolf in plasma's met meerdere ionsoorten (hetgeen het geval is in ICWC plasma's). Er werd geconcludeerd dat voor ICRF plasmaproductie, monopoolstrapfasering van de ICRF antennes het optimale operatiescenario is.

De geproduceerde plasmas doelen op het creëren van een gecontroleerde flux van deeltjes naar de wandoppervlakken om het verwijderen van onzuiverheden, de erosie van gecodepositioneerde lagen, de brandstofdesaturatie van de wandopervlakken, of het veranderen van hun isotoopverhouding te bewerkstelligen. Voor het ontladingsgas, gevoed via de injectieventielen, kan men kiezen voor inerte (bijv. He) of reactieve gassen (bijv. H_2, D_2, O_2), afhankelijk van het conditioneringsdoel. De deeltjes die intentioneel worden vrijgemaakt uit de wandoppervlakken dienen verwijderd te worden uit het vacuümvat. Hiervoor worden de standaard vacuümpompen gebruikt die continu operationeel zijn om vereiste vacuümvoorwaarden te bieden. Om een hoog conditioneringsrendement mogelijk te maken dient de vacuümpompsnelheid zo hoog mogelijk te zijn. De efficiëntie van de conditioneringstechniek voor het verwijderen van deeltjes uit de oppervlakken en vervolgens deze deeltjes te verwijderen uit het vacuümvat, kan worden beoordeeld via verschillende diagnostische systemen waaronder de belangrijkste de gasanalysesytemen zijn (bijv. drukmetingen, massaspectrometrie, ...).

PhD doelstellingen

De experimentele doelstelling van dit proefschrift is de studie en de optimalisatie van ICWC op meerdere tokamaks, TORE SUPRA, TEXTOR, ASDEX Upgrade en JET, hetgeen het testen van de conditioneringstechniek toelaat onder meerdere condities (verschillende antennesystemen en beschikbare frequenties, verschillende tokamakafmetingen, limiter- en divertorconfiguraties, koolstof-PFC's en wolfraam-PFC's). Omdat waterstof en helium voorlopig de meest geschikte conditioneringsgassen zijn voor ITER (bijv. O_2-ontladingen zijn niet toegestaan tijdens de DT-fase) is het onderzoek gelimiteerd tot waterstof en helium ICWC-ontladingen. ICWC-ontladingen zijn toroïdaal homogeen maar poloïdaal inhomogeen. De mechanismen die deze inhomogeniteiten veroorzaken dienen bepaald te worden, en methoden om de poloïdale homogeniteit te verbeteren dienen gevonden te worden. Ook de homogeniteit van de deeltjesflux naar de wand dient te worden beschouwd. Hiervoor moeten de belangrijkste fluxcomponenten worden gekarakteriseerd. Het effect van deze wandfluxcomponenten op de conditioneringsefficiëntie, en hun afhankelijkheden van de ontladingscontroleparameters dienen onderzocht te worden. De studie van H_2-ICWC (en

He/H_2-ICWC) omvat het bestuderen van het vermogen van de techniek om de wand-isotoopverhouding te veranderen en gecodepositioneerde lagen (tritium verwijdering) te verwijderen. De studie van He-ICWC omvat het testen van het vermogen van de techniek om de brandstofconcentratie in de wand te verminderen (desaturatie), evenals het aantonen van de operationele effectiviteit van He-ICWC om de normale werking te herstellen na tokamak-plasmadisrupties en om de basisdrukniveaus van onzuiverheden te verlagen. Voor zowel H_2 als He-ICWC dient de conditioneringsefficiëntie-afhankelijkheid van de ontladings-controleparameters (druk, RF-vermogen, toroïdale en poloïdale magnetische veldsterktes, vacuümpompsnelheid, ...) te worden behandeld, evenals de evolutie in de tijd, en het voordeel van gepulste ontladingen ten opzichte van continue RF-ontladingen. De ICWC efficiëntie om onzuiverheden te verwijderen dient te worden onderzocht, en de algemene efficiëntie van ICWC dient te worden vergeleken met andere technieken (GDC, Taylor conditioneringsontladingen (TDC)). Ook dient er ervaring te worden opgebouwd met betrekking tot de veilige werking van de ICRF antenne-installaties.

De ontwikkeling van modellen kunnen tot belangrijke inzichten leiden. Om het inzicht in ICWC te vergroten en om de bestaande modellen te verifiëren, werden de volgende modelleringsdoelstellingen vooropgesteld. Een bestaande 0D ICRF plasmacode voor atomaire waterstof dient te worden opgewaardeerd naar een beschrijving voor moleculair waterstof en helium. De implementatie van moleculair waterstof is noodzakelijk door de lage temperatuur van het plasma en de daarmee verband houdende onvolledige ionisatie van het neutrale gas. Het ontwikkelde model moet worden vergeleken met experimentele data van TORE SUPRA en TEXTOR, en moet de experimenten aanvullen met gegevens die niet gemeten kunnen worden. Het model dient de experimentele plasmadichtheden te reproduceren (de beschikbare elektron-temperatuursmetingen worden onbetrouwbaar geacht bij de typische lage temperaturen). Oorzaken van verschillen tussen het model en experimenten dienen onderzocht te worden. Wanneer de plasmadichtheden en hun afhankelijkheden van de ontladingscontroleparameters met voldoende nauwkeurigheid gereproduceerd kunnen worden, kunnen de belangrijkste plasmaparameters en wandfluxen worden geïdentificeerd. De gemodelleerde wandfluxen dienen te worden vergeleken met experimentele data. Om beter inzicht te verkrijgen in de plasma-wandinteractie (PWI), de 'uit de machine gepompte' fluxen, de wand-gedesorbeerde fluxen en de wand-bombarderende fluxen, dienen deze aan elkaar te worden gerelateerd. Om de experimentele isotoopuitwisselingsresultaten te interpreteren en om geoptimaliseerde ontladingsscenario's voor te kunnen stellen, dient er een model te worden beoogd dat de 0D plasmacode voor waterstof koppelt met een minimumbeschrijving van de plasma-wandinteractie.

Om de toepasbaarheid van ICWC op ITER te beoordelen dienen de verkregen resultaten tenslotte geëxtrapoleerd te worden naar ITER en dienen mogelijke implementaties van de techniek op ITER besproken te worden.

Ontladingshomogeniteit

Het tot stand brengen van homogene RF-conditioneringsontlading is noodzakelijk om te garanderen dat het maximum van het wandoppervlak effectief geconditioneerd wordt. Het is aangetoond dat de waargenomen radiale inhomogeniteiten kunnen worden verklaard in termen van RF-vermogen absorptie-eigenschappen, en dat de verticale inhomogeniteiten te wijten zijn aan de opsluitingseigenschappen van de magnetische configuratie. Het is waargenomen dat dicht bij de wanden, in regio's waar de magnetische veldlijnen worden gelimiteerd door wandstructuren zoals poloïdale begrenzers, de plasmadichtheid exponentieel afneemt, hetgeen het bestaan van een plasmarand in ICRF ontladingen aantoont. Als gevolg van deze rand zal de flux van geladen deeltjes, getransporteerd langs de magnetische veldlijnen, het grootst zijn op de eerste limiterende oppervlakken. Om een radiaal homogene RF ontlading te verkrijgen is een goede propagatie van de RF-golven, of minstens een grote verval lengte van het evanescente RF-veld vereist, zodat het plasma ook aan de sterke magnetische veldzijde (aan de centrale kolom van de torus) ondersteund wordt. Door het toepassen van een klein verticaal magnetisch veld dat het plasma in de verticale richting uitstrekt, kan de verticale homogeniteit worden verbeterd. Uit experimenten op JET, momenteel de grootste tokamak, uitgevoerd met ITER-gelijkende ontladingscontroleparameters blijkt de haalbaarheid van het homogeen vullen van de gehele vacuümvat met plasma: bij het opereren van de antenne met monopool strapfasering en bij de toepassing van een klein verticaal magnetisch veld werd er felle recyclingstraling waargenomen, zowel in de nabijheid van de centrale kolom aan de hoge magnetische veldkant en in het divertorgebied.

Conditioneringsefficiëntie

Om de efficiëntie van ICWC te bestuderen en te optimaliseren werden experimenten uitgevoerd op TORE SUPRA, TEXTOR, JET en ASDEX Upgrade. (1) De isotopenuitwisselingsefficiëntie van H_2 en H_2/He-ontladingen is onderzocht, (2) het rendement voor wand-desaturatie en herstel van tokamak operatie na plasmadisrupties met behulp van He-ontladingen is bestudeerd, en (3) de efficiëntie van ICWC voor het verwijderen van onzuiverheid is geanalyseerd.

Waterstof-ICWC is in staat om de wandoppervlaktetoestand te veranderen op korte tijdschaal (verwijdering van waterstofmonolagen binnen enkele minuten), zowel op koolstof machines TORE SUPRA, TEXTOR en JET als op de wolfraam tokamak ASDEX Upgrade. Het verwijderen van de wandisotopen kan gaan ten koste van een tot tien keer hogere ontladingsgasretentie. In isotoopuitwisselingsexperimenten is de ideale verhouding tussen retentie en recuperatie van deeltjes gelijk aan één. Er werd experimenteel

aangetoond dat deze verhouding aanzienlijk kan worden verbeterd door het optimaliseren van de RF-duty cycle. De ideale verhouding van één werd bereikt zowel op TORE SUPRA als op TEXTOR.

De retentieoorzaken werden onderzocht: door de gecombineerde experimentele resultaten inzake (i) het lange termijn retentiegedrag op TORE SUPRA, (ii) retentie op de wolfraam machine ASDEX Upgrade, (iii) retentie als functie van aanwezigheid en afwezigheid van resonante IC-absorptie (hetgeen een energetische flux van CX deeltjes veroorzaakt) op TEXTOR, (iv) retentie in vergelijking met de totale energetische CX flux op JET, (v) recuperatie van wanddeeltjes door GDC, werd de hypothese gemaakt dat ICWC-ontladingen wandoppervlakgebieden bereikt die niet toegankelijk zijn door GDC. Ook het bestaan van een substantiële niet-resonante ionen-wandfluxcomponent met energieën boven de typische GDC-wandflux, waardoor de retentie in de diepere lagen mogelijk is, kan op dit moment niet worden uitgesloten. Beide punten dienen nader bestudeerd te worden.

Een uitgebreide vergelijking van de isotoopuitwisselingsefficiëntie van ICWC en GDC op TORE SUPRA en TEXTOR leerde dat de gemeten hoge retentie tijdens ICWC-ontladingen kan worden opgevat als een effect van de hoge reionisatiewaarschijnlijkheid (voornamelijk als gevolg van de hogere elektronendichtheid in ICWC-ontladingen): de probabiliteit dat een neutrale molecule wordt geïoniseerd of gedissocieerd in plaats van verwijderd door de vacuümpompen. Dus de verwijderingsefficiëntie van wandgedesorbeerd deeltjes door de vacuümpompen is minder efficiënt in ICWC dan in GDC. Dit maakt dat, zelfs als slechts een zeer klein deel van de wandflux permanent in de wand blijft, de hoge wandfluxen tijdens ICWC en de lage pompefficiëntie kan leiden tot een retentiesnelheid dat vergelijkbaar is met de verwijderingssnelheid door de vacuümpompen. Omdat reionisatie en de wandfluxretentie enkel optreden tijdens een plasma-ontlading, en omdat werd aangetoond dat het grootste deel van het wandgedesorbeerde gas verwijderd wordt na de RF puls, vermindert het gebruik van kortere RF-pulsen ($\sim 1\,\mathrm{s}$), met voldoende tijd tussen de pulsen zodat wandgedesorbeerde deeltjes kunnen verwijderd worden door de pompen ($\sim 20\,\mathrm{s}$ op TORE SUPRA), de retentie zonder de totale hoeveelheid verwijderde deeltjes ernstig te verlagen.

Het is aangetoond dat de efficienctie van waterstof-ICWC groter is bij hogere druk en bij het verhogen van het RF-vermogen. Het ideale RF-vermogen is echter het vermogen waarbij de ontladingen geproduceerd kunnen worden op de meest betrouwbare wijze met betrekking tot de antennewerking, en waarbij de ontlading het meest homogeen is. De energetische CX-wandflux blijkt slechts een geringe invloed te hebben op de conditioneringsefficiëntie. Terwijl de toroidale magnetische veldsterkte slechts een beperkt effect heeft op de conditioneringsefficiëntie (voor eenzelfde gekoppelde vermogen), kan de ICWC conditioneringsefficiëntie worden verbeterd door het aanbrengen van een klein verticaal magnetisch veld.

He-ICWC-ontladingen werden met succes toegepast op TORE SUPRA om de wand te desatureren van waterstofisotopen. Het verwijderen van het gedesorbeerde waterstof door de vacuümpompen is het meest efficient na de RF-puls, waardoor het opnemen van voldoende tijd tussen twee RF-pulsen in de conditioneringsprocedure de efficiëntie vergroot. Verder is het aangetoond dat de efficiëntie ook verhoogt bij het toepassen van hogere gekoppelde RF-vermogens. He-ICWC werd met succes toegepast op TORE SUPRA om de normale tokamakwerking te recupereren na tokamak-plasmadisrupties, en het is aangetoond dat He-ICWC minstens zo efficiënt is als de routinematig gebruikte TDC-techniek, zowel voor het verwijderen van waterstof als voor het verwijderen van H_2O. Deze beide feiten geven aan dat de geoptimaliseerde He-ICWC ontladingen gebruikt kunnen worden voor inter-pulse conditionering tijdens de experimentele campagnes op TORE SUPRA.

Zowel op JET als op ASDEX upgrade werd geconstateerd dat in heliumbevattende ICWC-ontladingen, een aanzienlijke hoeveelheid van het geïnjecteerde helium verloren ging in de wand. Op JET zijn hiervoor vermoedelijk de beryllium elementen op de ICRF antennes verantwoordelijk. Op ASDEX Upgrade zijn heliumverliezen ook gekend voor He-GDC, en deze zijn te wijten aan de wolfraam PFC's. Aangezien ITER als plasma-blootgestelde wandmaterialen wolfraam en beryllium zal gebruiken is het belangrijk om dit effect verder te onderzoeken in de toekomst, bijv. op JET, momenteel uitgerust met een ITER-gelijkende wand. De pulscyclus-optimalisatiecriteria inzake de verhouding van de ontladingsgasretentie tot het aantal gerecupereerde wandgedesorbeerde deeltjes, gebruikt voor waterstof-ICWC, zou ook kunnen aangewend worden voor He-ICWC. De ideale verhouding voor He-ICWC, en bovendien voor elke He-gebaseerde conditioneringsontlading is gelijk aan 'nul'. Ook voor het beperken van de redepositie van de wandgedesorbeerde deeltjes moet het beperken van de RF-pulslengte in He-ICWC overwogen worden. In het geval dat de (eventuele) heliumretentie in beryllium en/of wolfraam PFC's tijdens helium-conditioneringsontladingen onaanvaardbaar blijkt voor de operatie van ITER, zullen conditioneringsontladingen in andere (edel-) gassen moeten worden ontwikkeld om heliumconditioneringsontladingen te vervangen.

Op JET werden relatief hoge snelheden voor het verwijderen van koolstof waargenomen, maar het kon niet worden vastgesteld of de verwijderde koolstof van gecodepositioneerde lagen afkomstig was. Ook de blootstelling van koolstofstalen aan TEXTOR ICWC-plasmas kon geen uitsluitsel geven inzake erosie of afzetting van koolstof. De efficiëntie voor het verwijderen van onzuiverheden wordt groter naarmate het gekoppelde RF-vermogen vergroot, en het is bewezen dat er geen duidelijke invloed is van de aanwezige energetische CX-wandflux op de onzuiverheids-verwijderingsefficiëntie. Experimenten met het markergas argon op TEXTOR illustreerden dat ICWC een groot deel van het wandoppervlak dat geconditioneerd wordt door GDC

bereikt. Tot slot werd geïllustreerd zowel op TEXTOR (H_2-ICWC) als op TORE SUPRA (He-ICWC) dat ICWC het zuurstofgehalte in het vacuümvat kan verminderen. Of de verwijderingsefficiëntie voldoende is om de tokamakwerking te garanderen kon niet getest worden in de loop van dit doctoraat. Ter illustratie werd vermeld dat de supergeleidende tokamak KSTAR routinematig He-ICWC toepast voor inter-puls- en lunchtijdconditionering, om de H_2O-druk in het vacuümvat onder de operationele limiet te houden.

0D model voor helium-waterstof ICWC-plasmas

De ontwikkeling van het 0D model voor helium-waterstof ICWC-plasma's is gemotiveerd door de noodzaak om inzicht te verkrijgen in de ICRF plasma parameters, de deeltjesfluxen naar de wand en de belangrijkste botsingsprocessen, hetgeen het fundamentele mechanisme is voor de opbouw van een plasma. Dit is van bijzonder belang, aangezien de meeste standaard tokamak-plasmadiagnostieken niet aangepast zijn om de typische lage temperaturen en lage dichtheden van RF-plasmas te diagnosticeren.

De 0D plasmabeschrijving is gebaseerd op de energie- en deeltjesbalansvergelijkingen voor negen deeltjes soorten: H, H^+, H_2, H_2^+, H_3^+, He, He^+, He^{2+} en e^-. Het houdt rekening met (1) elementaire atomaire en moleculaire botsingsprocessen, zoals excitatie, ionisatie, dissociatie, recombinatie, ladingsuitwisseling, enz. en elastische botsingen, (2) deeltjesverliezen ten gevolge van de eindige afmetingen van het plasmavolume en de opsluitingseigenschappen van de magnetische configuratie, en deeltjesrecycling, (3) gasverwijdering door de vacuümpompen en gasinjectie, (4) RF-verwarming van elektronen (en protonen) en (5) een kwalitatieve beschrijving van plasmaonzuiverheden.

Wanneer plasma-onzuiverheden worden opgenomen in de simulaties reproduceert het model de experimentele plasmadichtheidsafhankelijkheid van de druk en het gekoppelde RF vermogen, zowel voor waterstof-ontladingen ($n_e \approx (1-5)\cdot 10^{10}\,\mathrm{cm}^{-3}$) als voor helium-ontladingen ($n_e \approx (1-5)\cdot 10^{11}\,\mathrm{cm}^{-3}$). De gemodelleerde wandfluxen voor waterstof-ontladingen komen overeen met de experimentele schattingen: $\sim 10^{19}-10^{20}\,/\mathrm{m}^2\mathrm{s}$ voor H-atomen, en $\sim 10^{17}-10^{18}\,/\mathrm{m}^2\mathrm{s}$ voor H^+-ionen. In het geval van helium RF-ontladingen werd vastgesteld dat wandgedesorbeerde deeltjes een grote bijdrage leveren aan de wandflux. De belangrijkste wand-bombarderende flux bestaat uit neutrale waterstofatomen. De helium- en waterstofionenflux is van dezelfde grootte-orde, ookal is de partiele waterstofdruk, aanwezig als gevolg van wanddesorptie, veel lager dan het heliumdruk.

Het gepresenteerde 0D ICWC-plasmamodel reproduceert de experimentele druk-, dichtheid- en gekoppelde RF-vermogen-temporele afhankelijkheden van een TORE SUPRA H_2-ICWC ontlading vanaf de ontladingsinitiatiefase tot aan de steady-state plasmafase, en geeft inzicht in de evolutie

van de deeltjeswandfluxen en retentie. De wandinteractie, vertegenwoordigd in het model door een deeltjes-recyclingcoëfficiënt, heeft een grote invloed op de neutrale druk- en plasmadichtheid in H_2-ICWC-ontladingen (in geval van een constante gasinjectie). Tijdens de plasmadoorbreekfase worden deeltjes tijdelijk opgeslagen in de wand hetgeen zich manifesteert door een sterke drukval, terwijl tijdens de latere plasmafase een evenwichtsdruk gevormd wordt waar de permanente waterstofretentie ongeveer gelijk is aan de gasinjectiesnelheid. Dit modelleringsresultaat bevestigt nogmaals dat het gebruik van kortere RF-pulsen in plaats van lange of continue ontladingen, voordelig is om retentie te beperken en de recuperatie van tijdelijk opgeslagen deeltjes te maximaliseren.

Simulatie van de wandinteractie in H_2-ICWC

Een minimumstructuur voor een 0D reservoirmodel van de TORE SUPRA (carbon) wand is opgesteld om meer inzicht te krijgen in de experimentele isotoopuitwisselingsdeeltjesbalansen. De gebruikte hypothese voor de opbouw van het model is dat hetzelfde model in staat moet zijn om het wandgedrag te beschrijven tijdens zowel normale plasma's als conditioneringsprocedures. Het model bestaat uit een gereduceerd plasmamodel, gebaseerd op het 0D model dat hierboven werd beschreven, gekoppeld aan de wandbeschrijving (via wandfluxen en de desorptiesnelheden). De wandbeschrijving is gebaseerd op vier reservoirs: een toegankelijk reservoir waarin retentie, verwijdering en uitwisseling van deeltjes mogelijk is, een permanent reservoir waarin alleen retentie mogelijk is, een tijdelijk reservoir dat diffuserende deeltjes in de wand vertegenwoordigt en een extra reservoir dat effecten representeert die belangrijk worden wanneer de vullingsgraad van het toegankelijke reservoir hoog is.

Het is aangetoond dat door dezelfde wandparameters te gebruiken in het model als die die vastgesteld zijn om de wandinteractie te beschrijven tijdens lange TORE SUPRA tokamakontladingen, ook de H_2, HD en D_2 partiële drukken van ICWC isotoopuitwisselingsontladingen gesimuleerd kunnen worden. Het model bevestigt de experimenteel waargenomen sterke interactie met het typische toegankelijke waterstofreservoir in koolstof en toont aan dat de fractie van de wandflux dat verloren gaat in het permanente reservoir (permanente retentie) significant is. Bovendien illustreert het model duidelijk dat de wandflux zowel uit geïnjecteerde waterstofisotopen als wandgedesorbeerde waterstofisotopen bestaat. Indien de RF-duty cyclus niet geoptimaliseerd wordt, zal dit recyclingproces maken dat een groot deel van de gedesorbeerde wandisotopen verloren zullen gaan in het permanente reservoir. De opname in het model van de recuperatie van isotopen uit het permanente reservoir was niet noodzakelijk om de partiële drukken te reproduceren. Op dit moment is het niet duidelijk of de permanent opgeslagen deeltjes kunnen worden gerecupereerd, en dus of waterstof-ICWC

effectief kan worden toegepast voor het verminderen van de tritium inventarisopbouw in ITER. Bijkomende experimenten zijn nodig om dit verder te bestuderen.

Het model werd gebruikt om de isotoopuitwisselingsefficiëntie als functie van de ontladingstiming (RF pulslengte en het interval tussen de opeenvolgende RF-pulsen) en de vacuümpompsnelheid te bestuderen. Het was mogelijk om met het wandmodel de ideale RF pulslengte en pompinterval tussen opeenvolgende pulsen te identificeren die samen toelaten om de maximum hoeveelheid van de wandgedesorbeerde deeltjes te kunnen recupereren uit het vacuümvat, terwijl de permanente retentie van het ontladingsgas en van wandgedesorbeerde deeltjes geminimaliseerd wordt. De optimale tijdsduur tussen opeenvolgende RF-pulsen is afhankelijk van de wandparameters (materialen) en de vacuümpompparameters. Voor het bereiken van hoge conditioneringsrendementen is het zeer belangrijk dat de vacuümpompsnelheid hoog is.

Extrapolatie naar ITER

Er werd geconcludeerd dat ICWC een efficiënte wallconditioneringstechniek is, geschikt om te worden toegepast op ITER tijdens de operationele cycli, dwz. wanneer het toroïdale magnetische veld aanwezig is, voor interpulsconditionering en conditionering gedurende de nachten. De conditioneringsdoelen van He-ICWC voor ITER kunnen worden samengevat als: (a) recupereren van plasma start-up na disrupties, (b) desaturatie van de wanden van waterstofisotopen om plasma start-up te kunnen garanderen, en (c) het verbeteren van de plasmaprestaties door onzuiverheden te verwijderen. He-ICWC dient derhalve te worden toegepast voor de start van een tokamak plasma, dus voor inter-pulsconditionering. De conditioneringsdoelen van H_2-ICWC (of D_2-ICWC) zijn: (a) het veranderen van de wandisotoopverhouding om de plasma-isotoopverhouding te kunnen controleren, (b) het verbeteren van de plasma prestaties door het verwijderen van onzuiverheid, en (c) het verwijderen van tritium. H_2-ICWC kan worden toegepast voor conditionering gedurende de nachten, gevolgd door He-ICWC om lage recyclingwaarden in de daaropvolgende tokamakplasmas te verzekeren.

Geoptimaliseerde ontladingsscenario's werden voorgesteld, geëxtrapoleerd van geoptimaliseerde ontladingsresultaten op de huidige tokamaks. Op de huidige apparaten is een ideale ontladingshomogeniteit verkregen door het opereren van de antennes met monopoolfasering en door het toepassen van een klein verticaal magnetisch veld van typisch $1 - 1.5\%$ van het toroidale magnetische veld. Een 435 s lange He-ICWC-procedure werd voorgesteld voor ITER inter-pulsconditionering. De procedure bestaat uit 15×2 s RF-pulsen, met inachtneming van drie karakteristieke vacuümpompingstijden tussen twee opeenvolgende RF-pulsen, een heliumdruk van $2 \cdot 10^{-4}$ mbar en een gekoppeld vermogen tussen 4 en 5 MW. De voorgestelde gepulseerde

procedure bewerkstelligt de optimale verwijdering van de wandgedesorbeerd deeltjes en limiteert de eventuele heliumretentie in de PFC's. De procedure is in staat om 0.3 monolagen van waterstofisotopen uit de wand te verwijderen. De benodigde helium-gasinjectie voor deze procedure komt overeen met minder dan 1% van de cryopompcapaciteit. Ook voor H_2 of D_2-ICWC werd een 435 s lange procedure voorgesteld (die natuurlijk moet worden uitgebreid in geval van conditionering gedurende de nacht). De procedure bestaat uit 15×2 s RF pulsen, waar ook drie karakteristieke vacuümpompingstijden tussen twee opeenvolgende RF-pulsen in acht genomen zijn, een waterstofdruk van $2 \cdot 10^{-4}$ mbar en een gekoppeld RF-vermogen tussen 1.5 en 2 MW. Ook in het geval van waterstof-ICWC optimaliseert de voorgestelde gepulseerde procedure het verwijderen van wandgedesorbeerd deeltjes en beperkt het de ontladingsgasretentie. Een dergelijke procedure zou tot 1.7 monolagen waterstofisotopen kunnen verwijderen uit de wand, wat overeenkomt met 68 mg tritium in het geval van een 50:50 D:T wandisotoopverhouding. Het is verwacht dat slechts een klein deel van deze tritiumatomen afkomstig zal zijn van gecodepositioneerde lagen.

English summary

Introduction

Energy from magnetic fusion is a high potential alternative for present greenhouse gas emitting energy technologies. Fusion is acknowledged to be inherently much safer than energy production from nuclear fission, and unlike for the latter technologies, the fuel for fusion is abundantly available. Currently the ambitious worldwide ITER project is the leading subject of the research to magnetic fusion. The objective of the project is to demonstrate that it is possible to produce commercial energy from fusion. ITER is designed to deliver five to ten times the power it consumes, for a duration of up to 1000 seconds. In case of success, the ITER project will be followed by an industrial demonstration reactor project: DEMO (anno 2030-2040).

Energy out of nuclear fusion is produced by merging light nuclei together into heavier nuclei. This merging together is due to the attractive nuclear force and is achieved by bringing the positively charged nuclei very close to each other, so that the attractive nuclear force becomes larger than the repulsive electrostatic Coulomb force. To overcome the Coulomb barrier sufficient particle energy, in the order of millions Kelvin is required. Today's research on fusion energy is based on the D-T reaction, both isotopes of hydrogen, producing a (not radioactive) helium nucleus and a neutron with a combined energy of 17.6 MeV: $\mathrm{D} + \mathrm{T} \rightarrow {}^4\mathrm{He}\ (3.5\,\mathrm{MeV}) + \mathrm{n}\ (14.1\,\mathrm{MeV})$. At the required temperatures, the deuterium and tritium 'fuel' molecules will be broken into their constituent atoms. The atoms in turn will be ionized turning the fuel into a plasma, containing charged particles: positive ions (nuclei) and negative electrons. The plasma of an energy efficient fusion reactor has to induce a sufficient number of fusion reactions (1 GW of fusion power equals $3.5 \cdot 10^{20}$ D-T reactions/s), and the released energy has to exceed the external energy required to heat up the fuel. The situation where the plasma heats itself by fusion reactions so that external heating can be switched off is called ignition. The criteria to reach ignition is given by the triple product: $n_e T \tau_E \geq 3 \cdot 10^{21}\,\mathrm{m}^{-3}\mathrm{keVs}$, where n_e is the plasma electron density, T the plasma temperature and τ_E the energy confinement time, a measure of the rate at which the system loses energy to its environment. Magnetic fusion research aims at approaching the ignition condition by trapping the plasma ($n_e = 10^{20}\,\mathrm{m}^{-3}$) in a torus-shaped bottle created

by magnetic fields providing a high energy confinement time ($\tau_E = 3\,\mathrm{s}$) and maintaining it at very high temperature ($T = 10\,\mathrm{keV} \approx 10^8\,\mathrm{K}$).

The tokamak magnetic confinement configuration has been successfully used to produce fusion reactions and is currently the path that is studied the most. The magnetic configuration of a tokamak consist of helicoidal magnetic field lines forming torus shaped magnetic surfaces, drawn by the path of the field lines. The toroidal field component is generated by a series of current coils encirculating the plasma poloidally. A first poloidal magnetic field component is produced by an intense axial current flowing in the toroidal plasma itself, generated by induction like in a transformer. A second additional poloidal field component, employed to achieve plasma equilibrium and to optimize the shape of the magnetic surfaces, is produced by toroidal current coils. The experiments presented in this manuscript are carried out on European tokamaks TORE SUPRA (IRFM, CEA/Cadarache, France), TEXTOR (IPP-Jülich, Germany), ASDEX Upgrade (IPP-Garching, Germany) and JET (CCFE, UK), and frame in the preparation of the ITER tokamak operation.

To receive and extract the heat load from the plasma via the inevitable wall intersection points of the outer magnetic field lines, dedicated components are placed in the chamber of the above tokamaks. In limiter tokamaks (TORE SUPRA, TEXTOR) a solid toroidal surface defines the edge of the confined plasma (where the magnetic surfaces are closed) since it is the first material component intercepting the field lines with respect to the plasma center. A fusion reactor cannot rely on this configuration since the heat load on the limiter surface and the impurity production rate would be too elevated. In the divertor configuration (ASDEX Upgrade, JET), the last closed magnetic surface is determined solely by the magnetic field lines. The first solid surface, the divertor target, interacting with the plasma is at some distance from the last closed magnetic surface so that impurity penetration into the plasma center is reduced. ITER has adopted the divertor configuration.

The performance of the tokamak plasma center greatly depends on its interaction with the plasma edge close to the vessel walls, and with the plasma facing components (PFC's). Basic plasma surface interaction processes such as erosion (sputtering and chemical erosion), implantation, trapping, deposition, adsorption and desorption may induce release of wall material and thus introduce impurities in the plasma (impurity desorption), cause net release or retention of fuel (fuel recycling), and induce degradation of wall materials. Release of impurities has to be avoided since it may cool down the plasma by radiation, dilute the plasma fuel reducing the fusion power, lower the plasma stability and global energy confinement, and enhance the further production of impurities. Strong fueling by the vessel walls has to be avoided since it may prevent discharge initiation and make density control impossible. Retention of fuel is also problematic, since it is estimated that the administrative limit attributed to the tritium in-vessel inventory on

ITER, set to 640 g, can be attained in less than 1 year of ITER exploitation. To extend the ITER operation period, the tritium inventory build-up due to fuel retention by implantation and codeposition, thus has to be mitigated.

To control the described surface interactions and the tritium inventory build-up there are three actors: (1) proper selection of wall materials, (2) proper selection of tokamak magnetic configuration, e.g. divertor, limiters, and operation regimes and (3) control the wall surface state. This manuscript focuses on the third actor, namely wall conditioning. In present devices a set of wall conditioning techniques are used to set the wall surfaces in the desired state. The ITER relevant techniques are (a) heating of the wall materials (Baking) to induce thermal desorption of particles. Baking is an efficient but lengthy procedure (order of days). To reduce the tritium inventory on ITER, the estimated required bake frequency is around 2 to 8 times a year. (b) Glow discharge cleaning (GDC), which is a routine conditioning technique on almost all fusion devices. GDC was shown to be inefficient in presence of the toroidal magnetic field. In superconducting devices like ITER, where the toroidal magnetic field in the vessel will be present during operation cycles (periods of the order of weeks), the operation of GDC will thus be limited to machine shut-down periods. (c) The use of tokamak discharges for conditioning (separatrix scanning and controlled disruptions), which might require dedicated tokamak discharges since the control of the ramp down scenario (discharge ending) in ITER DT-plasmas is considered to be subtle and fragile. (d) Ion cyclotron wall conditioning (ICWC), which is the main topic of this PhD manuscript and currently the most promising technique to be employed on ITER during the operation cycles (in presence of magnetic field). (e) Electron cyclotron wall conditioning (ECWC) discharges, produced at nominal toroidal magnetic field by coupling RF waves in the electron cyclotron range of frequencies, using the standard tokamak electron cyclotron heating systems. The technique is found to be less efficient than ICWC and GDC, and moreover the poloidal discharge homogeneity is very poor. (f) Pulsed glow discharge conditioning (P-GDC) discharges, produced by using conventional GDC electrodes coupled to a high frequency power supply. This recent technique requires further study and development on multiple machines to optimize the homogeneity, demonstrate its efficiency, and assess the applicability for ITER.

The qualification of wall conditioning discharges applicable in presence of the toroidal magnetic field for inter-shot and overnight conditioning during ITER operation cycles is considered a high priority task. The conditioning discharges need to mitigate the tritium inventory build-up, to achieve the required low recycling levels at plasma start-up and to reduce impurity (and fuel) levels after plasma disruptions. Since ICWC has been successfully tested on several devices and proved favorable characteristics compared to ECWC, it has been included in the project functional requirements. This PhD work frames in the R&D program on ICWC, advancing to consolidate the ICWC technique and to qualify it for application in ITER and possibly

other future machines.

ICWC principle

ICWC, operated in presence of the toroidal magnetic field, makes use of four main tokamak systems: the ICRF antennas to initiate and sustain the conditioning discharge, the gas injection valves to provide the discharge gas, the machine pumps to remove the wall desorbed particles, and the poloidal magnetic field system to optimize the discharge homogeneity. Additionally neutral gas and plasma diagnostics are required to monitor the discharge and the conditioning efficiency.

ICRF discharge production can be divided into the pre-wave stage and the plasma wave stage. The initial breakdown phase corresponds to the pre-wave phase. The plasma density build-up in the initial breakdown phase is due to collisional ionization by electrons accelerated in the near antenna parallel electric field. In the wave phase, the electromagnetic field expands in the vessel volume causing further space ionization. In this phase the RF power is absorbed mainly collisionally by electrons. Antenna operation schemes are identified that improve the plasma breakdown time, the efficiency for RF power coupling to the plasma and the plasma homogeneity. These consist either of decreasing the cut-off density for fast wave (FW) propagation, namely operation at close to monopole strap phasing and/or operation at high cyclotron harmonic numbers (e.g. at strongly reduced toroidal magnetic field values), or rely on mode conversion scenarios of the evanescent FW into the slow wave or ion Bernstein wave in plasmas with multiple ion species (which is the case in ICWC plasmas). It was concluded that for ICRF plasma production, monopole strap phasing of the ICRF antennas is the optimal mode of operation.

Via the produced plasma one aims at creating a controlled flux of particles to the wall surfaces provoking either liberation of impurities, erosion of codeposited layers, desaturation of the subsurface fuel reservoirs, or changing their isotopic ratio. For the discharge gas, fed via the injection valves, one can choose inert (e.g. He) or reactive gases (e.g. H_2, D_2, O_2), depending on the conditioning purpose. The particles which are intentionally released from the wall surfaces need to be removed from the vacuum vessel. For this the standard machine pumps of the device are employed that are continuously operational to provide the required vacuum conditions. To allow for achieving high conditioning efficiencies it is important that the vacuum pumping speed is high. The efficiency of the conditioning technique for desorbing particles from the surfaces and removing these particles from the vacuum vessel, can be assessed via different diagnostic systems amongst which the most important are the neutral gas analyzers (e.g. pressure gauges, mass spectrometry, ...).

PhD aims

The experimental objectives of the PhD comprise the study and optimization of ICWC on multiple devices; TORE SUPRA, TEXTOR, ASDEX Upgrade and JET, which allows testing the conditioning discharge under multiple conditions (different antenna systems and available frequencies, wide range of vessel sizes, limiter and divertor configurations, carbon PFC and tungsten PFC). Since hydrogen and helium are likely the most suitable discharge conditioning gases for ITER (e.g. O_2 discharge conditioning is not allowed during the D-T phase), the research is limited to hydrogen and helium ICWC discharges. Since the discharges are found to be toroidally homogeneous but poloidally inhomogeneous, the mechanisms that cause these inhomogeneities have to be determined, and methods to improve the poloidal homogeneity have to be found. Also the homogeneity of the wall flux needs to be considered. For this the main wall bombarding species need to be characterized. The effect of the wall flux components on the conditioning efficiency and their dependencies on the discharge control parameters have to be investigated. The study of H_2- (and He/H_2)-ICWC comprises investigating the techniques ability to change the wall isotopic ratio and to remove codeposited layers (tritium removal). The study of He-ICWC needs to focus on the techniques ability to desaturate the wall surfaces from discharge fuel, as well as evidencing the operational effectiveness of He-ICWC to recover normal tokamak operation after plasma disruption events and to lower the vacuum base pressure levels of impurities. For both H_2 and He-ICWC, the dependency of the conditioning efficiency on the discharge control parameters (pressure, RF power, toroidal and poloidal magnetic field strength, pumping speed, ...), its evolution in time, and the advantage of pulsed ICWC compared to continuous RF discharges has to be treated. The ICWC efficiency to remove impurities has to be investigated, and the overall efficiency of ICWC has to be compared to other techniques (GDC, Taylor discharge cleaning (TDC)). Experience has to be gained with respect to safe operation of the ICRF antenna systems.

The development of models can lead to important insights. To increase the understanding and to verify the existent models, the following modeling objectives were defined. An existing 0D ICRF plasma code for atomic hydrogen needs to be upgraded to include molecular hydrogen and helium. The implementation of molecular hydrogen is motivated by the low temperature of the plasma and the related incomplete ionization of the neutral gas. The developed model needs to be benchmarked to experimental data of TORE SUPRA and TEXTOR, and needs to complement the experiments with data that cannot be measured. The model has to reproduce the experimental plasma densities (the available electron temperature measurements being unreliable at the typical low temperatures). Causes of discrepancies between model and experiments need to be investigated. Once the plasma density and its dependencies on the discharge control parameters can be

reproduced with sufficient accuracy, the main plasma and wall bombarding species can be identified. The deduced wall fluxes need be compared with experimental data. To better understand the plasma wall interaction (PWI), the out-pumped fluxes, wall desorbed fluxes and wall bombarding fluxes need to be related to each other. The model needs to allow proposing optimizations of the discharge control parameters to increase the conditioning efficiency. To interpret experimental isotopic exchange results and to propose optimized discharge scenarios for isotopic exchange, a final code, linking the 0D plasma code for hydrogen to a minimum description of the plasma wall interaction should be envisaged.

The obtained results need to be extrapolated to ITER, assessing the applicability and proposing implementations of ICWC on ITER.

Discharge homogeneity

Achieving homogeneous RF conditioning discharges is important to ensure the effective conditioning of the maximum vessel wall area. It is found that the observed radial inhomogeneities can be explained in terms of RF power absorption properties, and that vertical inhomogeneities are due to the confinement properties of the magnetic configuration. Close to the vessel walls, in regions where the magnetic field lines are limited by wall structures such as poloidal limiters, the plasma density is observed to decrease exponentially, which evidences the existence of a plasma edge in ICRF discharges. Due to the existence of this edge plasma, the ion wall flux is concluded to be largest on the first limiting surfaces. In order to obtain a radially homogeneous RF plasma in the vessel, proper wave propagation or at least a large decay length of the evanescent RF field is required, allowing to sustain the plasma also at the high field side (at central column). By applying a small vertical magnetic field that stretches the plasma in the vertical direction, the vertical homogeneity can be improved. Experiments on JET, the largest present device, set up in ITER like conditions evidenced the feasibility of filling the entire JET vacuum vessel with plasma: by operating the antenna with monopole strap phasing and on application of a small vertical field, bright recycling radiation was observed both at the central column on the high field side and in the divertor area.

Wall conditioning efficiency

To study and optimize the efficiency of ICWC, experiments are conducted on TORE SUPRA, TEXTOR, JET and ASDEX Upgrade. Firstly the isotopic exchange efficiency of H_2 and H_2/He discharges was studied, and secondly the efficiency for wall desaturation and recovery of normal tokamak operation after disruptions using He discharges were studied. Finally also, the ICWC efficiency for codeposited layer and impurity removal is discussed.

Hydrogen ICWC is able to change the surface state within short time scales (removal of hydrogen monolayers within minutes), both on carbon machines TORE SUPRA, TEXTOR and JET as on tungsten device ASDEX Upgrade. However the removal of wall isotopes can go at the price of an up to ten times higher retention of the discharge gas. In isotopic exchange experiments, the ideal ratio of retained over recovered particles equals one. It was shown experimentally that the ratio of retained over recovered atoms can be significantly improved by optimizing the RF duty cycle. The ideal ratio of one has been achieved both on TORE SUPRA and on TEXTOR.

The cause of the retention was investigated. From combined experimental results on (i) long term retention behavior on TORE SUPRA, (ii) retention on the tungsten device ASDEX Upgrade, (iii) retention as a function of presence and absence of resonant IC absorption (which lies at the basis of the energetic CX flux to the wall) on TEXTOR, (iv) retention compared to total energetic CX flux on JET, (v) recovery of retained particles by GDC, the hypothesis was made that ICWC discharges reach surface areas that are not accessible by glow discharges. Also the existence of a substantial non-resonant ion wall flux component with energies above the typical GDC flux, causing retention in deeper layers, can at this point not be excluded. Both points require further investigation.

An extensive comparison of the isotope exchange efficiencies of ICWC and GDC on TORE SUPRA and TEXTOR learned that the measured high retention during the ICWC discharges can be understood as an effect of the high reionization probability (mainly due to the higher electron density in ICWC discharges): the probability that a neutral molecule will be ionized or dissociated instead of removed by the machine pumps. Consequently the removal efficiency of wall desorbed species by the machine pumps is less efficient in ICWC than in GDC. This makes that even if a very small fraction of the wall flux remains permanently retained, the high wall fluxes during ICWC and the low pumping efficiency, can lead to a retention rate that is comparable to the removal rate by the machine pumps. Since reionization and wall flux retention only occurs during the plasma discharge, and since it was shown that most of the wall desorbed gas is recovered after the RF pulse, the use of shorter RF pulses ($\sim 1\,\mathrm{s}$) separated by sufficient time between pulses to recover the wall desorbed particles by the machine pumps ($\sim 20\,\mathrm{s}$ on TORE SUPRA) significantly reduces the retention, without severely lowering the total amount of removed particles.

It was found that the absolute removal efficiency of wall desorbed particles is higher at higher pressures and on increasing power. Nevertheless it is concluded that the ideal RF power is the power at which the discharge can be established most reliably from point of view of antenna operation, and at which the discharge is most homogeneous. The evidenced energetic CX flux is found to have only a minor influence on the conditioning efficiency. Whereas the toroidal field strength has a limited effect on the conditioning efficiency (at fixed coupled power), the ICWC conditioning efficiency can

be improved by applying a vertical magnetic field.

He-ICWC discharges were successfully applied on TORE SUPRA to desaturate the wall from hydrogenic particles. The hydrogen is mostly recovered after the RF pulse which indicates that including pumping time in the conditioning procedure increases the removal efficiency of wall desorbed particles. Furthermore, the removal efficiency increases also on increasing the RF coupled power. On TORE SUPRA, He-ICWC was successfully applied to recover normal tokamak operation after plasma disruption events, and it is found that the removal efficiency of He-ICWC is at least as efficient as that of the routinely operated TDC technique, both for hydrogen removal as for removal of H_2O. These both facts indicate that the optimized He-ICWC discharges can be used for inter-pulse conditioning during experimental campaigns on TORE SUPRA.

Both on JET and ASDEX Upgrade was found that during helium containing ICWC discharges, a significant amount of the injected helium was consumed by the wall. On JET, the beryllium elements on the ICRF antennas are thought to be responsible for this. On ASDEX Upgrade, helium losses are also reported for He-GDC, and are due to the tungsten PFC's. Since ITER will have as main plasma facing components tungsten and beryllium it is important to investigate this effect further in future, e.g. on JET which is presently equipped with an ITER like wall. The pulse cycle optimization criteria in terms of the ratio of retained discharge gas over recovered wall desorbed particles, used for hydrogen ICWC, might be adopted for He-ICWC as well. The ideal ratio for He-ICWC, and moreover for any He-based conditioning discharge, equals 'zero'. Also for limiting the redeposition of wall desorbed particles limiting the RF pulse length in He-ICWC should be considered. In case the (eventual) helium retention rates in beryllium and/or tungsten PFC's during helium discharge conditioning are unacceptable for ITER operation, conditioning discharges in other (noble) gases may need to be developed to substitute helium discharge conditioning.

Relatively high removal rates for carbon were recorded on JET, however it could not be determined whether the removed carbon stems from codeposited layers. Also the exposure of samples to TEXTOR ICWC plasmas to evidence carbon erosion or deposition remained inconclusive. It is found that the impurity removal efficiency improves on increasing the discharge power, and additionally it was evidenced that there is no clear influence of the measured energetic CX flux on the removal efficiency. Experiments with the marker gas argon on TEXTOR illustrated that ICWC reaches a large part of the wall area affected by GDC. Finally it was illustrated both on TEXTOR (H_2-ICWC) and TORE SUPRA (He-ICWC) that ICWC can reduce the oxygen content in the vacuum vessel. Whether this removal efficiency is sufficient to ensure tokamak operation, could not be tested in the course of this PhD. For illustration it was mentioned that the supercon-

ducting tokamak KSTAR routinely employs He-ICWC for inter-pulse and lunchtime conditioning, in order to keep the vessel H_2O pressure below the operational limit.

0D model for helium-hydrogen ICWC plasmas

The development of the 0D model for helium-hydrogen ICWC plasmas is motivated by the need to obtain insight on ICRF plasma parameters, particle fluxes to the walls and the main collisional processes, the latter being the fundamental mechanism for the build-up of a plasma. This is of particular importance since most standard tokamak plasma diagnostics are not adapted to diagnose the typical low temperature and low density RF plasmas.

The 0D plasma description is based on the energy and particle balance equations for nine principal species: H, H^+, H_2, H_2^+, H_3^+, He, He^+, He^{++} and e^-. It takes into account (1) elementary atomic and molecular collision processes, such as excitation/radiation, ionization, dissociation, recombination, charge exchange, etc. and elastic collisions, (2) particle losses due to the finite dimensions of the plasma volume and confinement properties of the magnetic configuration, and particle recycling, (3) active pumping and gas injection, (4) RF heating of electrons (and protons) and (5) a qualitative description of plasma impurities.

On inclusion of plasma impurities the model reproduces experimental plasma density dependencies on discharge pressure and coupled RF power, both for hydrogen RF discharges ($n_e \approx (1-5) \cdot 10^{10}\,\mathrm{cm}^{-3}$) as for helium discharges ($n_e \approx (1-5) \cdot 10^{11}\,\mathrm{cm}^{-3}$). The modeled wall fluxes of hydrogen discharges are in the range of what is estimated experimentally: $\sim 10^{19} - 10^{20}\,/\mathrm{m}^2\mathrm{s}$ for H-atoms, and $\sim 10^{17}-10^{18}\,/\mathrm{m}^2\mathrm{s}$ for H^+-ions. In case of helium RF discharges it is found that the wall desorbed particles contribute largely to the wall flux. The main wall bombarding flux are hydrogen neutrals. The helium and hydrogen ion flux can be of the same order of magnitude even though the hydrogen neutral pressure, stemming from wall desorption, is generally much lower than the helium pressure.

The presented 0D ICWC plasma model allowed to reproduce experimental pressure, density and coupled power temporal dependencies of a TORE SUPRA H_2-ICWC discharge from discharge initiation to steady state plasma, and gives insight into the evolution of the particle wall fluxes and retention rates. The wall interaction, represented in the model by a particle recycling coefficient, has a major influence on the neutral pressure and plasma density in H_2-ICWC discharges (in case of constant gas injection). During the breakdown phase, particles are transiently stored in the wall causing a steep pressure drop while during the plasma phase an equilibrium pressure is formed where the permanent hydrogen retention rate approximately equals the gas injection rate. This modeling result reconfirms that

employing shorter RF pulses instead of long or continuous discharges is favored to limit retention, while maximizing the recovery of transiently stored particles.

Simulation of wall interaction in H_2-ICWC

A minimum structure for a 0D reservoir model of the TORE SUPRA (carbon) wall was determined to obtain more insight in experimental isotopic exchange particle balances. The hypothesis used to build up the model is that the same model structure should be able to describe the wall behavior during normal plasmas and conditioning procedures. The model consists of a reduced plasma model based on the 0D model described above, coupled (via wall fluxes and wall release rates) to the wall description. The wall description is based on four reservoirs: an accessible reservoir in which trapping, detrapping and exchange of particles is possible, a permanent reservoir in which only retention is possible, a transient reservoir representing diffusing particles in the wall and an additional reservoir accounting for effects that become important on high filling degrees of the accessible reservoir.

Using the same wall parameters as those determined to describe the wall interaction during long TORE SUPRA tokamak discharges, the model allowed also to simulate the H_2, HD and D_2 partial pressures of ICWC isotope exchange discharges. The model confirms the experimental observed strong interaction with the typical accessible hydrogen reservoir in carbon and shows that the fraction of the wall flux that enters into the permanent reservoir (permanent retention) is significant. Moreover, the model illustrates clearly that the wall flux consists both of the injected hydrogen isotopes and the wall desorbed hydrogen isotopes. If not optimizing the RF duty cycle, this recycling process will make that a large part of the desorbed wall isotopes will be retained in the permanent reservoir. Removal from the permanent reservoir was not required to be included in the model to reproduce the partial pressures. At this point it is not clear whether the permanently stored particles can be retrieved, and thus whether hydrogen ICWC can be effectively applied for mitigating the tritium inventory build-up in ITER. Additional experimentation will be required to study this further.

The model is used to study the isotopic exchange efficiency as a function of the discharge timing (RF pulse length and interval between subsequent RF pulses) and the machine pumping speed. It was possible from the wall model to identify the ideal RF pulse length and pumping time between subsequent pulses to maximize the amount of recovered particles from the wall, while minimizing firstly the retention of injected gas, and secondly the implantation of wall desorbed particles into the permanent retention reservoir. The optimal discharge timing depends on the wall parameters (materials) and discharge parameters, and additionally to allow for achieving high con-

ditioning efficiencies it is very important that the vacuum pumping speed is high.

Extrapolation to ITER

It was concluded that ICWC is an efficient conditioning technique, suitable to be applied on ITER during the operational cycles, i.e. when the toroidal magnetic field is present, for inter-pulse and overnight conditioning. The conditioning aims for He-ICWC on ITER are summarized as: (a) recovering plasma start-up after disruptions, (b) desaturating the wall from hydrogen isotopes to ensure plasma start-up, and (c) improving the plasma performance by impurity removal. He-ICWC should consequently be applied before the start of a tokamak plasma, thus for inter-pulse conditioning. The conditioning aims for H_2-ICWC (or D_2-ICWC) are: (a) changing the wall isotopic ratio to control the plasma isotopic ratio, (b) improving the plasma performance by impurity removal, and (c) removing tritium. H_2-ICWC could thus be adopted for overnight conditioning, followed by He-ICWC to ensure low recycling in the subsequent tokamak plasma.

Optimized discharge scenarios were proposed, extrapolated from optimized discharge results on present tokamaks. On present devices, ideal discharge homogeneity was obtained by operating the antennas in monopole phasing and by applying a small vertical magnetic field of typically $1-1.5\%$ of the toroidal field. A 435 s long He-ICWC procedure is proposed for ITER inter-pulse conditioning. The procedure consists of 15×2 s RF pulses, respecting three characteristic pumping times between two subsequent RF pulses, a helium pressure of $2 \cdot 10^{-4}$ mbar and a coupled power of 4 to 5 MW. The proposed pulsed mode of operation allows optimal removal of wall desorbed particles and will limit eventual helium retention in the PFC's. The procedure is able to remove 0.3 monolayers of hydrogen isotopes from the first wall. The required helium gas injection for this procedure corresponds to less than 1% of the cryopump capacity. Similarly also a 435 s long H_2 or D_2-ICWC procedure is proposed (which of course should be extended in case of overnight conditioning). The procedure consists of 15×2 s RF pulses, respecting also three characteristic pumping times between two subsequent RF pulses, a hydrogen pressure of $2 \cdot 10^{-4}$ mbar and a coupled power of 1.5 to 2 MW. Also for hydrogen ICWC, the proposed pulsed mode of operation optimizes the removal of wall desorbed particles and limits discharge gas retention. Such a procedure would allow to remove 1.7 monolayers of hydrogen isotopes from the first wall, corresponding to 68 mg of tritium in case of a 50:50 D:T wall isotopic ratio. It is expected that only a small portion of these tritium atoms will stem from codeposited layers.

1 Introduction

1.1 Energy for future generations

The energy market has up until the present been dominated by fossil fuels: oil, gas and coal. The market share of renewable energy sources accounts presently only for 10% of the world marketed energy and also nuclear energy provides only 5% [1]. Even though renewables and nuclear energy are expected to have doubled their present capacity in 2035, it is not expected that the energy repartition will change much, since due to economic and demographic growths the world energy consumption will continue to increase year after year [1] (see Fig. 1.1). Taking into account the global fuel reserves (table 1.1) it is nevertheless clear that the energy landscape has to change significantly within this century. The time reserves for oil, which presently accounts for 35% of the marketed energy, and gas, 25% of the present marketed energy, are estimated at respectively 30-40 years and 50-60 years [1]. But this is not the only reason to question the present day energy mix. The huge emission of carbon dioxide due to energy production, 29.7 billion tons in 2007 ($\approx$ 1% of atmospheric CO_2 concentration, 350 ppmv[1]), puts the world energy consumption right in the center of the climate change debate. The past years a consensus is reached among scientists all over the world on the relation between climate change, or global warming, and the emission of greenhouse gases, mainly in the form of carbon dioxide, resulting primarily

[1] ppmv = parts per million in volumetric units.

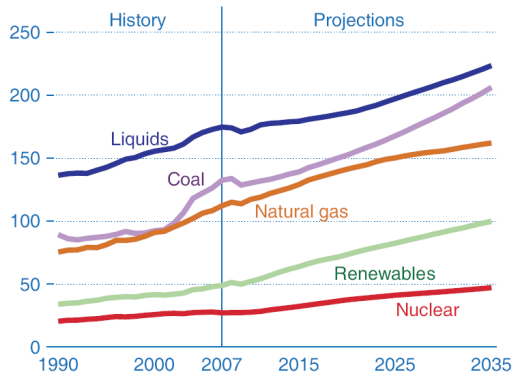

Figure 1.1: World marketed energy use by fuel type, 1990-2035, in quadrillion Btu [1]. (Btu = British thermal unit, equal to about 1055 joules)

from the combustion of fossil fuels. To reduce the impact of our energy consumption on the climate there is thus an urgent need to shift the energy mix to carbon free or carbon neutral energy sources. Present well known carbon free energy sources are for example nuclear and renewable energy sources.

Nuclear energy generation by fission is attracting new interest as countries seek to cope with the increasing demand for electric power, alternatives to fossil fuels, and to increase the diversity of their energy supplies. On employment of new generation breeder reactors, the fission fuel reserves could be extended to the order of thousands years. But still the considerable uncertainty associated with nuclear fission power remains. Issues that slow down the expansion of fission power include:

- Plant safety concerns triggered by e.g. Three Mile Island (1979), Chernobyl (1986), Tokaimura (1999) [3] and very recently Fukushima (2011),
- Radioactive waste disposal,
- Rising construction costs and investment risk (e.g. Superphénix reac-

Table 1.1: Global fuel reserves expressed in years at the current rate of consumption [1, 2] (*Estimation for Uranium without employment of breeder technology)

Fuel	Reserve	Time Reserve (years)
Liquids	$1.4 \cdot 10^{12}$ Barrels	30-40
Gas	$6.6 \cdot 10^{15}$ Cubic Feet	50-60
Coal	$9.1 \cdot 10^{12}$ Tons	129
Uranium*	$5.4 \cdot 10^{6}$ Tons	80

tor in France [4] and the German-Belgian-Netherlands project SNR[2] 300 in Kalkar, Germany [5])

- Nuclear material proliferation concerns.

These considerations open the doors widely for renewable energy sources such as photo-thermal and photovoltaic energy, wind turbines and bio-fuels. Although these will certainly continue increasing their market share, their contribution to the final energy mix will in future remain limited due to scale problems [6]. This makes that the availability of energy resources for next generations remains until now an unresolved question[3].

The Copenhagen Accord[4] to commit countries to collectively reduce their greenhouse-gas emissions and so limiting the global temperature increase to 2°C, and especially the failure to seal the agreement, neglecting the scientific rationales, shows clearly that it will be governments that will shape the future of energy on the longer term[5]. Their investments in research and new technologies, their stimulation of renewables and energy efficient industries, and their 'in-time acting' are indispensable to ensure the smooth energy mix transition required to guarantee energy supply continuity and global climate stability.

1.1.1 Prospects of nuclear fusion

The here presented manuscript frames in the world wide government supported research and development efforts aiming at demonstrating the feasibility of producing commercial energy from fusion. The fusion project is motivated by the advantageous features of fusion over existing energy sources (summarized from [6, 8]).

- The fuel for fusion is abundantly available. The long-term fuel security of fusion exceeds by far that of fission power and fossil-fuel energy.

[2] SNR: Sodium cooled Fast Breeder nuclear reactor

[3] Recently the intergovernmental panel on Climate Change published an assessment on the potential contribution of renewable energy sources (RE) bio energy, direct solar energy, geothermal energy, hydropower, ocean energy and wind energy, to the mitigation of climate change [7]. The majority of the 164 scenarios reviewed in the report show indeed an increase in the deployment of these RE sources by 2030, 2050. More than half of the scenarios show a contribution from RE in excess of a 17% share of primary energy supply in 2030 rising to more than 27% in 2050 (compared to 12.9% in 2008). The scenarios with the highest RE shares reach approximately 43% in 2030 and 77% in 2050.

[4] Result of the United Nations Climate Change Conference (COP15), December 2009.

[5] The World Energy Outlook 2010 report of the International Energy Agency shows that the commitment of the G-20 (Meeting of G-20 leaders in Pittsburgh, September 2009) and APEC (Asia Pacific Economic Cooperation) to "rationalize and phase out over the medium term inefficient fossil-fuel subsidies that encourage wasteful consumption" has the potential to, at least partly, balance the disappointment at Copenhagen.

- Fusion has a low environmental impact. Whereas fission stations produce spent fuel with half-lives of thousands of years, the only radioactive wastes produced from a fusion station would be from the intermediate fuel, tritium, and any radioactivity generated in structural materials. The radioactivity of tritium is short-lived, with a half-life of 12.34 years, and if chosen appropriately the structural materials have a half-life of around 100 years.

- Fusion is inherently safer than fission in that it does not rely on a critical mass of fuel. This means that there are only small amounts of fuel in the reaction zone, making core meltdown-like accidents far less probable, and its consequences less severe.

- Fusion power stations would present no opportunity to cause widespread harm (no greater than a typical fossil-fueled station) owing to the intrinsic safety of the technology. Fusion in a tokamak relies on a continuous external supply of fuel and external heating, without which the process soon dies away.

- As with fission, fusion power stations would provide energy at a constant rate, making them suitable for baseload electricity supply.

- Fusion electricity will be similar to fission electricity in its cost structure; a power station will require complex and expensive engineering, while fuel costs will be negligible in comparison.

- Fusion power stations would not produce fissile materials and make no use of uranium and plutonium, the elements associated with nuclear weapons. This reduces proliferation concerns associated with these elements, although in principle fusion is not completely free from proliferation risks [9–12].

In 1951 a first conceptual design of a fusion reactor, named stellarator[6], was made at the Princeton University by Lyman Spitzer. Around the same time the principle idea of a tokamak[7] was invented by Soviet physicists, followed by an experimental research program at the Kurchatov Institute in Moscow led by Lev Artsimovich. In the 60 years that followed multiple experimental devices have been built, designed with knowledge obtained from the previous ones, eliminating their weaknesses. These research efforts are converging into the design of the first commercial fusion reactor.

[6]The name stellarator refers to the possibility of harnessing the power source of the sun, a stellar object.

[7]The word tokamak is a transliteration of the Russian word токамак, an acronym of " тороидалная камера с аксиал'ным магнитным полем" (toroidal'naya kamera s aksial'nym magnitnym polem) - toroidal chamber with axial magnetic field.

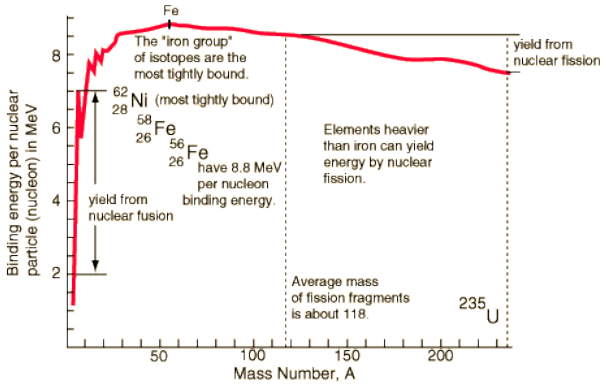

Figure 1.2: Binding energy per nucleon in MeV: Fission of heavy particles and fusion of light particles can yield energy [13].

Currently the ambitious ITER project is the leading subject of the fusion efforts with as objective to deliver five to ten times the power it consumes, for a duration of up to 1000 seconds (see section 1.3). In case of success, the ITER project will be followed by an industrial demonstration reactor project: DEMO (anno 2030-2040).

1.2 Controlled nuclear fusion

1.2.1 Nuclear energy

Nuclear energy can be released by splitting the nuclei of atoms (fission) or by merging nuclei together (fusion). Fig. 1.2 shows the binding energy per nucleon for common isotopes as a function of the number of nucleons in the nucleus. The binding energy is the energy required to disassemble a whole into separate parts. The curve has a maximum around the iron group, which are the most tightly bound or stable isotopes. As the products of nuclear reactions have different binding energies then their reactants, the reaction can be endothermic or exothermic. The fission of heavy particles (e.g. ^{235}U) into lighter nuclei releases nuclear binding energy. Similarly, the fusion of light particles (e.g. from hydrogen to boron) into heavier nuclei releases energy.

1.2.2 The fusion reaction

Since fusion reactions are induced in collisions between particles, the reaction cross section lies at the basis of the choice of the ideal fusion reaction.

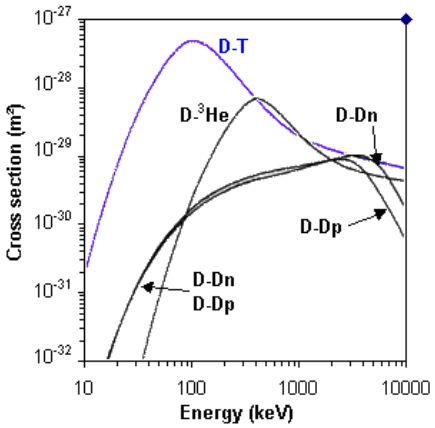

Figure 1.3: Cross sections for fusion reactions (1.1), (1.2), (1.3) and (1.4) as a function of the particle energies.

Fig. 1.3 shows the cross sections for the following four possible candidate reactions as a function of the particle energy:

$$\mathrm{D} + \mathrm{T} \longrightarrow {}^4\mathrm{He}\ (3.5\,\mathrm{MeV}) + \mathrm{n}\ (14.1\,\mathrm{MeV}) \tag{1.1}$$

$$\mathrm{D} + \mathrm{D} \xrightarrow{50\%} \mathrm{T}\ (1.01\,\mathrm{MeV}) + \mathrm{p}\ (3.02\,\mathrm{MeV}) \tag{1.2}$$

$$\xrightarrow{50\%} {}^3\mathrm{He}\ (0.82\,\mathrm{MeV}) + \mathrm{n}\ (2.45\,\mathrm{MeV}) \tag{1.3}$$

$$\mathrm{D} + {}^3\mathrm{He} \longrightarrow {}^4\mathrm{He}\ (3.60\,\mathrm{MeV}) + \mathrm{p}\ (14.7\,\mathrm{MeV}) \tag{1.4}$$

The steep decrease in cross section for lower energies is due to the repulsive electrostatic force between the positively charged nuclei. This Coulomb barrier must be overcome before the attractive nuclear force becomes sufficiently strong to achieve fusion, requiring reactant energies of the order of millions of Kelvin. Since energies above 100 keV ($\sim 10^9$ K) are considered to be impractically high for a commercial reactor, today's research on fusion energy is based on the D-T reaction (eq. 1.1), which clearly has the largest reaction probability (cross section) below 100 keV.

The fusion fuel, deuterium and tritium, are both isotopes of hydrogen. Deuterium is a naturally occurring isotope and hence universally available, with an isotope abundance of 0.015%. The large mass ratio of the hydrogen isotopes makes their separation rather easy compared to for example the uranium enrichment process. Tritium occurs naturally in only negligible amounts due to its radioactive half-life of 12.34 years. In a fusion power plant the production (breeding) of tritium can be done on site using the

following reaction:

$$\mathrm{n} + {}^{6}\mathrm{Li} \rightarrow \mathrm{T} + {}^{4}\mathrm{He} \tag{1.5}$$

The reaction with lithium-6[8] (eq. 1.5), for which the reactant neutron is supplied by the D-T fusion reaction (eq. 1.1), is exothermic, providing even a small energy gain for the reactor. The supply of lithium is more limited than that of deuterium, but still large enough to supply the world's energy demand for hundreds of years. To achieve tritium self-sufficiency, neutron multipliers such as beryllium or lead need to be employed to produce neutrons via (n,2n) reactions. The supply of presently foreseen neutron multipliers, especially beryllium, is limited and requires the further development of alternative sustainable solutions [14].

1.2.3 Fusion energy gain factor, Lawson criterion and triple product

Intuitively an energy efficient fusion reactor has to induce a sufficient amount of fusion reactions (1 GW of fusion power equals $3.5 \cdot 10^{20}$ D-T reactions/s), and the released energy has to exceed the energy required to heat up the reactants. The fusion energy gain factor, the Lawson criterion and the triple product are criteria that formalize this requirement. To initiate fusion reactions in a reactor, external heating has to be used to heat up the fuel to the required fusion temperatures. In this process all the molecular bonds will be broken, rendering the fuel first into its constituent atoms, while further heating will lead to ionization, turning the fuel into a plasma, containing charged particles: positive ions and negative electrons. When the plasma is sufficiently hot so that fusion reactions become possible, the external heating power, designated P_{heat}, can be lowered. A part of the total heating power will then come from the fraction of the fusion power contained in reaction products that remain in the plasma (namely the charged He^{2+} nuclei of 3.5 MeV, see further). This power may be designated fP_{fus}. The power that leaves the plasma can in principle be used as energy source. The **fusion energy gain factor** is defined as the ratio of fusion power produced in a reactor to the power required to maintain the plasma in steady state:

$$Q = \frac{P_{\mathrm{fus}}}{P_{\mathrm{heat}}} \tag{1.6}$$

Via the Q-factor we can define two important situations. The condition of $Q = 1$ is referred to as break-even. It is somewhat arbitrary, but it does mean that a significant fraction (20%) of the heating power comes

[8] The natural abundance of $^{7}\mathrm{Li}/^{6}\mathrm{Li}$ is 0.924/0.076.

from fusion. At conditions of ignition we have an infinite Q-factor which corresponds to a plasma that heats itself by fusion energy without external input. This is in fact not a necessary condition for a practical reactor but on the other hand, achieving $Q = 20$ requires conditions almost as good as that required to achieve ignition.

A general measure for a fusion plasma to reach ignition is given by the Lawson criterion and the triple product. The **Lawson criterion** is the requirement that the fusion heating exceeds the losses. It can be derived for the D-T reaction in the assumption that all the plasma species have the same temperature, and that there are no ions present other than the fuel itself, which is a 50-50 mixture of D and T. In that case, the ion density is equal to the electron density (n_e) and the energy density of both together is given by

$$W = 3n_e k_B T \tag{1.7}$$

where k_B is the Boltzmann constant and T is the plasma temperature. The volume reaction rate k_{fus} of fusion reactions is

$$k_{\text{fus}} = n_{\text{D}} n_{\text{T}} \langle \sigma v \rangle = \frac{1}{4} n_e^2 \langle \sigma v \rangle \tag{1.8}$$

where σ is the collision cross section (given in Fig. 1.3), v is the relative collision velocity, and $\langle\rangle$ denotes an average over the Maxwellian velocity distribution at temperature T. The product of k_{fus} with the energy released per reaction and available for heating, namely $E_{\text{He}^{2+}} = 3.5\,\text{MeV}$ (since the produced neutron is not confined in the plasma, see next section), gives then the volume rate of heating by fusion. A confinement time τ_E is needed as a measure of the rate at which the system loses energy to its environment. Starting from the Lawson criterion,

$$(f P_{\text{fus}} =)\ k_{\text{fus}} E_{\text{He}^{2+}} \geq P_{\text{loss}} = \frac{W}{\tau_E}, \tag{1.9}$$

a minimum value function is calculated for the product of n_e and τ_E as a function of the temperature T. For the D-T reaction, the minimum of the product occurs near $T = 25\,\text{keV}$ and is at least [15]

$$n_e \tau_E \geq 1.5 \cdot 10^{20}\,\text{m}^{-3}\text{s}. \tag{1.10}$$

As the reaction rate $\langle \sigma v \rangle$ varies proportional to T^2 in the temperature range relevant for a fusion reactor, the temperature dependency of the rhs of the above equation can be approximately canceled out by multiplying both sides with T. The resulting **triple product** provides a criterion for ignition that is especially useful for tokamaks because it is only a weak function of density and temperature and therefore a good measure of the efficiency

of the confinement scheme. For the D-T reaction, the ignition condition becomes [15]

$$n_e T \tau_E \geq 3 \cdot 10^{21}\,\mathrm{m}^{-3}\mathrm{keVs}, \tag{1.11}$$

which for example would be reached by $n_e = 10^{20}\,\mathrm{m}^{-3}$, $T = 10\,\mathrm{keV}$ and $\tau_E = 3\,\mathrm{s}$. The precise value of this ignition condition in for example tokamaks depends on the density and energy profiles.

1.2.4 Plasma confinement and the tokamak configuration

The triple product shows that high reactant temperatures, high reactant densities and a good energy confinement are required to obtain a sufficiently high Q factor. Reaching these conditions appears to be a real challenge. Any type of physical confinement like in fossil fuel or fission reactors cannot be used. First of all the materials would not withstand the high plasma temperatures, and secondly the energy confinement time τ_E of the plasma would be too small. Evidently, a gravitational type of confinement that provides a sufficient plasma pressure to maintain ignition conditions like in stars[9], is also not achievable in a reactor. Two paths are currently under study to produce and control high triple product conditions. The first, known as **inertial confinement**, by raising a small volume ($\approx 10\,\mathrm{mg}$) of matter for a very short time (nano seconds) to very high density ($\approx 10^{31}\,\mathrm{m}^{-3}$) and temperature ($\approx 50\,\mathrm{keV}$). In inertial confinement fusion one aims at obtaining the greatest possible number of fusion reactions before the plasma disperses. The second is trapping the plasma in a torus-shaped bottle created by magnetic fields, providing a magnetic pressure, and maintaining it at very high temperature. This is referred to as **magnetic confinement** ($T \approx 10\,\mathrm{keV}, n_e \approx 10^{20}\,\mathrm{m}^{-3}$ and $\tau_E \approx 10\,\mathrm{s}$). The work presented in this manuscript frames into the current research programs to magnetic confinement fusion.

Magnetic confinement relies on the fact that charged particles are affected by magnetic fields: any movement perpendicular to the field will be bent off by the Lorentz force, resulting in the spiraled charged particle trajectories along the magnetic field lines shown on Fig. 1.4, for a rectilinear magnetic field. To avoid particle and energy losses along the field lines, the magnetic field can be closed off in a torus, creating the basis of the **tokamak** confinement scheme (see Fig. 1.5). The resulting toroidal magnetic configuration significantly improves the energy confinement time, but appeared on its own not sufficient to attain the triple product conditions;

[9] In a star the plasma's tendency of dispersing and consequently cooling down is balanced out by gravitational forces.

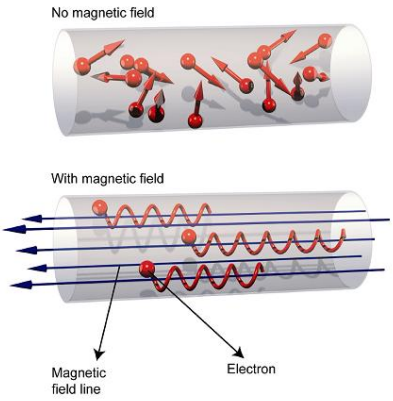

Figure 1.4: Illustration of charged particle confinement by magnetic fields. The top and bottom figure give respectively the charged particle motion in absence and presence of a rectilinear magnetic field, where in the latter case the degree of freedom is limited to one direction: namely along the field lines. [16]

since the toroidal magnetic field has inevitably a field gradient along its main radius R, there will be a drift of particles perpendicular to both the field and the field gradient. This drift works in opposite directions for positive and negatively charged particles creating a vertical electric field in the torus, which in turn will cause a drift of particles to the low magnetic field side. To minimize the particle and energy leakage even more, a circular poloidal magnetic field is added to the toroidal field, resulting in a helicoidal magnetic configuration. The resulting helicoidal magnetic field lines will form magnetic surfaces, drawn by the path of the magnetic field lines as indicated in Fig. 1.5 and 1.6, connecting the low field side magnetically to the high field side, and likewise the top to the bottom, which compensates the particle drifts. In a tokamak the toroidal field is generated by a series of magnets encirculating the plasma poloidally: the toroidal field coils (Fig. 1.5). The circular poloidal magnetic field is produced by an intense axial current flowing in the plasma itself, generated by induction like in a transformer. The first 'transformer' winding is the central solenoid (CS): a coil made up of horizontal layers placed in the center of the configuration. The secondary winding is the plasma itself. Additional poloidal field coils are employed to achieve plasma equilibrium and to optimize the shape of the magnetic surfaces.

The tokamak magnetic confinement configuration has been successfully used to produce fusion reactions [6], and is currently the path that has been

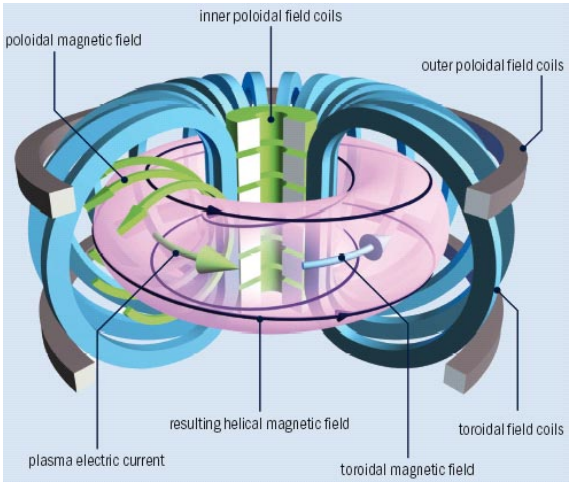

Figure 1.5: Schematic of the tokamak field coils and magnetic field configuration [17]. The toroidal magnetic field is induced by the toroidal field coils, the poloidal field coils add a first poloidal component to this field and the second poloidal component is induced by the plasma current, which is in turn induced by varying currents in the central solenoid.

studied the most. The helicoidal field configuration has also given birth to a second type of machine, namely the **stellarator**. Here the magnetic configuration is entirely based on external currents, flowing in helicoidal coils.

1.2.5 Plasma heating

In present tokamak devices three heating methods are employed to bring the plasma to the required high temperatures to achieve fusion reactions: ohmic heating, neutral injection and radio frequency heating.

1.2.5.1 Ohmic heating

In a tokamak the plasma is heated by the Joule effect via the current flowing in the plasma that is intended to complete the helicoidal magnetic field. At low temperature this heating is very strong but, because the resistance of the plasma varies with temperature as $T^{-3/2}$, it is less efficient at high temperatures [15]. Ohmic heating alone it is not sufficient to drive the plasma up to fusion conditions. The required current would be higher than the maximum physically achievable plasma current determined by the tokamak dimensions, toroidal magnetic field strength and the plasma safety factor.

1.2.5.2 Neutral beam injection

To heat up the plasma to higher temperatures a beam of energetic neutral atoms ($\approx$ 100 keV) can be injected into the plasma. These neutrals are produced by neutralizing accelerated deuterium ions, and will penetrate into the center plasma where they are ionized by collisions with plasma particles. The resulting ion, carrying most of the kinetic energy of the injected neutral atom, is confined by the magnetic field and will transfer its energy to the plasma through Coulomb collisions, causing the plasma to heat up.

1.2.5.3 Radio frequency heating

The plasma may absorb energy from electromagnetic waves at frequencies characteristic to the plasma. These waves are transmitted to the plasma by antennas. When an electromagnetic wave propagates in the plasma, the electric field of the wave accelerates particles which then heat up the plasma via collisions. There are wide varieties of wave modes observed in fusion plasmas which allows many different heating scenarios via the injection of electromagnetic waves. The choice of wave frequency defines the type of particles and the area through which the wave will be absorbed. We separate the ion cyclotron range of frequencies (ICRF, 10-100 MHz), the lower hybrid frequencies (LH, 1-10 GHz) and the electron cyclotron range of frequencies (ECRF, 50-150 GHz).

1.2.5.4 Heating by fusion reactions

As already mentioned, a fourth heating mechanism comes up when there are a great number of fusion reactions. The produced energetic and charged helium nuclei remain confined in the magnetic field and will contribute to the plasma heating by collisions. The produced neutrons are not confined, and will deposit their energy mainly in the vessel walls.

1.2.6 Limiter and divertor configuration

The confinement of the tokamak magnetic configuration is limited to the field lines that do not intersect with material components of the vessel walls [15, 18]. The inevitable wall intersection points of the outer field lines lead to the deposition of an enormous amount of energy (flux of the order of MW/m^2) due to the high plasma temperatures and the particle transport parallel to the field lines. In order to control these heat loads and to prevent wall damage, dedicated components are placed in the chamber to receive

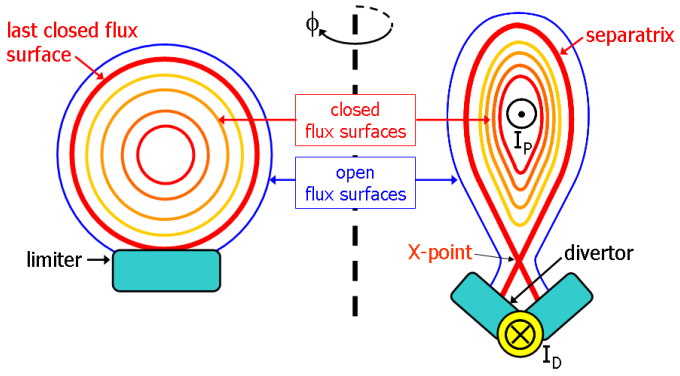

Figure 1.6: Poloidal cross section of two tokamak plasma configurations. Left: limiter configuration with circular plasma (e.g. TORE SUPRA and TEXTOR). The last closed flux surface delimits the border between closed field lines and open field lines. Right: divertor configuration with elongated plasma (e.g. JET, ASDEX Upgrade, ITER). The separatrix delimits the border between closed and open field lines. At the X-point, created by divertor coil currents, negative with respect to the plasma current, the poloidal magnetic field is zero (the magnetic field lines do not cross in this null point). [18]

and extract the heat load from the plasma. Two designs can be distinguished (Fig. 1.6): the limiter configuration and the divertor configuration.

1.2.6.1 Limiter

The limiter is a solid surface that defines the edge of the confined plasma since it is the first material component intercepting the field lines with respect to the plasma center. We distinguish the complete poloidal limiter, acting as diaphragm to the toroidal magnetic field, the incomplete poloidal limiter known as rails or bumpers which are used for example to protect vulnerable wall elements like antennas etc., and the toroidal limiter, limited in poloidal extent but complete in toroidal direction. In general the toroidal limiter defines the last closed flux surface (LCFS), delimiting the core region where field lines are closed, to the plasma boundary or edge where the field line are open and intercept the limiter. In this edge region, called the scrape-off layer (SOL), the plasma-wall interaction takes place (see section 1.4). Limiters play an important role in tokamak operation: (1) localizing the plasma surface interaction, (2) localizing particle recycling and (3) protecting wall from plasma when there are disruptions, runaway electrons, or other instabilities. The disadvantage of the limiter configuration is that released neutral impurity atoms from the limiter surface can enter directly into the confined plasma. Examples of tokamaks employing the limiter

configuration are TEXTOR and TORE SUPRA.

1.2.6.2 Divertor

In the divertor configuration, the LCFS is determined solely by the magnetic field lines so that the first solid surface, the divertor target, is at some distance from the LCFS. Outside the separatrix, separating the open from closed flux surfaces, the plasma will flow toward the divertor targets in which vicinity its heat flux will cool down significantly by radiation (due to the presence of recycled particles and seeded impurities). Eventual released impurities from the target will be ionized and swept back with the plasma flow to the target before they can reach the last closed flux surface, limiting the impurity contamination of the central plasma. Examples of tokamaks equipped with a divertor are ASDEX Upgrade, JET and ITER (see further).

1.2.7 The European tokamaks TORE SUPRA, TEXTOR, ASDEX Upgrade and JET

Throughout this manuscript, experimental results obtained on the tokamaks TORE SUPRA, TEXTOR, ASDEX Upgrade and JET are discussed. Here a short presentation of the devices is given, providing information relevant for our analysis. Table 1.2 gives an overview of their main parameters, and Fig. 1.8 illustrates a comparison of their plasma sizes.

1.2.7.1 TORE SUPRA

The tokamak TORE SUPRA is exploited by the Institute for Research on Magnetic Fusion (IRFM) inside CEA/Cadarache (France). The tokamak has a circular plasma in limiter configuration. TORE SUPRA's main features are its superconducting toroidal field system that enables the generation of a permanent toroidal magnetic field, and its actively cooled plasma facing components. These two features allow the study of plasmas with long pulse duration. Fig. 1.7 shows the inner vacuum vessel with some important parts numbered. The toroidal pumped CFC limiter on the bottom of the vessel can clearly be seen. It is actively cooled and capable of extracting 15 MW of power transferred by the plasma particles. In the same material, TORE SUPRA is also equipped with six pairs of inner bumpers, private protection limiters on the ICRH antennas and the LH antennas, and a movable antenna protection limiter. The whole area is covered by inox panels to protect the machine from radiation. Among other heating systems (see table 1.2) TORE SUPRA is equipped with three double loop ICRF antennas, each with two solid straps and tilted Faraday screen, able to provide all together $10 - 12$ MW of heating power for 30 s. The ICRH

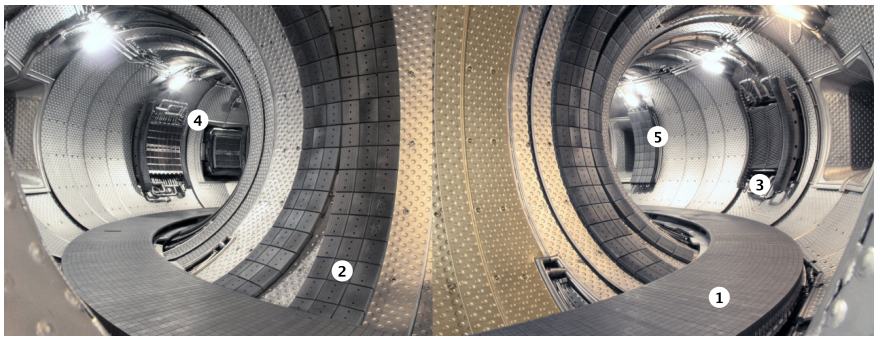

Figure 1.7: View inside the vacuum vessel of TORE SUPRA: 1. carbon limiter, 2. inner bumper (6 pairs), 3. ICRH antenna with carbon protections, 4. LH antennas with carbon protections and 5. movable antenna protection limiter (LPA).

frequency range is $40 - 70\,\mathrm{MHz}$. A scheme of TORE SUPRA's main vessel systems is given in appendix A.

1.2.7.2 TEXTOR

The tokamak TEXTOR is exploited by the Institute of Energy and Climate Research, Plasma Physics (IEK-4), inside the Jülich Forschungzentrum (Germany). TEXTOR is a Tokamak Experiment for Technology Oriented Research in the field of plasma wall interaction. The tokamak has a circular plasma in limiter configuration. It is equipped with a toroidal graphite limiter (ALT-II), poloidal limiters at the top and the bottom of the vessel, and an inconel liner shell. To facilitate the investigation of plasma surface interactions (PSI), two so-called limiter-locks have been developed and mounted at different toroidal sections on the bottom and the top of the vessel (see 'Lim lock' location on figure A.6 in appendix A.2) [19]. The positioning of material elements and diagnostic probes in these ports offers a wide range of possibilities for PSI research.

Among other heating systems (see table 1.2) TEXTOR is equipped with two double loop ICRF antennas, able to provide 2 MW of (generator) power each. Antenna A1 has two poloidal straps, each consisting of three parallel tubes without faraday screen, and antenna A2 has two solid poloidal current straps with faraday screen. The ICRH frequency range is $25 - 38\,\mathrm{MHz}$. Unlike for the A2 antenna, A1 can be switched from π-phasing to 0-phasing. A scheme of TEXTOR's main vessel systems is given in appendix A.

1.2.7.3 JET

The Joint European Torus (JET), Europe's largest fusion device, is exploited by the UK Fusion Association, inside Culham Centre for Fusion Energy, CCFE. As a joint venture, JET is collectively used by more than 40 laboratories of EURATOM Associations for which the European Fusion Development Agreement (EFDA) provides the work platform [20]. JET has a D-shaped plasma and is equipped with a pumped divertor. The main plasma facing component is carbon (CFC). Among other heating systems (see table 1.2) JET is equipped with four ICRF antennas, each consisting of four poloidal straps, able to provide altogether 32 MW of power, in a frequency range of $23 - 57$ MHz. On the ICRF antennas beryllium elements are present, such as the beryllium Faraday screen of the ITER like ICRH antenna [21].

Recently the installation of an ITER like wall has been finalized on JET, replacing the CFC wall elements by beryllium, tungsten coated elements, and tungsten divertor strike points [22].

1.2.7.4 ASDEX Upgrade

The ASDEX Upgrade (AUG) tokamak (Axially Symmetric Divertor EXperiment), is exploited by the Max-Planck-Institute for Plasmaphysics in Garching (Germany) and went into operation at Garching in 1991. ASDEX Upgrade is Germany's largest fusion device at present, and is dedicated to investigating crucial problems in fusion research under reactor-like conditions. The tokamak plasma has a D-shape in divertor configuration. Among other heating systems (see table 1.2), ASDEX Upgrade is equipped with an ICRH system consisting of four generators of 2 MW each and four double loop antennas. The generators, tunable in frequency from 30 to 120 MHz, cover several heating scenarios over a wide range of magnetic fields ($B_T = 1 - 3.9$ T) [23].

1.3 Fusion development and the ITER project

With the ITER project, a global collaboration is formed to push forward the development of fusion. The seven members of the international project are China, EU, India, Japan, Korea, Russia and USA [24]. The project represents a large-scale scientific experiment that aims to demonstrate the feasibility of producing commercial energy from fusion. The objective of the ITER project is to gain the knowledge necessary for the design of the next-stage device: a demonstration fusion power plant (DEMO). In ITER, scientists will study plasmas under conditions similar to those expected in

Table 1.2: Principle parameters of European tokamaks JET, TORE SUPRA (TS), ASDEX Upgrade (AUG) and TEXTOR, including a comparison with ITER: Major (R_0) and minor radii (a/b), plasma ($V_{\rm pl}$) and vessel volume ($V_{\rm vel}$), toroidal magnetic field strength (B_T), plasma current (I_p) available plasma heating systems (P), main plasma facing components, average pulse duration, and configuration.
† possible to operate with tritium
⋆ field provided by superconducting magnets

Tokamak	ITER†	JET†	TS	AUG	TEXTOR
R_0 [m]	6.2	2.96	2.4	1.65	1.75
a/b [m]	2/3.7	1.25/2.1	0.72	0.5/0.8	0.5
$V_{\rm pl}$ [m^3]	840	155	25	14	7
$V_{\rm vel}$ [m^3]	1400	185	50	41.56	17.4
B_T [T]	5.3⋆	3.45	4.5⋆	3.9	3
I_p [MA]	15	7	1.7	2	0.8
Pulse dur. [s]	> 400	~ 10	30-300	< 10	~ 10
$P_{\rm ICRH}$ [MW]	20	10	9	8	4
$P_{\rm ECRH}$ [MW]	20	-	0.7	2	0.8
$P_{\rm LH}$ [MW]	-	12	4	-	-
$P_{\rm NBI}$ [MW]	33	25	-	20	3
Main PFC	Be & W (+C)	C (+Be)	C	W (+C)	C C
Config.	Div.	Div.	Lim.	Div.	Lim.

a future power plant. ITER will be the first fusion experiment to produce net power; it will also test key technologies, including heating, control, diagnostics, and remote maintenance. The ITER site is located in south of France (Cadarache), covering a total area of 180 hectares. The scientific buildings and tokamak facilities are currently under construction. The first plasma is expected to take place in November 2019.

Next to the ITER project, each member state has its own fusion research framework. For Europe we distinguish the European Fusion Development Agreement (EFDA) which is an agreement between the European fusion research institutions and the European Commission to strengthen their coordination and collaboration, and to participate in collective activities [25]. Its activities include coordination of physics and technology in EU laboratories, the exploitation of the present world's largest fusion experiment, the Joint European Torus (JET) in the UK, training and career development in fusion and EU contributions to international collaborations. The European contribution to ITER is the responsibility of the European Domestic Agency called Fusion for Energy, which is based in Barcelona. The European Domestic Agency serves as the link between the European Commission and the

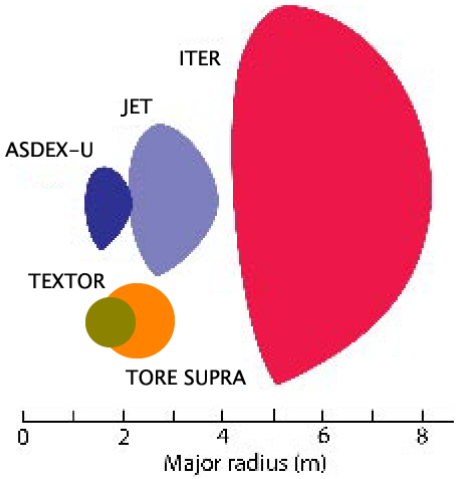

Figure 1.8: Comparison of the plasma sizes of TEXTOR, TORE SUPRA, ASDEX Upgrade, JET and ITER. ITER will be significantly larger than the largest present device JET.

ITER Organization. All of the seven members of the international ITER project have created Domestic Agencies to act as link between national governments and the ITER Organization.

It is important to mention that all research efforts by the constituent institutions of the above organizations aim to converge into the consolidation of fusion. Therefore every studied subject, whether it is of physical, technological or operational considerations, is encouraged to be ITER or DEMO-relevant. The presented work in this PhD manuscript handles one of these subjects, but is of course not the only one.

1.3.1 The objective of ITER

As mentioned above the ITER project aims to test the feasibility of fusion. In detail, the objectives of ITER are to demonstrate that it is possible to produce energy from the D-T reaction in a controllable manner, to confirm the availability of the fundamental techniques required to operate a fusion reactor, and to test the resistivity of wall materials to reactor like conditions [26]. To achieve these objectives, ITER was designed to satisfy following conditions [26]:

1. Maintaining fusion reactions for 400 s with the amplification factor $Q \geq 10$.

2. Achieving stable operation with $Q \geq 5$.

The principal design parameters of ITER are summarized in table 1.2 in comparison with current tokamaks.

1.3.2 The tokamak ITER

1.3.2.1 The magnetic system

The fully superconducting magnetic system [24] of ITER consists of 18 toroidal field coils, 6 poloidal field coils, a central solenoid (CS) and a set of correction coils that magnetically confine, shape and control the plasma inside the vacuum vessel (Fig. 1.9, left). In order to achieve superconductivity, all coils are cooled with supercritical helium to the temperature around 4 K. To provide thermal protection for the superconducting systems, the coils (and vacuum vessel) are enclosed within the cryostat. The toroidal field coils, formed in D-shape, are designed to withstand 1000 charging cycles from zero to full current during the whole ITER lifetime, and the superconducting material for both the central solenoid and the toroidal field coils is chosen/developed to achieve operation at high magnetic field (13 T).

1.3.2.2 Vacuum vessel

The vacuum vessel [24] is a hermetically-sealed steel container inside the cryostat (Fig. 1.9, left) that houses the fusion reaction and acts as a first safety containment barrier. Fig. 1.9 (right) shows a poloidal cross-sectional view of vacuum vessel. The toroidal vessel measures a little over 19 meters across by 11 meters high, and weight in excess of 5000 tons. The vessel has double steel walls, with cooling water flowing between them. The inner surfaces of the vessel are covered with blanket modules that will provide shielding from the high-energy neutrons produced by the fusion reactions. Some of the blanket modules will also be used at later stages to test materials for Tritium Breeding concepts.

1.3.2.3 The divertor

The ITER divertor [24] (Fig. 1.9, right) is located at the bottom of the vacuum vessel, and consists of 54 remotely-removable cassettes, each holding three plasma-facing components, or targets: the inner and the outer vertical targets, and the dome. The targets are placed at the intersection of magnetic field lines where the high-energy plasma particles strike the components. The heat flux received by these components is extremely intense and requires active water cooling. Next to the high heat handling capabilities (divertor

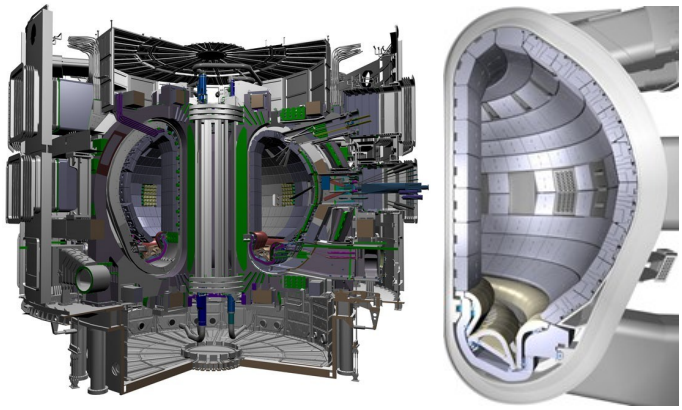

Figure 1.9: Left: Schematic of the ITER tokamak showing the doughnut-shaped vacuum vessel, the superconducting coils surrounding the vessel, the cryostat surrounding the vessel and coils (providing the thermal insulation for the superconducting systems), and the ports through which diagnostics and heating devices will be inserted. Right: A cut-away of the ITER vacuum vessel showing the blanket modules attached to the inner wall and the divertor at the bottom.

target temperatures are estimated to reach 3000 °C), the divertor is designed to efficiently remove the helium ash produced by fusion reactions.

1.3.2.4 The plasma facing components

The primary function of tokamak plasma facing components (PFC) is to provide adequate protection of in-vessel structures, sufficient heat exhaust capability and being compatible with the requirements of plasma purity [27]. The PFC's are chosen according to the following criteria:

1. To avoid high radiation in the plasma center, the blanket modules ($680\,\mathrm{m}^2$, $< 0.22\,\mathrm{MW/m}^2$) will consist of the low Z material beryllium.

2. For its low erosion and high melting point, the divertor will be made of the high Z material tungsten.

3. For its tolerance with excess loads the strike points ($6 - 8\,\mathrm{m}^2$, $< 10\,\mathrm{MW/m}^2$) of the divertor will in the first ITER operation stage be made of high heat resistive carbon composites. This material presents the advantage of high thermal conductivity and it enables an easier learning process for the first years of ITER operation. Then the second divertor set will be made of tungsten which has the advantage of featuring a lower erosion rate and thus a longer lifetime.

On ITER, long pulse high power operation, leading to significant material erosion, will be combined with severe restrictions on permitted plasma core impurity concentrations. In addition, the walls will be subject to transient energy loads on a scale unattainable in current devices [27]. This makes that the choice of wall materials, as well as the control of plasma wall interaction is an important and challenging research domain.

1.3.2.5 The IC heating and current drive system

Among other heating systems (20 MW of ECRH and 33 MW of NBI, see table 1.2), the ITER IC heating and current drive system is designed to couple 20 MW of power to the plasma in the frequency range of 40 to 55 MHz [28]. The IC system comprises two port plug antennas, consisting each of four parallel poloidal arrays of six straps [28, 29]. The radiated power spectrum of the antenna is foreseen to be adjustable by control of the toroidal phase differences between antenna voltages or currents to any desired set of angles, and by control of the voltage or current ratios between columns of straps [28].

1.4 Plasma wall interaction

Plasma wall interaction (PWI) is a key issue for steady state fusion devices. The understanding and the control of the strong and complex interaction between the plasma center, the edge and the wall, is an extensive research domain inside fusion research. In the following we will only give a basic overview of the PWI processes and resulting effects like impurity release, fuel recycling, fuel retention and dust formation. The overview of the PWI processes is required to set the basis of the subject of this manuscript, which is wall conditioning. The overview of the resulting effects is required to motivate the utility of wall conditioning.

1.4.1 Overview basic PWI processes

The basic plasma surface interaction processes discussed here are erosion (via sputtering and chemical erosion), implantation, trapping, deposition, adsorption and desorption. These processes may induce release of wall material and thus introduce impurities in the plasma (impurity desorption), affect the hydrogenic particle balance (fuel recycling) [30], and induce degradation of wall materials as will be discussed further.

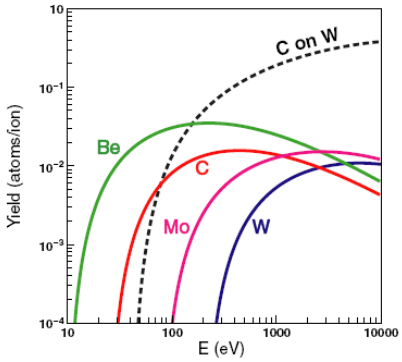

Figure 1.10: Physical sputtering yields for normal incidence deuterium impact on various fusion relevant substrates as a function of the impact energy, and comparison with the sputtering yield of C on W, illustrating the strong yield dependence on projectile mass. [31]

1.4.1.1 Erosion

Erosion of plasma facing components (PFC) happens via physical sputtering, chemical sputtering and chemical erosion. It is an important phenomenon in fusion devices, determining for example the co-deposition rate that results in fuel retention which will be discussed later in this section.

Sputtering is a momentum transfer process which releases atoms when energetic particles, hydrogen or impurities, ions or neutrals, strike solid surfaces. An important contribution to sputtering comes from energetic neutrals arising from resonant charge exchange between hot plasma-ions with cold neutrals. Once an energetic particle is incident on a solid surface, it will produce a collision cascade among the lattice atoms. Sputtering takes place when this cascade results in imposing sufficient energy on a surface atom to exceed the surface binding energy, of the order of a few electron volts for fusion relevant materials [15]. One can further distinguish physical sputtering processes from chemical sputtering. **Physical sputtering** is a threshold process with a yield that is strongly dependent on the target to projectile mass ratio, since momentum transfer improves rapidly as the incoming particle mass approaches that of the target atoms [31]. Fig. 1.10 taken from [31] shows the physical sputtering yields for deuterium bombardment on fusion relevant materials, illustrating its typical threshold behavior. The figure includes one particular ITER relevant case of carbon bombardment on tungsten to demonstrate the dramatic increase in yield for higher mass projectiles. For reactive species, sputtering can continue below the physical sputtering threshold energy, which is called then **chemical sputtering**.

The threshold energy for chemical sputtering is extremely low and so it will nearly always occur whenever chemically reactive species interact. Finally **chemical erosion** by non energetic species, an important process after for example sputtering, arcing and disruption events, contributes also to the degradation of the surface material and to impurity desorption. Chemical erosion by hydrogen and oxygen contributes strongly to the erosion of carbon materials, forming volatile hydrocarbons and carbon oxides [32].

The carbon erosion through chemical and physical sputtering on TEXTOR, mostly stemming from the toroidal belt limiter, is estimated to be $\approx 22\,\mathrm{gC/h}$. The carbon and beryllium erosion on JET in the 1999-2001 campaign was estimated to be respectively $\approx 32\,\mathrm{gC/h}$ and $\approx 1.4\,\mathrm{gBe/h}$, and for the ASDEX-Upgrade 2002-2003 campaign the tungsten erosion was estimated to be $\approx 1.4\,\mathrm{gW/h}$ [31].

1.4.1.2 Deposition and re-erosion

The eroded wall material is transported by the plasma flow in the SOL, and has a high possibility to be redeposited elsewhere on the wall surface. Repetition of the process of erosion and redeposition allows large amounts of material to migrate over the surface area. The extensive analysis in [31] shows that most of the eroded wall material, for which the erosion rate estimations are given above, is redeposited. Although material erosion, migration and redeposition is of no operational significance in current short pulse ($< 10\,\mathrm{s}$) tokamaks, it will be an important issue in ITER. Already on TORE SUPRA, there are clear indications of increasing operational limitations during the experimental campaigns due to presence of re-deposited layers that affect the high power and long pulse performance [33].

In case the eroded material is chemically reactive with the fuel species, as is especially the case for carbon, but also for beryllium, large amounts of hydrogen can be stored in so called co-deposited layers: H/C concentrations of about 0.4 [34]. In most of the present day tokamaks with low Z PFCs, long term fuel retention is dominated by co-deposition. In divertor machines, co-deposition occurs mainly on the inner divertor surfaces and shadowed areas of the outer divertor and limiters [31].

1.4.1.3 Implantation and bulk trapping

Co-deposition is not the only hydrogen retention mechanism. For instance for high Z materials, implantation and bulk trapping is the dominant hydrogen retention process. A study of Roth [34] summarizes the retention due to implantation and bulk trapping for fusion relevant materials: for beryllium at 300 K for an incident D-ion flux of 200 eV, the implantation

will stop after reaching a local concentration in range of about 30 at%. For a similar incident ion flux, CFC components show no saturation of the total implanted amount of hydrogen as a function of fluence[10]. Instead, the retained amount increases close to a square root of the ion fluence due to diffusion deep into the bulk of the material. In tungsten, deuterium is highly mobile and is only retained in radiation damage sites or defects of the crystal lattice. After saturating available traps, inward diffusion and subsequent trapping at deeper lattice defects increases the trapped inventory. The retention greatly depends on the crystalline structure of the substrate. The fuel retention properties of tungsten plasma facing materials may be enhanced due to radiation damage after high fluence n-irradiation.

1.4.1.4 Surface adsorption

Gases can be adsorbed on surfaces in a variety of states. In general, physisorption, which is due to Van der Waal's forces, has a low binding energy of typically $\leq 0.5\,\mathrm{eV}$, whereas chemisorption, involving the exchange or sharing of electrons in a chemical bond, has binding energies of typically several electron volts. On most surfaces there is a wide variety of different sites for adsorption due to imperfections, steps on the surface and multiple layers of adsorbed gas, leading to an almost continuous range of binding energies [35]. The presence of absorbed particles on the walls can be significant. Under normal vacuum conditions a surface will be covered by a layer of adsorbed gas coming from the surrounding atmosphere. An important example of such surface absorbed gas is oxygen, stemming from air exposure during chamber venting (order of 100 monolayers), or water in case of a water leak. A release of an atom surface coverage of 1 monolayer, accounting for $2 \cdot 10^{19}\,\mathrm{particles/m^2}$, increases the plasma density at least by $\sim 10^{19}\,\mathrm{particles/m^3}$, which comes close to the order of the fusion plasma density itself. As the binding energies of adsorbed atoms or molecules are much lower than the plasma temperature, the bindings can be easily broken by impinging plasma species: for long TORE SUPRA discharges the ion fluency from the edge plasma to the wall is of the order of $10^{22}\,\mathrm{D^+/s} \approx 1.5 \cdot 10^{20}\,\mathrm{D^+/m^2 s}$, i.e. high compared to the monolayer density, with energies around $\sim 200\,\mathrm{eV}$, i.e. 2 to 3 orders of magnitude higher than the binding energy [36].

1.4.1.5 Desorption

Besides material release due to sputtering and erosion we distinguish also other desorption processes as re-emission, thermal desorption, photon in-

[10] Fluence is the flux integrated over time.

duced desorption and more exotic types like desorption due to evaporation, shock (disruptions), arcing and blistering [35,37]. Re-emission and thermal desorption are of particular interest for our subject.

Physisorbed particles can be released by thermal desorption, for which the desorption rate will depend on the material temperature. For example, for a binding energy of $E_b = 1\,\text{eV}$ the time taken for surface depletion at 600 K is less than 1 second, whereas at 300 K the time taken would be more than 10 hours. More tightly bound molecules or atoms (with $E_b = 2.5\,\text{eV}$) will not be released in any realistic time, even at temperatures up to 700 K [35].

Diffusing particles in the material bulk will, as they reach the surface before encountering a trapping site, be re-emitted into the plasma. Chemically active particles such as hydrogen require generally to recombine, for example to hydrogen molecules or hydrocarbons, into volatile products that can be released from the wall surface. The characteristic time for particle release by this mechanism is defined by the diffusion coefficient D of the particle in the material, surface recombination coefficient K_r and volume recombination coefficient Γ. A description of diffusion and desorption is complex and needs to take into account, besides the above coefficients, the particle deposition profile of the plasma wall fluxes into the material, a spatially resolved trapping site concentration and its availability [38,39]

1.4.2 Impurity desorption

An important deleterious result of plasma wall interaction is due to the release of impurities. Impurity accumulation in the plasma has multiple unfavorable effects from which it is clear that their release has to be reduced[11] [30]:

- Cooling of the plasma by radiation ($T_e \searrow$). There are two types of processes involved. The first is the enhancement of bremsstrahlung because of the higher effective charge Z_{eff} of the plasma on introduction of charged plasma impurities [15]:

$$Z_{\text{eff}} = \frac{\sum_j n_j Z_j^2}{\sum_j n_j Z_j} \tag{1.12}$$

  with n_j and Z_j the ion density and its charge, and the sum over j represents the sum over all present ions. The second is the enhancement

[11] In section 1.2.6 a beneficial effect of impurities is mentioned, namely the enhanced radiation in divertor area, reducing the heat load to the divertor strike points. However, to achieve this enhanced radiation one will not rely on the impurities eroded from the plasma facing components, but controlled amounts of impurities will be injected into the divertor area.

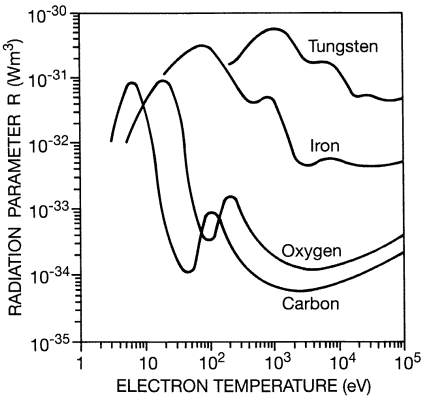

Figure 1.11: Radiation parameter R of various plasma impurities as a function of T_e. The radiated power $P_{\rm rad}$ is given by $P_{\rm rad} = Rn_e n_i$ where n_e and n_i are the electron and impurity densities, respectively. [30]

of the characteristic radiation. The radiated power by line radiation and bremsstrahlung increases strongly with the atomic number Z (see Fig. 1.11, taken from [30]).

- Dilution of the plasma fuel reducing the fusion power ($n_i \searrow$),
- Lower plasma stability and global energy confinement ($\tau_E \searrow$) by increasing the effective charge of the plasma and thus the plasma resistivity [15],

$$\eta = \eta_s Z_{\rm eff}, \quad \eta_s = 2.8 \cdot 10^{-8} T_e^{-3/2} \,\text{ohm m}, \text{ with } T_e \text{ in keV}, \qquad (1.13)$$

- Enhanced erosion of wall materials by sputtering due to multiply ionized impurities. As impurities enhance erosion of wall materials, the impurity accumulation in the vessel is strongly non-linear.

1.4.3 Hydrogen recycling

Under exposure to hydrogen plasmas the wall builds up a subsurface hydrogen concentration. The plasma will continuously exchange hydrogen with these so called hydrogen wall reservoirs, a non-negligible process known as hydrogen recycling. The characteristics of these hydrogen reservoirs depend strongly on the wall materials, whether they are metallic surfaces, ceramics such as graphite or boron and silicon containing layers. Most of the involved processes saturate after certain hydrogen fluence. The hydrogen recycling can vary from a state in which the wall strongly absorbs particles

(wall pumping) to a state in which the plasma is almost completely fueled by hydrogen from the wall. In the latter case it is impossible to control the density of the plasma.

For metals the recycling flux is determined by the value of the recycling constant $R = D/K_r$ where D is the hydrogen diffusivity in the bulk metal and K_r is the recombination rate constant for the recombination of hydrogen atoms into hydrogen molecules at the surface. After a characteristic recycling time $\tau_R = R/Q_{\mathrm{ftw}}$, 50% of the initially pumped hydrogen flux is re-emitted back from the surface (Q_{ftw} is the impinging hydrogen flux density) [30].

Hydrogen recycling in carbon devices is more complex. In steady state situation the recycling coefficient can be written as $R = Q_{\mathrm{sw}}/Q_{\mathrm{ftw}}$, where Q_{sw} is the wall released flux density. Carbon plasma facing components can store up to 0.4 H/C within the range of the impinging hydrogen particles ($\sim 6 \cdot 10^{22}\,\mathrm{D/m^2}$ [40]). The importance of particle induced hydrogen desorption from this accessible reservoir is a direct consequence of the large amounts of hydrogen that can be stored in this reservoir. Additionally on TORE SUPRA, a transient storage of hydrogen is observed, accounting for maximum $\sim 5 \cdot 10^{21}$ particles and saturating in the first $100 - 150\,\mathrm{s}$ of long discharges [41]. These particles are recovered at the end of the discharge. Next to these reservoirs, one distinguishes also a temporary reservoir representing hydrogen that is sticking to the wall surface that can be released at the start of a discharge, and a permanent reservoir representing co-deposited hydrogen and hydrogen implanted in deeper layers.

1.4.4 Tritium retention

The administrative limit attributed to the tritium in-vessel inventory for ITER is set to 640 g[12] [42]. A study on the tritium inventory build-up, due to retention, in ITER has been conducted by Roth et al. [34], taking into account T implantation in CFC, co-deposition of T with eroded C, T implantation in Be, T co-deposition with Be and T implantation in W. In this study the limit was set to 700 g as a figure of merit. The result, summarized in Fig. 1.12, shows that, dependent on the choice of wall materials, the tritium inventory limit is reached in 500 full power ITER discharges (400 s burning duration, 50:50% of D:T, $Q = 10$, 15 MA) for the initial wall design (CFC, W and Be), or, in case of a Be-W wall after 1400 to 4600 discharges, which explains why for the active phase of ITER the CFC in the divertor will be changed to tungsten. But even with this wall material design, the limit of say 3000 shots, can be attained in less than 1 year of

[12] Limit imposed by safety considerations [34].

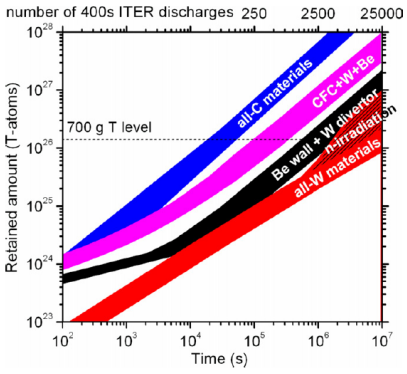

Figure 1.12: Estimations of the tritium inventory build-up in ITER for different wall materials: the initial material choice (magenta), all-C (blue), all-W (red), and the present preferred option, namely a W divertor and Be first wall (black). The assessment was performed assuming different particle fluxes to different divertor and wall areas. Divertor: $3\,\mathrm{m}^2$, $2 \cdot 10^{24}\,(\mathrm{D}+\mathrm{T})/\mathrm{m}^2\mathrm{s}$, $775\,\mathrm{K}$; baffle: $47\,\mathrm{m}^2$, $2 \cdot 10^{23}\,(\mathrm{D}+\mathrm{T})/\mathrm{m}^2\mathrm{s}$, $500\,\mathrm{K}$; and wall: $750\,\mathrm{m}^2$, $1-5 \cdot 10^{20}\,(\mathrm{D}+\mathrm{T})/\mathrm{m}^2\mathrm{s}$, $380-440\,\mathrm{K}$. [34]

ITER exploitation, counting for 20 shots per day, 11 operation days per operation cycle, and 35 operation cycles per 2 years, according to [42]. In this respect, the daily tritium inventory build-up is estimated to be $3-9\,\mathrm{gT/day}$ (20 DT-discharges).

Unless schemes for tritium recovery, or to mitigate the tritium inventory build-up, are implemented, retention would pose serious restrictions on the ITER operation lifetime. The ITER approach to manage the tritium inventory consists of a regime of controlled operations with a spectrum of recovery techniques called 'good housekeeping'. These good housekeeping strategies mentioned by Roth [34] are completely based on wall conditioning techniques.

1.4.5 Dust formation

To complete the overview of on plasma wall interactions, the formation of dust must be mentioned. Dust formation in future fusion reactors is attracting growing attention of researchers due to potentially crucial safety and operational issues arising from its high mobility and reactivity [43]. Furthermore, the amount of tritium stored in dust particles can be significant. Analysis after operation of the JET machine with the MKIIa divertor, showed that 10% of the deuterium and tritium introduced in the machine during this campaign can be stored in dust, flakes and deposits.

The chemical composition of the flake/deposits (180 g) and dust (30 g) material consisted mostly of carbon ($\sim$ 98%), with small amounts of beryllium and metals ($\sim$ 1% each) [44].

Dust can be formed in fusion reactors by various plasma wall interaction processes damaging inner tokamak surfaces, or grow in relatively cold, impurity-rich plasma regions inside the tokamak [45]. The PWI production mechanisms, strongly depending on the plasma facing materials, can be summarized as flaking of deposited layers, melting of surface layers, brittle wall surface destruction, hot spots and unipolar arcs [46]. The removal of dust from the tokamak vacuum vessel in future machines is currently a field under study. It considers a three stage process comprising material mobilization (unsticking materials from the surfaces including surface gaps), collection of the mobilized materials, and transport within the vessel for final removal [47], which is not evident to perform in a nuclear (T) and toxic (Be) environment.

1.5 Wall conditioning

To control the described surface interactions there are three actors: (1) proper selection of wall materials, (2) proper selection of tokamak magnetic configuration, e.g. divertor, limiters, and operation regimes and (3) control the wall surface state. This manuscript focuses on the third actor, namely wall conditioning. In present devices a set of wall conditioning techniques are used to set the wall surfaces in the desired state. Their main issues are:

1. controlling the generation of plasma impurities liberated from the wall,
2. controlling the recycling of hydrogenic fluxes,

In the good housekeeping approach of ITER there is a third important motivation for wall conditioning namely:

3. reducing the tritium inventory,

for which one will rely mostly on the removal of tritium-rich codeposited layers. From tokamak operational point of view, the three wall conditioning aims translate into:

- recover after torus vents to ensure plasma start-up,
- recover after leaks to ensure plasma start-up,
- recover after disruptions to ensure plasma start-up,
- desaturate the wall from hydrogen isotopes to ensure plasma start-up,

- change the wall isotopic ratio to control the plasma isotopic ratio,
- improve plasma performance by impurity removal or deposition of coatings
- extend tokamak operation license by removing tritium.

This section gives an overview of the current employed techniques and their aims, and explains the need for a new technique in future fusion devices.

1.5.1 Methods of wall conditioning

1.5.1.1 Baking

As mentioned in section 1.4.1.5, heating of wall material induces thermal desorption of particles. The conditioning technique 'baking' is based on this effect: the wall surfaces are heated up to temperatures up to 500 K (TORE SUPRA [48]), 500-700 K (TEXTOR [49, 50]), 470-510-620 K (respectively foreseen on ITER vessel, blanket and divertor cassettes [42]). Baking is a lengthy procedure (order of days) and is in most tokamaks only employed after machine venting and in-vessel interventions to remove absorbed oxygen and water. For example on TORE SUPRA baking is employed after ventings and continues until the water pressure is below 10^{-4} Pa which can take up to 2 or 3 days. On ITER it is expected that tritium stored in co-deposited Be-layers can be reduced by 90% by baking up to 620 K [42]. To reduce the tritium inventory on ITER, the estimated required bake frequency is around 2 to 8 times a year [42].

1.5.1.2 Discharge cleaning in hydrogen and other reactive gases

Hydrogen: Cleaning procedures using hydrogen plasmas are based on the reduction of metal oxides by atomic hydrogen, the hydrogenation of carbonaceous deposits to form volatile species in order to deplete the contamination layers on the wall surfaces [30], and on the capability to alter the hydrogenic isotopic ratio of the subsurface hydrogen concentration [51].

The reduction of metal oxides is generally represented by the following reactions [52],

$$\mathrm{MO} + \mathrm{H} \rightleftharpoons \mathrm{MOH} \tag{1.14}$$

$$\mathrm{MOH} + \mathrm{H} \rightarrow \mathrm{M} + \mathrm{H_2O} \tag{1.15}$$

from which it is clear that the cleaning rate will be proportional to the flux density of hydrogen atoms to the wall surface. Also the removal and hydrogenation of carbonaceous deposits needs sufficient wall flux, but additionally

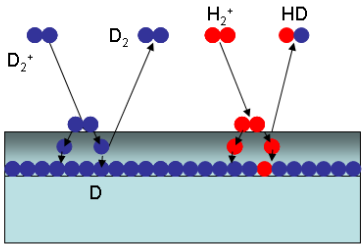

Figure 1.13: Schematic of isotopic exchange by GDC. Hydrogen isotopes are liberated from the wall as energetic hydrogen particles break the bonds between hydrogens and wall material. The remaining vacant trapping sites will be filled by the hydrogen flux to the wall, which allows changing the wall isotopic ratio.

this bombarding wall flux requires sufficient energy to break carbon bonds via chemical or physical sputtering (see Fig. 1.10, page 1-22). From this it is expected that the conditioning flux needs to consist of either energetic ions, or energetic charge exchange neutrals.

In **Isotopic Exchange** the conditioning discharge is employed to change the isotopic ratio of the subsurface hydrogen concentration. A schematic of isotopic exchange mechanism is given in Fig. 1.13. Wall hydrogen isotopes are released as energetic hydrogen particles break the bonds between hydrogens and wall material. The remaining vacant trapping sites will be filled by the hydrogen flux to the wall. The continuous external injection of hydrogen into the discharge and the continuous removal of hydrogen molecules by the machine pumps allows, after sufficient conditioning time to change over the wall isotopic ratio.

Oxygen: Also other reactive gases are used for wall conditioning of which the most important is oxygen. Other examples are nitrogen and ammonia [53]. The use of pure O_2 or He/O_2 mixtures is efficient for the removal of carbon layers through the formation of CO and CO_2 [52]. The concerned chemical reactions are

$$CH_n + (1 + \frac{n}{2})O \rightarrow CO + \frac{n}{2}H_2O \quad (1.16)$$

$$CH_n + (2 + \frac{n}{2})O \rightarrow CO_2 + \frac{n}{2}H_2O \quad (1.17)$$

Although the technique is very efficient for the removal of carbon deposits, e.g. 5.2 g in 4 hours on TEXTOR (O_2-GDC [54], see further) and thus for tritium removal, large amounts of injected oxygen will be retained on the wall surfaces, which might prohibit subsequent normal plasma start-up.

Dedicated oxygen removal cleaning discharges are thus required afterward: on TEXTOR, restart was possible after a long D_2 conditioning discharge followed by He conditioning and boronization [55]. Unfortunately oxidative removal techniques will not be allowed during the nuclear phase of ITER. Their use implies the production of large quantities of highly tritiated water (DTO), which is extremely corrosive and far beyond what the ITER Tokamak Exhaust Processing plant can handle. Moreover, the use of large quantities of oxygen in the exhaust gas is excluded for safety reasons [42].

1.5.1.3 Discharge cleaning in helium

Cleaning discharges in helium are particularly interesting for the desaturation of the subsurface hydrogen concentration. The primary release mechanism in helium cleaning discharges is particle-induced desorption of hydrogen by the energetic He-ions. As the hydrogen concentration in carbon can be significant, helium cleaning is often used in devices with large graphite coverage. Although helium does not intervene in chemical reactions, it is observed that upon exposure to a helium cleaning discharge, CO and hydrocarbon impurities are released from the carbon surfaces [30].

1.5.1.4 Metal film gettering

Metal film gettering makes use of the fact that large sticking probabilities are observed for various gaseous compounds on clean metal surfaces. Metallic tokamak wall surfaces, depleted from carbon and oxygen by discharge cleaning in hydrogen, show getter properties with respect to oxygen and carbon. As such, the controlled evaporation of metals (titanium, chromium & beryllium) has been used to cover large surface areas with a clean film for gettering purposes, which yields very high effective pumping speeds [30].

1.5.1.5 Plasma assisted deposition of thin films

The deposition of low Z films containing carbon, boron or silicon (called carbonization, boronization and siliconization) is very effective in suppressing metal impurities and for oxygen gettering. In addition a strong wall pumping capability and low recycling conditions can be achieved. Conventionally, deposition of thin low Z films is carried out by glow discharges (see further). High quality homogeneous thin films of up to about $0.3\,\mu$m thickness can be deposited onto the first wall by this technique [30, 56]. From different experiments on plasma thin film deposition by RF discharges (see further) it is concluded that in most of the cases, the layer formation is inhomogeneous and the films are limited in thickness and exhibit high hydrogen

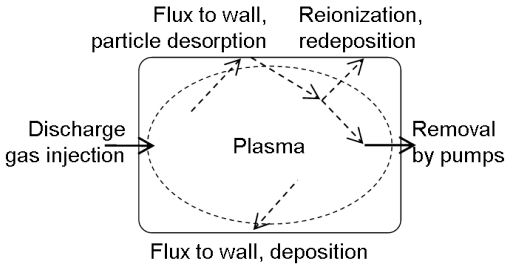

Figure 1.14: Schematic of discharge wall conditioning: the PWI processes initiated by the discharge aim at removing wall impurities, desaturating the walls from fuel, etc. The wall desorbed particles are removed from the vessel by the machine pumps. The plasma, and thus also the wall flux, will contain both injected and wall desorbed particles. As will become clear further during this manuscript, both discharge gas retention and retrapping of wall desorbed particles will occur.

contents [56]. Recent studies show that thin film deposition by Pulsed-GDC (see further) appears also possible [57], although no information on the homogeneity of the layer is available at this point.

Although positive plasma performances have been obtained with the help of this technique (see e.g. [49]), for long pulse operation (ITER: 400 s) it is less attractive since the deposited thin films on the plasma facing components can be completely eroded in a single discharge. Another disadvantage of the thin film deposition technique is related to tritium retention, since tritiated low Z films could be build up on the entire vacuum vessel [56].

1.5.2 Discharge wall conditioning techniques

In this section an overview is given of the presently employed tokamak discharge wall conditioning techniques. The techniques differ in the manner the plasma is produced, which has a direct influence on their specific cleaning efficiency. The efficiency of each technique depends on whether they can fulfill specific conditioning aims and at what speed the conditioning aim is attained. A simple schematic of conditioning discharges, valid for all techniques is given in Fig. 1.14. Every conditioning discharge requires a throughput of gas in the vacuum vessel. The gas is injected by the machine injection valves, either continuous or in short puffs. The machine pumping system evacuates the neutral gas that is present in the vessel, each with their characteristic pumping speed, which allows for the removal of wall desorbed particles. These wall desorbed particles arise from the interaction between the conditioning plasma and the wall surfaces. In the process of wall cleaning, the conditioning plasma will consist of both injected gas and

wall desorbed gas. As such, also the flux to the walls will consist not solely of the injected gas, which can lead to redeposition, or implantation of wall desorbed species. Therefore it is important that the formed products have low probability for being re-ionized or dissociated in the cleaning plasma itself. This requires plasmas with low electron temperature and a low ionization fraction. At the same time high wall fluxes are required to obtain sufficient cleaning rates. An additional method to reduce losses of desorbed particles to the wall are utilizing short discharge pulses with sufficient time between pulses to evacuate desorbed particles, as will be explained in later chapters.

1.5.2.1 Glow discharge conditioning

Glow discharge cleaning (GDC) is a technique routinely used on almost all fusion devices. The principle of GDC is to produce energetic ions that impact on the wall and release impurities through physical and/or chemical sputtering. The experimental arrangement for GDC of vacuum vessels involves one or more electrodes, depending on the size and geometry of the vessel, that are positioned within the vessel. This can be in port holes like on TEXTOR [58], on the inner wall close to ports like on TORE SUPRA [59], or on structures that can move into the vessel center like on KSTAR [60]. The electrodes (anodes) are powered by an excitation source which produces the glow discharge. The to be cleaned in-vessel structures, namely the vessel wall, the limiters and the divertor, are set at ground potential and serve as cathodes.

Although the temperature and density of glow discharges is generally low ($T_e < 10\,\mathrm{eV}, n_e \approx 3 - 4 \cdot 10^8\,\mathrm{cm}^{-3}$ [58]) the ions can have considerable energy, up to $250 - 300\,\mathrm{eV}$, as they are accelerated in the sheath in front of the wall. For hydrogen-GDC, the main species striking the wall are H_2^+-ions stemming from direct ionization of H_2: $Q_{\mathrm{ftw}} \approx 1 \cdot 10^{20}\,/\mathrm{s} = 2.9 \cdot 10^{18}\,/\mathrm{m}^2\mathrm{s}$ (TEXTOR), while also a contribution from neutral H-atoms is expected [58].

In TORE SUPRA, the glow discharge system consists of six anodes located in the upper part of the torus that are powered by a DC voltage. On TEXTOR the glow system consists of two electrodes separated by 180 degrees in the toroidal direction. The anodes consist of a helical coil to which a DC voltage is applied. On to the DC voltage a high frequency voltage (7 MHz) is superposed for igniting and sustaining the plasma [52].

Efficient operation of standard GDC requires the absence of magnetic fields. Fig. 1.15 shows that even on application of a small toroidal field in the order of 1 mT, the glow current in the toroidal device Tomas, measured by metal probes (plates) installed at the torus bottom on three different toroidal locations (0°, 90° and 180°) becomes inhomogeneous due to the

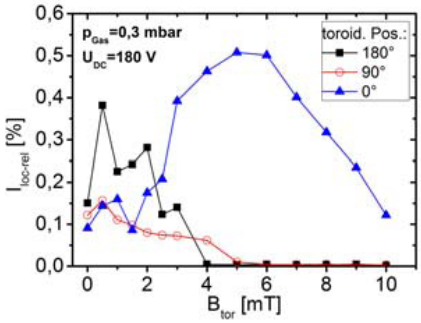

Figure 1.15: The local glow current (as a % of the total current to the chamber wall) measured on the Tomas device at 3 different toroidal positions (0°, 90° and 180° away from the glow antenna) [61].

preferred transport of charged particles along magnetic field lines. The current is given in percentage of the total discharge current to the chamber wall. On increasing the magnetic field to values higher than 4 mT the glow current drops even to zero on two toroidal positions. For efficient conditioning of the vessel walls the particle flux to the walls needs to be homogeneous, which requires a homogeneous plasma. Therefore, in future superconducting devices like ITER, where the toroidal magnetic field in the vessel will be present for long periods, in the order of weeks, the operation of GDC will be limited to machine shut-down periods. As mentioned in section 1.3.2, the total number of TF coil shutdowns foreseen in the ITER magnetic system design is 1000 times during the ITER lifetime [42] (20 years [62]).

1.5.2.2 Taylor cleaning discharges

Taylor discharge cleaning (TDC) using weakly ionized plasma by pulsing the central solenoid was first developed by Taylor [63]. The characteristics of TDC are low plasma current (< 30 kA) and low electron temperature ($2 - 5$ eV). The discharge, effectuated in presence of the nominal toroidal magnetic field, is tested on many devices and found to be very effective. Since the technique does not require to ramp down and afterwards ramp up the toroidal field, which can be time consuming (30 min.), it is routinely used during experimental programs on the superconducting device TORE SUPRA. On this device, the technique is mainly used to desaturate the wall and to recover after disruptions, for which it uses helium as discharge gas.

TDC cannot be used on the future fully superconducting device ITER since the superconducting central solenoid is not designed to withstand the pulsed voltage operation required for TDC. The risks involve heating up the

conductors which may lead to the loss of their superconductivity. Secondly, the high loop-voltage consumption would require repetitive charging of the central solenoid which would take typically 100 s of charging for creating a 1 s TDC-pulse [64].

1.5.2.3 Use of tokamak discharges for conditioning

Separatrix scanning: On ITER, during standard operation, the divertor plasma must be partially detached to satisfy the requirements of heat handling and helium exhaust simultaneously. To erode deposited layers of these H-mode plasmas, and so reduce tritium inventory, it is proposed to use low power L-mode hydrogen plasma and slowly scan the separatrix or limiter plasma along the PFC surfaces [42].

Controlled disruptions: For tritium recovery from the ITER main wall, which has limited bake out temperatures, it is proposed to employ the photonic flash from mitigated disruptions in the lower energy phase of discharge termination. In this manner, due to the high stored energy in the plasma, the beryllium vessel may heat up to $\approx$ 1070 K [42], enhancing the thermal desorption of tritium. Experience in present devices has indicated that this method improves plasma performance, and may even provide desired transient wall pumping for density control in the following discharge [65]. Although very appealing, this method is difficult to control since the ramp down scenario in ITER DT-plasmas requires a subtle and fragile scenario in order to keep the plasma in H-mode [64].

1.5.2.4 Ion cyclotron wall conditioning

Ion cyclotron wall conditioning (ICWC), which is the main topic of this PhD manuscript, is considered as a good candidate for inter-pulse and overnight conditioning on ITER: ICRF plasmas are fully compatible with the presence of a high toroidal magnetic field. The conditioning plasma is sustained by coupling RF power in the ion cyclotron range of frequencies, for which the standard ICRF systems can be used (e.g. JET, ASDEX Upgrade, TORE SUPRA, TEXTOR, W7-AS, LHD, KSTAR and HT-7). The tokamak EAST is equipped with a dedicated antenna for ICWC, and plans for the installation of dedicated ICWC antennas on TORE SUPRA and Wendelstein 7-X are ongoing. Chapter 2 of this manuscript will give an extensive overview of the ICWC technique. Chapter 3 to 6 will discuss in more detail experimental results and modeling efforts on ICWC effectuated during this PhD, and chapter 7 discusses the application of ICWC on ITER.

1.5.2.5 Electron cyclotron wall conditioning

Electron cyclotron wall conditioning (ECWC) discharges are produced at nominal toroidal magnetic field by coupling RF waves in the electron cyclotron range of frequencies, using the standard tokamak ECRH system, at a gas pressure of typically $10^{-3} - 1\,\mathrm{Pa}$ [56]. ECR discharge cleaning was first carried out on JFT-2 in 1980, by using the 2.45 GHz LH system and a magnetic field of 87.5 mT. Since then the technique is tested on many other devices, for example Alcator C-Mod, LHD, TRIAM-1M, TOMAS, JT-60U (1.7 GHz, 0.01 T) and HT-7 [57]. Also the TEXTOR ECRF system (110 GHz) was used for ECR discharge cleanings in helium ($p = 3 - 6 \cdot 10^{-2}\,\mathrm{Pa}$) at $1.65 - 2.28\,\mathrm{T}$ for an input power of $P_{\mathrm{ECRH}} = 200\,\mathrm{kW}$ resulting in a high density plasma ($n_e = 2.4 \cdot 10^{18}\,\mathrm{m}^{-3}$) [66]. Published studies comprise ECR discharges in He, H_2, D_2, Ar, CH_4 and CD_4 in the pressure range between $p = 10^{-4}$ and $6 \cdot 10^{-2}\,\mathrm{Pa}$, for studies on reactive and non-reactive cleaning, thin film deposition and removal of co-deposited layers [57].

The technique is found to be less efficient than ICWC and GDC, and moreover the poloidal homogeneity is very poor. The plasma is localized outwards of the resonance layer and shows a higher density on the microwave beam trajectory [56]. In case of incomplete absorption of the ECRH-beam the remaining beam power will be partially absorbed on the opposite vessel wall, which prevents continuous operation of the discharge, or would require constant sweeping of launching mirrors, which would make the discharge risky and complex [64].

1.5.2.6 Pulsed glow discharge conditioning

Recently a new method, operable in presence of nominal toroidal magnetic field, is demonstrated on superconducting tokamaks EAST and HT-7, named pulsed glow discharge cleaning (P-GDC) [57]. The discharges are produced by using conventional GDC electrodes coupled to a high frequency power supply: $U = 2.0\,\mathrm{kV}$, $f \approx 20 - 100\,\mathrm{kHz}$, $I \approx 10\,\mathrm{A}$.

Preliminary results showed that plasma can be easily initiated in hydrogen and helium, resulting in a glow, uniform in toroidal and poloidal direction depending on the filling pressure. At high pressure (from $10^{-2}\,\mathrm{Pa}$ to a few Pa) the plasma is localized around electrodes, while on lowering the pressure ($10^{-3}\,\mathrm{Pa}$ to $10^{-4}\,\mathrm{Pa}$) the plasma becomes more uniform especially in toroidal direction but also in poloidal direction [57]. At the lowest pressure around $10^{-4}\,\mathrm{Pa}$ the plasma is also uniform in poloidal direction.

The conditioning efficiency, from mass spectrometry measurements, is said to be similar to that of normal DC-GDC (without magnetic field) [57]

and ICWC [42]. The technique is possibly interesting for ITER operation since it is compatible with the presence of a magnetic field and does not require to use expensive hardware, unlike for example the ICRF antenna operation for ICWC, however it is not yet clear whether the planned ITER GDC system can be operated in P-GDC mode [42]. The recent technique P-GDC requires further study and development on multiple machines.

1.5.3 Wall conditioning in fully superconducting devices - ITER

A recent publication by Shimada [42] (proceedings and presentation slides) gives an overview of the foreseen wall conditioning interventions during ITER experimental campaigns. This paper is very instructive and delivers a good outline to illustrate the relevance of the subject of this manuscript for ITER.

During the foreseen ITER operational lifetime (20 years [62]) several experimental campaigns (**Operations Campaign**) will be carried out, that will take about 2 years each [26, 67]. The first planned campaigns are the Hydrogen-Helium Operations Campaign, the Deuterium Operations Campaign and the Deuterium-Tritium Operations Campaign. Each of these experimental campaigns will consist of about 35 operation cycles and 8 months shutdown. The planned wall conditioning techniques during the shutdown periods are baking and GDC, before and after machine vents (2 times a year), and Oxidative cleaning after the Hydrogen-Helium Operations Campaign and before the Deuterium-Tritium Operations Campaign (but not during or after the DT-phase). The **operation cycles** will take 2 weeks each, including 11 operation days during which the toroidal magnetic field will be continuously present in the vessel, followed by 3 maintenance days without toroidal field during which GDC is possible. For the **operation days**, for example in the Deuterium-Tritium Operations Campaign, one expects on average 20 shots per day, counting for 1 discharge every 30 minutes at a machine availability of 60%, taking into account the time to recover machine operation after disruptions. The wall conditioning techniques foreseen to be employed during the operation days and for overnight conditioning require to operate in presence of magnetic field. As mentioned earlier, the presence of the magnetic field prevents the use of standard GDC. Candidates are thus

- separatrix scanning and controlled disruptions, for which probably dedicated tokamak shots are needed, and
- ICWC (and/or P-GDC), for inter-pulse (500 s) and overnight conditioning.

Recently the qualification of inter-shot wall conditioning discharges became a high priority task for ITER [34] in order to mitigate the tritium inventory build-up, to achieve the required low recycling levels at plasma start-up and to reduce impurity levels after disruptions. Since ICWC has been successfully tested on several devices and proved favorable characteristics compared to ECWC, it has been included in the project functional requirements [28,68]. Currently a strong R&D program with various experiments on different devices and modeling efforts is advancing to consolidate ICWC and to qualify it for application in ITER and possibly other future machines. This PhD work is carried out in the frame of this ICWC-program.

As mentioned, the newly demonstrated technique P-GDC looks appealing for ITER, and could be complementary to ICWC. However to fully assess this technique for ITER more extensive tests on multiple machines are required, and its competitiveness with ICWC has to be proven.

1.6 PhD overview

This PhD manuscript is devoted to the study and optimization of the Ion Cyclotron Wall Conditioning (ICWC) technique. The ICWC plasmas are fully compatible with the presence of a high toroidal magnetic field, and have been successfully tested on several devices. The technique is considered for inter-pulse and overnight conditioning on ITER and is therefore included in the project functional requirements [28,68] of ITER.

In chapter 2 a general overview on ICWC is given. The main ICWC elements will be introduced, followed by the state of the art of the research on ICWC before the start of this PhD. From this review, the experimental and modeling objectives of this PhD work will be formulated. In the second part of this chapter three important ICWC elements are presented in more detail. A section is dedicated to the involved RF physics aspects which are of non negligible importance: the ICRF antennas both initiate and sustain the ICWC discharge and thus, although the focus of this manuscript is put on the characterization of the plasma parameters and the assessment and optimization of the conditioning efficiency, the RF aspects need to be included in this manuscript. Hereafter, the neutral particle cycle in the vacuum vessel will be discussed to provide the minimum technological and theoretical basis on this subject, namely on gas injection and particle removal by the pumps, that will allow to understand how wall desorbed particle removal is achieved and can be improved. Finally a short summary of the evidenced ICWC wall bombarding flux is given, this flux doing the actual wall conditioning.

Chapter 3 treats the ICRF discharge homogeneity and the confinement

properties of the employed magnetic field. In the first part we will discuss experimental facts on plasma homogeneity, and how experimental optimization led to its improvement. Where RF power absorption properties cannot explain the inhomogeneities, it is expected that the confinement properties of the toroidal magnetic field lie at the basis of these inhomogeneities. In the second part of the chapter the confinement properties of a partially ionized plasma in a toroidal magnetic field configuration with additional small vertical component are discussed. The magnetic configuration used in ICWC discharges was said to have insufficient confinement properties for ensuring a high enough energy confinement time (see section 1.2.4). We will discuss eventual contributions of these confinement properties to the inhomogeneities of the plasma and the wall flux.

Chapter 4 gives an overview of experimental results on the efficiency of ICWC, obtained on TORE SUPRA, TEXTOR, JET and ASDEX Upgrade. The aims of the presented experiments are the assessment and optimization of the conditioning efficiency and to provide information that allows an extrapolation to ITER. The chapter is divided into three parts. The first two parts are separated according to the discharge gas/conditioning aim: firstly H_2 and H_2/He discharges for isotopic exchange, and secondly pure He discharges for wall desaturation and recovery of normal tokamak operation after disruptions. In these parts, the ability of ICWC to change the surface state will be shown, the wall fluxes and corresponding PWI mechanisms will be characterized, and the particle desorption and retention rates will be calculated. Also the efficiency dependencies on RF power, discharge pressure, magnetic fields, etc. will be treated. And in a final (third) part the efficiency of ICWC for impurity and codeposited layer removal is discussed.

In chapter 5 a 0D kinetic description of hydrogen-helium RF plasmas is outlined. The model, describing the evolution of ICRF plasmas from discharge initiation to the (quasi) steady state plasma stage, is developed to obtain insight on ICRF plasma parameters, particle fluxes to the walls and the main collisional processes. The chapter is divided into two parts where first the implemented model equations are discussed in detail, and secondly the modeling results are presented. The 0D plasma description, based on the energy and particle balance equations for helium and hydrogen plasma species, takes into account (1) elementary atomic and molecular collision processes and elastic collisions, (2) particle losses to the walls and particle recycling, (3) active pumping and gas injection, (4) RF heating of electrons (and protons) and (5) a qualitative description of plasma impurities. The modeling results section includes first a discussion on the implemented elementary reactions, and the description of the plasma parameters as a function of the electron temperature. Hereafter the model is benchmarked

against experimental results. Experimental plasma density dependencies on discharge pressure and coupled RF power will be reproduced, both for hydrogen RF discharges as for helium discharges. Modeled wall fluxes will be compared to experimentally estimated wall fluxes. Finally a TORE SUPRA hydrogen RF discharge will be modeled from discharge initiation to steady state plasma. The particles flux to the wall, and the recycled flux during this discharge will be discussed.

Chapter 6 presents a minimum structure for a 0D reservoir model of the wall to investigate in deeper detail the ICWC plasma wall interaction during isotopic exchange experiments. The hypothesis used to build up the wall model is that the same model structure should be able to describe the wall behavior during normal plasmas and conditioning procedures. The wall module is coupled to a 0D hydrogen-deuterium plasma description, based on the model presented in chapter 5. In the first section of the chapter the model is presented: the wall description is derived from experimental facts and the plasma description is summarized. In a second section the model equations are given. The third section shows the capability of the model to reproduce experimental facts of normal plasma discharges. In a fourth section TORE SUPRA H_2-ICWC discharges are modeled, and proposals for ICWC optimization in terms of discharge timing are worked out. And finally a discussion is added comparing the developed phenomenological model to a recently published, physically more founded wall model.

Chapter 7 summarizes the findings of this PhD manuscript and extrapolates the results to the envisaged application of ICWC on ITER. Hereafter, in the last chapter a general conclusion is formulated.

Appendix A, at the end of this manuscript, contains schemes of the tokamaks TORE SUPRA, TEXTOR, ASDEX Upgrade and JET, illustrating the locations of the RF antennas and the diagnostic systems. In appendix B, an overview of the employed diagnostics is given, where especially attention is paid to the neutral gas analysis systems (pressure gauges, mass spectrometry, ...). And finally, appendix C provides an appendix to chapter 5, including a discussion on the benefits and limitations of a 0D approach, the plots of the relevant collision rates that are included in the model and a further discussion on particle confinement and energy confinement.

2

Ion Cyclotron Wall Conditioning

This chapter gives a general overview on Ion Cyclotron Wall Conditioning (ICWC), the subject of this PhD thesis. We will first explain the ICWC principle, introducing the main elements, followed by the state of the art of the research before the start of this PhD. From the latter section a 'ToDo' list is distilled containing the items that will be treated throughout this PhD manuscript. Then three of the presented ICWC elements will be discussed in more detail: a section on the involved RF physics aspects, a section on the neutral particle cycle in the vacuum vessel (gas injection and particle removal), and finally a summary of the particle wall flux.

2.1 Principle

The basic components of ICWC are designated in Fig. 2.1. It represents a toroidal vacuum vessel, with its characteristic wall materials, in presence of the nominal magnetic field B_T. This magnetic field is inhomogeneous in the radial direction R due its toroidal configuration. To the toroidal field, a smaller poloidal magnetic field can be added ($B_p \ll B_T$):

$$\vec{B}(R) = \frac{R_0}{R} B_T \hat{1}_\phi + B_p \hat{1}_p \tag{2.1}$$

where B_T is the magnetic field on axis, at the major radius $R = R_0$. As was stated in the introduction, the presence of the toriodal magnetic field justifies the use of ICWC, whereas in absence of the magnetic field standard

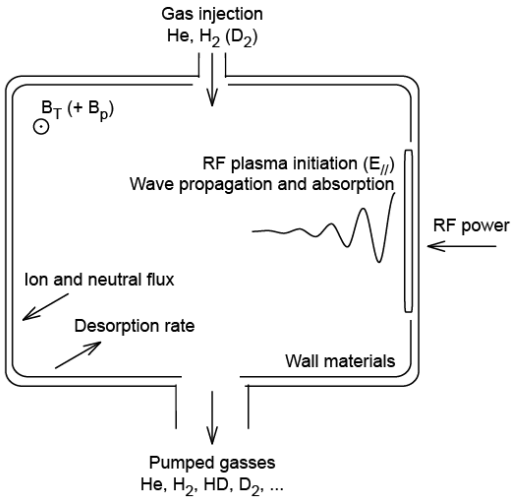

Figure 2.1: Schematic of ICWC showing the vacuum vessel with its wall materials, the present toroidal magnetic field and the required tokamak systems: gas injection valves, machine pumping systems and ICRF antennas. The conditioning plasma is initiated and sustained by the ICRF antennas. The provoked PSI lead to the release of impurities, codeposited layers and/or fuel particles. These released particles are removed from the vacuum vessel by the vacuum pumps.

GDC might be preferred for conditioning purposes. In the figure the wall materials are indicated, which are of fundamental importance for the conditioning technique as they represent the 'to be conditioned' surfaces and moreover determine the possible plasma surface interactions.

As shown on Fig. 2.1, next to the magnetic field systems, the operation of ICWC makes use of three other main tokamak systems: the ICRF antennas, the gas injection valves and the vacuum pumps. ICRH power in the ion cyclotron range frequencies (ICRF) is used to both produce and sustain the discharge. Mostly one employs the standard ICRF heating systems, although dedicated systems for ICRF conditioning are gaining more interest (e.g. EAST [69] and design projects on W7-X and TORE SUPRA). Resonant conditions where the applied RF frequency, ω, equals n ($\in \mathbb{N}_0$) times the gyration frequency of ions around the magnetic field lines, ω_{ci}, can exist along the vessel main radius[1] R:

$$\omega_{ci}(R) = \frac{qB(R)}{m_i} \tag{2.2}$$

[1]When $\omega = \omega_{ci}$ is located on-axis, it means that $\omega > \omega_{ci}$ (conventional ICRF range) from axis towards the LFS (antenna side) and $\omega < \omega_{ci}$ (Alfven wave range) from axis towards HFS.

The presence of these resonances influences the RF power coupling efficiency to the plasma and the discharge homogeneity. An overview of the involved RF physics is given in section 2.3.

For the discharge gas, fed via the injection valves, one can choose inert (He, Ar) or reactive gases (H_2, D_2, O_2, N_2, ...), depending on the conditioning purpose (wall desaturation, fuel removal, removal of codeposited layers, ...). Via the produced plasma one aims at creating a controlled flux of particles to the wall surfaces provoking either liberation of impurities, erosion of codeposited layers, desaturation of the subsurface fuel reservoirs, or changing their isotopic ratio. The particles which are intensively released from the wall surfaces need to be removed from the vacuum vessel. For this one employs the standard machine pumps of the device that are continuously operational to provide the required vacuum conditions. In section 2.4 the neutral gas cycle in the vacuum vessel is shortly reviewed, providing a key element to the wall conditioning efficiency.

The efficiency of the conditioning technique for desorbing particles from the surfaces and removing these particles from the vacuum vessel, can be assessed via different diagnostic systems amongst which the most important are the neutral gas analyzers; namely mass spectrometry, Penning gauge spectroscopy and gas chromatography. For plasma and wall flux characterization one employs interferometry, neutral particle analyzers, Langmuir probes, lithium beam spectroscopy, etc... The employed diagnostic systems throughout this manuscript are discussed in appendix B.

2.2 State of the art and formulation of PhD objectives

In this section an overview is given of ICWC results that were published before the start of this PhD (2008). The progress on the subject achieved during this PhD, supported by an international collaboration between European institutes; ERM/KMS Brussels (Be), IRFM CEA/Cadarache (Fr), IPP Jülich (De), IPP Garching (De) and CCFE Culham (GB), into which this PhD work frames, will be the subject of the next sections and chapters. The presented overview aims at acknowledging the scientists and institutions that have made progress on this subject, and setting the basis from which the work in this manuscript starts. The emphasis in this section is put on experimental and modeling efforts, concentrating on plasma characterization and conditioning efficiency. An overview of the RF-physics aspects is included in section 2.3.

The discovery of ICWC is strongly related to the study of plasma initiation methods for stellarators using ICRF power [70]. Consequently, the

first results on ICRF wall conditioning in fusion machines, published by Nazarov et al. in 1987 [71], were obtained on the Uragan-3 torsatron. The conditioning plasmas, with an electron density of $n_e = 10^{12}\,\mathrm{cm}^{-3}$ and electron temperature of $T_e = 10\,\mathrm{eV}$, were produced at a hydrogen pressure of $\sim 10^{-4}\,\mathrm{mbar}$, RF frequency of 5.4 MHz and magnetic field of $20 - 50\,\mathrm{mT}$ ($\omega \approx 18\omega_{ci}$). Series of numerous ($> 10^4$) short pulses (50 ms) were applied with RF power less than 100 kW, at a repetition rate of 0.2 pulses/s. Subsequent to the cleaning of the metal wall surfaces, significantly improved plasma parameters were obtained where separately a high plasma density, less impurities and more efficient heating of the plasma are mentioned.

In 1996 a review article on wall conditioning in fusion devices, and its influence on plasma performance was published by Winter [30]. In this paper the issue of wall conditioning for future superconducting machines was clearly stated for the first time:

> *The long pulse lengths of the next generation of devices implies that superconducting magnets will be used. The magnetic field will be maintained for long times to avoid cycling the coils. Thus wall conditioning techniques will have to be compatible with magnetic fields. Glow discharges are not suited to these circumstances.* [J. Winter 1996]

Around the same period, ICRF plasma production applications were for the first time performed on tokamaks, namely TEXTOR and TORE SUPRA. The first ICRF plasma production studies, supported by 1-D/0-D self-consistent modeling, were carried out on TEXTOR in 1994 and published in 1995 by Lyssoivan et al. [72]. The first ICRF wall conditioning experiments were performed both on TORE SUPRA and TEXTOR and published respectively by de la Cal and Gauthier et al. [51,73], and Esser et al., also in 1997 [74]. Since then ICWC has been successfully tested in many other devices such as HT-7 [75–78], W7-AS [79], ASDEX Upgrade [80–82], JET [80, 81] and LHD [83]. Also more recently the tokamak EAST and KSTAR [60] successfully employed ICWC.

In parallel to the experimental efforts there has also been considerable progress on the physics aspects of ICWC. The first paper on the modeling of RF plasma production in large scale tokamaks was published by Lyssoivan et al. [84] in 1992, followed up until now by numerous refinements by the same author. Criteria allowing for the optimization of the RF conditioning efficiency were defined by de la Cal and Gauthier in 1997 [51], and were later refined by the same authors in 2005 [56]. The first theoretical modeling efforts on deuterium ICRF discharges, predicting the main plasma parameters and particle fluxes to the wall, were published by de la Cal in

2006 [85].

In the following 4 subsections we will present first an overview on the obtained experimental results, where the focus is put on the wall conditioning efficiency and plasma characterization (section 2.2.1). This kind of overview has already been published by other authors [56, 64, 86], but remains necessary to be repeated here independently to set the basis of the presented work. After this overview the experimental objectives of this PhD are presented in section 2.2.2. Similarly, in the third part (section 2.2.3) a review is given of the modeling efforts on ICWC, whereafter in section 2.2.4 the modeling objectives of this PhD work are formulated.

2.2.1 Experimental results

2.2.1.1 TORE SUPRA

The first ICWC discharges on TORE SUPRA [51, 73] in 1995-98, reported very positive wall conditioning results. The discharges were carried out in deuterium and helium at an RF frequency of 48 MHz and magnetic field of 3.8 T. A wide range of pressures ($p = 2 \cdot 10^{-1} - 10^{-3}$ Pa) and powers ($P_{\mathrm{RF}} = 20 - 350$ kW) are tested. The discharges were found to be toroidally homogeneous, but poloidally asymmetric, especially at higher pressures ($> 10^{-2}$ Pa). Both the electron density and temperature were found to increase on increasing RF power. In helium, for the given power range and at fixed pressure of $p = 10^{-1}$ Pa, the temperature ranged from $T_e \approx 1.6 - 2.5$ eV, and density from $n_e \approx (1 - 6) \cdot 10^{11}\,\mathrm{cm}^{-3}$. For deuterium plasmas the electron density was much lower: $n_e = (3 - 16) \cdot 10^{10}\,\mathrm{cm}^{-3}$ for an RF power range of $P_{\mathrm{RF}} = 20 - 100$ kW. During D_2-ICWC a surface normalized total flux of fast CX-atoms of $F_{\mathrm{CX}} = 10^{17}\,\mathrm{m}^{-2}\mathrm{s}^{-1}$ (H and D) was measured, with Maxwellian energies of 1 keV for hydrogen and 0.4 keV for deuterium, at an RF power of $P_{\mathrm{RF}} = 100$ kW and discharge pressure $p = 10^{-2}$ Pa [73]. The presence of these particles was related to the resonant cyclotron absorption of RF power by hydrogen ($\omega = \omega_{c,\mathrm{H}^+}$) and deuterium ($\omega = 2\omega_{c,\mathrm{D}^+}$) ions, and was considered to be a major asset of the RF discharges with respect to their conditioning capabilities.

The removal rate of HD from the vessel, estimated from mass spectrometry, was 10^{19} HD/s during a 30 s D_2-ICWC discharge. In conclusion the ICWC discharges are found to be efficient for isotopic exchange. The removal rate of impurities in the form of CD_4, D_2O and CO is around 50 to 500 times lower than the removal rate of HD. These low removal rates are attributed to the well conditioned state of the vessel. During He-ICWC, high H_2 removal rates were recorded, with a maximum of $7 \cdot 10^{-2}\,\mathrm{Pam}^3/\mathrm{s}$ and on average $10^{-2}\,\mathrm{Pam}^3/\mathrm{s} \approx 2 \cdot 10^{19}\,\mathrm{H}_2/\mathrm{s}$.

The initial solely positive perspectives for ICWC following the experimental days in 1995 and January 1996 on TORE SUPRA were distorted with the damaging of one of the RF capacitors in the antenna matching circuit. Conductive deposits were found on the capacitor ceramics which likely caused them to break due to thermal stress. Since the capacitors are water cooled, the end of the experimental day was reported due to a water leak in the vessel. In 1997 an optic system was installed on one RF antenna that allowed to detect the presence of plasma inside the antenna box, at the level of the capacitors. Subsequent RF discharges evidenced the presence of plasma in sight of the optic fibers. In 1998 dedicated experiments were carried out for antenna coupling analysis [87]. The optic system is presently not operational anymore. Further details on RF physics and deleterious effects on the antennas will be discussed in section 2.3.

2.2.1.2 TEXTOR

The first TEXTOR ICWC discharges [74] were carried out in helium ($p = 10^{-3} - 10^{-1}$ Pa), with a magnetic field of $B_T = 2.25$ T, RF frequency of 32.5 MHz and an RF power range of $P_{\mathrm{RF}} = 100 - 800$ kW. Plasmas with density and temperature in the range of $n_e = 5 \cdot 10^{10} - 3 \cdot 10^{12}\,\mathrm{cm}^{-3}$ and $T_e = 10 - 40$ eV were obtained. The discharges were applied in series of four short 1 s pulses with 1 s between each pulse. The H_2 removal decreased from shot to shot with a maximum of $9 \cdot 10^{19}\,H_2/s$, which is much larger than the TORE SUPRA He-ICWC efficiency, taken into account the tokamak wall surface area. This is expectedly due the effectuated 10 minutes long H_2-GD to load the TEXTOR wall with hydrogen that preceded the He-ICWC. In five ICWC discharges one could remove $6.5 \cdot 10^{20}$ H atoms, which is of the order of one monolayer. Furthermore, also promising preliminary results were reported using the technique for thin Si-layer deposition.

ICWC experiments were later also successfully carried out in reactive gases on TEXTOR [55]. Several reactive gases (H_2, D_2, O_2, N_2, NH_3) and their mixtures with helium were tried and preliminary results about their efficiency to clean the wall from impurities and to release the retained fuel have been obtained. An oxygen-helium mixture is found to be the most effective scenario to remove carbon from the wall. The efficiency was mainly limited by the maximum allowed pressure in the antenna box. ICWC in deuterium was found to be effective to remove hydrogen via HD formation and to remove CO. A helium-ammonia gas mixture was found to be effective to remove deuterium and showed a better uniformity than ICWC in helium-hydrogen mixtures. Nitrogen-hydrogen and nitrogen-deuterium gas mixtures were found to be ineffective for wall cleaning under the wall conditions in TEXTOR, due to strong nitrogen consumption by the wall.

2.2.1.3 ASDEX Upgrade

On ASDEX Upgrade [81] He-ICWC discharges were initiated using 1 to 4 ICRH antennas in π-phasing with an RF power of $P_{\mathrm{RF}} = 3 - 120\,\mathrm{kW}$ per antenna, at a frequency of 30 MHz and magnetic field of $B_T = 1 - 2\,\mathrm{T}$. The helium pressure ranged from $p = (1 - 8) \cdot 10^{-2}\,\mathrm{Pa}$. High-energetic fluxes of H (with energies up to 60 keV) and of D-atoms (up to 25 keV) were detected by a neutral particle analyzer (NPA). Line integrated density measurements gave electron density values of $n_{e,l} \leq 6 \cdot 10^{11}\,\mathrm{m}^{-2}$. During later ASDEX Upgrade experiments, the removal of argon during He-ICWC discharges was compared with He-GDC [88]. The maximum obtained argon removal rates were on average 4.5 times higher in ICWC than in GDC. The argon partial pressure peak occurring after the ICWC discharge initiation decreases rapidly, as was also the case for the neutral pressure in the vessel.

2.2.1.4 JET

On JET [81], ICWC discharges were tested using pure helium and helium-hydrogen gas mixtures (80/20 $\mathrm{He/H_2}$, without feedback control). Antenna C was operated in π-phasing with an RF power of $P_{\mathrm{RF}} = 130 - 245\,\mathrm{kW}$ at a frequency of 34 MHz and magnetic field of $B_T = 1.85 - 2.45\,\mathrm{T}$. The experiments on JET were performed at lower gas pressure in the torus, $p_{\mathrm{tot}} \approx (1 - 8) \cdot 10^{-3}\,\mathrm{Pa}$, due to technical constraints: the pressure trip level of the antenna vacuum transmission line (VTL) is $\sim 1 \cdot 10^{-2}\,\mathrm{Pa}$. The plasma extended radially over the vessel center towards the HFS when a gas mixture of helium and hydrogen was injected which was predicted in advance by electron power deposition profile calculation using TOMCAT [89]. The electron temperature, estimated from line radiation in the VUV spectroscopy data, was in the range of $T_e = 2 - 5\,\mathrm{eV}$, inversely proportional to the discharge pressure.

2.2.1.5 HT-7

On the superconducting HT-7 tokamak [75], RF conditioning discharges were firstly produced at low RF power of $P_{\mathrm{RF}} = 8 - 10\,\mathrm{kW}$, at a frequency of 22.5 MHz and a toroidal magnetic field of $B_T = 0.1 - 1.6\,\mathrm{T}$, repeating multiple 300 ms RF pulses every 1 s for 30 to 60 minutes. On increasing the toroidal magnetic field during the RF discharges it was observed that the plasma radiation, which was strongly peaked around the second ion cyclotron resonance harmonic ($\omega = \omega_{c,\mathrm{D}^+}$) in the center of the vessel, shifted along with the resonance layer to the LFS. Both D_2 and He-ICWC were tested in a pressure range of $p = 10^{-4} - 1\,\mathrm{Pa}$. Compared to He-GDC, He-ICWC was found 10 times more efficient for hydrogen removal. A low

vacuum base pressure was achieved by 4 hours of He-ICWC, due to the efficient removal of H_2O, CO and CO_2. In conclusion ICWC is said to be 3 times more efficient than GDC or TDC. During the last 2006 HT-7 campaign (32 days of operation) the total ICRF conditioning time was 33 hours. Later, ICWC was also applied at higher powers, up to $P_{RF} = 50\,kW$ [77]. Because of its high efficiency compared to GDC, and its possibility to operate in presence of the toroidal field, ICWC became a routine conditioning technique on HT-7.

On HT-7, ICWC is also successfully employed for thin film deposition (B and Si), and co-deposited layer removal. For the latter, O_2-ICWC discharges with $P_{RF} = 40\,kW$ (cycles of 1 s on, 2 s off) and $p_{O_2} = 9 \cdot 10^{-2}\,Pa$ were used. The maximum removal rates of H, D and C atoms was $2.6 \cdot 10^{22}$ atoms/h, $7.8 \cdot 10^{22}$ atoms/h and $1.5 \cdot 10^{22}$ atoms/h which are promising results with respect to long duration ICWC operation, and to co-deposited layer removal (however O_2-ICWC cannot be used during the active phase of ITER). It corresponds to a removal rate of co-deposited films of 317 nm/day (7.2 gC/day). Strong oxygen retention in the vessel ($1.7 \cdot 10^{22}$ O-atoms) after the oxygen conditioning discharges required the use of He-ICWC cleaning (removal of $5.4 \cdot 10^{21}$ O-atoms in 50 minutes) and ~ 60 disruptive plasma start-up attempts to recover normal operation of the device. In later experiments on HT-7 it was found that D_2-ICWC is about 5 to 10 times more efficient for oxygen removal [90] than He-ICWC.

2.2.2 Formulation of experimental objectives

From the given overview one can conclude that ICWC is a promising candidate technique for inter-pulse and overnight conditioning on ITER, i.e. in presence of the toroidal magnetic field. Ranges were set for the operational parameters (RF power, RF frequency, antenna phasing, toroidal magnetic field, discharge pressure and discharge gas) and plasma parameters (electron density, electron energy and presence of fast particles). Further studies on ICWC remain however required to fully consolidate the technique before its operation in ITER. Many principle ideas for further experimental studies can be extracted from the given overview and are listed below. The work presented in this manuscript, supported by the mentioned institutions and involved scientists, will attempt to cover these points at its best.

- Since hydrogen and helium are likely the most suitable discharge conditioning gases for ITER (e.g. O_2 discharge conditioning is not allowed during the D-T phase), it was decided to concentrate the research to hydrogen and helium ICWC discharges.
- The discharges are found to be toroidally homogeneous, but poloidally

inhomogeneous. We will determine the mechanisms that cause these inhomogeneities, and investigate how to improve the poloidal homogeneity.

- Related to the previous point also the homogeneity of the wall flux will be considered. For this the main wall bombarding species will be characterized. The effect of the fast CX component of the wall flux on the conditioning efficiency, and the dependencies of the wall flux on the discharge control parameters will be investigated.

- H_2-ICWC and He/H_2-ICWC:

  - The ability of H_2 and He/H_2-ICWC to change to wall isotopic ratio will be assessed.
  - The dependency of this efficiency on the discharge control parameters (pressure, RF power, toroidal and poloidal magnetic field strength, pumping speed, ...), its evolution in time, and the advantage of pulsed ICWC compared to continuous RF discharges will be treated.
  - And the efficiency of H_2-ICWC to remove impurities and codeposited layers (tritium removal) will be investigated.

- He-ICWC:

  - The ability of He-ICWC to desaturate the wall surfaces from discharge fuel will be assessed.
  - The dependency of this efficiency on the discharge control parameters, its evolution in time and the advantage of pulsed ICWC compared to continuous RF discharges will be treated.
  - Also the efficiency of helium ICWC to remove impurities will be investigated.
  - The operational effectiveness of the technique to recover normal tokamak operation after plasma disruption events and to lower the vacuum base pressure levels of impurities will be evidenced.

- The efficiency of ICWC will be tested on multiple devices; TORE SUPRA, TEXTOR, ASDEX Upgrade and JET, which allows to test ICWC under multiple conditions (different antenna systems and available frequencies, wide range of vessel sizes, limiter and divertor configurations, carbon PCF and tungsten PFC).

- The conditioning efficiency of ICWC will be compared to other techniques (GDC, TDC).

- Recommendations will be made according to the gained experience to avoid deleterious effects on the antenna systems.
- An extrapolation of the experimental results to ITER will be presented.

2.2.3 Modeling of ICWC discharges

2.2.3.1 Wall conditioning efficiency

An important contribution to the parameterization of the wall conditioning efficiency of D_2-ICWC was published by de la Cal [56]. The maximum conditioning efficiency is obtained when the maximum pumping rate for a given atom or molecule 'A' is achieved. The presented model relates the out-pumped flux of A, $Q_{\mathrm{p,A}}$, to the machine pumping speed for the given particle, S_{A}, the discharge pressure, $\sim n_{\mathrm{D_2}}$, the plasma temperature, T_e for electrons and T_i for ions, and the relevant reaction rates.

The analysis starts from the consideration of the probability that a wall desorbed particle will be pumped out of the vessel. The characteristic pumping time in RF discharges, τ_S, is much larger than the cracking time by dissociation or ionization, τ_c, of a molecule:

$$\tau_S = \frac{V}{S_{\mathrm{A}}} \gg \tau_c = \frac{1}{n_e(k_{\mathrm{ion,A}} + k_{\mathrm{dis,A}})} \tag{2.3}$$

where V is the chamber volume, n_e the electron density and $k_{\mathrm{ion,A}}$ and $k_{\mathrm{dis,A}}$ the ionization and dissociation on electron impact reaction rates for the wall desorbed particles. As such the pumping probability of a wall desorbed particle is found as

$$\alpha = \frac{\tau_S^{-1}}{\tau_S^{-1} + \tau_c^{-1}} \approx \frac{\tau_c}{\tau_S} = \frac{S_{\mathrm{A}}}{V} \frac{1}{n_e(k_{\mathrm{ion,A}} + k_{\mathrm{dis,A}})} \tag{2.4}$$

Via this probability, the out-pumped throughput of wall desorbed molecule A, $Q_{\mathrm{p,A}}$, can be related to its wall desorbed flux, $Q_{\mathrm{sw,A}}$: $Q_{\mathrm{p,A}} = \alpha Q_{\mathrm{sw,A}}$. The latter wall desorbed flux is taken proportional to the wall bombarding flux Q_{ftw} via the yield Y_{A}: $Q_{\mathrm{sw,A}} = Y_{\mathrm{A}} Q_{\mathrm{ftw}}$. This yield will depend firstly on the energy of the bombarding specie, $T_{\mathrm{n,CX}}$, but also on the wall characteristics. In the paper [56] the wall bombarding flux is said to consist mainly of energetic neutrals that stem from energetic neutralized ions via charge exchange reactions with D_2 molecules. In this way the total wall bombarding flux can be estimated as $Q_{\mathrm{ftw}} = V n_e n_{\mathrm{D_2}} k_{\mathrm{CX}}$. As such the out-pumped throughput is described as:

$$Q_{\mathrm{p,A}} = \frac{Y_{\mathrm{A}}(T_{\mathrm{n,CX}}) S_{\mathrm{A}} n_{\mathrm{D_2}} k_{\mathrm{CX}}(T_{\mathrm{D_2}}, T_i)}{k_{\mathrm{ion,A}}(T_e) + k_{\mathrm{dis,A}}(T_e)} \tag{2.5}$$

where interestingly the out-pumped is apparently independent on the electron density. From eq. (2.5) it can be concluded that the wall conditioning efficiency can be optimized by

- increasing the pumping speed S_{A},
- increasing the neutral pressure $n_{\mathrm{D_2}}$,
- choosing proper plasma temperature (T_e and T_i),

a conclusion which will remain standing after further analysis in this manuscript, although the analysis will be refined.

2.2.3.2 Steady state plasma parameters and wall flux

A second important contribution, published by de la Cal [85], concerns a calculation of the plasma parameters for D_2-RF discharges. From the presented 0D model it was possible to obtain the steady state concentrations of D, D^+, D_2^+, D_3^+, the electron density n_e and the electron temperature T_e. The model takes into account 10 elementary hydrogen reactions, including the charge exchange reactions $H^+ + H_2$ and $H_2^+ + H_2$. It was found that the electron temperature remains approximately constant around $T_e = 3\,\mathrm{eV}$ for a wide range of plasma densities ($10^{10} - 10^{12}\,\mathrm{cm}^{-3}$) and for a neutral pressure of $10^{-2}\,\mathrm{Pa}$. Furthermore, the electron density is proportional to the injected RF power, for the typical low ionization degrees, and the repartition of the ion fractions strongly depends on the neutral pressure. For a neutral pressure of $10^{-2}\,\mathrm{Pa}$ the concentration of D^+, D_2^+ and D_3^+ relates approximately as $10^{11}/10^{10}/10^{9}\,\mathrm{cm}^{-3}$. In the paper of de la Cal [85] it is stated that neutral D-atoms are the main wall bombarding species. These neutrals stem from the neutralization of the principle ion specie D^+ in charge exchange collisions with neutral D_2 molecules. Also in this case most of the found conclusions remain standing.

2.2.3.3 Time dependent plasma parameters

At LPP-KMS/ERM (Brussels) a 0D model was developed to describe (atomic) hydrogen RF plasmas from discharge initiation to the establishment of steady state plasma parameters [91]. The model solves time dependently the particle and energy balance equations for atomic hydrogen, hydrogen ions and electrons, assuming Maxwellian energy distributions for all the species. The elementary collisions included in the equations are excitation and ionization on electron impact (from the ground state), recombination of ions and electrons, and the charge exchange reaction between H and H^+.

The model, describing the RF plasma production based on collisional absorption of RF power by the electrons and electron collisional ionization, is able to reproduce experimental breakdown times of TEXTOR, JET and ASDEX Upgrade as a function the discharge pressure ($10^{-3} - 10^{-1}$ Pa). The predicted electron energies are in the range of what is predicted by de la Cal ($T_e = 3$ eV) [85]. The plasma ions gain their energy via coulomb collisions with electrons and will have approximately the same energy. The ion (particle and energy) losses to the walls are calculated from the confinement properties of the magnetic configuration. The predicted electron densities, using the coupled RF power, the discharge pressure and the magnetic field as model inputs, are one order of magnitude higher than the experimental data (TEXTOR). It is proposed that this discrepancy between the experimental and modeling data is due to the presence of plasma impurities.

2.2.4 Formulation of modeling objectives

The above overview shows that important insights can be obtained from the modeling of ICWC discharges. The main physical mechanism governing the plasma breakdown was identified (electron collisional ionization), the main ion specie was found (H^+), the plasma density and energy could be estimated ($10^{10} - 10^{12}$ cm^{-3}, ~ 3 eV), the main wall bombarding species could be deduced (H-atoms), and the discharge control parameters were related to the conditioning efficiency which learns us how to optimize the efficiency. To increase the understanding and to verify the presented models, the modeling efforts have to be continued. The modeling aims for this PhD work are listed in the following points:

- A model similar to the first presented model will be developed, relating the out-pumped fluxes, wall desorbed fluxes and wall bombarding fluxes to each other (chapter 4). The model allows to estimate the magnitude of the wall bombarding flux and to propose optimizations of the discharge control parameters to increase the conditioning efficiency. The analysis will be done both for GDC and ICWC, illustrating some important differences between the two techniques.

- The physics of the second and third model will be combined into one code (chapter 5). For this the 0D code for atomic hydrogen will be upgraded to molecular hydrogen, including its most important elementary collisions. The implementation of molecular hydrogen is motivated by the low temperature of the plasma, resulting from the incomplete ionization of the neutral gas. The presence of molecular hydrogen will thus be considerable.

- As helium is an important gas for discharge wall conditioning, the same model will be developed for helium and helium-hydrogen plasmas. For this the balance equations for neutral helium and helium ions are added to the molecular hydrogen code.
- A qualitative description of plasma impurities will be included in the model by adding balance equations for atomic carbon and its ions.
- The developed model will be benchmarked to experimental data of TORE SUPRA and TEXTOR, and will be used to complement the experiments with data that can't be measured accurately:
  - The model has to reproduce the experimental plasma densities (the available electron temperature measurements being unreliable at the typical low temperatures).
  - Causes of discrepancies between model and experiments will be investigated.
  - Once the plasma density and its dependencies on the discharge control parameters can be reproduced with sufficient accuracy, the main plasma and wall bombarding species can be identified.
  - The deduced wall fluxes will be compared with experimental data, which allows to gain confidence in both the experimental data and the modeling results.
- A final code will be developed, linking the 0D plasma code for hydrogen to a minimum description of the plasma wall interaction. The model allows interpreting the experimental isotopic exchange results and to propose optimized discharge scenarios for isotopic exchange (chapter 6).

2.3 RF physics aspects

The RF physics aspects of ICWC discharges (discharge initiation and sustainment) have been well described by Lyssoivan [66, 72, 80–82, 84, 86, 87, 92–97]. Large part of this section will be based on his work. The aim of this RF section is giving an overview on ICRF plasma production, coupling properties of ICRF power to the plasma, and eventual deleterious effects on antenna operation.

2.3.1 RF systems in ICWC mode of operation

Below we give an overview of important RF terms, the employed RF antennas on TORE SUPRA, TEXTOR, ASDEX Upgrade and JET, the ICWC

mode operation settings and possible deleterious effects on the antennas.

2.3.1.1 Important RF terms

The power for each antenna is delivered by RF generators (P_{G}) via transmission lines. The power transmitted to the antenna ($P_{\mathrm{tr,Ant}}$) equals the forward minus reflected power at the level of the antenna (resp. $P_{\mathrm{F,Ant}}$ and $P_{\mathrm{R,Ant}}$), and is approximately equal to the generator power.

$$P_{\mathrm{tr,Ant}} = P_{\mathrm{F,Ant}} - P_{\mathrm{R,Ant}} \approx P_{\mathrm{G}} \tag{2.6}$$

The RF power at the antenna can also be written as a function of the complex antenna voltage, strap current and impedance values (resp. V_{Ant}, I_{Ant} and $Z_{\mathrm{Ant}} = R_{\mathrm{Ant}} + jX_{\mathrm{Ant}}$):

$$P_{\mathrm{tr,Ant}} = \frac{1}{2}\mathrm{Re}\left(V_{\mathrm{Ant}} I^*_{\mathrm{Ant}}\right),\ I^*_{\mathrm{Ant}} = \frac{V^*_{\mathrm{Ant}}}{Z^*_{\mathrm{Ant}}},\ P_{\mathrm{tr,Ant}} = \frac{1}{2}V^2_{\mathrm{Ant}}\mathrm{Re}\left(\frac{1}{Z^*_{\mathrm{Ant}}}\right) \tag{2.7}$$

The real part of the impedance (resistance R_{Ant}) consists of ohmic vacuum losses and the actual plasma loading: $R_{\mathrm{Ant}} = R_{\mathrm{v.loss}} + R_{\mathrm{pl}}$. Usually, the imaginary part has an inductive nature ($X_{\mathrm{Ant}} = \omega L_{\mathrm{Ant}}$) and is much larger than the real part: $X_{\mathrm{Ant}} \gg R_{\mathrm{Ant}}$. Taking these considerations into account we obtain:

$$P_{\mathrm{tr,Ant}} = \frac{V^2_{\mathrm{Ant}}}{2}\mathrm{Re}\left(\frac{1}{R_{\mathrm{v.loss}} + R_{\mathrm{pl}} + jX_{\mathrm{Ant}}}\right) \tag{2.8}$$

$$= \frac{V^2_{\mathrm{Ant}}}{2}\mathrm{Re}\left(\frac{R_{\mathrm{v.loss}} + R_{\mathrm{pl}} - jX_{\mathrm{Ant}}}{(R_{\mathrm{v.loss}} + R_{\mathrm{pl}})^2 + X^2_{\mathrm{Ant}}}\right) \tag{2.9}$$

$$= \frac{V^2_{\mathrm{Ant}}}{2}\frac{R_{\mathrm{v.loss}} + R_{\mathrm{pl}}}{X^2_{\mathrm{Ant}}} \approx P_{\mathrm{G}} \tag{2.10}$$

From the latter equation (eq. 2.10) we can deduce the part of the power that is absorbed by the plasma:

$$P_{\mathrm{pl}} = \frac{V^2_{\mathrm{Ant}}}{2}\frac{R_{\mathrm{pl}}}{X^2_{\mathrm{Ant}}} \tag{2.11}$$

The antenna coupling efficiency is defined as the fraction of the generator power that is coupled to the plasma, and can with eq. (2.10) and (2.11) be written as:

$$\eta = \frac{P_{\mathrm{pl}}}{P_{\mathrm{G}}} = \frac{R_{\mathrm{pl}}}{R_{\mathrm{v.loss}} + R_{\mathrm{pl}}} \tag{2.12}$$

This allows to calculate the coupled power to the plasma by measuring the generator power (or forward minus reflected power at the antenna) and the antenna resistance.

In RF plasmas as well as in fusion plasmas, the aim is to couple the highest possible fraction of generator power to the plasma, firstly for power efficiency (eq. 2.12), and secondly to decrease the voltage at the antenna side for safety aspects (eq. 2.10). The antenna coupling efficiency depends on the extent wherein the structure of the antenna radiated RF field matches to the structure of the field of excited plasma waves. The poloidal loop-type antennas used in our experiments (see Fig.2.2) are designed to efficiently excite the Fast Wave (FW) in plasmas. Therefore, these antennas will demonstrate a good coupling efficiency in the ICWC mode of operation if we find scenarios with FW excitation in low density ICWC plasmas. As will be shown later, these scenarios have been found.

Non-perfect matching of the antenna impedance to the transmission line impedance results in the partial reflection of RF power at the level of the antenna ($P_{\mathrm{R,Ant}}$), which will cause standing wave pattern formation along the transmission line. The power stored in these standing waves will be partially dissipated in the transmission lines and the standing waves can even provoke arcing inside the transmission lines[2].

2.3.1.2 Employed RF antennas in ICWC mode of operation

Fig. 2.2 shows images of the TEXTOR, TORE SUPRA, ASDEX Upgrade and JET ICRF antennas. The TEXTOR, TORE SUPRA and ASDEX Upgrade antennas are of the double loop type: two parallel RF current straps placed into an antenna box. The JET ICRF A2 antenna consists of four current straps. The current straps can be fed either out of phase, e.g. π-phasing (dipole) which is commonly used for heating scenarios, or in phase (called zero-phasing or monopole). To reduce the deleterious effects on E_z-field generation during dense plasma RF heating and the resulting impurity generation, a Faraday screen (FS) consisting of multiple parallel rods is placed in front of the straps [99]. The antennas are generally placed on the LFS of the vacuum torus due to the technical difficulty of mounting an antenna and its transmission lines at the HFS. For each tokamak the toroidal locations of the antennas are shown in appendix A on a toroidal cross section. As described in the introduction (1.2.7), TEXTOR is equipped with two ICRH antennas, TORE SUPRA has three water cooled ICRH antennas with actively cooled antenna protection limiters [100], ASDEX Upgrade and JET are both equipped with four ICRH antennas.

[2]The most dangerous places for arcing generation are vicinities of the nodes in the standing wave pattern, thus where the RF voltage is low. The low RF voltage range ($0.5 - 2\,\mathrm{keV}$) is the most efficient voltage-range for secondary electron emission (SEE) generation and subsequent RF multipactor breakdown. Also high-voltage breakdown in vacuum or vacuum arcs are possible (see [98]).

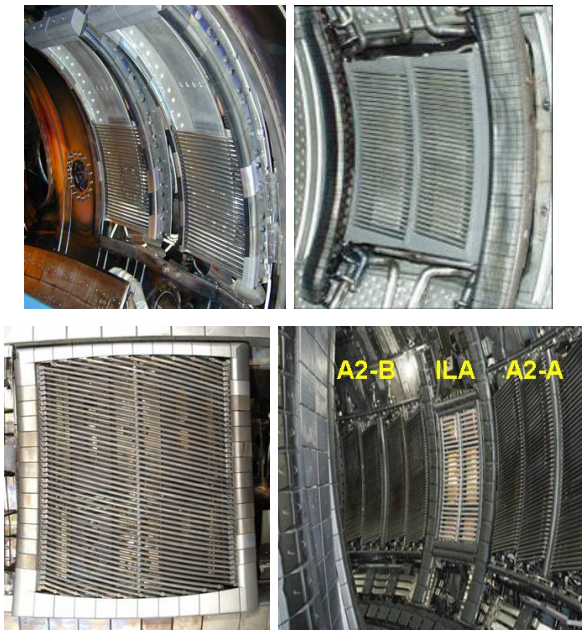

Figure 2.2: Pictures of the employed ICRF antennas. From left to right: TEXTOR T-Antenna ($f = 25 - 38\,\mathrm{MHz}$), TORE SUPRA Antenna ($f = 40 - 70\,\mathrm{MHz}$), ASDEX Upgrade Antenna ($f = 23 - 120\,\mathrm{MHz}$), JET A2 Antennas ($f = 23 - 57\,\mathrm{MHz}$). The given frequency ranges are not continuous.

For the ICWC mode of operation in JET [101], special Voltage Standing Wave ratio (VSW) cards were developed to provide better antenna matching, and the feedback control for the RF power was disabled. The allowed frequency range is limited between 25 MHz and 28 MHz to keep the voltage node away from the sensitive bellow area of the VTL. The maximum allowed pressure in the vacuum transmission lines (VTL) was set at 10^{-4} mbar and the maximum transmission line voltage set at 20 kV. The ICRF antennas are switched on before any gas is injected and the employed antennas (module C and D) were monitored at all time with CCD cameras. The maximum number of RF tripping events was set to 10 trips per pulse and 100 trips for the whole experiment. On TORE SUPRA [102], the standard matching circuits and phase control are switched off during ICWC operation (which requires some manual re-cabling work), and the antenna matching points are set manually. The antenna protection system controls the ratio of reflected power to forward power, which in case of arcing events (too high ratio during 10 μs) cuts the RF power feeding temporally. After 20 subsequent triggers the discharge will be interrupted. On ASDEX Upgrade [103], the ICRF

antennas are operated in pairs, each pair having two generators. A phase regulation between two generators from each antenna pair is required (in case 0-$\pi/2$ phasing is requested) which is active from $\sim 200\,\mathrm{kW}$/generator and higher. To allow power levels $< 400\,\mathrm{kW}$ from one antenna pair, one of the two generators is typically disabled for ICWC experiments, and to allow for monopole operation, only one strap per antenna is fed. The double stub matching system is set at fixed positions before a discharge. Two kinds of arc detection systems are available ($P_{\mathrm{for}}/P_{\mathrm{rev}}$), one main system at the level of the combiner and splitter of 'generators to antennas' feeding line, and four complementary systems at the level of both antennas and both generators. As on ASDEX Upgrade, on TEXTOR [104] no major changes in the antenna circuit configuration are required for the ICWC mode of operation. On TEXTOR each antenna is fed by its own generator, and equipped with an auto tuning system (matching is thus adapted during the discharge). As on other tokamaks the arcing protection system relies on $P_{\mathrm{for}}/P_{\mathrm{rev}}$. As the ratio $P_{\mathrm{for}}/P_{\mathrm{rev}}$ changes on plasma breakdown, the protection systems sometimes triggers on plasma breakdown.

To reduce the RF voltage in the breakdown phase a power ramp up scenario can be employed. On TORE SUPRA, the antenna generator power is ramped up linearly from 30 to 60 kW in the first 0.3 s, whereafter the full power is applied within a short ramp-up time ($< 0.1\,\mathrm{s}$). On TEXTOR, JET and ASDEX Upgrade, when employing multiple antennas breakdown is achieved with only one antenna, whereafter the second antenna couples extra power to the present plasma.

It was shown experimentally that strap phasing close to monopole is beneficial for plasma production. Breakdown is achieved faster, and the antenna voltage is strongly reduced after breakdown indicating a better power coupling (eq. 2.10), illustrated for the TORE SUPRA Q2 antenna on Fig. 2.3 (left). This point will be further discussed in section 2.3.6. Further on we will also see that operation at higher pressures ($> 0.1\,\mathrm{Pa}$) is not recommended in order to avoid spurious plasma formation in the antenna box, or at the level of the Faraday screen (section 2.3.4).

2.3.1.3 Possible deleterious effects

Fig. 2.4 shows images of the Q2 and Q5 TORE SUPRA antennas, taken respectively after the 2008 and 2010 experimental campaigns. The antennas, both used in ICWC experiments, show strong carbon deposition on the antenna straps ($\sim 100\,\mathrm{nm}$), and a deposition or heating pattern on the FS. On the straps (but not the FS) also arcing traces are visible that appear to remove the deposited carbon. Since the other TORE SUPRA antennas did not show any deposited carbon after these campaigns, the ICWC session is

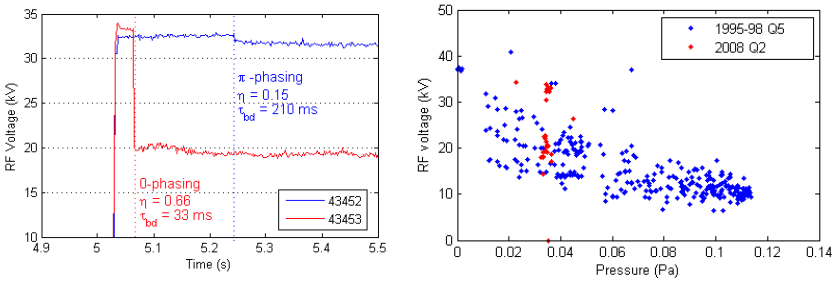

Figure 2.3: Left: RF voltages for 2 ICWC discharges on TORE SUPRA (Q2 antenna, 2008) resp. in π (blue) and 0-phasing (red), indicating plasma breakdown by steep voltage drop. 0-phasing has a shorter breakdown time and a better coupling efficiency. Right: RF voltage after breakdown as function of pressure for 1995-1998 discharges (blue, mostly π-phasing) 2008 discharges (red, π and 0-phasing).

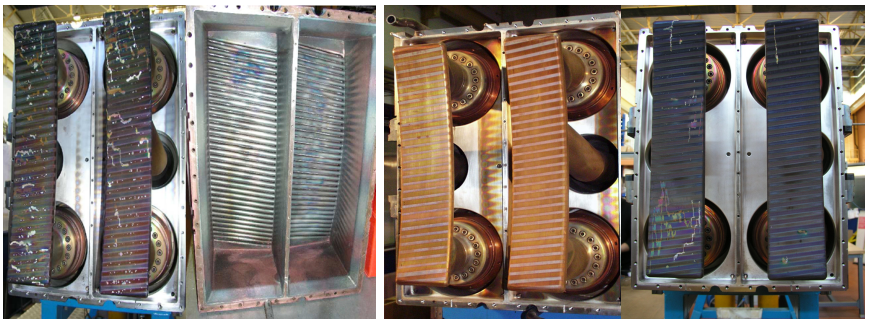

Figure 2.4: Left: TORE SUPRA Q2 antenna and FS after the ICWC session in 2008. Right: TORE SUPRA Q5 antenna before and after the ICWC session in 2010. The antenna straps feature as a result of the ICWC sessions a clear carbon coating ($\sim$ 100 nm). Also on the FS there are deposition or heating patterns visible. Finally, shallow arcing traces that have removed the deposited layer are visible on the straps. It is however not sure whether the latter is due to ICWC.

held responsible. Regarding the arcing spots, the RF engineers do however not exclude the possibility that they stem from subsequent experimental sessions [102].

This serious issue of substantial carbon deposition is not fully understood. The Paschen curve like dependence of the antenna voltage on the discharge pressure in TORE SUPRA (Fig. 2.3, right) might indicate that an electrode is involved in the RF discharge [103]. The ASDEX Upgrade RF voltage does not show a pressure dependence at all, which in turn might indicate an electrode less discharge. The carbon deposition could thus be

due to the presence of plasma inside the antenna box. Experiences on TEXTOR, JET and ASDEX Upgrade do not report similar problems. Important differences between the TORE SUPRA RF discharges and the TEXTOR, JET and ASDEX Upgrade discharges are the higher RF voltage, the higher applied RF frequency (see table 2.1), and the cooled antenna straps. In

Table 2.1: Antenna voltages during ICWC operation on TORE SUPRA, TEXTOR, ASDEX Upgrade and JET, and applied RF frequencies. [101–104]

TORE SUPRA	$15 - 25\,\mathrm{kV}$ (0-phasing, after breakdown)	
	up to $35\,\mathrm{kV}$ (π-phasing)	$48\,\mathrm{MHz}$
TEXTOR	$< 10\,\mathrm{kV}$	$29\,\mathrm{MHz}$
ASDEX U.	$< 10\,\mathrm{kV}$	30 & $36.5\,\mathrm{MHz}$
JET	$10 - 20\,\mathrm{kV}$	$25\,\mathrm{MHz}$

section 2.3.4 it is shown that the possibility to initiate a plasma inside the antenna box increases on increasing antenna frequency (however during recent TORE SUPRA ICWC experiments using 42 MHz the problem persisted). In section 1.4.1.5 we saw that the thermal desorption of adsorbed molecules is less probable at low surface temperatures.

2.3.2 From pre-wave ionization to plasma wave regime

ICRF plasma initiation in a toroidal magnetic field results from collisional absorption of RF energy, mainly by electrons [84, 87, 92–95]. The first ionization reactions are caused by the assumed background density of free electrons present in the neutral gas. On switching on the RF field, these electrons, moving freely along the magnetic field lines are accelerated in the $\tilde{E}_z$-field, which is parallel to the magnetic field, obtaining as such sufficient energy for ionization. Since electromagnetic waves in the typical ICRF band ($\sim 10 - 100\,\mathrm{MHz}$) do not propagate in vacuum in the present size fusion devices, the vacuum RF parallel electric field $\tilde{E}_z$ will exist only in the region near the antenna, from where it will be evanescent in toroidal and radial directions. Consequently the initial ionization will occur predominantly at the low field side in the vicinity of the RF antenna. This stage of the discharge will be discussed further in detail in the next sections. When the electron multiplication is sufficiently high to compensate eventual electron losses, a plasma density will build up. After this **pre-wave local ionization phase**, as soon as the plasma frequency, $\omega_{pe} \approx 8980\sqrt{n_e}\,\mathrm{Hz}$, becomes of the order the applied RF frequency, $\omega_{pe} \geq \omega$ ($n_e = 10^{12} - 10^{14}\,\mathrm{m}^{-3}$), plasma waves can start to be excited and propagate in the torus volume. As the waves propagate, the electromagnetic field expands in the vessel volume causing further space ionization. This regime is called the **wave**

phase of the plasma. In order to obtain a homogeneous RF plasma, proper wave propagation scenarios or at least a large decay length of the evanescent RF field is required, allowing to sustain the plasma also at the high field side. The standard ICRF antennas are designed for efficient heating of dense ($n_e > 10^{19}\,\mathrm{m}^{-3}$) target plasma via excitation of the FW. It is aimed to transport the RF energy by the FW to selected areas, remote from the antenna where FW energy should be absorbed. For this purpose, a high k_z-spectrum is formed with π-phasing (180 degree phase between adjacent antenna straps). In low density plasmas $n_e \sim 10^{16} - 10^{17}\,\mathrm{m}^{-3}$, and standard ICRF antenna operation, the FW will not excite/propagate. In section 2.3.6 on antenna coupling in the ICWC mode of operation we will see that the antenna parallel wave vector k_z spectrum is an important parameter determining both the cut off density for FW propagation and the decay length of the evanescent RF field. Furthermore, proper wave propagation is expected to occur also via mode conversion scenarios of the evanescent fast wave into the SW and ion Bernstein wave if $\omega > \omega_{ci}$ or at the Afvén resonance if $\omega < \omega_{ci}$. Although the latter scenarios are very likely interplaying in plasma production, they are difficult to be confirmed experimentally, as shown further.

2.3.3 Antenna RF field components and absorption of RF power

The absorption of the RF power by the particle populations, both in prewave as in wave phase, happens mostly non-resonant by random collisions in the plasma, with only a minor resonant absorption contribution localized around the ion cyclotron resonance layers in the vessel. In this section the EM-field components and their influence on the ions and electrons are considered. The acceleration of the plasma particles in the RF electric field is naturally due to the Lorentz force:

$$\vec{F}_L = m\frac{\mathrm{d}\vec{v}}{\mathrm{d}t} = q(\vec{E} + \vec{v} \times \vec{B}_z) \tag{2.13}$$

With $\vec{v}$ the particle velocity, $\vec{B}_z$ the toroidal magnetic field and $\vec{E}$ the applied RF electric field. The electric field in the vessel will have a component parallel to the magnetic field lines, E_z, and two components perpendicular to the magnetic field lines E_x and E_y which are often represented as two circularly polarized components, E_+ and E_-, from which the left handed, E_-, rotates in the same direction as the ion gyration. ICRF fusion plasma ion-heating scenarios mostly rely on the perpendicular E_- component. The parallel electric field contributes to electron heating scenarios via Landau damping. The presence of the parallel field is very fortunate for ICRF

plasma discharges. It is generated both electrostatically due to the RF voltage difference between antenna strap and sidewalls, and electromagnetically due to an induced RF voltage by the oscillating magnetic flux between the tilted FS bars [105]. The non-resonant acceleration of the electrons and the resonant cyclotron acceleration of the ions is respectively due to the parallel component and the left handed component of the electric field. For the applied ion cyclotron range of frequencies, the electrons experience the electric field as being quasi constant and will consequently not be able to obtain sufficient energy for ionization in the perpendicular electric field due to the $\vec{v} \times \vec{B}_z$ term. On the other hand, the acceleration in the parallel electric field is not restricted allowing the electrons to obtain energy beyond the ionization potential. Ions, due to their lower mobility (higher mass), will not be able to cumulate enough energy for ion impact ionization in the parallel electric field. The latter may however be achieved with cyclotron absorption of RF energy by ions in the perpendicular electric field. Its efficiency is strongly peaked around **resonance layers**, where the ion gyration frequency (eq. 2.2) or its harmonics equal the RF frequency, and resonant absorption becomes possible. Ion cyclotron resonance layers in a toroidal magnetic field correspond to cylindrical surfaces with radius corresponding to

$$R_{ci}^{n} = eR\frac{Z_i}{m_i}\frac{nB_T}{\omega} \tag{2.14}$$

with Z_i and m_i the ion charge and mass, B_T the magnetic field at the major radius R_0, ω the angular RF frequency, and n the cyclotron harmonic number ($n = 1, 2, ...$), where $n = 1$ represents the fundamental resonance. Fig. 2.5 gives a representation of eq. (2.14) by plotting $\frac{Af}{nZ_iB_T}$, with A the mass number of the atom (or molecule), as a function of a normalized radius R/R_0. Resonant absorption is most efficient for the fundamental resonance ($\omega = \omega_{ci}$) where the ion gyration has a constant phase with respect to the left handed E_- field. The efficiency decreases with increasing cyclotron harmonic number n ($\omega = n\omega_{ci}$).

2.3.4 Breakdown conditions

In the following, two models will be presented that describe together the breakdown conditions of RF plasmas as a function of the discharge parameters: RF frequency, RF field strength and pressure. These models are the main employed tools in choosing the proper discharge parameters in RF discharges and are of particular concern for antenna safety considerations. For the pre-wave stage it is expected that the magnitude of the toroidal magnetic field has only a secondary importance, whereas it certainly plays a role in the wave stage of the discharge.

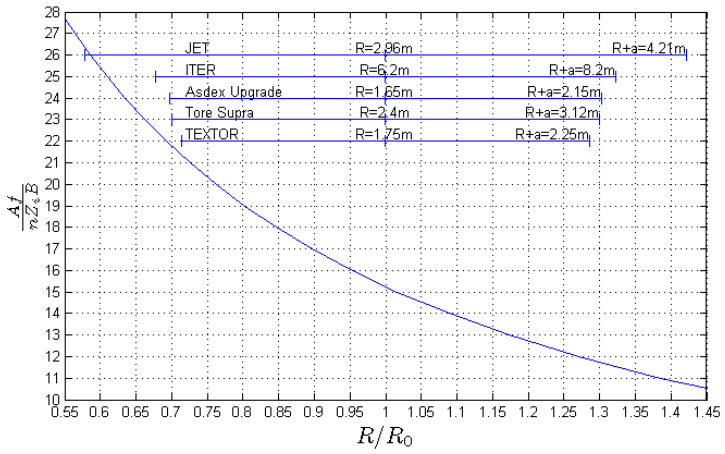

Figure 2.5: Plot of eq. (2.14), giving $\frac{Af}{nZ_iB_T}$ as a function of the normalized radius R/R_0, with A the mass number of the charged particle, Z_i its charge, n the cyclotron harmonic number, f the RF frequency and B_T the magnetic field at the major radius R_0. E.g. the fundamental resonance layer of deuterium in case of $f = 25\,\mathrm{MHz}$ (JET), $B_T = 3.3\,\mathrm{T}$ will be located on axis ($\frac{Af}{nZ_iB_T} = 15.15$). The second harmonic of helium is located at the same radius.

2.3.4.1 Dependency on RF field and frequency

To determine breakdown conditions as a function of the RF field and frequency, a model was developed by Carter and Lyssoivan et al. [84, 106] describing the electron motion due to the Lorentz force in the near antenna parallel electric field. Although the aim of the model is to provide criteria for neutral gas breakdown, frictional forces due to electron collisions are neglected since the collision frequency ν_c is much below the oscillation frequency $\nu_c \ll w$. As a consequence the model does not describe the pressure dependency of breakdown. The Lorentz force exerted on the electrons is written as:

$$F_L(z_0 + z_1) = m_e \frac{\mathrm{d}v_e}{\mathrm{d}t} = eE_z(z_0 + z_1)\cos(\omega t) \tag{2.15}$$

$$\approx eE_z(z_0)\cos(\omega t) - \frac{e^2}{4m_e\omega^2}\frac{\mathrm{d}|E_z(z_0)|^2}{\mathrm{d}z} \tag{2.16}$$

The electron motion is divided into a fast oscillatory motion (around z_0 and represented by z_1) due to force $F_f(z_0)$, namely the first term of the rhs of eq. (2.16), to which a slower drift motion due to force $F_s(z_0)$, the second term of the rhs of eq. (2.16), is superimposed. The latter force, called the ponderomotive force, originates from a Taylor expansion of the

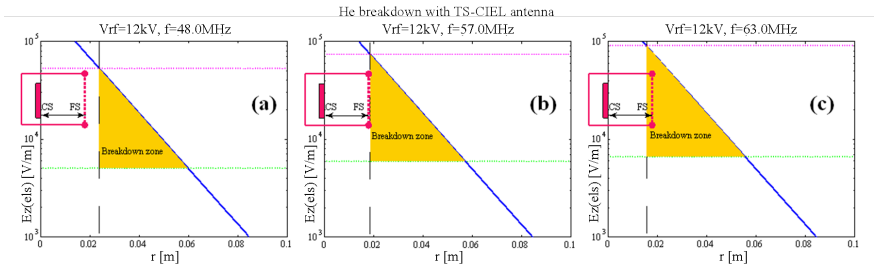

Figure 2.6: Calculation of the ICRF breakdown zone for the TORE SUPRA antenna at different frequencies: (a) $f = 48\,\mathrm{MHz}$; (b) $f = 57\,\mathrm{MHz}$; (c) $f = 63\,\mathrm{MHz}$, for constant RF voltage at the antenna current strap $V_{\mathrm{RF}} = 12\,\mathrm{kV}$. [107]

Lorentz force $F_L(z_0 + z_1)$ around z_0, and represents an average force resulting from the oscillation in the inhomogeneous electric field distribution along the magnetic field lines. The model assumes that the electron multiplication reactions contributing to a build-up of electron density happen predominantly in front of the antenna. The criterion for breakdown considers thus (i) the oscillation energy of the electrons in the near antenna field, and (ii) the residence time of these electrons in front of the antenna. From eq. (2.16) a lower value is calculated for the electric field, expressing the requirement that the oscillation energy has to exceed the ionization threshold ϵ_i. Secondly an upper value for the ponderomotive force is set, expressing that this force has to be smaller than the oscillatory force to allow for electron multiplication before the electrons are expelled from the antenna region. Via these criteria and using the radial decay of the parallel electric field $\tilde{E}_z(\delta r) = \tilde{E}_z(0)\exp(-k_z\delta r)$, with $\tilde{E}_z(0)$ the electric field at the strap, δr the distance from the strap and k_z the parallel wave vector, one can determine the breakdown area along the radial direction:

$$\frac{\omega}{e}\sqrt{2m_e\epsilon_i} \leq \tilde{E}_z(r) \leq 0.2\frac{m_e}{e}\omega^2 L_z \tag{2.17}$$

where $L_z = \tilde{E}_z/(\mathrm{d}\tilde{E}_z/\mathrm{d}z)$ is the parallel length scale of the ponderomotive potential. Eq. (2.17) is of particular importance since it allows to study the effect of the RF frequency, for a known RF vacuum field, on the radial width and position of the breakdown region. Fig. 2.6 shows the breakdown area in the vacuum RF field of the TORE SUPRA antennas for a strap voltage of 12 kV and three standard ICRF frequencies. For the lowest RF frequency (48 MHz) the breakdown zone is located outside the antenna box, at a safe distance from the FS. It can be concluded from the figure that for a given antenna voltage, lowering the RF frequency moves the radial breakdown region away from the antenna. A longer decay length of the evanescent

vacuum RF field will expand the breakdown region.

A few remarks have to be made to this model. (1) The presented breakdown criterion considers only electron multiplication collisions in front of the antenna. As indicated by Schüller [64], electrons expelled by the ponderomotive force can obtain substantial energy from the E_z-field so that ionization is also possible along the torus where the vacuum field is zero. From his analysis it follows that electron multiplication along the torus can be equally important as ionization in the near antenna RF field. This remark however does not render eq. (2.17) without purpose. All RF antennas are equipped with antenna protection limiters which will collect the electrons that are expelled at the level of the FS. The constraint of eq. (2.17) provides thus still the criteria for limiting the residence time of electrons in the RF field close to the FS and thus to avoid spurious plasma formation in this area. An electron expelled from the antenna region, and not collected by a limiter however will travel around the torus and enter back in the antenna region from the other side where it can, depending on its velocity phase compared to the electric field phase, be further accelerated or decelerated. As such these electrons obey a chaotic movement around the torus determined by their initial positions and velocities, the length of the magnetic field line along which they move, and the RF field. Radial regions with too high ponderomotive force are thus not necessarily excluded from the presence of plasma.

(2) A second remark by Schüller [64] is related to the definition of the ponderomotive potential. The applied Taylor expansion to the Lorentz force is only valid in case the amplitude of the oscillation is small compared to the characteristic length scale of the ponderomotive potential. The upper limit that was put on the electric field in order to have breakdown in front of the antenna, $F_s \leq F_f$, is thus the limit of the validity of the model and in principle does not prevent ionization to take place, albeit either in front of or away from the antenna.

(3) Independently of this there is a second argument that could lead to less tight constraints. The mean free path for collisions of the electrons, and thus for multiplication reactions is of the order of hundreds of electron oscillations, dependent on the neutral pressure. By choosing to exclude this effect from the constraint, eq. (2.17) features a safety margin.

(4) As is acknowledged by Lyssoivan, the near antenna parallel electric field features a complex three-dimensional character. In the vertical direction, the electrostatic EM field will vary from the antenna strap feeding points (max) to the grounded points. The shape of the EM field in the toroidal direction, and thus the ponderomotive force, will depend on the antenna design (dimensions) and phasing. And this specific toroidal shape

will vary in the radial direction. A consistent representation of the initial discharge phase has in principle to take into account all these dimensionalities, which is a very complicated task. In the presented model the vertical inhomogeneity is neglected. The toroidal inhomogeneity is included by including the ponderomotive force, and the radial inhomogeneity is included only by considering a radially decaying electric field. The scale length of the ponderomotive force is considered radially constant. This is presently the best approximation, although it is acknowledged to be incomplete. Especially the fact that the separation of the Lorentz force into a fast oscillatory and slow ponderomotive force can become invalid close to the antenna needs to be further investigated.

2.3.4.2 Dependency on pressure

The breakdown criterion (eq. 2.17) describes the dependency on RF field and frequency, but it does not describe the dependency on the neutral gas pressure. Driven by the fact that at pressures above 10^{-1} Pa the danger of spurious plasma formation at the strap surface or inside the antenna-box on TORE SUPRA is thought to increase, Schüller [64] proposed an extension of the model, determining the maximum allowed pressure below which plasma formation at the FS should not take place. Plasma formation can be expected to take place when the residence time of the oscillating electrons in front of the antenna is longer than the characteristic time for ionization in the electric field $1/\nu_i^{\mathrm{RF}}$, with the collision frequency ν_i^{RF} estimated as [64]:

$$\nu_i^{\mathrm{RF}} = 1.78 \cdot 10^7 \frac{\tilde{E}_z^*}{f^*} n_{\mathrm{H}_2} \langle \sigma_{\mathrm{ion}} \rangle \quad [\mathrm{s}^{-1}] \tag{2.18}$$

with $\tilde{E}_z^*$ the maximum electric field in front of the antenna in [kV/m], f^* the RF frequency in [MHz], n_{H_2} the neutral hydrogen density which is of course proportional to the pressure and $\langle \sigma_{\mathrm{ion}} \rangle$ the time averaged cross section over one oscillation. The latter cross section can be expressed as a function of $\tilde{E}_z/f$ since the oscillation energy amplitude is proportional to $(\tilde{E}_z/f)^2$. In the calculation of the threshold pressure the worst case scenario is considered taking the maximum cross section $\sigma_{\mathrm{ion}} = 6.6 \cdot 10^{-20}\,\mathrm{m}^2$, for an $\tilde{E}_z^*/f^*$ value of 0.25 kV/m/MHz. The residence time is estimated as $\tau_{\mathrm{pdm}} \approx (W_{\mathrm{ant}} + L_z)/v_{\mathrm{pdm}}$ with W_{ant} the antenna width and $v_{\mathrm{pdm}} = \sqrt{2\epsilon_{\mathrm{pdm}}/m_e}$ the final ponderomotive drift velocity obtained by an electron oscillating in the ponderomotive potential, with ϵ_{pdm} its corresponding final energy [64]:

$$\epsilon_{\mathrm{pdm}} = 1115 \left(\frac{\tilde{E}_z^*}{f^*} \right)^2 \quad [\mathrm{eV}]. \tag{2.19}$$

This leads to the following constraint on the pressure (in [Pa]):

$$p_{H_2}(W_{ant} + L_z) \ll 1\,\text{Pa m} \tag{2.20}$$

which indeed indicates that one should avoid hydrogenic torus pressure values in excess of $\sim 10^{-1}$ Pa [64].

The two presented models allow thus to set firstly the optimal RF frequency for a given antenna electric field distribution. This frequency should not be too high to avoid plasma formation inside the antenna box or at the level of the Faraday screen. Secondly the maximum allowed working pressure can be estimated for the chosen $\tilde{E}_z^*/f^*$-value which again should not be too high to avoid the same problem.

2.3.5 Simulation of the initial breakdown phase

To obtain information on whether the plasma builds up mainly in front of the antenna, or whether the electron multiplication of expelled electrons significantly contributes, further efforts to model the initial plasma phase are carried out during this PhD. Although the analysis remained fruitless at this point it is shortly presented here. As for the above models, it was chosen to consider a 1D situation along the toroidal magnetic field lines, for a toroidal inhomogeneous electric field distribution.

2.3.5.1 Mean free path of electrons

Fig. 2.7 shows the mean free path $\lambda = (\sigma_i n_{H_2})^{-1}$ of a single electron as function of its energy, for direct ionization of H_2 (cross section from [108]), for a neutral pressure of $p = 10^{-3}$, 10^{-2} and 10^{-1} Pa. The mean free path is strongly dependent on the electron energy. The minimum, around $T_e = 45$ eV for usual discharge pressures below $p_{H_2} = 2 \cdot 10^{-2}$ Pa, is comparable to or larger than the torus circumference. Since the mean free path is much larger than the oscillation lengths of electrons in the near antenna electric field it was chosen to firstly model the initial breakdown phase without collisions.

2.3.5.2 Study of 1D electron distribution function in the breakdown phase

Instead of studying particle time traces of a few individual electrons a more robust approach was chosen. In an attempt to obtain a complete description the Vlasov equation is solved, giving the evolution of the electron velocity and spatial distribution function $f_e(\vec{r}, \vec{v}, t)$ in the torus during the initial

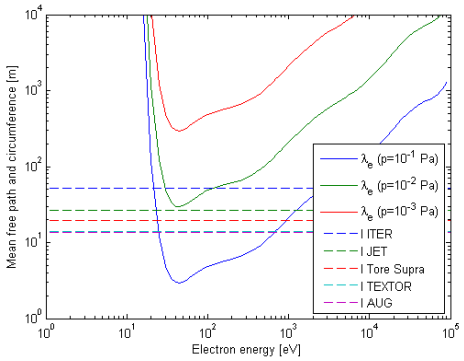

Figure 2.7: Comparison of the electron mean free path for reaction $e + H_2 \rightarrow e + H_2^+ + e$ (cross section from [108]) as a function of the electron energy and neutral particle density, with the toroidal circumference of ASDEX Upgrade, TEXTOR, TORE SUPRA, JET and ITER

breakdown phase:

$$\frac{\partial}{\partial t} f_e(\vec{r}, \vec{v}, t) + \vec{v} \cdot \nabla_r f_e(\vec{r}, \vec{v}, t) - \frac{q_e}{m_e}(\vec{E} + \vec{v} \times \vec{B}) \cdot \nabla_v f_e(\vec{r}, \vec{v}, t) = 0 \quad (2.21)$$

The electron movement along the toroidal magnetic field lines in the parallel electric field is a 1D problem, and thus the Vlasov equation simplifies to

$$\frac{\partial}{\partial t} f_e(z, v, t) + v \frac{\partial}{\partial z} f_e(z, v, t) - \frac{q_e}{m_e} E(z, t) \frac{\partial}{\partial v} f_e(z, v, t) = 0 \quad (2.22)$$

As edge condition for $f_e(z, v, t)$, to account for the periodicity of the magnetic field lines we set $f_e(-\pi R, v, t) = f_e(\pi R, v, t)$, and the initial velocity distribution function at $t = 0$, uniform along the torus (T_e in eV) equals

$$f_e(z, v, 0) = \left(\frac{m_e}{2\pi k_b T_e 11600}\right)^{3/2} e^{\frac{-1/2 m_e v^2}{k_b T_e 11600}}. \quad (2.23)$$

The electric field distribution is strongly simplified, taking only the electrostatic electric field originating from the voltage difference between the strap and antenna box. As such, the electric field is taken equal to zero around the torus and in front of each strap, and $-E$ or $+E$ for the gaps between the antenna straps and antenna box. Fig. 2.8 shows the normalized electric field distribution both for monopole and dipole strap phasing.

The numerical solution of eq. (2.22) requires the definition of a spatial grid. In this grid one wants a strong spatial resolution in front of the antenna (e.g. one velocity distribution every millimeter, for a 1 m antenna region equals 1000 points), and a less but still high enough resolution for the rest

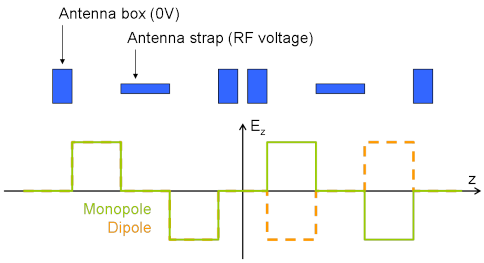

Figure 2.8: Schematic of the electrostatic electric field between the straps and antenna box in monopole and dipole.

of the torus (one velocity distribution every centimeter, for a $2\pi(R_0 + a)$ m torus circumference equals > 1000 points). Implementing the equation in this manner is complex since it needs to take into account different grids resolutions, and connect in front of the antenna, zones with and without electric field. Also the number of distribution functions over which one would need to iterate is very high (> 2000). For these reasons, solving the equation via its spatial Fourier transform appeared more attractive.

The simplified electric field 'blocks' shown in Fig. 2.8 can easily be represented as a sum of its Fourier components. The Fourier components of a rectangular function

$$f(z) = \begin{cases} 1 & \text{if } z \in A = [z_0 - h, z_0 + h], \\ 0 & \text{if } z \notin A. \end{cases} \tag{2.24}$$

with z_0 the center of the block and h its half width, are obtained from the Fourier integral:

$$\int_{z_0-h}^{z_0+h} e^{-ikz}\,\mathrm{d}z = \left[\frac{e^{-ikz}}{-ik}\right]_{z_0-h}^{z_0+h} = \frac{e^{-ik(z_0+h)} - e^{-ik(z_0-h)}}{-ik}$$

$$= e^{-ikz_0}\frac{e^{-ikh} - e^{ikh}}{-ik} = \frac{2}{k}\sin(kh)e^{-ikz_0} \tag{2.25}$$

For the TEXTOR antenna we superpose four electric field rectangles ($h = 0.065$ m) with their centers at $z_0 = [-30, -10, 10, 30]$ cm. In 0-phasing the polarity of the blocks are respectively $[+1, -1, +1, -1]$ and for π-phasing we have $[+1, -1, -1, +1]$ (see Fig. 2.8). In case of 0-phasing the total spectrum will thus be:

$$\begin{aligned} E(k) &= \frac{2}{k}\sin(kh)(e^{i0.3k} - e^{i0.1k} + e^{-i0.1k} - e^{-i0.3k}) \\ &= \frac{4i}{k}\sin(kh)(\sin(0.3k) - \sin(0.1k)) \end{aligned} \tag{2.26}$$

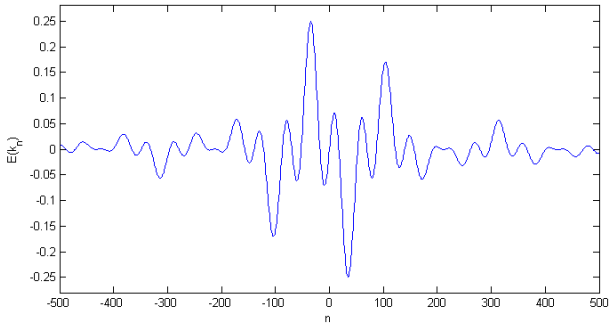

Figure 2.9: Representation of eq. (2.26): $E(k)$ as a function of n.

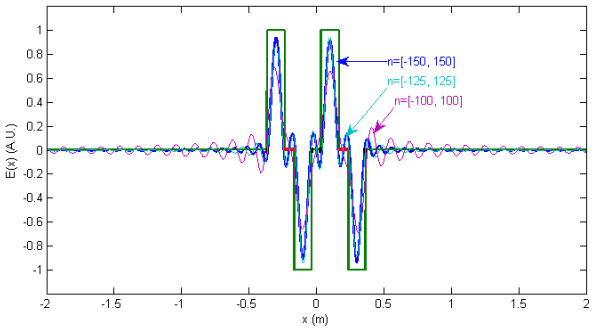

Figure 2.10: Fourier recomposition of near antenna electric field

which is represented in Fig. 2.9. As edge condition, to cope with the periodicity of the torus we must keep only the wave vectors that are multiples of $1/(R_0 + a)$:

$$k_n = \frac{n}{R_0 + a} \text{ for } n \in \aleph_0. \tag{2.27}$$

With the inverse Fourier transform we recover the spatial distribution where we truncate the sum for the lowest reasonable value of n.

$$E(z) = \frac{1}{2\pi} \int_{-\infty}^{\infty} E(k) e^{ikz} \, \mathrm{d}k \approx (R_0 + a) \frac{1}{2\pi} \sum_{n=-\infty}^{\infty} E(k_n) e^{ik_n z} \tag{2.28}$$

Where $(R_0 + a)$ accounts to correct the amplitude of $E(z)$. The result for $n = [-100 : 100], [-125 : 125]$ and $[-150 : 150]$ is given in Fig. 2.10. The figure illustrates that the number of Fourier components (distribution functions) has to be higher than $2 \times 125 + 1$ to reproduce an electric field that sufficiently resembles the original one[3].

[3]In fact, we do not want the exact block function since in that case the previously

For the numerical implementation of the 1D Vlasov equation (eq. 2.22) we apply a Fourier transform in space:

$$\frac{\partial}{\partial t} f_e(k,v,t) + ikv f_e(k,v,t) - \int \frac{q_e}{m_e} E(z,t) \frac{\partial}{\partial v} f_e(z,v,t) e^{-ikz}\,\mathrm{d}z = 0 \quad (2.29)$$

which with

$$\begin{aligned} \int E(z,t) g(z,v,t) e^{-ikz}\,\mathrm{d}z &= \frac{R_0+a}{2\pi} \int \sum E(k_n,t) e^{ik_n z} g(z,v,t) e^{-ikz}\,\mathrm{d}z \\ &= \frac{R_0+a}{2\pi} \sum E(k_n,t) \int e^{-i(k-k_n)z} g(z,v,t)\,\mathrm{d}z \\ &= \frac{R_0+a}{2\pi} \sum E(k_n,t) g(k-k_n,v,t) \qquad (2.30) \end{aligned}$$

results in

$$\frac{\partial}{\partial t} f_e(k_m,v,t) = -ik_m v f_e(k_m,v,t) + \frac{R_0+a}{2\pi} \frac{q_e}{m_e} \sum E(k_n,t) \frac{\partial}{\partial v} f_e(k_m - k_n, v, t)$$

Or if we truncate the number of distribution functions to $m = [-150 : 150]$

$$\begin{aligned} \frac{\partial}{\partial t} f_e(k_m,v,t) &= -ik_m v f_e(k_m,v,t) \\ &+ \frac{R_0+a}{2\pi} \frac{q_e}{m_e} \sum_{n=-150-m}^{150-m} E(k_n,t) \frac{\partial}{\partial v} f_e(k_{m-n},v,t) \qquad (2.31) \end{aligned}$$

To agree with the initial condition, the inverse Fourier transform of $f_e(k,v,t)$ at $t = 0$ needs to result in eq. (2.23):

$$f_e(z,v,0) = \frac{1}{2\pi} \sum f_e(k_n,v,0) e^{ik_n z} \qquad (2.32)$$

from which we know that

$$f_e(k_n,v,0) = \begin{cases} 2\pi f_e(z,v,0) & \text{if } n = 0, \\ 0 & \text{if } n \neq 0 \end{cases} \qquad (2.33)$$

Eq. (2.31) can be solved explicitly or implicitly. The implicit solution requires the inversion of a large matrix, which could be done manually. However the resulting code was too slow to obtain sufficient simulation time. For the explicit solution, the accuracy and calculation time were found to be very sensitive to the chosen time step and velocity grid ($v_{\min}$, $v_{\max}$ and $\mathrm{d}v$). Only 7 RF periods could be simulated with the explicit scheme for which the calculation time took approximately 2 CPU days. On continuing the calculation for further RF periods the result mostly becomes unstable

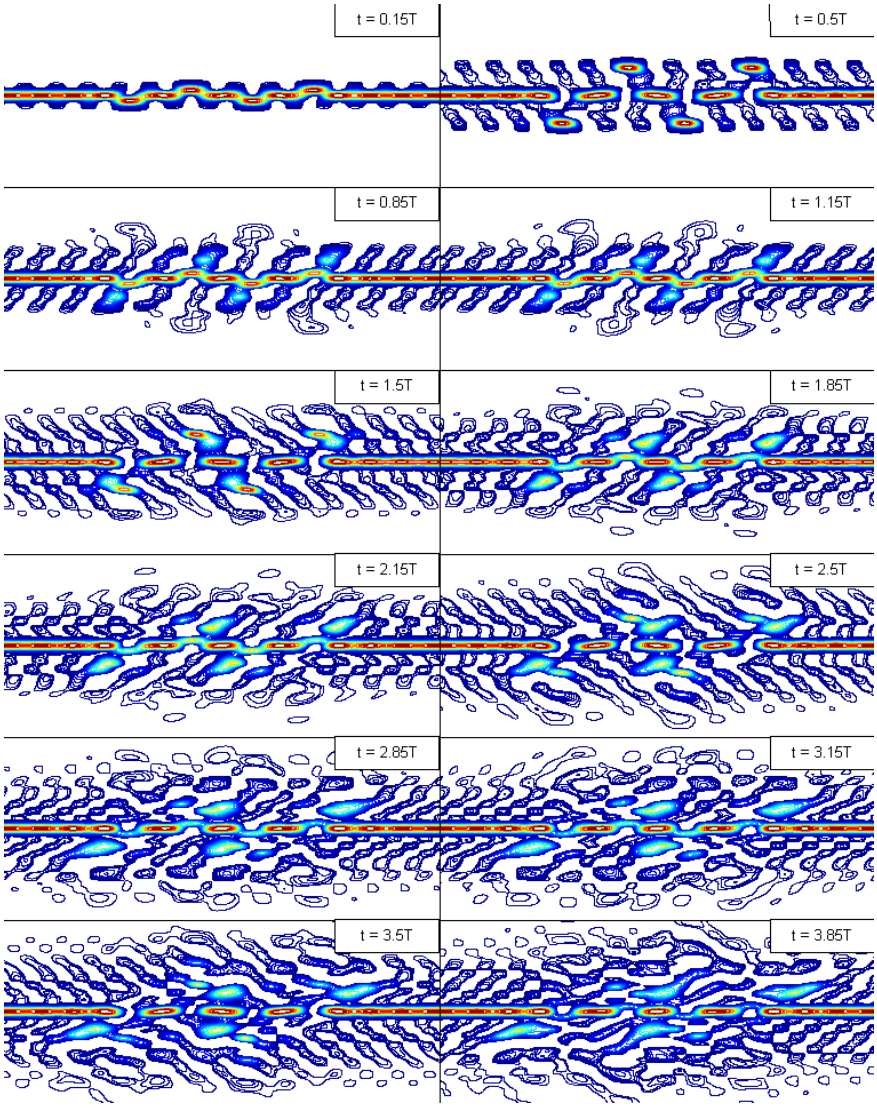

Figure 2.11: Evolution of the electron distribution for the simplified TEXTOR antenna electric field (and torus) dimensions in monopole phasing, with parallel electric field amplitude of $E_0 = 3\,\mathrm{kV/m}$, RF frequency $f = 48\,\mathrm{MHz}$, initial electron energy distribution function of $0.5\,\mathrm{eV}$, $n = [-135 : 135]$ and velocity array $v = [-8v_o : 8v_o]$ (length = 3001) with $v_o = eE_0/2\pi f m_e$, the oscillation velocity amplitude in a homogeneous oscillating electric field with amplitude E_0. The time instance for each plot is given as a function of the RF period, the x-axis represents the length scale along the magnetic field [-1 to 1 m], and the y-axis, the parallel velocity [-10^7 to 10^7 m/s]. (The ionization threshold velocity equals $v^i_{\mathrm{th}} = 2.2 \cdot 10^6 m/s$)

due to repeatedly summing over the first derivatives of the spectral distribution functions. Fig. 2.11 shows a simulation result for the TEXTOR antenna (and torus dimensions) in monopole phasing, with parallel electric field amplitude of $E_0 = 3\,\mathrm{kV/m}$, RF frequency $f = 48\,\mathrm{MHz}$[4], initial electron energy distribution function of $0.5\,\mathrm{eV}$, $n = [-135 : 135]$ and velocity array $v = [-8v_o : 8v_o]$ (length = 3001) with $v_o = eE_0/2\pi f m_e$, namely the oscillation velocity amplitude in a homogeneous oscillating electric field with amplitude E_0. The two top figures for $t = 0.15T$ and $t = 0.5T$ show that the electron distribution function in front of the antenna strap-box gaps shifts entirely in velocity space due to the electric force. These shifts occur periodically and represent electrons that oscillate with the RF period in the electric field in front of the antenna. The maximum obtained velocity after $t = 0.5T$ ($v_e \approx 3 \cdot 10^6\,\mathrm{m/s}$) on the right top figure is sufficient for ionization ($v^i_{\mathrm{th}} = 2.2 \cdot 10^6 m/s$). Already after the first oscillation it is clearly visible that groups of electrons leave the electric field regions[5]. Electrons leaving at the left side having a negative velocity will travel around the torus and enter the antenna region again from the right side (in case of no collisions). The same happens for electrons leaving at the right side; they will go around the torus and enter the antenna region from the left. Electrons leaving from the central two electric field regions move towards the center ($z = 0$), and will finally reach the other electric field region where they will either undergo a net acceleration or deceleration, depending on the electric field polarization. Some part of these electrons will be sent back to the center region, and one can imagine that again a part of these electrons will remain trapped in 'resonant' trajectories between two electric field regions. Depending on the electric field distribution (strength and ponderomotive force), a certain electron fraction will undergo a chaotic movement around the torus, being accelerated or decelerated every time they pass the antenna region. Although it was not possible to confirm this by the simulation it is expected that after some time an equilibrium periodically oscillating electron distribution will be formed around the torus that could be used to couple with collisions and as such deliver a complete description of the breakdown phase.

2.3.6 Antenna coupling in ICWC mode of operation

As mentioned in section 2.3.2, the conventional antennas are designed for dense target plasma heating ($n_e \gg 10^{18}\,\mathrm{m^{-3}}$) through excitation of the FW with high coupling efficiency ($\eta > 0.9$) [94]. ICWC-plasmas have generally

discussed ponderomotive force would be infinite at the edges of the electric field regions.

[4]The RF frequency of $f = 48\,\mathrm{MHz}$ is not available on TEXTOR.

[5]The choice of initial antenna electric field polarization ($+E(r)\cos(\omega t)$ or $-E(r)\cos(\omega t)$) determines the direction of the electron groups.

a lower density ($n_e \sim 10^{16} - 10^{18}\,\mathrm{m}^{-3}$) which results mostly in a poor coupling ($\eta_0 \sim 0.2-0.3$) if standard ICRH heating settings are used. During the many experimental sessions on different machines improvements on the coupling efficiency were evidenced that allowed to increase the coupling efficiency 3 to 4 times. A recent publication of Lyssoivan [94] summarizes these findings and shows that they can be explained in terms of (a) the antenna parallel wave vector (k_z) spectrum and (b) wave mode conversions.

2.3.6.1 Antenna k_z spectrum

The antenna k_z spectrum depends strongly on the antenna strap phasing: for close to monopole phasing the spectrum is concentrated around longer wave lengths, for dipole phasing around shorter wave lengths. The radial decay length ($E_z^{\mathrm{vac}}(\delta r) \propto e^{-\delta r k_z}$) of the vacuum parallel electric field which is determined by the wave vector spectrum, will thus likewise depend on the antenna phasing. In monopole phasing the field will thus extend further into the vessel. The observed faster breakdown time in monopole phasing compared to dipole phasing, shown in Fig. 2.3, is a first example that can be related to the larger extension of the vacuum RF field. Secondly it was observed that also the coupling efficiency improves in case of low k_z values. In case the FW wave remains non propagative, this is thought to be purely related to the wider radial spreading of the vacuum RF field. However it is possible to obtain a regime wherein the FW becomes propagative, since the cut-off density for FW propagation is dependent on the parallel wave vector [105]:

$$\omega_{pi}^2 = \left(\frac{k_z^2 c^2}{\omega^2} - 1\right)\left(1 + \frac{\omega}{\omega_{ci}}\right)\omega_{ci}^2 \tag{2.34}$$

with ω_{pi} the ion plasma frequency, dependent on the ion density, ω the wave frequency and ω_{ci} the ion cyclotron frequency. A change from dipole to monopole phasing can change the cut-off density over a few orders of magnitude (from $10^{19}\,\mathrm{m}^{-3}$ to $6\cdot10^{16}\,\mathrm{m}^{-3}$ [105], JET). Fig. 2.12 (left) shows the coupling efficiency (left axis) as a function of the parallel wave vector spectrum for the JET A2 antenna, and the FW cut-off density on the right axis. For lower k_z values the coupling clearly increases, and in case of monopole phasing it is expected that the FW is even propagative, allowing for homogeneous plasma formation in the radial direction.

Monopole phasing of the antennas is thus the ideal mode of operation for ICWC. The further extension of the RF field in the vessel and the lower cut-off density for wave propagation in monopole phasing lead to better coupling efficiencies, lower RF voltages, a more homogeneous plasma distribution and shorter breakdown times than in dipole phasing.

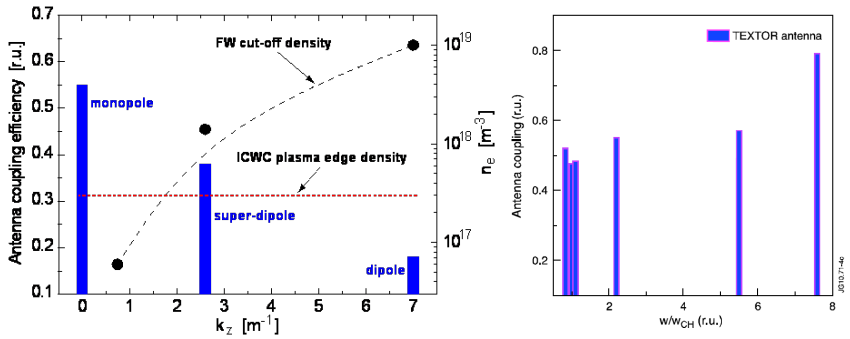

Figure 2.12: Antenna coupling efficiency to ICWC plasmas ($n_e \sim 3 \cdot 10^{17}\,\mathrm{m}^{-3}$). Left: Antenna coupling efficiency vs. k_z-spectrum of the radiated RF power for standard ICRF antennas [105], Right: Antenna coupling efficiency vs. ion cyclotron harmonic number [94].

2.3.6.2 Mode conversion scenarios

On the other hand, it was observed that such homogeneous plasma distribution can also be obtained when operating the antennas in dipole phasing. In this case one needs to rely on mode conversion (MC) scenarios or dual frequency operation, for which the experimental proof is shown in Fig. 2.13. Conversion of the FW to the SW or ion Bernstein wave (IBW) becomes possible in plasmas with multiple ion species (typically the case in ICWC plasmas), and is localized at mode conversion layers, between ion-ion hybrid resonance layers and harmonic cyclotron resonance layers. The left picture, which is a top view CCD image of a pure helium RF plasma, thus in principle without MC, shows that the plasma is located at the low field side. On injecting hydrogen into the plasma MC becomes possible and the plasma extended further into the vessel (center picture). The fundamental

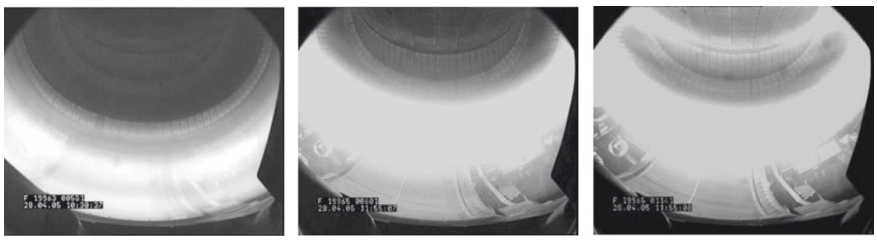

Figure 2.13: Top view CCD images of ICWC plasmas on ASDEX Upgrade: pure He ICWC plasma (left), $H_2/(He + H_2) \approx 0.3$ gas mixture (center) and for dual frequency operation in the same gas mixture (right, 30 MHz and 36.5 MHz). Discharge parameters: $B_T = 2.4\,\mathrm{T}$, $p \approx 4 \cdot 10^{-2}\,\mathrm{Pa}$, $P_{\mathrm{RF,coupled}} \approx 50\,\mathrm{kW}$

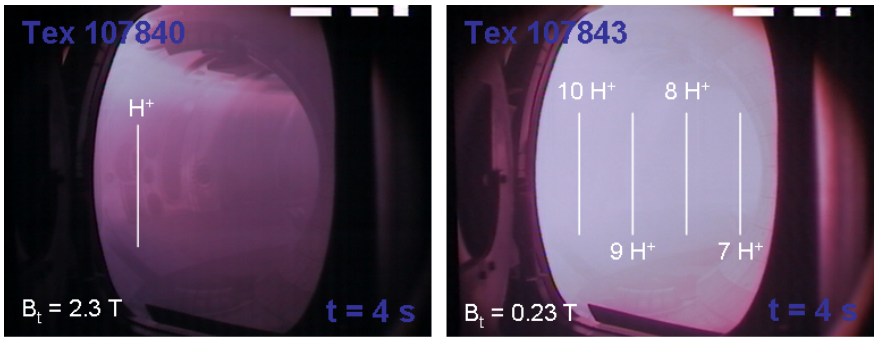

Figure 2.14: CCD images (tangential view) of TEXTOR He/H_2-ICWC discharges at resp. $B_T = 2.3\,\mathrm{T}$ (left) and $B_T = 0.23\,\mathrm{T}$ (right), both at the same generator power ($P_{\mathrm{RF,gen}} = 1 \times 80\,\mathrm{kW}$) and discharge pressure ($P_{\mathrm{tot}} = 5 \cdot 10^{-4}\,\mathrm{mbar}$).

cyclotron resonance layer in these two cases is located close to the antenna ($R = 2\,\mathrm{m}$, $30\,\mathrm{MHz}$). On adding a resonance layer, by changing the frequency of one of the antennas a second mode conversion can occur for this resonance layer ($R = 1.65\,\mathrm{m}$, $36.5\,\mathrm{MHz}$), which causes the further radial expansion of the plasma as can be seen on the right picture. The proof is strengthened by the confirmation of the observed radial plasma distribution with the 1D full wave RF code TOMCAT [89] (see [97]). In chapter 5 we will see that from atomic physics point of view, when keeping input power and total pressure constant, the plasma parameters of a hydrogen-helium plasma, can be significantly different from that of a pure helium plasma, which might also explain wider radial plasma extension. The further extension on application of two RF frequencies can however not be explained in terms of atomic physics only.

2.3.6.3 High harmonic scenarios

It is observed that ICWC operation at lower toroidal magnetic fields also increases the coupling efficiency. Fig. 2.12 (right) shows the coupling efficiency as a function of the ion cyclotron harmonic number calculated using the on axis magnetic field. The coupling efficiency of discharges at the 8th cyclotron harmonic number is 1.6 times higher than at the fundamental resonance. This is due to the strongly reduced cut-off density for FW excitation in case of high cyclotron harmonic (HCH) operation [87] (via the ion cyclotron frequency the cut-off density is a function of the magnetic field, see eq. 2.34). In this case the FW can become propagative even with antenna high k_z-spectrum (π-phasing) [87, 92]. Besides the higher coupling efficiency, the presence of multiple resonance harmonics in the low B_T case

allows also multiple mode conversions along the radius which can significantly improve the plasma homogeneity, due to a more homogeneous radial electron power deposition profile. Both effects are clearly visible by visual imaging. Fig. 2.14 shows CCD images of two almost identical ICWC discharges on TEXTOR, the left one at high toroidal field, and the right at low toroidal field.

2.4 Neutral cycle in vacuum vessel

Every discharge conditioning technique relies on the throughput of gas. The requested discharge gas is injected via valves while the neutral gas mixture in the vessel is continuously removed by the machine vacuum systems, called vacuum pumps. During ICWC experiments on current tokamaks, the available gas injection and vacuum pumps of the machines are used in their standard setup since changes in hardware are complex (or even not allowed). Nevertheless it is acknowledged that the efficiency of the conditioning technique strongly relies on the gas throughput, or more precisely on the efficiency for removing the wall released gas. In devices under conception (ITER) one has thus to foresee efficient pumping systems. In the following we give an overview of the involved gas dynamics, and the available pumping systems.

2.4.1 Vessel pressure evolution

The pressure p [Pa $= 10^{-2}$mbar], density $n = N/V$ [m^{-3}] and temperature T [K] of a gas are related by the very well known ideal gas law: $pV = NkT$. The total pressure in the vessel is the sum of the partial pressures of the different components of the gas mixture $p = p_{\rm A} + p_{\rm B} + ...$ in the vessel. The time evolution of the partial pressure of atom (or molecule) A can be expressed by the following equation:

$$\frac{{\rm d}p_{\rm A}}{{\rm d}t} = \frac{Q_{\rm sv,A}}{V} + \frac{Q_{\rm sw,A}}{V} - \frac{p_{\rm A} S_{\rm A}(p)}{V} - \sum_{ij} k^i_{j{\rm A}} n_j p_{\rm A} \qquad (2.35)$$

The equation includes injection of A by the valves, $Q_{\rm sv,A}$ [Pa.m^3/s][6], release of A from the vessel walls, $Q_{\rm sw,A}$ [Pa.m^3/s], removal of A by the pumps, $p_{\rm A} S_{\rm A}(p)$ [Pa.m^3/s], with $S_{\rm A}$ the pumping speed of A [m^3/s] which can be

[6]For completion we mention that injection flows are often given as a volume flow in ccm = cm^{-3}/min. To obtain the flow in Pa.m^3/s one has to know the pressure of the injection system. To express an amount of injected gas, or remaining gas in the injection balloons often the unit [mbar.l] is used. To obtain the correct number of injected, outpumped or present particles one logically always needs to take into account the temperature of the considered gas.

dependent on the pressure, and the last term represents losses of A due to elementary reactions in the plasma, where i labels the possible reactions (mainly ionization and dissociation) between plasma specie j and neutral gas A. The 0D character of eq. (2.35) is valid if the mean free path of the neutral molecules is large compared to the vessel dimensions. This condition is mostly fulfilled for the applied ICWC plasma parameter range. Separately, the last term in eq. (2.35) accounting for the loss of particles into the plasma can become very high compared to the injection rate by the valves and removal by the pumps. This will be discussed in detail chapter 4 and chapter 5.

Eq. (2.35) is very important, as will become clear further in this manuscript, since it allows to assess the removal efficiency of conditioning discharges (pS). It is used to obtain accurate particle balances for the discharges, or for example to predict the pressure in absence of plasma and compare with experimental measurements in presence of plasma. The pressure evolution in absence of plasma can be obtained numerically from eq. (2.35):

$$\begin{aligned} p_{\mathrm{A}}(t_2) &= p_{\mathrm{A}}(t_1) + \Delta p(\Delta t) \\ &= p_{\mathrm{A}}(t_1) + \frac{Q_{\mathrm{s,A}}(t_1)}{V}\Delta t - \frac{p_{\mathrm{A}}(t_1)S_{\mathrm{A}}}{V}\Delta t \\ &= \frac{Q_{\mathrm{s,A}}(t_1)}{V}\Delta t + p_{\mathrm{A}}(t_1)\exp(-\frac{S_{\mathrm{A}}}{V}\Delta t) \\ &= \frac{Q_{\mathrm{s,A}}(t_1)}{V}\Delta t + p_{\mathrm{A}}(t_1)\exp(-\frac{\Delta t}{\tau_{\mathrm{S,A}}}) \end{aligned} \tag{2.36}$$

where $\tau_{\mathrm{S,A}} = V/S_{\mathrm{A}}$ is the characteristic pumping time of A. The pumping speed S of a gas can thus be found experimentally by the exponential decay of the pressure in the vessel, as shown on Fig. 2.15.

2.4.2 Pumping systems

The employed pumping systems during conditioning discharges, required to remove wall desorbed particles from the vessel are connected to the vacuum vessel via pumping ducts. For efficient removal of neutralized gas in standard tokamak discharges the ducts are connected to the vessel on multiple locations along the toroidal limiter in limiter machines, and divertor in divertor machines. We distinguish two types of pumps, namely turbomolecular pumps and cryopumps.

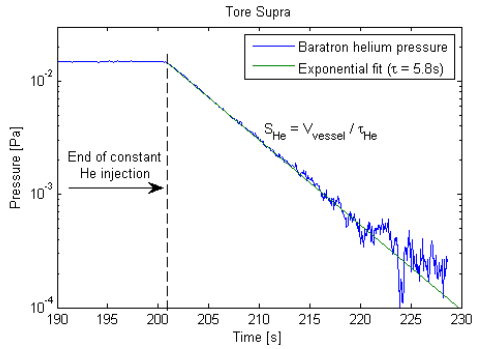

Figure 2.15: Exponential decay of the helium (baratron) pressure after ending the continuous helium gas flow ($t = 201\,\mathrm{s}$), showing that the helium pumping speed of the TORE SUPRA turbo pumps is pressure independent over 2 orders of magnitude, and can be described by a time constant $\tau_{\mathrm{S,He}}$.

2.4.2.1 Turbomolecular pumps

A turbomolecular pump [109] consists basically of multiple layers of fast rotating blades that will literally push the gas particles in a required flow direction: the particles receive impulse on impact with the rapidly moving surfaces. The pumps mostly require a vacuum pressure lower than a few Pascal to become efficient. The efficiency is inversely proportional to the square root of molecule mass ($1/\sqrt{m_{\mathrm{A}}}$), and requires that the rotor speed is larger than the speed of the molecules. On tokamaks TEXTOR, ASDEX Upgrade and TORE SUPRA the turbomolecular pumps are able to efficiently remove light particles such as H_2, D_2 and He ($\tau_{\mathrm{S}} < 10\,\mathrm{s}$). The JET turbopumps do not efficiently pump H_2 ($\tau_{\mathrm{S}} > 100\,\mathrm{s}$) and the pumping speed for He is very low $S_{\mathrm{He}} = 5\,\mathrm{m}^3/\mathrm{s}$ ($\tau_{\mathrm{S}} = 37\,\mathrm{s}$). For most machines, the pumping speed is only weakly dependent on the pressure in the applied range of conditioning pressures.

2.4.2.2 Cryopumps

The working of a cryopump [110] is based on the physisorption of particles on cooled surfaces. In principle cryopumps can thus pump all gases including noble gases, if the temperature is sufficiently low. Cryopumps are only efficient above the gas specific saturation pressure. Fig. 2.16 shows saturation vapor pressures for cryocondensation as a function of the cryosurface temperature. The JET cryopanels for example, which are at 4.8 K, do not efficiently pump hydrogen below 10^{-5} mbar, and also helium is not efficiently pumped. Deuterium, having a much lower saturation pressure, is efficiently adsorbed on the panel surfaces with high pumping speed $S_{\mathrm{D}_2} = 115\,\mathrm{m}^3/\mathrm{s}$

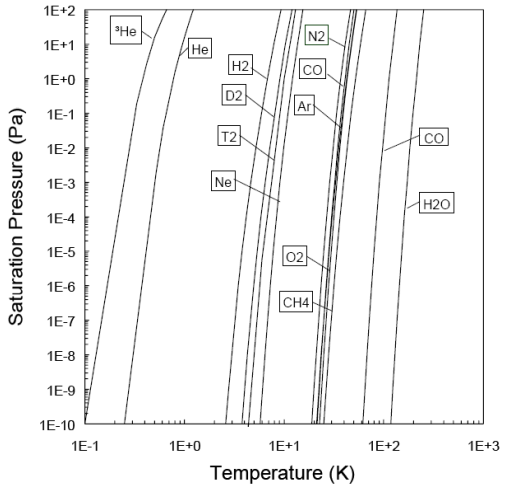

Figure 2.16: Saturation pressure curves of common gases as a function of the cooled surface temperature [110].

($\tau_S = 0.6\,s$). The total amount of molecules that can be accumulated on the cryosurfaces with high pumping speed is limited. When this limit is attained, the panels can still continue accumulating more gas (cryosorption) but with a strongly reduced pumping speed. Furthermore, a concurrent pumping of gases can occur in case of gas mixtures by entrainment (cryotrapping) of gas particles which are not condensible at the given temperatures and pressure conditions [111]. Due to the weak physical bondings the cryopanels can simply be regenerated on increasing the surface temperature. During regeneration, the content of the desorbed gas can be analyzed by gas chromatography (JET), which will be discussed in appendix B.

2.4.2.3 Pumping systems on ITER

The present ITER design is equipped with five cryopumps connected directly to the vessel, and three cryopumps on a branched duct. The charcoal coated cryopanels will be cooled to 4 K and are expected to efficiently pump helium, and all hydrogen isotopes. Table 2.2 gives the estimated pumping speeds of a single torus cryopump for common gases. The pumping speed for helium is expected to be $S = 52\,m^3/s$. The effective pumping speed of the pumps is due to the torus to pump connection conductivity properties however lower, $44\,m^3/s$ for a direct pump and $31\,m^3/s$ for a branched pump. The maximum attainable pumping time is thus $\tau_S = 1400\,m^3/313\,m^3/s = 4.5\,s$, which is slightly better than in current tokamak vacuum vessels. However

Table 2.2: Molecular pumping speeds S [m^3/s] at 293 K for a single ITER torus cryopump.

	He	H_2	D_2	DT	N_2
S [m^3/s]	52	78	55	50	21

on ITER the cryopumps will not all be operated at the same time. Since the capacity of a cryopump is limited, $\sim 45\,\mathrm{kPa.m^3}$ for ITER pumps (He), the operation scenarios for the pumps require the inclusion of pump regeneration time windows. The accumulated amount of gas per torus pump in a 400 s D/T discharge is of the order of $25\,\mathrm{kPa.m^3}$. It is therefore foreseen that the pumps are operated in sequences so that at any given time four out of eight pumps are operational. A pump that is operated during one plasma discharge, will be regenerating during the subsequent discharge. The foreseen pumping time during plasma discharges and wall conditioning discharges will thus be $\tau_S \approx 9\,\mathrm{s}$.

The required injection rate to obtain a typical ICWC pressure of 10^{-2} Pa on ITER can be calculated from eq. (2.35): $Q_{sv} = pV/\tau = 1.6\,\mathrm{Pa.m^3/s}$. A 500 s wall conditioning discharge would give thus a minor contribution to the total gas load to the pumps $0.8\,\mathrm{kPa.m^3} \approx 0.2\,\mathrm{kPa.m^3/pump}$.

2.5 Characterization of wall flux

In this section we will provide an overview of the characterized wall flux during ICWC discharges. Hydrogen ICWC:

- Neutral particles: In section 4.1.3 we will find that the wall flux in ICWC discharges is of the order of $\sim 10^{19} - 10^{20}\,/\mathrm{m^2 s}$ (TEXTOR and JET analysis). In chapter 5 on the 0D modeling of ICWC discharges we will find that this number corresponds to the flux of low energy neutral particles ($T \approx 3 - 5\,\mathrm{eV}$), stemming predominantly from the dissociation of neutral hydrogen molecules. These low energy particles can cause chemical erosion of surfaces. Since neutrals are not constrained by the magnetic field the neutral flux can be considered homogeneous.

- Energetic neutral particles: In case of resonant absorption of RF power, a flux of fast CX neutrals will occur. This wall flux can also be considered to be homogeneous. The fast CX flux measured on JET (see e.g. Fig. 4.7) is of the order of $10^{15} - 10^{17}\,/\mathrm{m^2 s}$, with Maxwellian energies of $T = 1 - 10\,\mathrm{keV}$. These high energies are sufficient to reach deeper surface layers and to cause physical sputtering. As will be

shown in section 4.1.2, the contribution of the high energy CX flux to the conditioning effect was found to be limited.

- Ions: On TEXTOR, the ion current on one of the ALT limiter blades was measured during H_2-ICWC while biasing the surface to $-300\,V$, resulting in an ion current of $10^{17} - 10^{18}\,/m^2s$. This number is confirmed in chapter 5 on the 0D modeling of ICWC discharges. The energy of this wall flux is not known. It is expected that, as in the case of GDC, sheath effects can increase the ion impact energy on the wall. Since ions are transported along the magnetic field lines, the ion flux is likely not homogeneous. The highest flux will be on limiting surfaces (see section 3.1).

Helium ICWC:

- Ions: 0D modeling results for TORE SUPRA He-ICWC discharges, presented in chapter 5, showed that the helium ion wall flux is of the order of $5 \cdot 10^{16} - 5 \cdot 10^{17}\,/m^2s$, and is an increasing function of the coupled RF power. Similar as for the H_2-ICWC ion wall flux, it is expected that sheath effects can increase the ion impact energy, and that the flux is likely not homogeneous due to ion transport along the magnetic field lines. The modeling results showed also that wall desorbed species can contribute largely to the wall flux: in case of a 4.5% hydrogen content in the discharge neutral pressure, the hydrogen ion wall flux is of the same order as the helium ion wall flux.

- Neutrals: The same 0D modeling results for TORE SUPRA He-ICWC discharges, presented in chapter 5, showed that the neutral hydrogen atom flux stemming from wall desorbed hydrogen can be of the order of $10^{18} - 10^{19}\,/m^2s$, thus larger than the ion fluxes.

3

ICRF plasma homogeneity and confinement properties

To ensure the ability of a discharge conditioning technique to effectively reach the whole wall area with a sufficient particle flux, the discharges are required to be homogeneous. In section 2.3 we saw that proper setting of the RF parameters is a first step to obtain homogeneous ICWC plasmas. However as will be shown in this chapter, some of the experimental findings on discharge homogeneity can not be explained in terms of RF power absorption properties.

In the first part of this chapter we will discuss experimental facts on plasma homogeneity, and how experimental optimization led to its improvement. In case when RF power absorption properties cannot explain the inhomogeneities, it is expected that the confinement properties of the toroidal magnetic field lie at the basis of these inhomogeneities. Therefore, in the second part of this chapter the confinement properties of a partially ionized plasma in a toroidal magnetic field configuration with additional small vertical component are discussed. In a final section of this chapter an equation for the plasma confinement time is given, from which the charged particle fluxes to the wall can be estimated. The latter is additionally motivated by the fact that in the 0D plasma model that will be discussed in chapter 5, the particle confinement times are required to calculate the particle and energy losses to the walls. Furthermore to justify the relevancy of a 0D approach to study RF plasma parameters, a proper consideration of the homogeneity

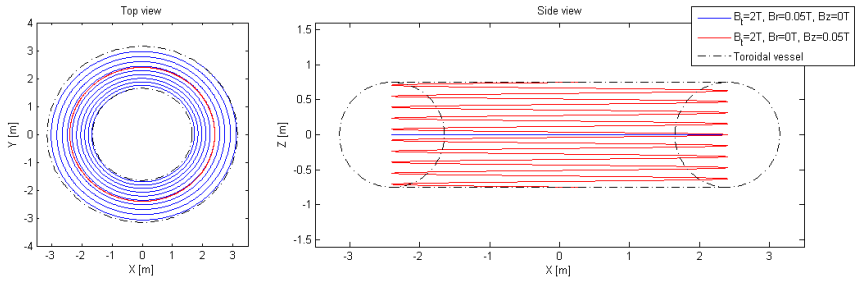

Figure 3.1: Simulated magnetic field lines resulting from a strong toroidal field (2 T), inhomogeneous in the radial direction, superimposed with a weaker homogeneous poloidal field (50 mT). The blue line results from an applied radial field, and the red line from a vertical field. Both simulated lines pass through the center of the vessel ($R = R_0$, $z = 0$, TORE SUPRA dimensions). Left: top view of the vessel, right: side view of the vessel.

of the RF plasmas is needed.

As an introduction to this chapter, we will start with a short summary on the ICWC magnetic configuration.

3.1 The magnetic field

The ICWC magnetic configuration consists of a high toroidal magnetic field $B_\phi(R)$, inhomogeneous in the radial direction, to which a smaller homogeneous poloidal field ($B_p = \text{cst}$) is superimposed[1]:

$$\vec{B}(R) = \frac{R_0}{R} B_\phi(R) \hat{1}_\phi + B_p \hat{1}_{z,R} \tag{3.1}$$

with R_0 the major radius. For the poloidal field, mostly a constant vertical field B_z is chosen since it was found experimentally that this field can improve the plasma homogeneity (see further). But also radial fields (B_R) or even time varying fields are possible. An illustration of the resulting field lines is given in Fig. 3.1. The figure shows two magnetic field lines passing though the center ($R = R_0$, $z = 0$) of the TORE SUPRA vacuum vessel, for a toroidal field of $B_\phi(R) = 2\,\text{T}$ and respectively a radial (blue) and vertical (red) field of $B_{R,z} = 50\,\text{mT}$. In case of a homogeneous radial field, the field lines (blue) will describe a spiral in the horizontal plane, from the inner wall to the outer wall. In case of a vertical field, the field lines (red) will describe a helix with constant radius (the major radius in this example) from the bottom of the vessel to the top. As stated in the introduction,

[1] In this chapter the toroidal magnetic field B_T is designated B_ϕ, the vertical field B_V is designated B_z.

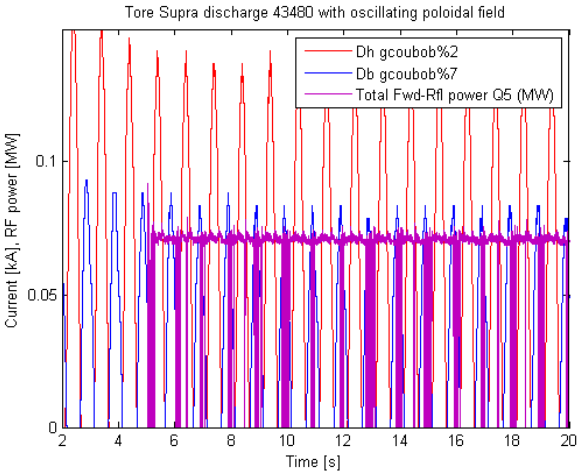

Figure 3.2: Currents in two outer poloidal field coils, Dh and Db (see Fig. A.4 for location), and forward minus reflected RF power for He-ICWC discharge. RF tripping events occurred with the same frequency as the applied poloidal field oscillation.

the poloidal field is generated by properly setting currents ($\sim$ kA) in the poloidal field coils, as is for example shown in Fig. A.5 in appendix A. By applying oscillating currents to the coils, the poloidal field will oscillate as well. This allows to sweep the plasma over the wall surface, which is confirmed by CCD camera images on both TEXTOR and TORE SUPRA. On TORE SUPRA however it was observed that RF tripping events occurred with the same frequency as the applied poloidal field oscillation (Fig. 3.2), making that this mode of operation is not recommended.

In tokamak plasmas with toroidal transform one speaks of the confined plasma and the plasma edge. The last closed flux surface separates these two areas (see section 1.2.6). In RF plasmas, in absence of the poloidal transform, a similar effect can be found (Fig. 3.3). For a purely toroidal magnetic field (top figure) all field lines in the plasma center are closed (red). The field lines at the 'edge' are limited by wall structures (green). In presence of a vertical field (bottom figure) one can distinguish long field lines (red), connecting the top half to the bottom half, and short ones (green) that are limited by wall structures. In analogy with the SOL in tokamak plasmas with rotational transform, the density is expected to decrease radially for limited areas. The density profile in the RF plasma edge depends than in

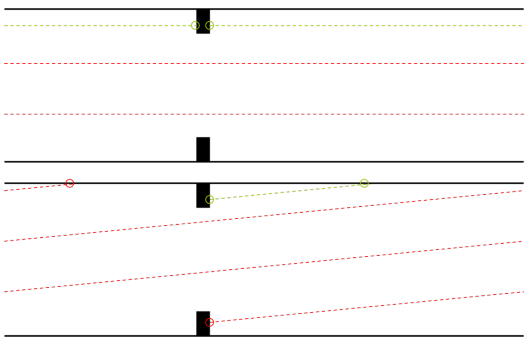

Figure 3.3: Schematic of the magnetic field lines (dashed lines) in the toroidal vessel (full lines), on a horizontal side view of the vessel. For a purely toroidal magnetic field (top figure) all field lines in the plasma center are closed (red). The field lines at the 'edge' are limited by wall structures (green). Similarly In presence of a vertical field (bottom figure) one can distinguish long field lines (red), connecting the top half to the bottom half, and short ones (green) that are limited by wall structures.

principle on a diffusion coefficient, and the decay length λ is given by [112]

$$\lambda = \sqrt{\frac{D_\perp L_c}{c_s}} \tag{3.2}$$

with $D_\perp$ the transverse diffusion coefficient, L_c the connection length between the limiters and c_s the ion sound velocity. The approximate radial density profile in the edge is then

$$n(r) = n(0)\exp(-r/\lambda). \tag{3.3}$$

The cross field diffusion coefficient, in absence of a vertical field, could be estimated on TEXTOR via the radial plasma density decay length (λ) close to the wall, shown below in Fig. 3.11.

3.2 Experimental observations on plasma homogeneity

3.2.1 Inhomogeneities in the plasma center

Due to particle transport along the magnetic field lines, RF plasmas are considered homogeneous in the toroidal direction. An experiment was proposed on TORE SUPRA to evidence this by measuring the currents on the six glow electrodes located at the top of the vessel (one in each Q-sector, see Fig. A.1) but unfortunately this experiment could not take place. In the

poloidal plane RF plasmas are known to feature inhomogeneities for which sufficient experimental data is available.

3.2.1.1 Vertical inhomogeneities

Experimental data shows a tendency of the plasma to be concentrated at the top of the vessel, which is most pronounced at higher RF powers. Fig. 3.4 shows an extreme example of an ASDEX Upgrade plasma where all four RF antennas were employed ($f_{\mathrm{RF},1-2} = 36.5\,\mathrm{MHz}$ and $f_{\mathrm{RF},3-4} = 30\,\mathrm{MHz}$), with a total generator power of $P_{\mathrm{RF,gen}} = 400\,\mathrm{kW}$ and pressure of $p_{\mathrm{He}} \approx 3 \cdot 10^{-5}\,\mathrm{mbar}$. The foreseen helium pressure during this discharge was $p_{\mathrm{He}} = 2 \cdot 10^{-4}\,\mathrm{mbar}$, but due to the consumption of helium by the vessel walls the pressure during the discharge was much lower (see section 4.2.5). The high RF power, combined with relative low pressure and small ASDEX Upgrade vacuum vessel volume, make that the ionization during this discharge is close to complete. This is confirmed by the fact that the recorded density by interferometry ($n_e \approx 10^{18}\,\mathrm{m}^{-2}$ for approximately 1 m viewing lines) is in agreement with the helium density derived from the neutral pressure measured in the divertor area ($3 \cdot 10^{-5}\,\mathrm{mbar} \approx 7.5 \cdot 10^{17}\,\mathrm{m}^{-3}$ at 300 K). The visible light image, obtained with a fast CCD camera and overlaid to the ASDEX Upgrade inner wall reconstruction[2], shows the strong poloidal inhomogeneity of the plasma. Almost no light is emitted from the lower vessel part, and seemingly even the lower part of the RF antenna area has a limited plasma density. Based on this result it is assumed that plasma drifts rather than RF power coupling properties lie at the origin of the vertical inhomogeneity.

On JET it was shown that on applying a small vertical field, the vertical homogeneity can be improved, and that the divertor area can be reached. Fig. 3.5 shows CCD images of two identical RF discharges respectively without (left) and with (right) vertical field ($B_z = 30\,\mathrm{mT}$). On application of the vertical field more light, resulting from collisional processes of recycled neutral particles, is emitted from the divertor area on the bottom of the vessel. Furthermore the plasma is also clearly brighter at the high field side which indicates that the vertical field also influences the radial homogeneity. Fig. 3.6 confirms both facts with help of interferometry data. The density from horizontal HCN viewing lines 5 and 8 is clearly higher on application of a vertical field, and the densities from vertical viewing lines (1 and 4, respectively at high and low field side) approach each other on application of a vertical field (see appendix A for the geometry of the HCN viewing lines). The fact that the plasma can be stretched in the vertical direction on ap-

[2]Thanks to dr. Tillman Lunt, IPP-Garching

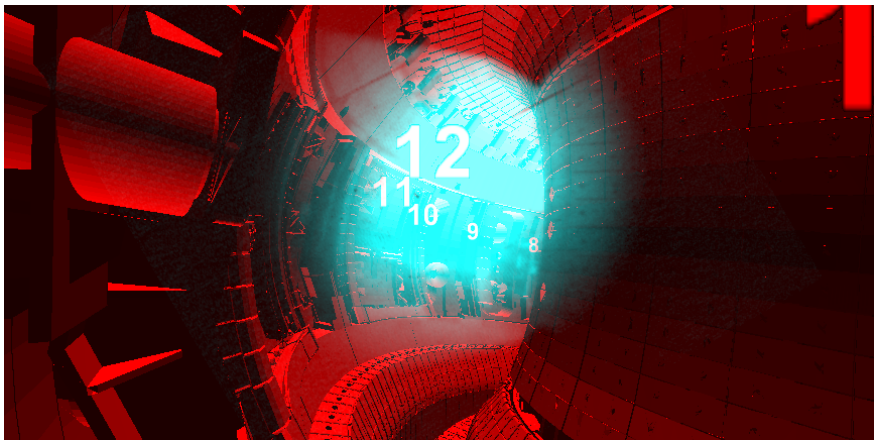

Figure 3.4: Fast CCD camera image of ASDEX Upgrade ICWC discharge 24852: $f_{\mathrm{RF}} = 36.5 + 30\,\mathrm{MHz}$, $P_{\mathrm{RF,gen}} = 400\,\mathrm{kW}$ and $p < 1.0 \cdot 10^{-4}\,\mathrm{mbar}$. The visible light image shows the strong poloidal inhomogeneity of the plasma.

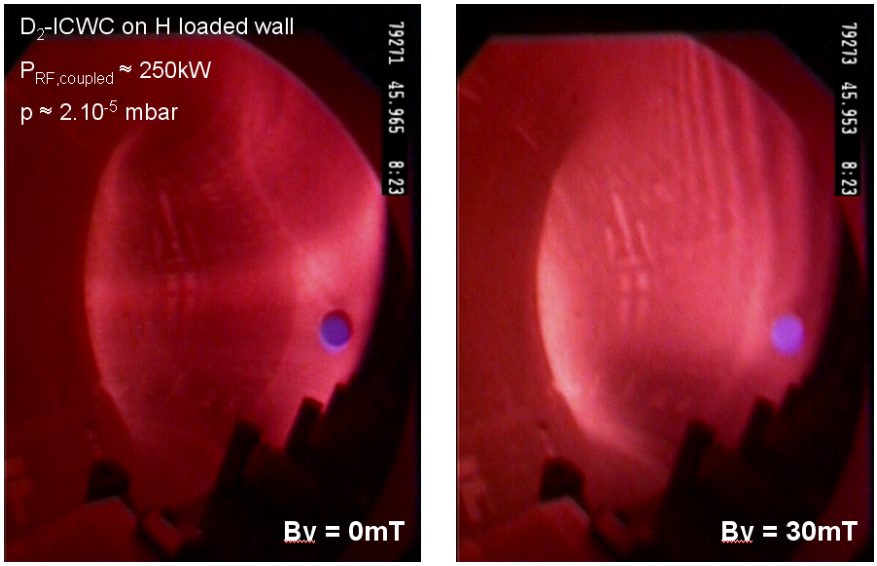

Figure 3.5: CCD image of JET ICWC discharges 79271 and 79273, respectively without (left) and with (right) vertical magnetic field of $B_z = 30\,\mathrm{mT}$: $f_{\mathrm{RF}} = 25\,\mathrm{MHz}$, $P_{\mathrm{RF,coupled}} = 250\,\mathrm{kW}$ and $p = 2.0 \cdot 10^{-5}\,\mathrm{mbar}$. The visible light image shows the overall improvement of the poloidal homogeneity on application of the vertical magnetic field.

plying a small vertical field can be understood from particle transport along the upwards spiraling magnetic field lines. Interpreting the improvement in

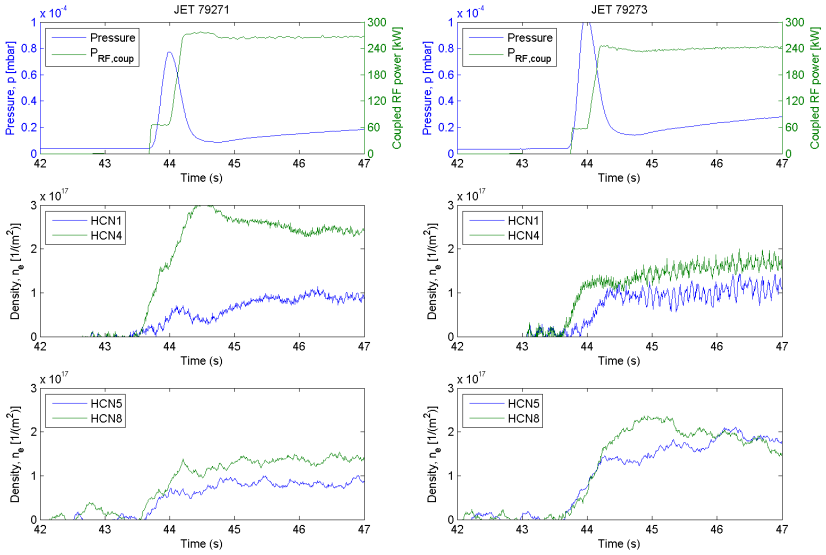

Figure 3.6: JET discharge 79271 and 79273, respectively without (left) and with (right) vertical magnetic field of $B_z = 30\,\mathrm{mT}$: $f_{\mathrm{RF}} = 25\,\mathrm{MHz}$, $P_{\mathrm{RF,coupled}} = 250\,\mathrm{kW}$ and $p = 2.0 \cdot 10^{-5}\,\mathrm{mbar}$. The HCN density data (KG1) shows an improvement of the radial homogeneity on application of a small vertical magnetic field.

the radial direction is less straight forward since it probably results from a synergy of improvement of the vertical homogeneity and RF power coupling properties. The possibility that the improvement of the radial homogeneity stems from the reduction of the radial outward plasma drift by the vertical magnetic field is analyzed below, and is thought to be negligible.

The plasma extension in the vertical direction was also evidenced on TEXTOR by Li-beam T_e and n_e measurements. The diagnostic was located in the TEXTOR bottom limiter lock. Fig. 3.7 shows the measured electron temperature, density and electron pressure ($n_e k_B T_e$) as a function of the applied poloidal magnetic field (1 mT) oscillation (10 Hz). Although only five measurement points per oscillation period could be obtained, the two maxima per period in all quantities are located where the oscillating field is mainly vertical [113][3].

[3]During later TEXTOR experimental sessions using vertical fields and where even a systematic scan of B_z is effectuated, the Li-beam was either not operational or if operational, the data could unfortunately not be processed due to a missing characteristic radiation line.

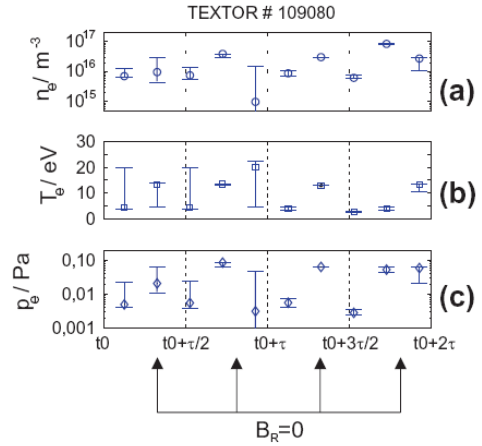

Figure 3.7: (a) Electron density, (b) electron temperature and (c) electron pressure measured by Li beam diagnostics conditionally averaged over two oscillation periods of the radial magnetic field B_R and vertical field B_z. [113]

3.2.1.2 Radial inhomogeneities

On TEXTOR a systematic scan of the vertical field was effectuated in hydrogen discharges with $f_{\mathrm{RF}} = 29\,\mathrm{MHz}$, $B_\phi = 2.3\,\mathrm{T}$, $P_{\mathrm{RF,gen}} = 2\times 50\,\mathrm{kW}$ and $p = 5.0\cdot 10^{-4}\,\mathrm{mbar}$ (feedback pressure). The scan was done mainly to investigate the wall conditioning effect as a function of the vertical field. The radial density profile obtained from vertical interferometry lines is shown on Fig. 3.8 (left). It shows clearly that the radial homogeneity of the discharge is not a simple function of the vertical field. The electron density in the center of the vessel is relatively high at $B_z = 0\,\mathrm{mT}$, and decreases first to obtain a second maximum at $B_z = 40\,\mathrm{mT}$. This behavior is at this point not understood. Also two peaks are observed in the profiles, one at $R = 1.95\,\mathrm{m}$ and one at $R = 1.57\,\mathrm{m}$ while the fundamental resonance layer for protons lies at $R = 2.1\,\mathrm{m}$. At this point there is no clear explanation for these peaks, not in terms of B_z-field, nor in terms of RF coupling properties (the partial pressure ratio of H_2, HD and D_2 was 37/46/17). The peaks, or drop of density in the center, is not present for a vertical field of 40 mT. From visual inspection of CCD images it was also found that the plasma homogeneity is optimal for this B_z-value. Although, as already mentioned, this data remains mainly uninterpreted, further experiments on TEXTOR are carried out with the 40 mT vertical field value. The right plot in Fig. 3.8, shows for similar TEXTOR hydrogen discharges that the radial homogeneity is also dependent on the RF power ($P_{\mathrm{RF,gen}} = 2\times 100\,\mathrm{kW}$) and discharge pressure ($p = (1-5)\cdot 10^{-4}\,\mathrm{mbar}$). On increasing the RF power, the density

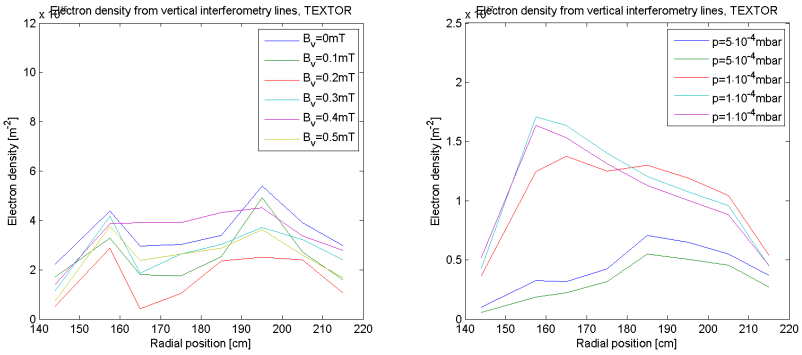

Figure 3.8: Radial density profile of TEXTOR hydrogen ICWC discharges ($f_{\mathrm{RF}} = 29\,\mathrm{MHz}$, $B_\phi = 2.3\,\mathrm{T}$, 113192:113198). Left: profiles as a function of the applied vertical magnetic field ($P_{\mathrm{RF,gen}} = 2\times 50\,\mathrm{kW}$ and $p = 5.0\cdot 10^{-5}\,\mathrm{mbar}$). Right: profiles as a function of the discharge pressure ($B_z = 40\,\mathrm{mT}$, $P_{\mathrm{RF,gen}} = 2\times 100\,\mathrm{kW}$, 113240:113244).

at the HFS remains practically unchanged, while the density at the LFS increases. The observed maximum on the LFS could be explained by the fact that the RF electric field is higher close to the antenna, located at the LFS. However on decreasing the pressure, the maximum shifts to the HFS. The latter could be due the improved wave propagation at higher density.

For helium ICWC discharges, the plasma density and temperature appears to be systematically higher on the LFS than on the HFS. Similar as for hydrogen discharges the higher density and temperature at the LFS is thought to be due to the RF field distribution in the vessel for which the electric field strength is highest close to the antennas, located at the LFS. Fig. 3.9 shows electron density profiles from reflectometry for TORE SUPRA He-ICWC discharges with $p_{\mathrm{He}} = 1.8\cdot 10^{-4}\,\mathrm{mbar}$, $P_{\mathrm{RF,gen}} = 100$, 200 and 400 kW, $B_\phi = 3.8\,\mathrm{T}$ and $B_z = 0\,\mathrm{T}$. The TORE SUPRA reflectometer is located in the center toroidal plane (see Fig. A.1). The distance of $R = 3.12\,\mathrm{m}$ corresponds to the location of the antenna protection limiter (indicated on Fig. 1.7). The fundamental resonance layer for protons lies at $R = 2.9\,\mathrm{m}$ while the hydrogen partial pressure in these discharges is about $p_{\mathrm{H_2}} = 1\cdot 10^{-5}\,\mathrm{mbar}$. No density peak is observed around the resonance layer. The obtained densities are in close agreement with interferometry data.

Fig. 3.10 shows measured ECE temperature profiles (electron cyclotron radiation temperature, see appendix B.2.3) along the radius as a function of the discharge time, for a JET $\mathrm{He/D_2}$ discharge ($\sim 0.75\cdot 10^{-5}/0.25\cdot 10^{-5}\,\mathrm{mbar}$) with $P_{\mathrm{RF,coupled}} = 60\,\mathrm{kW}$. The plasma temperature clearly

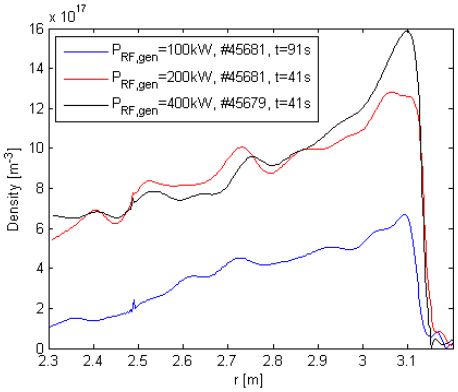

Figure 3.9: Reflectometry electron density profiles for TORE SUPRA He-ICWC discharges ($p_{\mathrm{He}} = 1.8 \cdot 10^{-4}$ mbar, $P_{\mathrm{RF,gen}} = 100$, 200 and 400 kW, $B_\phi = 3.8$ T and $B_z = 0$ T). The plasma density decreases clearly from the LFS to the HFS.

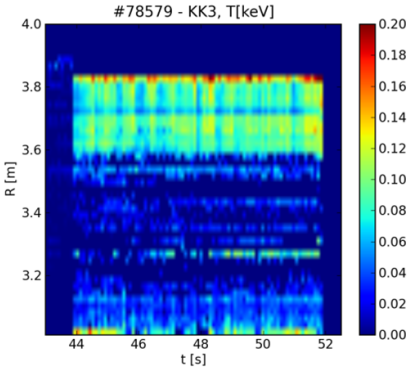

Figure 3.10: ECE (KK3) temperature as function of radial position and time for JET ICWC discharge 78579 ($f_{\mathrm{RF}} = 25$ MHz, $P_{\mathrm{RF,coupled}} = 60$ kW and $p = 1 \cdot 10^{-5}$ mbar).

decreases from the LFS to the HFS. The fundamental resonance layer for deuterium ions lies in the center of the vessel ($R \approx 3$ m) which might explain the apparent increase of density on the bottom of the figure. No temperature measurements are obtained for $R > 3.85$ m at the LFS: the horizontal ECE viewing line is located about 13 cm above the vacuum vessel mid-plane [114], where the radial location of the antenna protection limiters (A2 antennas) corresponds to ~ 3.88 m [115]. Similar as on JET, the ASDEX Upgrade ECE data showed also a clear temperature peak along the radius. However, due to uncertainties on the mapping of the ECE profiles, the radial position of the peak could not be determined.

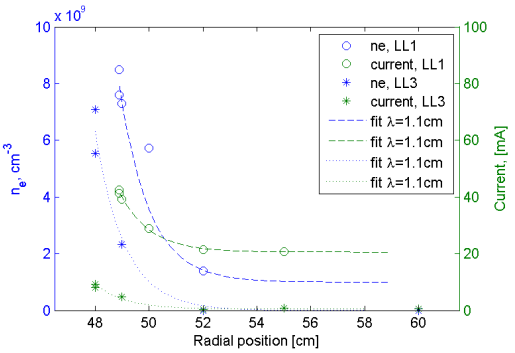

Figure 3.11: Measured electron density decrease of near the vessel wall at the bottom (LL1) and the top (LL3) of the TEXTOR vessel, where the toroidal magnetic field lines are limited by poloidal limiters. Left axis: electron density obtained from 2 double Langmuir probes, right axis: collected current on biased probe holder ($-100\,\mathrm{V}$). ($p_{\mathrm{H_2}} = 5 \cdot 10^{-4}\,\mathrm{mbar}$, $P_{\mathrm{RF,gen}} = 2 \times 50\,\mathrm{kW}$, $B_\phi = 2.3\,\mathrm{T}$)

3.2.2 Inhomogeneities at the edge of the plasma

The above TORE SUPRA reflectometry and JET ECE data illustrate the existence of a plasma edge, with low plasma density (too low to obtain ECE data), from the antenna protection limiters to outer torus wall. As discussed above, the density profile in the RF plasma edge depends on a cross field diffusion coefficient. This diffusion coefficient, in absence of a vertical field, could be estimated on TEXTOR via the radial plasma density decay length λ close to the wall. Two identical structures equipped with a double Langmuir probe (see B.6) were inserted in the plasma ($p_{\mathrm{H_2}} = 5 \cdot 10^{-4}\,\mathrm{mbar}$, $P_{\mathrm{RF,gen}} = 2 \times 50\,\mathrm{kW}$, $B_\phi = 2.3\,\mathrm{T}$) at the top and bottom of the vessel via the TEXTOR limiter locks. Both limiter locks were biased at $-100\,\mathrm{V}$. The electron density, temperature and total collected current on the structures could be recorded as a function of their radial position. The toroidal magnetic field lines at these positions are limited by a poloidal limiter, namely one at the top and one at the bottom of the vessel (as in the schematic on Fig. 3.3). The connection length L_c of the magnetic field lines is thus one toroidal rotation $L_c = 11\,\mathrm{m}$. Figure 3.11 shows the measured densities as a function of the radial position on the left axis. Because of the limited number of data points, the data is cross-checked with the total collected bias current on the structures (right axis) which is proportional to the local plasma density. Limiter lock 1 is located in the same sector as RF antenna A2. This is thought to cause the observed background current and density values via rectified RF current at large radial positions $r > 54\,\mathrm{cm}$. On limiter lock 3, located at least $3.5\,\mathrm{m}$ away from both RF

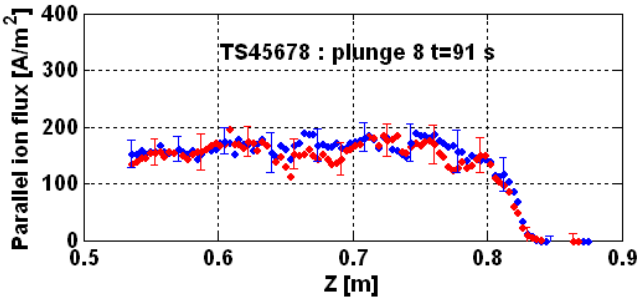

Figure 3.12: Langmuir probe data for TORE SUPRA He-ICWC discharge 45678: $f_{\mathrm{RF}} = 48\,\mathrm{MHz}$, $P_{\mathrm{RF,gen}} = 300\,\mathrm{kW}$ and $p_{\mathrm{He}} = 1.8 \cdot 10^{-4}\,\mathrm{mbar}$.

antenna A1 and A2, the background is not present. The four data sets can be approximately fitted with a same exponential decay length of $\lambda = 1.1\,\mathrm{cm}$ (dashed and dotted lines). From eq. (3.2) the cross field diffusion coefficient can be measured, which results in $D_{\mathrm{meas}} = 0.70 \pm 0.1\,\mathrm{m}^2/\mathrm{s}$. In section 3.3.5 we will see that this value corresponds to Bohm diffusion.

On TORE SUPRA also clear indications for a plasma edge are found at the top of the vessel. The radial plasma distribution could be measured by a RFA (see section B.2.5), shown on Fig. 3.12. The signal, representing the parallel ion flux along the field lines (red = ion side, blue = electron side, referring to the plasma current in ohmic discharges[4]), has a stable value for $z < 0.8\,\mathrm{m}$ from where it starts to decrease to become zero at $z > 0.84\,\mathrm{m}$. The probe is located in a top port at $R = 2.53\,\mathrm{m}$. At this position, the region of long magnetic connections begins at approximately $z \approx 0.82\,\mathrm{m}$ which corresponds roughly to the location of the decay of the signal (the uncertainty on the probe position is estimated to be 5 mm [116]). The limiting structure at this position are cooling tubes that protect the port from electron ripple losses. The red and blue signals are almost equal indicating the fact that there is no net plasma current in the RF discharges.

The observed decay of the plasma density close to the wall on TEXTOR, TORE SUPRA and JET is as mentioned due to the large parallel charged particle fluxes, and the intersection of the edge magnetic field lines by wall structures. The JET wide angle infrared camera images (Fig. 3.13) showed that these intersecting wall elements close to the plasma, such as the antenna limiters in the center of the picture and the inner poloidal bumpers on the left side of the picture, heat up during RF discharges. From this it can be concluded that these limiting surfaces receive a considerable fraction

[4] In TORE SUPRA the plasma current and B-field both point in the counter-clockwise direction viewed from above.

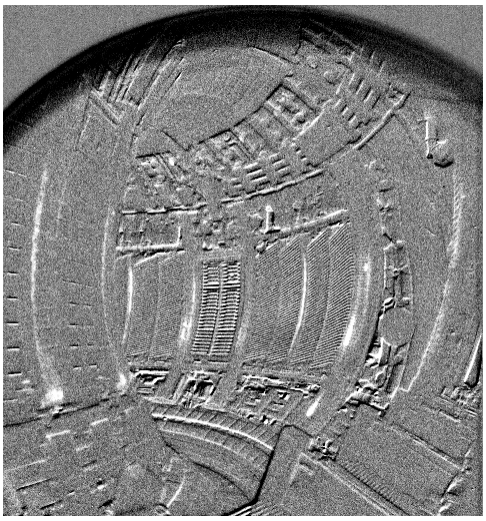

Figure 3.13: Wide angle IR camera (KL7) image of the 8 s He/D_2 (90/10) JET ICWC discharge 78579: $P_{RF,gen} = 200 - 350$ kW and $p = 1 \cdot 10^{-5}$ mbar during the discharge. Particle transport along magnetic field lines caused heating of field line intersecting wall elements (brighter areas).

of the ion wall flux. To increase the wall conditioning efficiency it might thus be interesting to adjust the poloidal field during a discharge to obtain optimal surface coverage. For example, a positive vertical field will improve cleaning of one side of a limiter, while a negative allows to condition the other side (see Fig. 3.3). One has to keep in mind however the RF trips that can occur on applying an oscillatory poloidal field, illustrated in Fig. 3.2. Alternatively the vertical field can be adjusted between subsequent conditioning discharges.

3.3 Confinement properties of toroidal magnetic field configurations

RF physics plays an important role on plasma homogeneity (see section 2.3). To ensure a homogeneous plasma, proper wave propagation in the vessel is mandatory to sustain the plasma also at the high field side. In the previous section we showed experimental facts on plasma homogeneities, and we indicated that not all of them can be explained purely in terms of RF physics, such as the strong vertical inhomogeneity and the decrease of plasma density close to the wall. It is expected that confinement properties of the toroidal magnetic field lie at the basis of this. In this section we

will give an overview of the confinement properties, including plasma drifts, losses along the magnetic field lines and diffusion across the magnetic field.

To have an idea of the magnitude of the derived quantities, a value will be given for a standard set of plasma parameters. For these examples we consider a H_2 discharge in TEXTOR ($R_0 = 1.75\,\mathrm{m}$, $a = 0.47\,\mathrm{m}$) with a magnetic field of $B_\phi(R = R_0) = 2.3\,\mathrm{T}$. The plasma parameters are calculated with the 0D model presented in chapter 5 ($p_{H_2} = 5.0 \cdot 10^{-4}\,\mathrm{mbar}$, $P_{\mathrm{coup}} = 100\,\mathrm{kW}$, without including plasma impurities):

$$T_e = 2.3\,\mathrm{eV} \qquad n_e = 8.1 \cdot 10^{11}\,\mathrm{cm}^{-3} \tag{3.4}$$

$$T_{H^+} = 1.3\,\mathrm{eV} \qquad n_{H^+} = 8.1 \cdot 10^{11}\,\mathrm{cm}^{-3} \tag{3.5}$$

$$T_H = 1.5\,\mathrm{eV} \qquad n_H = 1.3 \cdot 10^{12}\,\mathrm{cm}^{-3} \tag{3.6}$$

$$T_{H_2} = 0.9\,\mathrm{eV} \qquad n_{H_2} = 6.2 \cdot 10^{12}\,\mathrm{cm}^{-3} \tag{3.7}$$

with T the Maxwellian temperature and n the density. The reaction rates of importance are (see reactions in table 5.1 on page 5-5, and reaction rate figures in Appendix C.2)

$$k^{\mathrm{exc}}(H) = 1.3 \cdot 10^{-9}\,\mathrm{cm}^3/\mathrm{s} \tag{3.8}$$

$$k^{\mathrm{ion}}(H) = 2.6 \cdot 10^{-11}\,\mathrm{cm}^3/\mathrm{s} \tag{3.9}$$

$$k^{\mathrm{exc}}(H_2) = 2.6 \cdot 10^{-9}\,\mathrm{cm}^3/\mathrm{s} \tag{3.10}$$

$$k^{\mathrm{dis}}(H_2) = 4.2 \cdot 10^{-10}\,\mathrm{cm}^3/\mathrm{s} \tag{3.11}$$

$$k^{\mathrm{cx}}(H^+ + H) = 8.9 \cdot 10^{-9}\,\mathrm{cm}^3/\mathrm{s} \tag{3.12}$$

$$k^{\mathrm{cx}}(H^+ + H_2) = 5.0 \cdot 10^{-11}\,\mathrm{cm}^3/\mathrm{s} \tag{3.13}$$

from which we can deduce the collision frequency

$$\begin{aligned} \nu_{in} &= k^{\mathrm{cx}}(H^+, H) n_H + k^{\mathrm{cx}}(H^+, H_2) n_{H_2} \\ &= 1.4 \cdot 10^4\,\mathrm{s}^{-1} \end{aligned} \tag{3.14}$$

$$\begin{aligned} \nu_{en} &= (k^{\mathrm{exc}}(H) + k^{\mathrm{ion}}(H)) n_H + (k^{\mathrm{exc}}(H_2) + k^{\mathrm{dis}}(H_2)) n_{H_2} \\ &= 2.3 \cdot 10^4\,\mathrm{s}^{-1} \end{aligned} \tag{3.15}$$

The thermal velocity of the ions is

$$v_T = \sqrt{\frac{kT}{m_i}} = 1.1 \cdot 10^4\,\mathrm{m/s}, \tag{3.16}$$

and the mean free path of the ions is $\lambda = v_T/\nu_{in} = 0.75\,\mathrm{m}$.

At the end of this section we will formulate a general formula for the charged particle confinement time as a function of the particle energies, densities and vertical magnetic field. To obtain this expression only the steady state plasma is considered, as in [117]. However, the initial plasma phase plays an important role as well and will be described based on [118] and additional results from [117].

3.3.1 Summary of confinement properties

The confinement properties of the magnetic field given in eq. (3.1) can be summarized as follows: in the vertical direction the plasma is subject to '$\vec{B} \times \nabla B$' drifts stemming from the field curvature and gradient. The drift velocities are equal in size for electrons and for ions but in opposite directions: up for electrons and down for ions for standard clockwise B_ϕ-direction. Charge accumulation in the plasma edge due to the '$\vec{B} \times \nabla B$' drift induces an electric field causing an outward drift velocity [117] ('$\vec{E} \times \vec{B}$' drift). Both plasma drifts make that the plasma is inherently not in equilibrium. In a tokamak plasma the circular poloidal field component is generated by the plasma current to tackle this problem. In current-free ICWC plasmas this poloidal component is absent.

The latter vertical electric field will be build up during the initial discharge phase by the '$\vec{B} \times \nabla B$' drift current until a steady state value is reached. The changing vertical electric field in this initial phase will cause a polarization drift. As a result of the polarization drift the plasma moves as a whole to the top of the vessel in the initial discharge phase (for a clockwise toroidal magnetic field). We will investigate the magnitude of all mentioned drifts, and see whether they contribute to the plasma inhomogeneity.

On application of a poloidal magnetic field, an additional contribution to the particle wall flux will come from the transport of particles along the titled field lines, which will be analyzed in below as well.

Furthermore, the charged particles will diffuse across the magnetic field, which will be discussed at the end of this chapter.

3.3.2 Vertical drift

It is known that ions and electrons drift in opposite directions in an inhomogeneous magnetic field. Two mechanisms lie at the origin of this drift, namely the '$\vec{B} \times \nabla B$' drift and the curvature drift of which the velocities are given respectively by eq. (3.17) and eq. (3.18):

$$\vec{v}_{D_{\perp,1}} = \frac{m v_\perp^2}{2Ze} \frac{\vec{B} \times \nabla B}{B^3} \tag{3.17}$$

$$\vec{v}_{D_{\perp,2}} = \frac{m v_\parallel^2}{Ze} \frac{(\vec{B} \cdot \nabla)\vec{B} \times \vec{B}}{B^4} \tag{3.18}$$

with Ze the charge of the particle. Eq. (3.18) can be simplified since we consider $B_\phi \gg B_z$.

$$\vec{v}_{D_{\perp,2}} \approx \frac{m v_\parallel^2}{Ze} \frac{\vec{B} \times \nabla B}{B^3} \tag{3.19}$$

which makes that both drifts can be referred to as '$\vec{B} \times \nabla B$' drift. The direction of the drift velocity follows from

$$\begin{aligned} \vec{B} \times \nabla B &= \vec{B} \times (-\frac{C}{R^2})\hat{1}_R = \vec{B} \times (-\frac{B_\phi}{R})\hat{1}_R \\ &= -\frac{B_\phi B_z}{R}\hat{1}_\phi + \frac{B_\phi^2}{R}\hat{1}_z = \frac{B_\phi}{R}(B_\phi \hat{1}_z - B_z \hat{1}_\phi) \end{aligned} \tag{3.20}$$

and is thus perpendicular to the total magnetic field and the radial direction. The total perpendicular drift velocity is given by

$$\vec{v}_{\nabla B} = \frac{m}{2Ze}(v_\perp^2 + 2v_\parallel^2)\frac{\vec{B} \times \nabla B}{B^3}. \tag{3.21}$$

In case the kinetic energy of the particles is equally distributed over the degrees of freedom we have on the average $m(\frac{1}{2}v_\perp^2 + v_\parallel^2) = 2kT$ [118]. So eq. (3.21) simplifies to

$$\vec{v}_{\nabla B} = \frac{2kT}{Ze}\frac{\vec{B} \times \nabla B}{B^3} \approx \frac{2kT}{ZeRB_\phi} \approx \frac{2kT}{ZeRB}. \tag{3.22}$$

From eq. (3.22) it is clear that this drift is inversely proportional to the strength of the toroidal magnetic field B_ϕ. Thus for particle losses due to the vertical drift counts "the stronger the magnetic field, the better the confinement".

The total current density that can be attributed to this velocity in a hydrogen helium plasma is given by

$$\vec{j}_{\nabla B} = 2k\sum_j (n_j T_j)\frac{\vec{B} \times \nabla B}{B^3}, \tag{3.23}$$

with $j = \{e, \mathrm{H}^+, \mathrm{H}_2^+, \mathrm{H}_3^+, \mathrm{He}^+, \mathrm{He}^{2+}\}$, which for practical cases can be simplified to

$$j_{\nabla B} = \frac{2k}{RB}(n_e T_e + n_{\mathrm{H}^+} T_{\mathrm{H}^+} + n_{\mathrm{He}^+} T_{\mathrm{He}^+}). \tag{3.24}$$

To make the ions flow downwards and the electrons upwards, the magnetic field should be negative in a right handed system (clockwise) ($C < 0$). For our reference plasma we have $v_{\nabla B} = 0.6\,\mathrm{m/s}$, logically much smaller than the thermal velocity, and $j_{\nabla B} = 0.2\,\mathrm{A/m^2}$. The perpendicular current is about 3 to 4 orders of magnitude smaller than the measured parallel ion fluxes in ICWC, e.g. shown on Fig. 3.12 (for a helium plasma).

3.3.3 Radial drift and outward plasma acceleration

3.3.3.1 Radial drift

In the macroscopic approach from Müller [117] the opposite drift directions for ions and electrons lead to a vertical electric field due to charge accumu-

lation at the plasma boundaries. This electric field induces an $\vec{E} \times \vec{B}$ drift, directed outward to the LFS. The velocity of this drift can be described by the general formula for a drift in a force field,

$$\vec{v}_D = \frac{\vec{F} \times \vec{B}}{ZeB^2} = \frac{\vec{E} \times \vec{B}}{B^2} \tag{3.25}$$

To estimate the velocity, the accumulated electric field E is required. This poses a problem because no direct measurements for TORE SUPRA and TEXTOR are available. A derivation for this field can be found in [117] and gives

$$E_z = \frac{m_e}{q_e} \frac{\vec{\nu}_{\parallel}^{e/i} \vec{v}_{\nabla B}}{\sin^2(\theta)} \tag{3.26}$$

With $\vec{\nu}_{\parallel}^{e/i}$ the parallel collision frequency for ions and electrons, and $\theta = \arctan(\frac{B_z}{B_\phi})$ the angle of the magnetic field. An experimental value for a smaller device is given in [119] and can be used as guide line.

$$E_z(0) \approx 5 \frac{T_e(\text{eV})}{a(\text{m})} \tag{3.27}$$

For our reference plasma this gives $E_z(0) = 24\,\text{V/m}$ and a related drift velocity of $v_D = 10\,\text{m/s}$, which is about 10 times higher than the vertical drift. This is in contradiction to what is found below. In the further presented analysis we will derive these both formulas (3.26 and 3.27) independently, and we will show that the electric field and the related radial drift are likely negligible.

It is clear that the vertical electric field in the vessel, which is formed due to charge accumulation in the edge, can not increase infinitely. If the plasma is confined by conducting limiters or a conducting vacuum vessel, currents can flow in closed loops. Charge accumulation at the plasma edge, in principle negative at the top and positive at the bottom will thus be limited, and a quasi steady state situation will be formed. It is sometimes argued that the radial drift stemming from the electric field can be neglected because of these short circuiting currents in the conducting chamber walls [119, 120]. Below we will have a closer look at this point. Although the magnitude of the current in the walls is difficult to estimate we will show that the vertical electric field is very small.

As indicated by [117] it has been proposed since the 1960's that a small superimposed vertical magnetic field can allow the particles to generate additional short circuiting currents in the plasma that limit the electric field. In this manner the plasma might be confined for a significantly longer time than with a pure toroidal field, and the radial homogeneity might be improved. We will discuss this point further below.

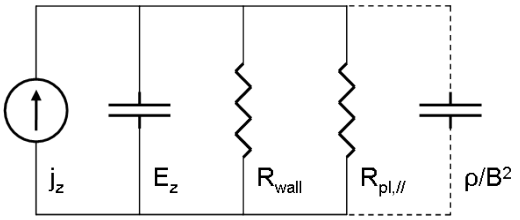

Figure 3.14: Equivalent electric scheme for the formation of an accumulated vertical electric field E_z in the vessel, due to the vertical plasma drift current (j_z is the '$\vec{B} \times \nabla B$' current source), short circuit currents in wall (via R_{wall}) and parallel to field lines (via R_{pl}). Polarization drifts can be described by an additional capacitor ρ/B^2.

3.3.3.2 Installation of steady state electric field

Before the installation of any quasi equilibrium, the electric field (E_z) will not be constant. The changing electric field causes a vertical polarization drift [15],

$$\vec{v}_p = -\frac{m_j}{e_j B^2} \frac{\mathrm{d}}{\mathrm{d}t} \frac{(\vec{E} \times \vec{B}) \times \vec{B}}{B^2} = \frac{m_j}{e_j B^2} \frac{\mathrm{d}\vec{E}}{\mathrm{d}t} \tag{3.28}$$

which is thus parallel to $\vec{E}$. This drift velocity is in opposite direction for electrons and ions, and much greater for the ions due to their mass. The current related to this is thus mostly an ion current

$$\vec{j}_p = \frac{\rho}{B^2} \frac{\mathrm{d}\vec{E}}{\mathrm{d}t} \tag{3.29}$$

with $\rho = n_j m_j$.

The polarization current is opposite in direction to the '$\vec{B} \times \nabla B$' current and will thus intuitively slow down the installation of the steady state electric field. To illustrate this we look at the equivalent electric scheme of the plasma drift currents, the accumulated charges and the closing currents in plasma and wall (Fig. 3.14). It consists of a current source ($\vec{j}_{\nabla B}$) in parallel with a capacitor over which stands E_z, and two parallel resistors representing the connection of top and bottom via the field lines and the wall conductivity. In this scheme, for a constant $\vec{j}_{\nabla B}$, the electric field approaches exponentially its steady state value. From the form of eq. (3.29) we see that the polarization current comes into this scheme as an additional parallel capacitor which will thus slow down the establishing of the steady state electric field[5].

[5]Although this representation already gives an idea of what happens, the plasma movement to top (v_p) and low field side ($v_{D,R}$) needs in principle to be taken into account. Further analysis in this direction was published by Müller [117].

3.3.3.3 Outward plasma acceleration and polarization drift

To obtain a value for the polarization drift, first the outward acceleration has to be introduced. In the initial plasma phase in a pure toroidal magnetic field it can be found that a force is acting on the plasma resulting in an outward acceleration [118]. This force can not be compensated by the plasma and thus the plasma can not be in equilibrium. The value obtained hereafter for the initial upward polarization velocity of the plasma ($\sim 0.6\,\mathrm{m/s}$, upwards) might explain the experimental observation that the plasma density is generally higher at the top of the vessel.

1. Outward acceleration

   An expression for the outward acceleration of the plasma based on the equation of motion of a volume element of the plasma is given in [118],

   $$\rho a_R = -j_z B - \frac{\partial p}{\partial R} \tag{3.30}$$

   with a_R the outward acceleration, j_z the local vertical current, B the local magnetic field and the kinetic pressure $p = n_i k(T_i + ZT_e)$. The equation shows clearly the relation of the acceleration and the vertical current. In terms of magnetic field, with the help of Maxwell equations ($\mu_0 j_z = \frac{1}{R}\frac{\partial}{\partial \mathrm{R}}(RB_\phi)$) we have

   $$\rho a_R = -\frac{B^2}{\mu_0 R} - \frac{\partial}{\partial R}(\frac{B^2}{2\mu_0} + p) \tag{3.31}$$

   with the magnetic pressure $\frac{B^2}{2\mu_0}$. It follows that the outward acceleration is zero in case the magnetic field B in eq. (3.31) is exactly equal to the vacuum magnetic field and when the plasma profile is homogeneous. However, even a small variation of the local magnetic field, due to the diamagnetic effect, can cause huge accelerations. Van der Laan [118] showed that the outward acceleration of the plasma (in case the acceleration in the z direction is zero) equals to:

   $$a_R = \frac{B_{\mathrm{vac}}^2 - B^2}{\mu_0 R\rho} = \frac{2p}{R\rho} \approx \frac{2k}{m_i R}(T_i + ZT_e) \tag{3.32}$$

   with B_{vac} the vacuum magnetic field. The resulting expression above remains valid when superposing a small homogeneous vertical magnetic field. A typical value for the outward acceleration for our reference ICWC plasma parameters at $R = R_0$ is $a_R = 3.9 \cdot 10^8\,\mathrm{m/s^2}$ which is an enormous value, but one has to keep in mind that the formula (eq. 3.32) is only valid in the initial situation, where the outward velocity is smaller than the velocity of the gyrating particle. The

required deviation of the local magnetic field to the vacuum magnetic field (diamagnetic effect) to obtain this acceleration is negligibly small $B_{\mathrm{vac}}^2 - B^2 = 1.2 \cdot 10^{-6}\,\mathrm{T}^2$. In an ICWC plasma the diamagnetic effect is as expected very small.

2. Polarization drift

   In the previous section we already discussed the polarization drift. In addition to this we derive here a value for its magnitude.

   In the paper of Van der Laan [118] an expression of the total vertical current is given in case of a purely toroidal field.

$$j_z = j_{\nabla B} - \frac{n_e}{ZB}(m_i + Zm_e)a_R \tag{3.33}$$

   The first term is the normal '$\vec{B} \times \nabla B$' drift found in eq. (3.24), the second term is the polarization drift current. The polarization drift is much smaller for the electrons than for the ions, whereas the '$\vec{B} \times \nabla B$' drift velocity for both electrons and ions are equal. From eq. (3.24), (3.32) and (3.33) we see that the vertical current of the '$\vec{B} \times \nabla B$' drift is completely compensated by a polarization current of the ions, resulting in an overall movement of the plasma given by the '$\vec{B} \times \nabla B$' drift velocity of the electrons ($\sim 0.6\,\mathrm{m/s}$).

$$v_z = -\frac{2kT_e}{eBR} \tag{3.34}$$

   Since we have chosen a 'negative' B this movement is directed to the top of the vessel. Experimental observations showed that especially at high power, the light emission of RF plasmas stems mostly from the top of the vessel (e.g. CCD images ASDEX Upgrade, Fig. 3.4). This might be a consequence of this effect since the finite dimensions of the torus will give rise to a steady state situation in the plasma profiles.

For the further analysis the outward acceleration will not be regarded and thus in case of purely toroidal field ($B_z = 0$) the vertical current is taken as

$$j_z = j_{\nabla B}. \tag{3.35}$$

3.3.4 Self consistent perpendicular electric field

To get a value for the outward '$\vec{E} \times \vec{B}$' drift we need to estimate the vertical electric field. The electric field from eq. (3.26) is infinite for a pure toroidal field, and the experimental scaling (eq. 3.27) is independent on the vertical field and toroidal field. In the following we want thus to find a self consistent

perpendicular electric field, determined by the perpendicular drift and the short circuit current along the tilted magnetic field lines. The self consistent vertical electric field will depend on the total vertical current:

$$j_z = SE_z \tag{3.36}$$

with S a conductance which might be dependent on θ. For the determination of the self consistent vertical electric field we derive first an expression for the total vertical current.

3.3.4.1 Total vertical current

In the presence of a vertical magnetic field ($B_z \neq 0$) the '$\vec{B} \times \nabla B$' drift remains perpendicular to the magnetic field and thus it is tilted with respect to $\hat{1}_z$ by an angle of $\theta = \arctan(\frac{B_z}{B_\phi})$. The total vertical current will have an additional component stemming from the short circuit current parallel to the field lines. This component is proportional to the accumulated electric field. If we call E_z the electric field along the $\hat{1}_z$ direction we will thus have for the perpendicular electric field $E_\perp = E_z\cos(\theta)$, and for the parallel electric field $E_\parallel = E_z\sin(\theta)$. The relation between the two fields is $E_\parallel = E_\perp\tan(\theta)$.

The induced current along the field line by $E_\parallel$ can be found via the Langevin equation for electrons (neglecting short circuit currents by ions):

$$m_e\frac{\mathrm{d}v_e}{\mathrm{d}t} = -eE - \nu_{in}m_ev_e, \tag{3.37}$$

which leads to a steady state velocity of

$$v_e = \frac{eE_\parallel}{\nu_{en}m_e}. \tag{3.38}$$

The related current to this velocity is

$$j_\parallel = -en_ev_e = -\frac{e^2n_eE_\parallel}{\nu_{en}m_e} = -\frac{e^2n_eE_\perp\tan(\theta)}{\nu_{en}m_e} = -\sigma E_\perp\tan(\theta). \tag{3.39}$$

with conductance $\sigma = \frac{e^2n_e}{\nu_{en}m_e}$ [S/m]. The total current in the vertical direction is then

$$j_z = j_{\nabla B}\cos(\theta) + j_\parallel\sin(\theta). \tag{3.40}$$

with $j_{\nabla B}$ from eq. (3.24) and $j_\parallel$ from eq. (3.39).

3.3.4.2 Self consistent electric field

As mentioned, the self consistent vertical electric field will depend on the total vertical current:

$$j_z = SE_z = j_{\nabla B}\cos(\theta) + j_\parallel\sin(\theta). \tag{3.41}$$

With eq. (3.39) this becomes

$$S\frac{E_\perp}{\cos(\theta)} = j_{\nabla B}\cos(\theta) - \sigma E_\perp \sin(\theta)\tan(\theta). \tag{3.42}$$

$$S = \frac{j_{\nabla B}}{E_\perp}\cos^2(\theta) - \sigma\sin^2(\theta) \tag{3.43}$$

Fig. 3.14 showed that the system can be regarded as a current source in parallel with a capacitor and two parallel resistors representing the connection of top and bottom via the field lines and the wall conductivity. In steady state, the vertical electric field is then simply the vertical component of the '$\vec{B} \times \nabla B$' drift multiplied with a resistivity. If we consider for the moment infinite wall resistivity we obtain from eq. (3.39) and (3.40), with zero net vertical current in the steady state situation:

$$E_\perp = \frac{j_{\nabla B}}{\sigma}\frac{\cos^2(\theta)}{\sin^2(\theta)} \tag{3.44}$$

or

$$E_z = \frac{j_{\nabla B}}{\sigma}\frac{\cos(\theta)}{\sin^2(\theta)} \tag{3.45}$$

Which is the same as we would find from eq. (3.43) taking $S = 0$. When we fill in the full expression for σ we find:

$$E_\perp = j_{\nabla B}\frac{\nu_{en}m_e}{e^2 n_e}\frac{\cos^2(\theta)}{\sin^2(\theta)} \tag{3.46}$$

Where we find thus back eq. (3.26) from [117] but with an extra $\cos(\theta)$ which is, due to the relatively small vertical magnetic field, approximately equal to one.

In case of a pure toroidal field ($\theta = 0$) we see that $E_\perp$ goes to infinity, which can be understood from the equivalent electric scheme with infinite wall resistivity. The wall resistivity is in reality of course finite. The total conductivity to be used in previous equations is thus

$$\sigma = \sigma_{\text{wall}} + \sigma_{\text{plasma},\parallel} \tag{3.47}$$

with

$$\sigma_{\text{plasma},\parallel} = \frac{e^2 n_e}{\nu_{en}m_e}\frac{\sin^2(\theta)}{\cos^2(\theta)}. \tag{3.48}$$

To estimate the steady state vertical electric field, the wall conductivity needs to be estimated. Below we will use an intermediate value ($\sigma_{\text{wall}} = 10^3\,\text{S/m}$), considering the conductivity of graphite ($\sigma_{\text{wall}} \approx 1\,\text{S/m}$) and stainless steel which may be six orders of magnitude higher. Fig. 3.15 shows

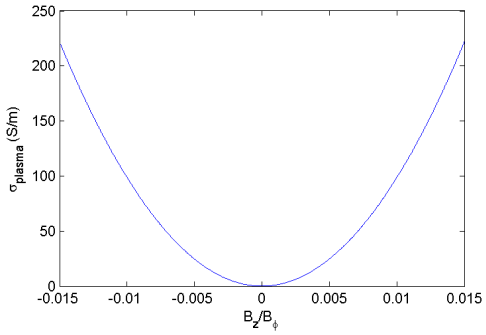

Figure 3.15: Vertical plasma conductivity σ_{plasma} ([S/m]) as a function of the parameter $\tan(\theta) = B_z/B_\phi$.

the dependency of the plasma conductivity in the z-direction on the parameter $\tan(\theta)$. It is clear that for practical cases of B_z the plasma conductivity will always be below the conductivity of the wall elements ($\approx 10\%$). If we neglect the plasma conductivity, the self consistent electric field is independent of the vertical magnetic field and behaves proportional to the experimental scaling given above (eq. 3.27):

$$E_\perp = \frac{j_{\nabla B}}{\sigma} \propto \frac{(T_e + T_i)}{RB} \tag{3.49}$$

which leads, unlike the experimental scaling [119], to a negligible low vertical electric field ($0.2 \cdot 10^{-3}\,\text{V/m}$). The radial drift from this field

$$\vec{v}_{D,R} = \frac{\vec{E}_\perp \times \vec{B}}{B^2} = \frac{j_{\nabla B}}{\sigma B}\hat{1}_R \tag{3.50}$$

will thus also be negligible compared to the vertical drift.

From this analysis we can conclude that the radial inhomogeneity is not due to drifts, but rather to inhomogeneous RF power absorption, whereas the vertical plasma inhomogeneities are due to plasma drifts.

3.3.5 Diffusion across the magnetic field

Charged particles diffuse across the toroidal magnetic field due to random collisions in the plasma (see Fig. 3.16). The diffusion coefficient is given by

$$D_\perp = {\rho_c}^2 \nu_c$$

with ρ_c the average length of the step the particle takes on each collision, and ν_c its collision frequency. The step length can be considered to be the

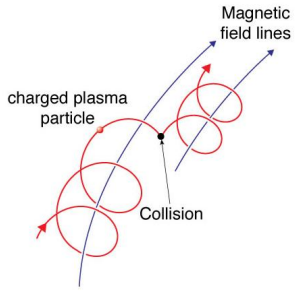

Figure 3.16: Illustration of collisional diffusion: charged particles in a magnetic field spiral around the "guiding" field line. In a collision the guiding field line is changed which results of diffusion of particles perpendicular to the magnetic field. [20]

gyration radius:

$$\rho_c = \frac{\sqrt{m k_b T}}{eB}$$

In the well known Bohm scaling [15] the collision frequency is set equal to the cyclotron frequency,

$$D_\perp = \frac{k_b T}{eB}$$

resulting in a diffusion coefficient valid for all charged plasma particles that only depends on the particle energy. Empirically Bohm found that a more correct value for the diffusion is lower:

$$D_{\mathrm{Bohm}} = \frac{1}{16}\frac{k_b T}{eB} \tag{3.51}$$

The particle confinement time related to Bohm diffusion is [85]:

$$\tau_{\mathrm{Bohm}} = \frac{a^2}{2D_{\mathrm{Bohm}}} \tag{3.52}$$

with a diffusion velocity of

$$v_{\mathrm{Bohm}} = \frac{2D_{\mathrm{Bohm}}}{a}. \tag{3.53}$$

Earlier in this chapter we found a value for the cross field diffusion coefficient from the decay of the plasma density in the plasma edge, measured by Langmuir probes, which resulted in $D_{\mathrm{meas}} = 0.70 \pm 0.1\,\mathrm{m}^2/\mathrm{s}$. Via the electron temperature obtained in these same discharges from the two Langmuir probes ($T_e \approx 30 \pm 10\,\mathrm{eV}$, Fig. 3.17) and the toroidal magnetic field strength ($B_\phi = 2.3\,\mathrm{T}$) one obtains via eq. (3.51) a Bohm diffusion coefficient of $D_{\mathrm{Bohm}} = 0.82 \pm 0.2\,\mathrm{m}^2/\mathrm{s}$ which thus experimentally confirms Bohm diffusion in ICWC plasmas. The confinement time related to Bohm diffusion is for our reference plasma of the order of 0.2 s.

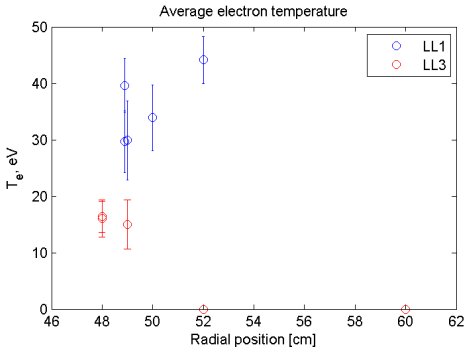

Figure 3.17: Average electron temperatures measured by Langmuir probes for TEXTOR hydrogen ICWC discharges, as a function of the radial position.

3.3.6 Plasma confinement time

The confinement time is found from (i) the outward velocity v, (ii) the approximate average distance l the particles need to travel to reach the walls of the toroidal chamber, and (iii) the particle mean free path in the plasma λ:

$$\tau = \frac{l}{v} e^{l/\lambda} \tag{3.54}$$

The wall flux of a charged particle population p is then found by dividing the total amount of these charged particles by their confinement time

$$Q_{\text{ftw},p} = \frac{n_p V}{\tau_p} = \frac{n_p V v_p}{a} e^{-a/\lambda_p} \tag{3.55}$$

which is thus weighted by the probability that the particles will travel a distance a without being lost by a collision (e^{-a/λ_p}), with a the torus minor radius.

The charged particle confinement time of an ICWC (quasi steady state) plasma, depends on four terms: (1) losses due to vertical drifts, (2) losses due to radial drifts, (3) losses due to diffusion of particles across the magnetic field and (4) losses of particles along the tilted magnetic field lines. In this chapter we derived velocities for the first three terms. The last term can be estimated via the vertical component of the average particle velocity along the field lines. The expression for the total charged particle confinement time is then

$$\tau_p = \frac{a}{(v_{Dz,p} + v_{DR,p} + v_{\text{Bohm},p}) e^{-a/\lambda_p} + v_{T,p} B_z / B_\phi e^{-a B_\phi / B_z \lambda_p}} \tag{3.56}$$

where B_ϕ and B_z the toroidal and vertical field, λ_p the mean free path of the ion, $v_{Dz,p}$ is the '$\vec{B} \times \nabla B$' drift velocity, $v_{DR,p}$ is the radial outward

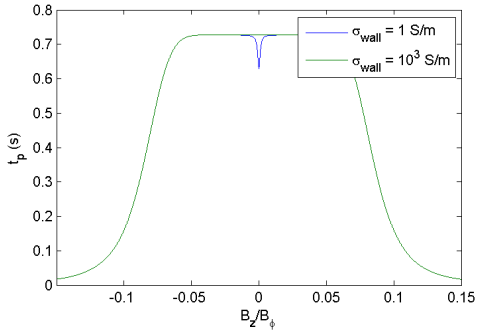

Figure 3.18: Plasma confinement time as a function of the strength of the vertical field for two wall conductivity values: 1 S/m ($\sim$ carbon) and 10^3 S/m, and our standard ICWC plasma parameters.

'$\vec{E}\times\vec{B}$' drift velocity, $v_{\mathrm{Bohm},p}$ is the cross field diffusion velocity and $v_{T,p}$ the thermal velocity. The velocity $v_{Dz,p}$ is given by eq. (3.22) where in principle a correction factor $\cos(\theta)$ (≈ 1) should be taken into account, $v_{DR,p}$ can be found from eq. (3.50) and $v_{\mathrm{Bohm,p}}$ from eq. (3.53).

Fig. 3.18 shows the dependency of the plasma confinement time on the strength of the vertical field for our standard ICWC plasma parameters. The curve is plotted for two wall conductivity values to show that the radial drift has only a minor effect on plasma confinement. Only in case of poor wall conductivity, the vertical field improves the plasma confinement by decreasing the radial drift. From the figure we learn that the plasma confinement time remains unaffected over a wide range of vertical magnetic fields. The vertical magnetic field can thus be safely applied to for example vertically extend the plasma and to improve the conditioning efficiency.

3.4 Conclusion

Achieving homogeneous RF conditioning discharges is important to ensure the effective conditioning of the maximum vessel wall area. In this chapter we presented firstly experimental facts on plasma inhomogeneities. It is concluded that the observed radial inhomogeneities in the plasma center can be explained in terms of RF power absorption properties: the higher electric field strength at the LFS causes for example higher electron densities and temperatures on the LFS. Vertical inhomogeneities of the plasma center can however not be explained from RF power absorption properties. It was proposed that the confinement properties of the magnetic configuration are responsible for these vertical inhomogeneities. By applying a small

vertical magnetic field that stretches the plasma in the vertical direction, the vertical homogeneity can be improved. Furthermore, the plasma density is observed to decrease exponentially close to the vessel walls where the magnetic field lines are limited by wall structures. The exponential decrease is characterized by Bohm diffusion. Due to the existence of this edge plasma, the ion wall flux will be largest on the first limiting surfaces.

In the second part of the chapter, the contribution of the confinement properties of the ICWC magnetic configuration to the inhomogeneities was analyzed. The plasma is firstly subject to a vertical plasma drift due to the gradient and the curvature of the toroidal magnetic field. The drift velocity is equal in size for ions and electrons, but works in opposite directions: upwards for electrons and downwards for ions (for clockwise toroidal magnetic field). The resulting charge accumulation in the plasma edge induces a vertical electric field that causes an outward radial plasma drift. From the analysis it is expected that this outward drift velocity is very small, much smaller than the vertical drift velocity, confirming the conclusion that radial plasma inhomogeneities are related to RF physics aspects. It was also investigated whether an applied vertical magnetic field can reduce the induced vertical electric field by creating a short circuit current along the tilted magnetic field lines. This could reduce the radial plasma drift and thus improve the radial homogeneity. However, the latter short circuit current is estimated to be much smaller than the short circuit currents flowing in the vessel walls. Next to the above static drifts, the existence of a vertical polarization drift during the plasma breakdown phase was introduced. The polarization drift velocity is proportional to the particle mass and affects thus mostly the plasma ions, and the velocity is equal in size and direction as the vertical electron drift. As a consequence, during plasma breakdown, the plasma will move as a whole to the top of the vessel, explaining the observed higher plasma densities at this location.

In the last part of this chapter, a formula is derived for the charged particle confinement time, taking into account charged particle drifts, diffusion and losses along the tilted magnetic field lines. It is found that for partially ionized plasmas the confinement time is only weakly dependent on the applied small vertical magnetic field.

4

Assessment of the ICRF wall conditioning efficiency

This chapter gives an overview of experimental results on the efficiency of ICWC, obtained on TORE SUPRA, TEXTOR, JET and ASDEX Upgrade in the course of this PhD work. The aims of the presented experiments are the assessment and optimization of the conditioning efficiency and to provide information that allows an extrapolation to ITER (subject of chapter 7). The conditioning aims for ICWC during the ITER operational cycles, namely when the toroidal magnetic field is present, are controlling the in-vessel impurity content, controlling the recycling of hydrogenic fluxes and reducing the tritium inventory (as part of the good household approach proposed by Roth et al. [34] to keep the in-vessel tritium level below the administrative limit of 640 g). The chapter is divided into three large parts. The first two parts are separated according to the discharge gas/conditioning aim: firstly H_2 and H_2/He discharges for isotopic exchange, and secondly pure He discharges for wall desaturation and recovery of normal tokamak operation after disruptions. In these parts, the ability of ICWC to change the surface state will be shown, the wall fluxes and corresponding PWI mechanisms will be characterized, and the particle desorption and retention rates will be calculated. Also the efficiency dependencies on RF power, discharge pressure, magnetic fields, etc. will be treated. In a final (third) part the efficiency of ICWC for impurity and codeposited layer removal is discussed.

4.1 H_2 and H_2/He-ICWC for isotopic exchange

In isotope exchange conditioning discharges one aims at exchanging hydrogen isotopes stored in the close subsurface ($0 - 100\,\text{nm}$) by other hydrogen isotopes, which is required to control the plasma isotopic ratio of tokamak discharges. Separately, isotopic exchange experiments allow to assess the ability of a conditioning technique such as ICWC to change the wall surface state. The efficiency of an isotopic exchange technique can be expressed as the rate at which the technique can change the isotopic ratio of the walls and the total induced extra retention it causes. These two points will be discussed in the first two parts of this section. In the third part the results of ICWC are compared with isotope exchange experiments using conventional glow discharges on the same machines with typically the same wall pre-treatment conditions. A separate section will be dedicated to the motivation for favoring short RF pulses ($\sim 1\,\text{s}$) instead of continuous RF discharges. In a last section the conditioning efficiency will be discussed as a function of the discharge parameters. We remind that an overview of the wall bombarding flux was given in section 2.5.

4.1.1 Illustration and analysis of the isotopic exchange efficiency on TORE SUPRA, TEXTOR, JET and ASDEX Upgrade

4.1.1.1 TORE SUPRA

A first illustration of the high isotopic exchange efficiency of ICWC was achieved on TORE SUPRA. In the experiment the wall was preloaded with deuterium by D_2-GDC. After the glow, the wall isotopic ratio was measured by NPA during a reference ohmic discharge (D_2, $I_p = 1\,\text{MA}$, $R = 2.38\,\text{m}$) (blue curve on Fig. 4.1, left). At the end of the experimental day, consisting of 15 cumulated RF discharge minutes in helium-hydrogen mixtures (multiple $\sim 60\,\text{s}$ long RF pulses), followed by 3 cumulated minutes of ICWC in pure helium to desaturate the wall, the isotopic ratio had increased from 4 to 40% (red curve on Fig. 4.1, left). This significant change shows clearly the ability of ICWC to change the wall state, and has motivated further experiments on TORE SUPRA itself, and on TEXTOR, JET and ASDEX Upgrade.

There are however two possible ways to change the isotopic ratio of the wall. The ideal way is to exchange every single deuterium particle by one hydrogen particle. Another way is to store extra hydrogen into the deuterium wall. Particle balance analysis allows to look at this more carefully. Via the partial pressures, obtained from mass spectrometry (see appendix B), the

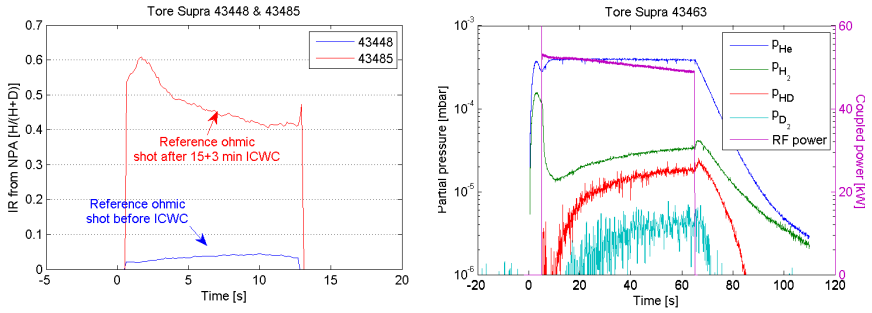

Figure 4.1: Left: Change in the plasma isotopic ratio (approx. equal to wall isotopic ratio) measured by NPA during two reference ohmic shots (D_2, I_p = 1 MA, R = 2.38 m) resp. before and after 18 minutes of ICWC (15 minutes of H_2/He-ICWC and 3 minutes of He-ICWC, $\sim$ 60 s long RF pulses). Right: partial pressures (left axis) and coupled power (right axis) of a TORE SUPRA H_2/He-ICWC discharge with feedback controlled injection of a hydrogen/helium mixture (30/70), $P_{RF} \approx 50$ kW and discharge length of 60 s (antenna Q2 2008).

gas injection signals and eq. (2.35) it is possible to calculate the amount of removed deuterium from the vessel (and thus from the wall) and the amount of hydrogen retained into the vessel (injected minus recovered by the machine pumps). Fig. 4.1 (right) shows the partial pressures of a H_2/He-ICWC discharge with feedback controlled injection of a hydrogen/helium (30/70) gas mixture, $P_{RF} \approx 50$ kW and discharge length of 60 s (antenna Q2, 2008). The result of the particle balance for this discharge is summarized in table 4.1. From this result one can conclude that the removal of deuterium from

Table 4.1: Particle balance for TORE SUPRA discharge 43463 (Fig. 4.1, right). H injected: $N_{sv,H}$, H retained: $N_{r,H} = N_{sv,H} - N_{p,H}$, D recovered: $N_{p,D}$

Deuterium loaded wall	$N_{sv,H}$	$N_{r,H}$	$N_{p,D}$	$N_{r,H}/N_{p,D}$
H_2/He-ICWC	3.2e21	2.3e21	1.4e20	16

the wall goes at the price of a 16 times higher retention of hydrogen. The total particle balance for the ICWC discharges between the reference ohmic discharges shown in Fig. 4.1 (left) evidenced a total removal of $4 \cdot 10^{21}$ D atoms ($\sim$ 2.5 monolayers), and a retention of $4 \cdot 10^{22}$ H atoms. Ideally the ratio between retention and recovery should be close to one, in order to avoid excessive wall loading during the conditioning discharge.

Throughout this section we will show that the problem of high retention reoccurs on all four tokamaks, but that by simply adapting the RF discharge length this ratio can be significantly optimized.

A comment must be made to the applied method of gas injection. The

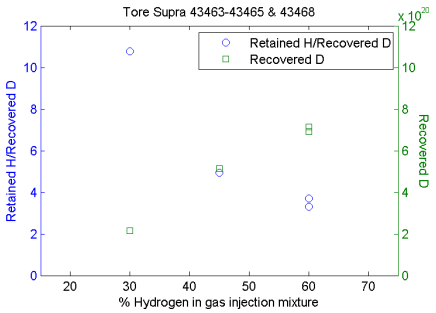

Figure 4.2: Ratio of retained H over recovered D and total amount of recovered D in 60 s long TORE SUPRA RF discharges ($P_{\mathrm{RF}} \approx 50\,\mathrm{kW}$) with feedback controlled gas injection ($p_{\mathrm{tot}} \approx 5 \cdot 10^{-4}\,\mathrm{mbar}$) as a function of the H_2 concentration in the gas injection mixture.

gas injection consisted of a fixed H_2/He mixture, controlled by a feedback loop on the total pressure. For the discharge in Fig. 4.1 (right) this ratio was 30/70. It is clear from the figure that the total hydrogenic partial pressure during the discharge is less than 10% of the helium pressure. This can be understood from the significant hydrogen consumption by the walls, observable via the steep hydrogen pressure decrease after the discharge initiation at $t = 5\,\mathrm{s}$. The lost hydrogen will be partially compensated by helium injection (feedback, 30/70 H_2/He mixture). An equilibrium helium pressure is reached about 4 s after the discharge initiation. If one wants to control the hydrogenic content of the discharge it is recommended to pre-program the helium injection and put the feedback only on hydrogen as is done on TEXTOR (see further). Fig. 4.2 shows that on increasing the hydrogen concentration in the injected gas mixture, the removal efficiency of D increases, and the ratio of injected hydrogen over removed deuterium comes closer to one. This motivated the choice for conditioning in pure gases during later experiments on TORE SUPRA, without any problems regarding discharge initiation or sustainment.

4.1.1.2 TEXTOR

Following to the TORE SUPRA results, also on TEXTOR multiple isotope exchange experiments have been carried out. Fig. 4.3 (left) shows spectroscopic measurements of the H_α and D_α emission lines in two ohmic discharges, respectively before (blue line) and after (green line) a H_2/He-ICWC session containing 26 nearly identical ICWC discharges ($\sim 4\,\mathrm{min.}$ of cumulated discharge time, $P_{\mathrm{RF,gen}} = 60{-}75\,\mathrm{kW}$, $f_{\mathrm{RF}} = 29\,\mathrm{MHz}$, $B_T = 1.9{-}2.3\,\mathrm{T}$, pulse length of $6{-}8\,\mathrm{s}$, $p_{\mathrm{He}} = 2.9{\cdot}10^{-4}\,\mathrm{mbar}$ and $p_{\mathrm{tot}} = 4{\cdot}10^{-4}{-}5{\cdot}10^{-4}\,\mathrm{mbar}$).

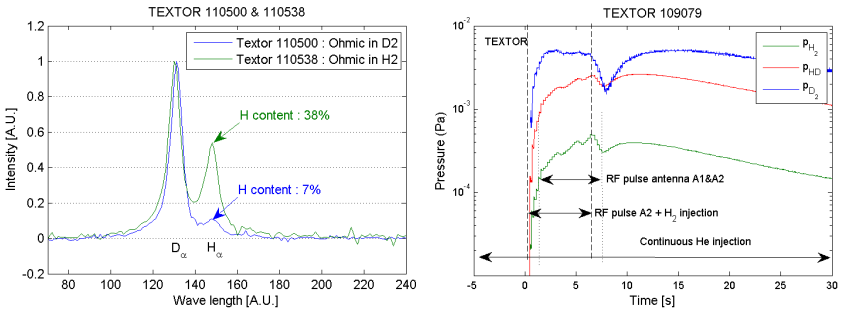

Figure 4.3: Left: Spectroscopic measurements of the H_α and D_α emission lines in two ohmic discharges, respectively before (blue line) and after (green line) a H_2/He-ICWC session containing 26 nearly identical ICWC discharges (~ 4 min of cumulated discharge time, $P_{\mathrm{RF,gen}} = 60 - 75$ kW, $f_{\mathrm{RF}} = 29$ MHz, $B_T = 1.9 - 2.3$ T, pulse length of $6 - 8$ s, $p_{\mathrm{He}} = 2.9 \cdot 10^{-4}$ mbar and $p_{\mathrm{tot}} = 4 \cdot 10^{-4} - 5 \cdot 10^{-4}$ mbar). Right: Partial pressures of TEXTOR discharge 109079 ($B_T = 1.9$ T, $f_{\mathrm{RF}} = 29$ MHz, $p_{\mathrm{He}} = 3.5 \cdot 10^{-4}$ mbar and $p_{\mathrm{tot}} = 5.0 \cdot 10^{-4}$ mbar).

The D_2-glow prior to the session makes that the hydrogen content is initially low ($\sim 7\%$). At the end of the session the hydrogen content had increased to $\sim 38\%$. Although the plasma isotopic ratio reflects the wall isotopic ratio it must be mentioned that the first ohmic discharge was carried out in deuterium, while during the second one only hydrogen was injected. Whereas in the first discharge a minor amount of deuterium is injected at the start of the discharge, whereafter the plasma is completely fueled by the wall (due to the preceding D_2-GDC loading), the hydrogen discharge was entirely fueled by the wall. The presented isotopic ratios represent thus the wall isotopic ratio. Nevertheless, for similar experiments in the future it is recommended to measure the isotopic ratio by ohmic discharges in the wall loaded isotope (deuterium in this case due to the preceding D_2-GDC), both before and after the set of conditioning discharges.

The total particle balance for the ICWC session between the reference ohmic discharges shown in Fig. 4.3 (left) evidenced a total removal of $6.5 \cdot 10^{21}$ D particles (~ 9 monolayers), and retention of $1.9 \cdot 10^{22}$ H particles. The ratio of retained hydrogen over recovered deuterium equals 2.9 and is thus significantly better than the result of TORE SUPRA. This is attributed both to the shorter discharge length, as will be explained further, and the higher hydrogen pressure during the discharges. During these TEXTOR discharges the feedback control was set only on the hydrogen injection. The helium flow was continuously constant.

Analysis of the partial pressures (from mass spectrometry) allowed to estimate the deuterium wall release rate and to compare it to the deu-

terium removal rate by the machine pumps. Fig. 4.3 (right) shows the hydrogen partial pressures of a 6 s He/H_2-ICWC discharge in TEXTOR. This discharge is the fifth discharge after a wall preloading by D_2-GDC, in a series of similar ICWC discharges where, as in the previous TEXTOR example, the helium injection flow was constant ($p_{\mathrm{He}} = 3.5 \cdot 10^{-4}$ mbar) and the hydrogen injection was feedback controlled on the total pressure ($p_{\mathrm{tot}} = 5.0 \cdot 10^{-4}$ mbar). The coupled RF power was 50 kW at an RF frequency of 29 MHz and a toroidal magnetic field of $B_T = 1.92$ T. The figure shows that during the RF discharge the H_2 partial pressure is lower than that of HD and D_2. Since the only source of deuterium in the vessel is the wall, it is concluded that during this discharge the wall is acting as the major particle source. The magnitude of this wall source follows from the balance equation for neutral molecules in the vessel in a 0D approach, which is valid in case the mean free path of the molecules is larger than the dimensions of the vessel (adapted from eq. 2.35):

$$\frac{\mathrm{d}p_{\mathrm{H_2}}}{\mathrm{d}t} = \frac{Q_{\mathrm{sv,H_2}}}{V} + \frac{Q_{\mathrm{sw,H_2}}}{V} - \frac{p_{\mathrm{H_2}} S}{V} - (k^{\mathrm{d}} + k^{\mathrm{i}}) p_{\mathrm{H_2}} n_e \qquad (4.1)$$

Here $p_{\mathrm{H_2}}$ is the partial pressure of H_2 (mbar), $Q_{\mathrm{sv,H_2}}$ and $Q_{\mathrm{sw,H_2}}$ are the neutral gas sources, respectively the external injection and the wall release (mbar l/s), V is the volume of the vessel (l), S is the machine pumping speed (l/s, approx. equal for H_2, HD and D_2), k^{i} and k^{d} are the ionization rate and dissociation rate (cm^3/s, approx. equal for H_2, HD and D_2) and n_e is the electron density (cm^3). The recombination rate, being very low, is omitted in eq. (4.1) which allows writing it in the same form for HD and D_2. Also the direct loss at the wall of neutral H_2 molecules, having a temperature in the range of the gas injection balloon (~ 300 K) and wall (~ 450 K) temperature, is neglected in eq. (4.1) as they are assumed to be mainly reflected on the wall surface. Knowing $Q_{\mathrm{sv,H_2}}$ ($= 4.3 \cdot 10^{19}$ H_2/s) from the gas injection valves ($Q_{\mathrm{sv,HD}} = Q_{\mathrm{sv,D_2}} = 0$), the wall sources $Q_{\mathrm{sw,HD}}$ and $Q_{\mathrm{sw,D_2}}$ can be deduced from eq. (4.1) in a steady state approximation:

$$Q_{\mathrm{sw,D_2}} = (Q_{\mathrm{sv,H_2}} + Q_{\mathrm{sw,H_2}}) \frac{p_{\mathrm{D_2}}}{p_{\mathrm{H_2}}}, \quad Q_{\mathrm{sw,HD}} = (Q_{\mathrm{sv,H_2}} + Q_{\mathrm{sw,H_2}}) \frac{p_{\mathrm{HD}}}{p_{\mathrm{H_2}}} \qquad (4.2)$$

After the D_2-GD prior to the ICWC session the isotopic ratio of the wall, D/(H + D), is close to one. From this it is expected that at the start of the ICWC session $Q_{\mathrm{sw,H_2}}$ is very small compared to $Q_{\mathrm{sw,HD}}$ and $Q_{\mathrm{sw,D_2}}$, which allows to derive a meaningful lower value estimate for the release rate of HD and D_2 in the form of:

$$Q_{\mathrm{sw,D_2}} \geq Q_{\mathrm{sv,H_2}} \frac{p_{\mathrm{D_2}}}{p_{\mathrm{H_2}}}, \quad Q_{\mathrm{sw,HD}} \geq Q_{\mathrm{sv,H_2}} \frac{p_{\mathrm{HD}}}{p_{\mathrm{H_2}}} \qquad (4.3)$$

Applied to the considered discharge at $t = 3\,\mathrm{s}$ this leads to $Q_{\mathrm{sw,HD}} \geq 3.3 \cdot 10^{20}\,\mathrm{HD/s}$ and $Q_{\mathrm{sw,D2}} \geq 7.2 \cdot 10^{20}\,\mathrm{D_2/s}$, equal to $Q_{\mathrm{sw,D}} \geq 1.8 \cdot 10^{21}\,\mathrm{D/s}$. The removal rate by the external pumps at this same time however gives $Q_{\mathrm{p,D}} = (2p_{\mathrm{D_2}} + p_{\mathrm{HD}})S = 5.2 \cdot 10^{18}\,\mathrm{D/s} = 1.5 \cdot 10^{17}\,\mathrm{D/m^2s}$. The flux of particles released by the wall is thus at least 350 times higher than the flux that is actually removed from the vessel. The numbers are summarized in table 4.2. In section 4.1.3 we will compare the found numbers with values for standard GDC and explain eventual differences in terms of the reionization probability in ICRF discharges and glow discharges.

Table 4.2: Rates for hydrogen injection ($Q_{\mathrm{sv,H}}$), deuterium wall release ($Q_{\mathrm{sw,D}}$) and deuterium removal by machine pumps ($Q_{\mathrm{p,D}}$).

$Q_{\mathrm{sv,H}}$	$Q_{\mathrm{sw,D}}$	$Q_{\mathrm{p,D}}$
$8.6 \cdot 10^{19}\,\mathrm{H/s}$	$\geq 1.8 \cdot 10^{21}\,\mathrm{D/s}$	$5.2 \cdot 10^{18}\,\mathrm{D/s}$

The total particle balance for the TEXTOR discharge, including discharge phase and post discharge phase, giving the total amount of hydrogen lost to the walls, $N_{\mathrm{r,H}} = N_{\mathrm{sv,H}} - N_{\mathrm{p,H}}$, and the total amount of deuterium pumped out of the system, $N_{\mathrm{p,D}}$, results in $N_{\mathrm{p,D}} = 2.3 \cdot 10^{20}$ and $N_{\mathrm{r,H}} = 4.5 \cdot 10^{20}$, and thus $N_{\mathrm{r,H}}/N_{\mathrm{p,D}} \approx 2$ meaning that for each removed D-atom almost two H-atoms are retained into the wall. From the total particle balances of both the TEXTOR and TORE SUPRA ICWC discharges we can conclude that the total recycling coefficient R of the particle flux to the wall Q_{ftw}, defined as $Q_{\mathrm{sw}} = RQ_{\mathrm{ftw}}$, must be $R < 1$ during ICWC. This result will be used in further analysis.

The JET isotopic exchange experiments presented in the next section consist of D_2-ICWC discharges performed on a H-loaded wall, instead of the above presented H_2-discharges on a D-loaded wall. Fig. 4.4 shows particle balances for respectively five subsequent He/H_2-ICWC discharges preceded by D_2-GD wall preloading and four subsequent He/D_2-ICWC discharges preceded by H_2-GD wall preloading ($B_T = 1.9\,\mathrm{T}$, $f_{\mathrm{RF}} = 29\,\mathrm{MHz}$, $p_{\mathrm{He}} = 3.5 \cdot 10^{-4}\,\mathrm{mbar}$ and $p_{\mathrm{tot}} = 5.0 \cdot 10^{-4}\,\mathrm{mbar}$). The figure illustrates the symmetric removal and retention rates of H_2-ICWC and D_2-ICWC, which can be understood from the isotopic exchange schematic given in Fig. 1.13.

4.1.1.3 JET

The isotopic exchange experiments on JET are especially motivated by the possibility to simulate D_2-ICWC in ITER full field conditions. By operating the JET antennas at 25 MHz in presence of $B_T = 3.3\,\mathrm{T}$, the resonance layer for D^+ ions is located on axis at $r'/a = 0$, i.e. above the divertor (r'/a is the normalized radius: $-1 \geq r'/a \geq 1$, r' is the radial distance to the plasma

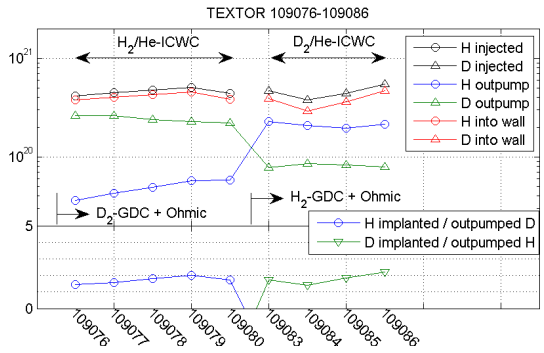

Figure 4.4: Particle balances for respectively 5 subsequent He/H_2-ICWC discharges preceded by a D_2-GDC wall preloading and 4 subsequent He/D_2-ICWC discharges preceded by a H_2-GDC wall preloading illustrating the close to symmetric removal and retention rates ($B_T = 1.9\,\mathrm{T}$, $f_{\mathrm{RF}} = 29\,\mathrm{MHz}$, $p_{\mathrm{He}} = 3.5 \cdot 10^{-4}\,\mathrm{mbar}$ and $p_{\mathrm{tot}} = 5.0 \cdot 10^{-4}\,\mathrm{mbar}$).

center: $r' = R - R_0$), as will be the case on ITER in full field conditions ($B_T = 5.3\,\mathrm{T}$ and using $f_{\mathrm{RF}} = 40\,\mathrm{MHz}$)[1]. As shown in chapter 3, the JET RF plasmas were reliably produced. Although the JET vessel dimensions are significantly larger than those of TEXTOR, TORE SUPRA and ASDEX Upgrade, the plasma stretches over the whole vessel radius, clearly reaching the central column and seemingly also the divertor area (Fig. 3.5).

On JET, the wall was preloaded by H_2-GDC, after which eight nearly identical (previously optimized) D_2-ICWC discharges were effectuated. Fig. 4.5 (left) shows the change in isotopic ratio from discharge to discharge, measured in two manners: first by an optical Penning gauge located in a duct connected to the divertor, giving thus the isotopic ratio of the neutral gas in the divertor, and secondly the plasma isotopic ratio obtained from spectroscopical measurements from a vertical line of sight in the vessel midplane. Both measurements show an increase of the isotopic ratio, D/(D + H), by 30 to 50% from the first to the last discharge, which reflects the changing wall state. The cumulated discharge time of the session was $8 \times 9\,\mathrm{s} = 72\,\mathrm{s}$, with pre-programmed gas injection resulting in $p \approx 2 \cdot 10^{-5}\,\mathrm{mbar}$ during the discharge and $B_V = 30\,\mathrm{mT}$. Due to encountered difficulties in coupling the RF power to the plasma in the first discharges, the coupled power varied between 50 and 250 kW.

The total particle balance for these eight discharges, including discharge

[1] In ITER, the use of ICWC during the inter-pulse period of nominal D:T plasma shots implies that the toroidal field is fixed at 5.3 T. The possible RF frequencies on ITER range from 40 to 55 MHz which means that the ICR layer for D^+ ions will range from on axis at $r'/a = 0$, above the divertor, to $r'/a = -0.6$.

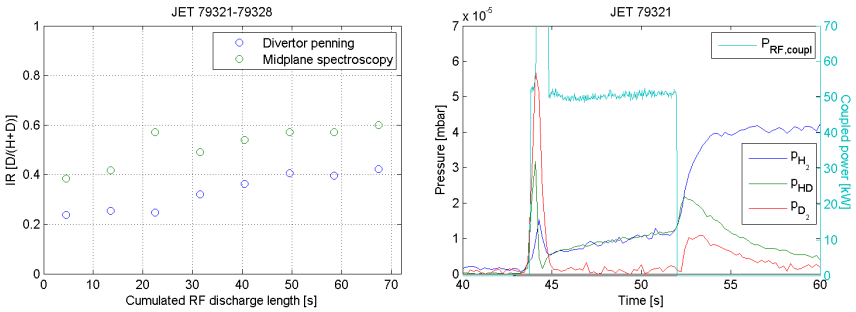

Figure 4.5: D_2-ICWC discharges on JET (H loaded wall). Left: Evolution of plasma (midplane spectroscopy) and neutral gas (Penning gauge spectroscopy) isotopic ratio during 8 nearly identical subsequent D_2-ICWC discharges ($P_{\mathrm{RF,coup}} \approx 50-250\,\mathrm{kW}$, $p \approx 2\cdot10^{-5}$ mbar). Right: Partial pressures and coupled power of discharge 1/8.

and post discharge phase, is summarized in table 4.3. Within these limited number of RF pulses it was possible to remove $1.8 \cdot 10^{22}$ hydrogen particles from the wall ($= 1.2 \cdot 10^{20}\,\mathrm{H/m^2} \approx 6$ monolayers), which corresponds to approximately 10% of the short term retention accessible by plasma operation [121]. This result is considered to be a great step forward in demonstrating the applicability of ICWC on ITER for fuel removal. (It does however not illustrate the capability of ICWC to remove tritium-rich codeposited layers. In chapter 6 this point will be further studied.)

Table 4.3: Particle balance for JET discharges 79321-79328: D retained: $N_{\mathrm{r,D}}$, H recovered: $N_{\mathrm{p,H}}$

Hydrogen loaded wall, D_2-ICWC	$N_{\mathrm{r,D}}$	$N_{\mathrm{p,H}}$	$N_{\mathrm{r,D}}/N_{\mathrm{p,H}}$
Mass spectrometry & penning gauge	5.2e22	1.8e22	2.9
Gas chromatography	4.8e22	1.6e22	3

Fig. 4.5 (right) shows the partial pressures of the first ICWC discharge, obtained from mass spectrometry and Penning gauge spectroscopy. The same effect as on TEXTOR can be observed: although we inject D_2 during the discharge, both the H_2 and HD partial pressures are higher than the D_2 partial pressure ($p_{H_2} \approx 9 \cdot 10^{-6}$ mbar, $p_{\mathrm{HD}} \approx 9 \cdot 10^{-6}$ mbar and $p_{D_2} \approx 1 \cdot 10^{-6}$ mbar). From these partial pressures, again an estimation of the wall release rate can be made and compared to the removal rate by the pumps, summarized in table 4.4: also in the case of JET RF discharges, the wall removal rate ($Q_{\mathrm{sw,H}} = 1.8 \cdot 10^{20}\,\mathrm{H/m^2 s}$) is at least 370 times larger than the removal rate by the pumps[2].

[2]This value is slightly overestimated since H_2 is not as efficiently pumped as D_2, as

Table 4.4: Rates for deuterium injection ($Q_{\mathrm{sv,D}}$), hydrogen wall release ($Q_{\mathrm{sw,H}}$) and hydrogen removal by the machine pumps ($Q_{\mathrm{p,H}}$), for JET discharge 79321.

$Q_{\mathrm{sv,D}}$	$Q_{\mathrm{sw,H}}$	$Q_{\mathrm{p,H}}$
$2.0 \cdot 10^{21}$ D/s	$\geq 2.7 \cdot 10^{22}$ H/s	$7.3 \cdot 10^{19}$ H/s

4.1.1.4 ASDEX Upgrade

From the results of the carbon machines TORE SUPRA, TEXTOR and JET, it can be concluded that one can remove significant amounts of hydrogen isotopes from the wall with ICWC, at the price of a 2 to 3 times higher retention of the discharge gas. Later we will show that the ratio can be optimized. During the active phase of ITER, there will be no carbon plasma facing components. So it is important to assess the efficiency also on devices with ITER relevant wall materials, such as on the tungsten device ASDEX Upgrade. ICWC experiments on ASDEX Upgrade showed that within 14 H_2-ICWC discharges, $7.3 \cdot 10^{21}$ D particles could be removed, corresponding approximately to 12 monolayers. Most of the discharges contained two RF pulses with variable pulse lengths (50 ms to 10 s), $P_{\mathrm{RF,gen}} = 100 - 600$ kW, $f_{\mathrm{RF}} = 30$ MHz in monopole phasing and dipole phasing, $B_T = 1.9 - 2.3$ T and continuous gas injection to obtain $p_{\mathrm{H_2}} \approx 2 \cdot 10^{-4}$ mbar in absence of plasma. Just as on the carbon machines, also on ASDEX Upgrade the additional retention of hydrogen into the walls was significant: $3.5 \cdot 10^{22}$ H. It was shown that the retention on a tungsten machine can also be limited by adapting the RF pulse length, without severely limiting the amount of recovered particles (see below, in section 4.1.4).

4.1.2 Study of discharge gas retention

In this section we will attempt to identify the mechanisms that cause the observed discharge gas retention observed on the four tokamaks. The following retention mechanisms are proposed:

- retention in near surface layers
- retention in deeper layers
- retention by codeposition
- retention in remote areas

explained in section 2.4.2. Eq. 4.3 should thus more correctly be:

$$Q_{\mathrm{sw,H_2}} \geq Q_{\mathrm{sv,D_2}} \frac{p_{\mathrm{H_2}}}{p_{\mathrm{D_2}}} \frac{S_{\mathrm{H_2}} + (k^{\mathrm{d}} + k^{\mathrm{i}}) n_e V}{S_{\mathrm{D_2}} + (k^{\mathrm{d}} + k^{\mathrm{i}}) n_e V}$$

which will only give a minor correction due to the high ionization probability of ICWC plasmas (see section 4.1.3.3).

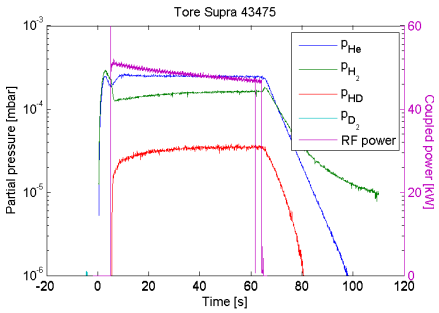

Figure 4.6: Partial pressures (left axis) and coupled power (right axis) of a TORE SUPRA H_2/He-ICWC discharge with feedback controlled injection of a hydrogen/helium mixture (60/40), $P_{\mathrm{RF,forw-refl}} \approx 50\,\mathrm{kW}$ and discharge length of 60 s (antenna Q2 2008).

A distinction is made between storage in near surface layers and storage into deeper layers to take into account the interaction depth of the impinging particle flux, characterized by the particle energy and wall material. A wall loading with D_2-GDC ($T_{D^+} = 250\,\mathrm{eV}$) is thought to saturate the first 5 to 10 nm of carbon wall components. Unless by creating additional trapping sites, no extra retention is possible in this saturated layer; the retention in the near surface layer is compensated by an equal release. The unsaturated deeper layers ($> 5 - 10\,\mathrm{nm}$) can store extra hydrogen. To reach these layers the particle energies need to be higher than that of glow discharges [36, 122]. The third point, retention by codeposition, is an important fuel retention mechanism in tokamak discharges, and can in principle also occur in conditioning discharges. By retention in remote areas one means the retention of hydrogen in areas, e.g. near surface layers, that are not reached by GDC, and are thus not saturated during a GD wall preloading.

Although it was not possible to evidence the main retention mechanism, the following experimental observations clear up some important questions.

4.1.2.1 No long-term saturation of retention

Fig. 4.6 shows the partial pressure of a TORE SUPRA H_2/He-ICWC discharge with similar setup as the discharge given in Fig. 4.1 (right): 60 s long ICRF discharge, $B_T = 3.8\,\mathrm{T}$, $f_{\mathrm{RF}} = 48\,\mathrm{MHz}$, $P_{\mathrm{RF,coup}} \approx 30\,\mathrm{kW}$, feedback H_2/He (60/40) injection at $p_{\mathrm{tot}} = 4.0 \cdot 10^{-4}\,\mathrm{mbar}$. At $t = 65\,\mathrm{s}$, the cumulated RF discharge time of the H_2/He-ICWC session equaled 15 min. The total particle balance of this discharge, summarized in table 4.5, illustrates that even after 15 minutes still more isotopes can be retained than recovered: in total 5.5 times more hydrogen is retained than deuterium re-

covered. Also in the TEXTOR session of 26 nearly identical H_2/He-ICWC

Table 4.5: Particle balance for TORE SUPRA discharge 43475. H injected: $N_{sv,H}$, H retained: $N_{r,H} = N_{sv,H} - N_{p,H}$, D recovered: $N_{p,D}$

Deuterium loaded wall	$N_{sv,H}$	$N_{r,H}$	$N_{p,D}$	$N_{r,H}/N_{p,D}$
H_2/He-ICWC	5.7e21	1.8e21	3.2e20	5.5

discharges mentioned above, no sign of long term wall saturation was observed. At the start of the session, right after the glow discharge almost all injected hydrogen was lost to the walls. The retention decreased in the first ~ 10 discharges, and remained then constant in the subsequent discharges. The amount of recovered deuterium continued to decrease from shot to shot. The retention stabilized, but remained higher than the wall recovery: ~ 2.5 (15th discharge) to 3.5 (26th discharge).

For this reason it is expected that mechanisms such as retention in deeper layers, retention by codeposition, and retention in remote areas, might play an important role in ICWC discharges[3].

4.1.2.2 Retention by codeposition

Eroded wall materials (especially carbon in present devices) can be redeposited elsewhere on the wall surface, taking large amounts of hydrogen with it. In section 4.3, the carbon removal during ICWC will be discussed. As will be shown, it was not possible to determine whether the removed carbon stems from codeposited layers, and whether a part of the eroded carbon is redeposited on the wall. However, an indication that indeed certain amounts of carbon are eroded and redeposited during ICWC was given in Fig. 2.4. The TORE SUPRA antenna straps of the antenna used for ICWC conditioning were covered by a thin deposited layer. Although not confirmed by surface analysis, it is expected that the layer consist of deposited carbon, and from the dark layer color it is expected that the layer must be at least 100 nm thick [123]. To have an idea of the involved orders of magnitude we can assume a 100 nm thick layer, a 600 cm^2 strap surface and an amorphous carbon mass density of 2 g/cm^3, which leads to 12 μg of carbon, or either $6 \cdot 10^{20}$ C atoms. The generally accepted hydrogen concentration in amorphous carbon is 0.4 H/C resulting in a possible retention of about $2.5 \cdot 10^{20}$ H atoms per strap, which is one order of magnitude below the total hydrogen retention given in table 4.5. This result makes codeposition a candidate for the retention mechanism on carbon devices TORE SUPRA, TEXTOR and JET.

[3] Future experimentation on wall saturation during H_2-ICWC, e.g. on TORE SUPRA, should envision cumulated RF discharge times larger than 15 minutes.

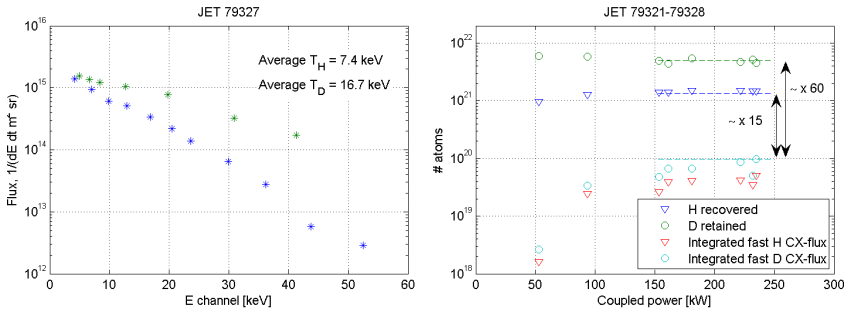

Figure 4.7: Left: CX spectra of deuterium (blue) and hydrogen (green) in a JET D_2-ICWC discharge, $P_{\mathrm{RF,coup}} \approx 240\,\mathrm{kW}$, $p \approx 2 \cdot 10^{-5}\,\mathrm{mbar}$. Right: Particle balance for each of the JET D_2-ICWC discharges shown in Fig. 4.5 as a function of the coupled power, including the time integrated total fast CX neutral flux.

However, the high hydrogen retention was also observed on full tungsten device ASDEX Upgrade. On ASDEX Upgrade the retention can not be dominated by codeposition with carbon. Mechanisms other than codeposition have to be considered on ASDEX Upgrade, and thus likely also on the carbon devices.

4.1.2.3 Retention due to energetic CX particles

It is proposed that the extra retention might be due the high energy neutral particle flux stemming from the resonant absorption of RF power by ions at the ion cyclotron resonance layers, followed by the neutralization of these ions in charge exchange reactions (see reactions 17-24 in table 5.1 on page 5-5). Fig. 4.7 (left) shows a typical time averaged fast particle spectrum measured along a radial line of sight by NPA (located in sector 3, see Fig. A.9), for a JET D_2-ICWC discharge. The spectra are fitted by a Maxwellian distribution resulting in Maxwellian energies of $T_{\mathrm{D}} = 16.7\,\mathrm{keV}$ for deuterium and $T_{\mathrm{H}} = 7.4\,\mathrm{keV}$ for hydrogen. These energies are sufficient to reach deeper surface layers, and thus cause extra retention. The fast particle flux measured during the isotope exchange experiment on JET presented in previous section, and from which the discharge in Fig. 4.7 (left) is the seventh discharge, ranged from 10^{15} to $10^{17}\,/\mathrm{m^2 s}$. These values are in agreement with the TORE SUPRA result ($10^{17}\,/\mathrm{m^2 s}$) published in [73], and mentioned in section 2.2.1. Fig. 4.7 (right) compares the total fast particle flux with the total retention and the total amount of recovered wall desorbed hydrogen for each of these discharges. The values are given as a function of the coupled power. The total fast particle flux is obtained by assuming that the wall flux is isotropic, integrating the spectra over energy

($E = [1:50]\,\mathrm{keV}$) and time (see section B.2.9). The deuterium fast particle flux increases with the coupled power, but even at maximum power, the total flux is 60 times lower than the measured deuterium retention. The high observed retention is thus not solely due to the presence of the fast particle flux. Additionally it is expected that the fast particle flux also has a limited influence on the removal efficiency since the total amount of recovered hydrogen atoms is an order of magnitude higher than the fast particle flux.

The correctness of the above analysis depends on the validity of the assumption that the fast particle flux is isotrope. The NPA measurement location is a quarter of a toroidal length away from the closest RF antenna (module C). Presently no information is available on the toroidal homogeneity of the fast ion population.

On TEXTOR the isotopic exchange efficiency was compared at high and low toroidal magnetic field strength ($B_T = 2.3\,\mathrm{T}$ and $B_T = 0.23\,\mathrm{T}$). The presence of the fast particle population depends on the efficiency of the resonant RF power absorption ($f_{\mathrm{RF}} = 29\,\mathrm{MHz}$). At $B_T = 2.3\,\mathrm{T}$, the fundamental H^+-ion resonance is present in the vessel, and at $B_T = 0.23\,\mathrm{T}$, only higher harmonics are present (see Fig. 2.14). Since resonant RF absorption is most efficient in presence of the fundamental resonance, and inefficient at high harmonics, only the high B_T discharges will feature a fast particle population. The presence of such a 'warm' population is detectable in D_α/H_α spectra, respectively located around 6561.0 Å/6562.8 Å, as shown on Fig. 4.8: ions undergoing charge exchange reactions will de-excite directly after being neutralized. The Doppler effect will make that the H_α spectrum of the fast population will appear as a broader Maxwellian distribution superimposed on the H_α spectrum of the thermal (lower energy) particles. Fig. 4.8[4] shows D_α/H_α spectra of two TEXTOR discharges, respectively at high B_T (red line) and low B_T (black line), from a vertical channel of the CX-spectroscopy diagnostic, operated in a passive mode (without neutral beam injection). The line of sight crosses the fundamental resonance layer at high B_T, and the tenth harmonic at low B_T. Except for broader D_α (left) and H_α (right) peaks at high B_T due to the Zeeman effect, a signal increase is visible at the right side of the H_α peak. This increase is thought to be due to the fast population, although it is not understood why the Maxwellian distribution ($\sim 500\,\mathrm{eV}$, determined by fitting a Maxwellian spectrum to the warm spectrum component) is shifted to the higher wave lengths. The shift indicates a downward velocity of the fast ions which is presently not understood (the related velocity is too high to be attributed to the '$\vec{B} \times \nabla B$' drift). The particle balance for these both discharges, for which the cou-

[4]Thanks to Simon Freutel, IPP Juelich

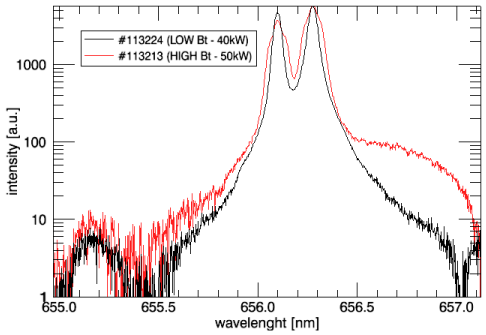

Figure 4.8: D_α and H_α spectra of 2 TEXTOR H_2-ICWC discharges, respectively at high B_T (red line) and low B_T (black line), showing the presence of the resonant ion population (at high B_T) by the signal increase on the rhs.

pled power is similar, is summarized in table 4.6. Both the discharge gas

Table 4.6: Particle balance for TEXTOR discharges 113213 and 113224. H retained: $N_{r,H} = N_{sv,H} - N_{p,H}$, D recovered: $N_{p,D}$

Deuterium loaded wall	$N_{r,H}$	$N_{p,D}$	$N_{r,H}/N_{p,D}$
H_2-ICWC $B_T = 2.3\,T$	6.4e20	3.5e20	1.8
H_2-ICWC $B_T = 0.23\,T$	6.9e20	4.0e20	1.7

retention and the amount of recovered wall desorbed deuterium atoms are similar for the two toroidal field strengths. This confirms the JET result, and concludes that the fast ion population likely has only a minor influence on the retention and removal rates.

4.1.2.4 Recovery of retained particles by He-GDC

To know whether the retained hydrogen can be recovered from the wall, a He-GD was carried out on ASDEX Upgrade right after the ICWC session which was presented in section 4.1.1.4. During this H_2-ICWC session $7.3 \cdot 10^{21}$ D particles could be removed from the wall at the price of a retention of $3.5 \cdot 10^{22}$ H atoms. The extra retention due to the ICWC discharges is thus $2.8 \cdot 10^{22}$ atoms. Fig. 4.9 (left) shows the partial pressures of the helium glow discharge, consisting of five pulses of about 10 s with 50 s between each pulse. Fig. 4.9 (right) gives the amount of removed H and D atoms. The number decreases linearly from pulse to pulse and can be extrapolated to become zero after the seventh pulse. The total amount of recovered particles, including the extrapolation, equals $4.0 \cdot 10^{21}$ H atoms and another $1.5 \cdot 10^{21}$ D atoms. This means that $\sim 11\%$ of the total retained H could

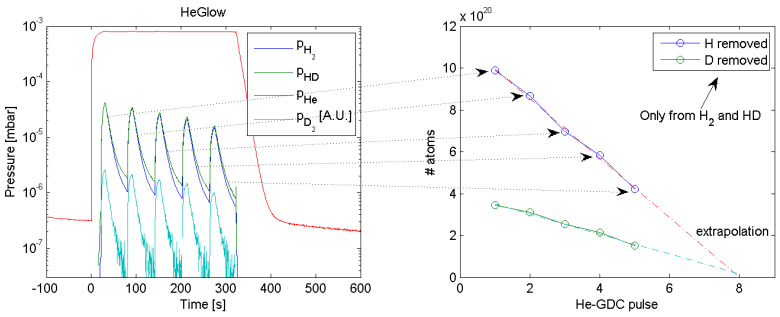

Figure 4.9: Left: Partial pressures of a He-GD discharge consisting of 5 pulses of about 10 s with 50 s between each pulse on ASDEX Upgrade. The GDC is effectuated after a H_2-ICWC session. Right: Particle balance for each pulse cycle including the linear extrapolation to higher pulse numbers.

be recovered by He-GDC. The retained hydrogen is thus partially stored in the typical near surface layers accessible by the GDC. Unfortunately, no further He-ICWC could be carried out to check whether ICWC could remove the remaining hydrogen. At the start of the next experimental day, an additional $8.7 \cdot 10^{20}$ H particles could be removed from the wall by D_2-GDC (three pulses of 10 s).

Even though the H-quantity removed by GDC is of the same order of magnitude than that retained by ICWC, still a large fraction of the retained hydrogen remains in the wall. This retention is, as concluded before, not due to codeposition (tungsten wall) nor solely due to the fast particle fluxes ($\sim 10^{15}\,/\mathrm{m}^2\mathrm{s}$, 2009 ASDEX Upgrade experiments). The most plausible explanation is that ICWC discharges reach areas that are not accessible by glow discharges. Also the existence of a substantial non resonant ion wall flux component with energies above the typical GDC flux can at this point not be excluded.

4.1.3 Comparison with GDC

In this section the presented results of ICWC are compared with isotope exchange experiments using conventional glow discharges with typically the same wall pre-treatment conditions, both on TORE SUPRA and on TEXTOR (Fig. 4.10, resp. left and right figure). The walls were preloaded by a 30 min. D_2-GD on TEXTOR, respectively H_2-GD on TORE SUPRA, hereafter on both machines the gas injection was changed, proceeding with H_2-GDC on TEXTOR and D_2-GDC on TORE SUPRA. On TEXTOR the continuous constant gas injection resulted in a baratron pressure of $p_{\mathrm{tot}} = 8.5 \cdot 10^{-3}$ mbar. On TORE SUPRA the gas injection was feedback

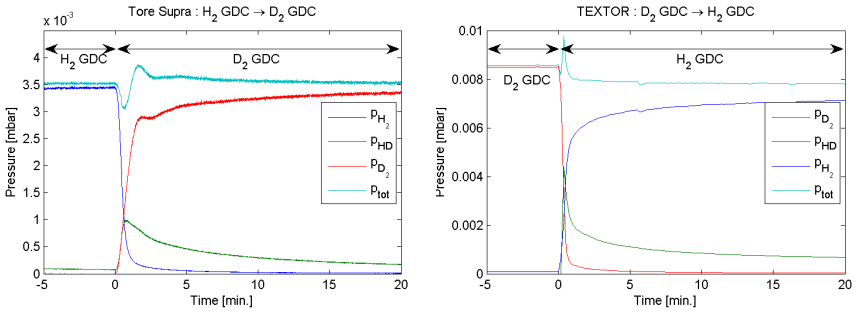

Figure 4.10: Isotopic exchange with conventional glow discharges. Left: gas injection changeover from H_2-GDC to D_2-GDC on TORE SUPRA. Right: changeover from D_2-GDC to H_2-GDC on TEXTOR.

controlled on the total pressure $p_{\mathrm{tot}} = 3.5 \cdot 10^{-3}$ mbar. The physics of GDC is well documented [52,58] (see section 1.5.2.1). The flux of particles to the wall consists mainly of ions $Q_{\mathrm{ftw}} \approx 1 \cdot 10^{20}$ /s $= 2.9 \cdot 10^{18}$ /m^{2}s (TEXTOR) with ion energies of typically $T_i \approx 250$ eV, obtained in the cathode fall in front of the walls. Also an additional conditioning contribution of neutrals is not excluded [58]. From the hydrogenic partial pressures after the gas injection changeover it is clear that the wall isotopes are mainly released in the form of HD molecules (green lines). Right after the change over, the HD pressure is higher than the discharge gas pressure, whereas the total pressure remains approximately constant. The release of HD decreases in time, while the partial pressure of the discharge gas increases, showing the gradual change of the isotopic ratio of the wall. After 15 min. there is still HD production (as in case of ICWC, see TORE SUPRA: Fig. 4.6). The pressure peak right after the change over on the TEXTOR figure might be due to the slow sampling rate of the mass spectrometer.

4.1.3.1 Comparison of absolute removal rates

The absolute removal rate of HD molecules 1 min. after the changeover on TEXTOR equals $Q_{\mathrm{p,HD,GDC}} = 3.4 \cdot 10^{19}$ HD/s $= 9.7 \cdot 10^{17}$ HD/m^{2}s, which is about six times higher than the removal rate of D during ICWC on TEXTOR reported above, also taken at approx. 1 min. of accumulated RF time after the glow discharge (see discharge in Fig. 4.3). A similar comparison between GDC and ICWC is done on TORE SUPRA, respectively 15 min. after the change over from H_2-GDC to D_2-GDC, and 15 min. of accumulated RF time ($t = 65$ s in discharge shown in Fig. 4.6). The following removal rates were recorded: $Q_{\mathrm{p,HD,GDC}} = 2.7 \cdot 10^{19}$ HD/s $= 3.8 \cdot 10^{17}$ HD/m^{2}s and $Q_{\mathrm{p,HD,ICWC}} = 5.3 \cdot 10^{18}$ HD/s $= 7.7 \cdot 10^{16}$ HD/m^{2}s. The removal rate of D

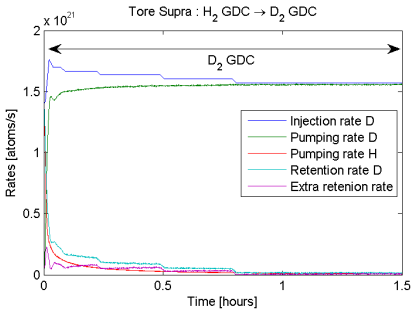

Figure 4.11: D injection rate, the D and H removal rates, the D retention rate and total extra retention rate as a function of time for a standard D_2-GDC on TORE SUPRA

for GDC is here about five times higher than for ICWC. The values of this comparison are summarized in table 4.7.

Table 4.7: Comparison of removal rates in ICWC and GDC during isotopic exchange experiments.

Time	ICWC	GDC	
~ 1 min.	$1.5 \cdot 10^{17}\,\mathrm{m^2 s}$	$9.7 \cdot 10^{17}\,\mathrm{m^2 s}$	TEXTOR
15 min.	$7.7 \cdot 10^{16}\,\mathrm{m^2 s}$	$3.8 \cdot 10^{17}\,\mathrm{m^2 s}$	TORE SUPRA

It might be expected that the higher removal rates for GDC compared to ICWC are due to the approximately one order of magnitude higher neutral pressure in the analyzed GDC discharges than in the ICWC discharges, both in TEXTOR and TORE SUPRA. However, the different physical properties of ICWC and GDC do not allow drawing a general dependency for the pumping rates of wall desorbed species in conditioning discharges as a function of discharge gas pressure. The last term in eq. (4.1) indicates that the source of particles in the plasma is not only a function of the pressure, but also of the electron density and the reaction rates. We will see further that the electron density is an important factor, and in section 4.1.5 we will discuss the effect of the neutral pressure on the isotopic exchange efficiency in H_2-ICWC discharges.

4.1.3.2 Particle recycling during GDC

Fig. 4.11 shows the deuterium injection rate, the deuterium and hydrogen removal rates by the pumps, the deuterium retention rate and total extra retention rate (deuterium injection minus deuterium and hydrogen removal rates) as a function of time, for the D_2-GD on TORE SUPRA. After 1 hour

of D_2-GDC, the deuterium injection rate becomes approximately equal to the deuterium removal rate. This indicates that from this time instance on the deuterium consumption by the walls is limited and that the wall surfaces become saturated with deuterium. Before this equilibrium situation, it seems that the retention rate of deuterium is slightly higher than the removal rate of hydrogen and thus that the glow discharge also causes some extra retention. A similar result is obtained on TEXTOR, where the gas injection was continuously constant. The neutral pressure in absence of the glow plasma approximately equaled the neutral pressure during the D_2-GD right before the change over. The observations from TORE SUPRA and TEXTOR indicate that firstly the ionization degree in glow discharges is very low, and also that the consumption of particles by the walls is limited.

Based on eq. (4.1) we can say that during GDC (a) $Q_{\mathrm{sv}} \approx pS$, and consequently that (b) $Q_{\mathrm{sw}}/V \approx (k_{\mathrm{d}} + k_{\mathrm{i}})pn_e$, on the condition that Q_{sw} and $(k_{\mathrm{d}} + k_{\mathrm{i}})pn_eV$ are not negligible compared to Q_{sv} and pS. The latter is indeed the case: right after the change over the partial pressure of HD is higher than the pressure of the injected gas; $p_{\mathrm{H_2}}$ in case of TEXTOR and $p_{\mathrm{D_2}}$ in case of TORE SUPRA. These HD molecules can only stem from plasma wall interaction, indicating that the ionization/dissociation rates, fluxes to the wall (Q_{ftw}) and release rates from the wall (Q_{sw}) are not negligible compared to the gas injection rate (Q_{sv}). From point (a) it follows that the net loss of hydrogen isotopes to the wall during GDC is not significant. Similarly from point (b) it follows that the total recycling coefficient for GDC, R_{GDC}, must be close to one.

4.1.3.3 Retention as a function of the reionization probability

For isotopic exchange with glow discharges it was concluded that the recycling coefficient of the wall flux is close to one and that extra storage of particles into a saturated wall (by GDC) is not significant. On the other hand, during isotope exchange experiments with ICWC in case of saturated walls, still more particles can be retained into the wall.

An explanation of the found values ($Q_{\mathrm{r,H,GDC}} \approx Q_{\mathrm{p,D,GDC}}$ and $N_{\mathrm{r,H,ICWC}} > N_{\mathrm{p,D,ICWC}}$) can be sought in terms of the reionization probability f. Eq. (4.1) states that a molecule in the vessel will be either ionized or dissociated, or pumped by the machine pumps. The ionization probability, or equally the reionization probability of wall desorbed molecules, is here defined as the probability that a molecule in the vessel gets ionized or dissociated. The reionization probability for the ICWC discharge on TEXTOR discussed in the previous section (Fig. 4.3) can be estimated at first by comparing the wall release rate of D, $Q_{\mathrm{sw,D}}$, with the removal rate of D,

$Q_{\mathrm{p,D}}$:

$$f_{\mathrm{ICWC}} = \frac{Q_{\mathrm{sw,D}} - Q_{\mathrm{p,D}}}{Q_{\mathrm{sw,D}}} \tag{4.4}$$

Taking the estimated values for this shot (table 4.2) this results in $f_{\mathrm{ICWC}} = 99.7\%$. Secondly, the reionization probability can also be estimated from the plasma parameters [56]:

$$f_{\mathrm{ICWC}} = \frac{\tau_{\mathrm{i}}^{-1}}{\tau_{\mathrm{ex}}^{-1} + \tau_{\mathrm{i}}^{-1}} \tag{4.5}$$

Here τ_{ex} is the characteristic time constant for the pumping speed ($p = p_0 e^{-t/\tau_{\mathrm{ex}}}$) and $\tau_{\mathrm{i}} = [n_e(k^{\mathrm{d}} + k^{\mathrm{i}})]^{-1}$ [56] is the characteristic effective time constant for dissociation (k^{d}) and ionization (k^{i}). With plasma parameters $n_e = 1 \cdot 10^{17}\,\mathrm{m}^3$, measured by interferometry, $T_e = 3\,\mathrm{eV}$, estimated from the 0D kinetic model for hydrogen plasmas (see chapter 5), and effective reaction rates $k^{\mathrm{d}} = 1.09 \cdot 10^{-9}\,\mathrm{cm}^3/\mathrm{s}$ and $k^{\mathrm{i}} = 4.9 \cdot 10^{-11}\,\mathrm{cm}^3/\mathrm{s}$, given in Fig. C.3 and C.4, this results in $f_{\mathrm{ICWC}} = 99.8\%$, in good agreement with the previously calculated value. In a similar way as for ICWC, a reionization probability for GD plasmas can be estimated from typical GD plasma parameters (eq. 4.5): $n_e = 10^{14}\,\mathrm{m}^{-3}$ and $T_e = 10\,\mathrm{eV}$ [58]. The significantly lower density in GD plasmas directly leads to a much lower reionization probability: $f_{\mathrm{GDC}} = 86\%$. This value is an upper limit since the electron temperature, measured by Langmuir probes, is expected to be overestimated. The reionization probability can be verified by using the partial pressures in the same way as was done for ICWC. We first analyze eq. (4.3) to find the hydrogen wall release rate shortly after the gas injection change over. For this equation (in the case of D_2-conditioning) we need the deuterium injection rate. Using $p_{\mathrm{H_2}}(t < 0) = 8.5 \cdot 10^{-3}\,\mathrm{mbar}$ we find $Q_{\mathrm{sv,H}}(t < 0) = Q_{\mathrm{sv,D}}(t > 0) = 8.8 \cdot 10^{20}\,/\mathrm{s}$. We analyze the equation at the time instance where the HD pressure is maximum: $p_{\mathrm{HD}} = 4.4 \cdot 10^{-3}\,\mathrm{mbar}$. The D_2-pressure and H_2-pressure at this time are $p_{\mathrm{D_2}} = 2.2 \cdot 10^{-3}\,\mathrm{mbar}$ and $p_{\mathrm{D_2}} = 3.2 \cdot 10^{-3}\,\mathrm{mbar}$. This leads to $Q_{\mathrm{sw,HD}} = 1.8 \cdot 10^{21}\,/\mathrm{s}$ and $Q_{\mathrm{sw,H_2}} = 1.3 \cdot 10^{21}\,/\mathrm{s}$. The removal by the pumps equals $Q_{\mathrm{p,HD}} = 2.3 \cdot 10^{20}\,/\mathrm{s}$ and $Q_{\mathrm{p,H_2}} = 1.7 \cdot 10^{20}\,/\mathrm{s}$. Putting the values for $Q_{\mathrm{sw,H}}$ and $Q_{\mathrm{p,H}}$ into eq. (4.4) we obtain a comparable value of $f_{\mathrm{GDC}} = 87\%$.

The high re-ionization probability in ICWC compared to GDC, mainly due to the higher electron density, has a large influence on the retention rates in both techniques. In the following an isotopic exchange experiment with conditioning discharges in H_2 and a D-saturated wall is considered. The reionization probability f relates then per definition the wall desorption rate of D, $Q_{\mathrm{sw,D}}$, with the removal rate of D by the pumps via $Q_{\mathrm{p,D}} = (1 - f)Q_{\mathrm{sw,D}}$, since the only source of D is the wall. If the isotopic ratio

of the wall $D/(H+D) \approx 1$, then the desorption rate of D is also related to the total flux of particles to the wall, Q_{ftw}, via the total recycling coefficient R[5]. The outpumped flux of D can thus be written as a function of the total particle flux to the wall:

$$Q_{\mathrm{p,D}} = (1-f)RQ_{\mathrm{ftw}} \tag{4.6}$$

For the sake of comparison it is now assumed that the recycling coefficient for ICWC is as in the case of GDC close to one, e.g. $R_{\mathrm{ICWC}} = R_{\mathrm{GDC}} = 0.998$. Using the estimated reionization probabilities and the measured removal rates of D, $Q_{\mathrm{p,D}}$, it is possible to estimate equally the required flux of particles to the walls, Q_{ftw}, with eq. (4.6), as well as the related total extra retention rate, Q_{er}. The total extra retention rate is defined as $Q_{\mathrm{er}} = (1-R)Q_{\mathrm{ftw}}$ and in principle disregards whether the incoming or outgoing particle consists of D or H. The results of these estimations are summarized in table 4.8. It is found that even if a small percentage of the flux of particles to the wall is permanently retained into the wall, in the considered example $(1-R) = 0.2\%$, the total retention rate during the discharge can be of the same order as the removal rate by the pumps when the particle flux to the wall is high enough, as in the case of ICWC.

Table 4.8: Overview estimated values for reionization probability f, pumping rate of D ($Q_{\mathrm{p,D}}$, s^{-1}), total wall flux (Q_{ftw}, s^{-1}) and total extra retention rate (Q_{er}, s^{-1}), for the analyzed ICWC and GDC discharges on TEXTOR.

	f	$Q_{\mathrm{p,D}}$	Q_{ftw}	Q_{er}	$Q_{\mathrm{er}}/Q_{\mathrm{p,D}}$
GDC	0.86	$3.4 \cdot 10^{19}$	$2 \cdot 10^{20}$	$4 \cdot 10^{17}$	0.01
ICWC	0.998	$5.2 \cdot 10^{18}$	$3 \cdot 10^{21}$	$6 \cdot 10^{18}$	1.2

4.1.3.4 Comparison GDC with optimized pulsed ICWC

It was found that although the ratio of retained particles over recovered particles in ICWC discharges is larger than one, the recycling coefficient can still be very close to one ($R \approx 1$), which opens doors for eventual optimization of the technique. Since reionization and wall flux retention only occurs during the plasma discharge, it is proposed to use shorter RF pulses ($\sim 1\,\mathrm{s}$) separated by sufficient time between pulses to recover the wall desorbed particles by the machine pumps. In the next section we will show that this significantly improves the ratio of implanted over recovered particles, without severely lowering the total amount of removed particles. Fig. 4.12

[5] In the model of de la Cal [56] presented in section 2.2.3, this coefficient was called the yield Y.

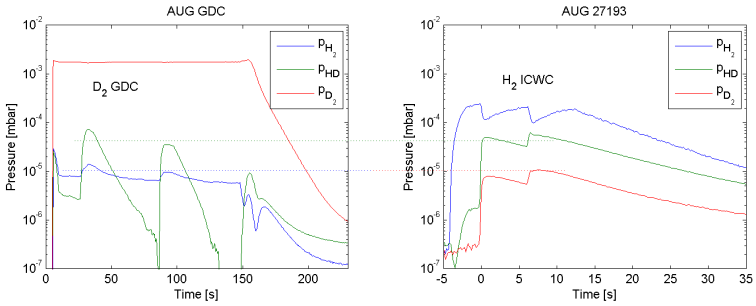

Figure 4.12: Comparison of D_2-GDC and H_2-ICWC partial pressures on ASDEX Upgrade.

shows the partial pressures of such an optimized H_2-ICWC discharge and a D_2-GD on ASDEX Upgrade. The H_2-ICWC discharge is the 11th discharge from the ICWC session mentioned in section 4.1.1, and contained two RF pulses of resp. 250 ms and 500 ms (at $t = 0$ s and $t \approx 6$ s). The D_2-GD is effectuated after five He-GDC pulses. The HD partial pressures are of the same order of magnitude in both conditioning procedures, and the H_2 partial pressure of the D_2-GD is approximately equal to the D_2 partial pressure of the H_2-RF discharge.

4.1.4 Pulsed ICWC

In the previous section we showed that neutral molecules in ICWC discharges have a large ionization probability f. The probability to evacuate wall desorbed molecules before they are ionized or dissociated $(1-f)$ is thus very low. To increase the removal efficiency it is proposed to simply include pumping time (PT, i.e. without plasma) in the ICWC procedure [56]. An additional advantage of applying multiple short pulses is that it results in less extra retention of discharge gas, since retention of the wall bombarding particles only occurs during the RF discharge. In recent experiments it is shown that the ratio of retained over recovered hydrogenic particles can be brought close to one by optimizing the duty cycle of the RF pulses, as illustrated on Fig. 4.13. The data points on this figure are taken from two subsequent multi-pulse H_2-ICWC discharges on TORE SUPRA where the wall was preloaded by D_2-GDC. The H_2 injection was continuous constant with $p_{H_2} = 2.0 \cdot 10^{-4}$ mbar. The RF power at the generator was 60 kW at a frequency of 48 MHz, and the toroidal magnetic field was respectively 3.8 T and 3.2 T. Fig. 4.13 (left) shows that shorter RF pulses (e.g. 2 s RF + 38 s PT) limit the amount of retained H with respect to longer pulses (e.g. 5 s RF + 35 s PT and 10 s RF + 30 s PT) without severely lowering the amount

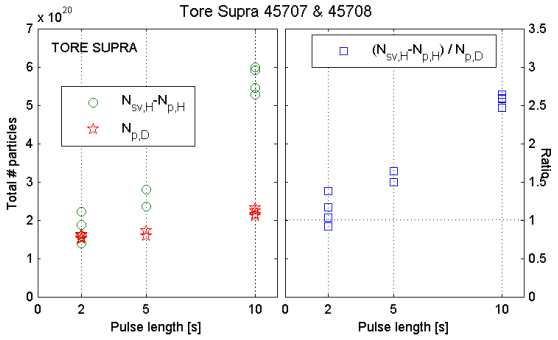

Figure 4.13: Isotope exchange efficiency as function of pulse length taken from two subsequent multi-pulse H_2-ICWC discharges on TORE SUPRA, calculated separately for each duty cycle. $N_{\mathrm{sv,H}}$, $N_{\mathrm{p,H}}$ and $N_{\mathrm{p,D}}$ are respectively the total injected H, total pumped H and total pumped D over one duty cycle (40 s). Discharge parameters: constant H_2 gas injection with $p_{H_2} = 2.0 \cdot 10^{-4}$ mbar, $P_{\mathrm{RF,generator}} = 60$ kW, $f_{\mathrm{RF}} = 48$ MHz, pulse cycle $t(P_{\mathrm{RF,on}})/t(P_{\mathrm{RF,off}}) = x\,\mathrm{s}/(40 - x\,\mathrm{s})$, $B_T = 3.2 - 3.8$ T and wall preloading by D_2-GDC.

of out-pumped deuterium. This can be understood as a combination of two effects: first, as already mentioned, because the particle flux to the wall and thus also the particle retention is only present during the RF pulse. And secondly, as indicated by the increase in gas pressure after the RF discharge clearly visible in for example the TEXTOR discharge on Fig. 4.3 (right), the release of particles from the wall continues after the RF pulse, with a characteristic time scale depending on the wall material and the physical process (e.g. release dominated by thermal detrapping, diffusion, surface recombination, or their combinations [124], see also section 6.1.3). The figure shows that a ratio of retained H over pumped D equal to one (as in GDC) was also achieved with ICWC, illustrating that the problem of high retention during ICWC can be overcome (Fig. 4.13, right).

Similar experiments have been carried out on TEXTOR (H_2-ICWC discharges on D-preloaded wall, one RF pulse per discharge). Two sets of data points are given in Fig. 4.14. The RF power at the generator was 2×50 kW for set 1 and 2×100 kW for set 2, at a frequency of 29 MHz and toroidal magnetic field of 2.3 T. The H_2 injection was feedback controlled to $p_{\mathrm{tot}} = 5.0 \cdot 10^{-4}$ mbar. Also on TEXTOR, the ideal ratio of retained H over pumped D could be achieved with ICWC (Fig. 4.14, right) by limiting RF the pulse length. Additionally it was found that for a same discharge length, retention is more important at high power. The amount of recovered particles is less sensitive to the discharge length, as was found on TORE

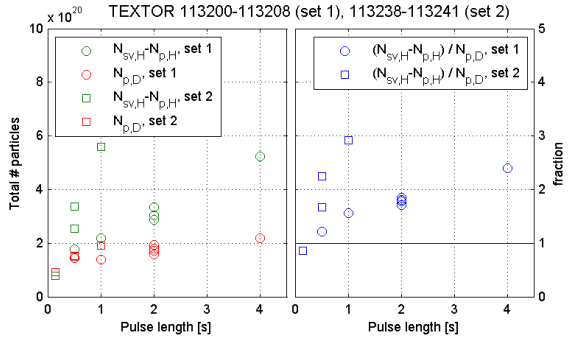

Figure 4.14: Isotope exchange efficiency as function of pulse length taken from two sets of H_2-ICWC discharges on D-preloaded wall. $N_{\mathrm{sv,H}}$, $N_{\mathrm{p,H}}$ and $N_{\mathrm{p,D}}$ are respectively the total injected H, total pumped H and total pumped D for each discharge. The H_2 injection was feedback controlled with $p_{\mathrm{H_2}} = 5.0 \cdot 10^{-4}$ mbar. The RF power at the generator was 2×50 kW for set 1 and 2×100 kW for set 2, at a frequency of 29 MHz and the toroidal magnetic field of 2.3 T.

SUPRA, nor to the discharge power.

Also on tungsten machine ASDEX Upgrade it is advantageous to reduce the RF discharge length in order to optimize the conditioning efficiency. The motivation for applying shorter RF pulses instead of continuous RF discharges is clearly illustrated on Fig. 4.15, giving the H_2 and HD partial pressure time traces for four similar RF discharges with different pulse lengths. The H_2 injection was continuously constant (until $t = 15$ s) with $p_{\mathrm{H_2}} = 2.5 \cdot 10^{-4}$ mbar. The RF power at the generator was 300 kW (monopole phasing), at a frequency of 30 MHz and a toroidal magnetic field of 2.3 T. Since the gas injection was continuously constant, the gas consumption by the walls is not compensated by extra injection, which is clearly visible from the H_2 pressure drop on switching on the RF power. The longer the RF pulse, the deeper the pressure drop, until at $t \approx 1$ s a steady state pressure level is formed. The HD partial pressure first starts to increase on switching on the RF power, which illustrates the strong wall interaction, while for the longer RF pulses at $t > 250$ ms it decreases again. The latter is not due to depletion of the wall, but rather to the drop of the total pressure; for longer pulse lengths, the initial wall released HD will be reimplanted into the wall. The optimal pulse length in this figure is the pulse of 250 ms. For this pulse the maximum p_{HD} is reached, whereafter the discharge is stopped and the outgassed HD can be recovered from the vessel by the pumps. For shorter pulses the maximum is not reached, so the HD removal efficiency will be lower. For longer pulses, the HD pressure

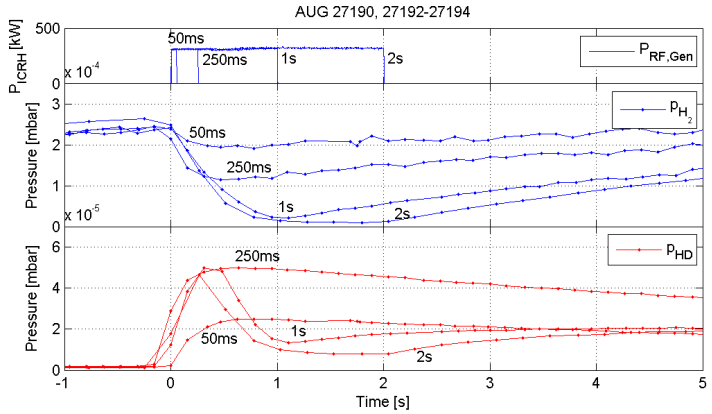

Figure 4.15: Partial pressure time traces (p_{H_2} and p_{HD}) for 4 similar ASDEX Upgrade discharges with different pulse lengths. The H_2 injection was continuous constant with $p_{H_2} = 2.5 \cdot 10^{-4}$ mbar. The RF power at the generator was 300 kW (monopole phasing), at a frequency of 30 MHz and the toroidal magnetic field of 2.3 T.

will decrease again with the total pressure, which causes also a lower HD removal efficiency by the pumps ($p_{HD}S$).

An analysis, determining the ideal pulse cycle (RF pulse length and pumping time) for TORE SUPRA H_2-ICWC discharges with $p_{H_2} = 1.75 \cdot 10^{-4}$ mbar, $P_{RF,gen} = 60$ kW is presented in chapter 6. In this section also the influence of the machine pumping speed on the conditioning efficiency will be discussed.

4.1.5 Optimization of control parameters

4.1.5.1 Efficiency as a function of power and pressure

Fig. 4.16 shows the conditioning efficiency of D_2-ICWC on JET as a function of the coupled power and discharge pressure (given as total injected deuterium). The data points are taken from a series of five 9 s RF discharges from which three had a similar coupled power ($\sim$ 275 kW) and discharge pressures of resp. $p_{tot} \approx 0.5 \cdot 10^{-5}$ mbar, $2 \cdot 10^{-5}$ mbar and $5 \cdot 10^{-5}$ mbar, and three had a similar discharge pressure ($p_{tot} = 2 \cdot 10^{-5}$ mbar) and coupled powers of resp. $P_{RF,coup} \approx 125$ kW, 190 kW and 275 kW. From the right top figure follows that the deuterium retention in the D_2-ICWC discharges increases linearly with the amount of injected deuterium. This is due to the simple fact that almost all injected gas is retained in the walls. In the previous section we saw that this retention can be limited by shortening the pulse length. The same right top figure shows that the amount of

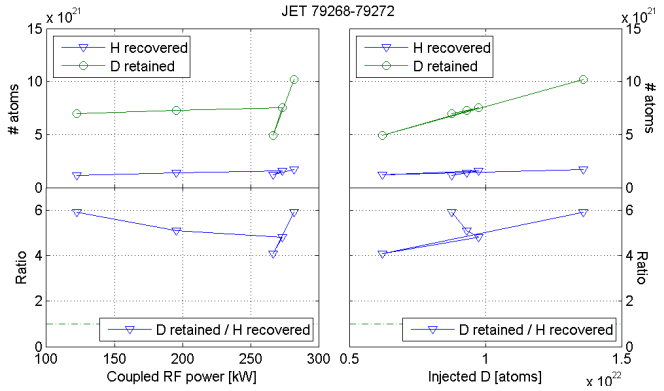

Figure 4.16: Isotopic exchange efficiency of D_2-ICWC on JET as a function of the coupled power and discharge pressure (given as total injected deuterium). The data points are taken from a series of 5 9 s RF discharges from which 3 had similar coupled powers (~ 275 kW) and discharge pressure of resp. $p_{\text{tot}} \approx 0.5 \cdot 10^{-5}$ mbar, $2 \cdot 10^{-5}$ mbar and $5 \cdot 10^{-5}$ mbar, and 3 had similar discharge pressure ($p_{\text{tot}} = 2 \cdot 10^{-5}$ mbar) and coupled power of resp. $P_{\text{RF,coup}} \approx 125$ kW, 190 kW and 275 kW.

recovered hydrogen is less dependent on the discharge pressure. The right bottom figure shows that the ratio of retained D over recovered H improves by lowering the discharge pressure[6]. The left bottom figure shows that for a given pressure, the best retained D over recovered H ratio is achieved at higher coupled power.

The 'long' RF discharges on JET make that on Fig. 4.16 the effect of discharge power is not very much pronounced. The constant gas injection makes that the gas retention is more related to the discharge length instead of the discharge power. In the previously discussed TEXTOR result given in Fig. 4.14 the gas injection was feedback controlled. In this case, as already mentioned, the retention becomes a strong function of both the RF power (more power, more retention) and the discharge length (longer pulse, more retention). As is the case for the pulse length, the efficiency for removal of particles is only weakly dependent on the coupled power. The optimal RF power has to be chosen as the power at which the RF discharge can be produced most reliably (antenna operation), and at which the discharge is most homogeneous.

Fig. 4.17 shows the particle balances for eight subsequent 500 ms long H_2-ICWC pulses on TEXTOR ($P_{\text{RF,gen}} = 2 \times 100$ kW, $f_{\text{RF}} = 29$ MHz and $B_T = 2.3$ T). The first four discharges are operated at higher feedback pressure

[6] On TORE SUPRA we saw earlier that this ratio improves on increasing the hydrogen content of the feedback injected H_2/He mixture (Fig. 4.2), which was due to the resulting significant increase of the total amount of recovered wall desorbed particles.

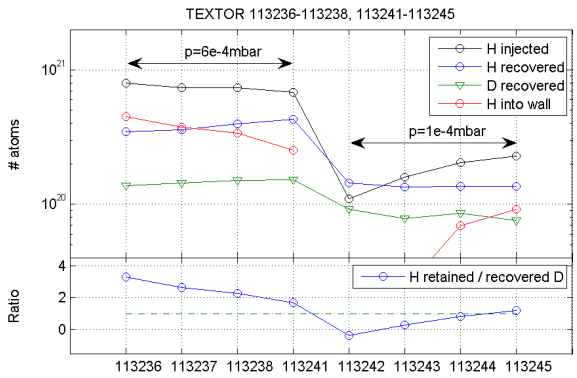

Figure 4.17: Particle balance for 8 subsequent 500 ms long H_2-ICWC pulses on TEXTOR. The H_2 injection was feedback controlled with $p_{H_2} = 5.0 \cdot 10^{-4}$ mbar for the first 4 discharges and $p_{tot} = 1 \cdot 10^{-4}$ mbar for the last. The RF power at the generator was 2×100 kW, at a frequency of 29 MHz and the toroidal magnetic field of 2.3 T.

($p_{tot} = 5 \cdot 10^{-4}$ mbar), and the second four at lower feedback pressure ($p_{tot} = 1 \cdot 10^{-4}$ mbar). From discharge to discharge, at high pressure, less hydrogen is retained into the wall, and thus less hydrogen is required to reach the total pressure of $5 \cdot 10^{-4}$ mbar. This saturation effect makes also that less wall desorbed deuterium is re-implanted into the wall, which is visible by the fact that from discharge to discharge more deuterium is removed from the vessel. For the fourth discharge, the ratio of H retained over D removed equals 1.7, and it seems that the ratio can improve even more (saturation not complete). When switching to a lower total gas pressure, at first more hydrogen is recovered from the vessel than injected. The ratio of H retained over D removed is thus negative. It increases in the subsequent shots, and becomes again higher than one at the fourth discharge (1.2). It is concluded that for each combination of discharge pressure, coupled power, and discharge length a specific steady state ratio of H retained over D removed will be attained. For the presented TEXTOR case it seems that for the given discharge length and generator power the high pressure discharges perform better than the low pressure ones. The total amount of removed deuterium is higher and the ratio of H retained over D removed evolves in time to one that is close to one.

4.1.5.2 Efficiency as a function of magnetic fields

The analysis of the wall conditioning efficiency as a function of the applied toroidal and poloidal magnetic fields is a difficult matter since the

improvement of the efficiency is generally small and masked by the constantly changing wall state. In section 4.1.2 we already mentioned that the improvement in conditioning efficiency for high and low B_T discharges on TEXTOR (when keeping the coupled RF power approx. constant) is only small. So far it was not possible to show a clear effect of the radial location of the fundamental resonance layer on the conditioning efficiency. It can thus be concluded that the choice of the toroidal field is not crucial for the conditioning efficiency, and should be determined by plasma production considerations.

As discussed in chapter 3, the application of a poloidal magnetic field can improve the poloidal discharge homogeneity so that distant areas, such as the divertor region on JET, can be reached. On TEXTOR it was shown that the deuterium removal efficiency of H_2-ICWC increases by 5% on application of a stationary vertical magnetic field ($\sim 10\,\mathrm{mT}$, last three discharges of the ICWC session resulting in the isotopic ratio increase shown in Fig. 4.3, left). At the same time also the retention increased by 5%. This might be understood from the increasing or changing wall surface area that is reached by the plasma wall flux, by tilting the magnetic field lines (see chapter 3). The magnectic field lines close to the wall surfaces are in present devices mostly limited by dedicated wall structures (e.g. antenna protection limiters at LFS or inner bumpers at HFS). As charged particles are transported along field lines, tilting these field lines will slightly change the conditioned surfaces. The ITER wall will be completely shaped [125], meaning that there won't be any dedicated structures serving as poloidal limiters, except for the wall itself. As already proposed in chapter 3, varying the sign of the poloidal field from a set of RF pulses to an other set (e.g. 10 pulses at $+B_{V,\max}$ and 10 pulses at $-B_{V,\max}$) might increase the conditioning efficiency.

4.2 He-ICWC for fuel removal and recovery from disruptions

4.2.1 Fuel removal

Fig. 4.18 shows the H_2 and HD partial pressure as a function of time for three identical He-ICWC discharges on TORE SUPRA ($15 \times 2\,\mathrm{s}$ pulses with $18\,\mathrm{s}$ between subsequent pulses, $p_{\mathrm{He}} = 2 \cdot 10^{-4}\,\mathrm{mbar}$ and $P_{\mathrm{RF,gen}} = 150\,\mathrm{kW}$). The discharges are effectuated after a H_2-ICWC session, for which the wall was preloaded by D_2-GDC. After this session the walls were partially desaturated by one non sustained ohmic breakdown and one ohmic discharges (natural density, $I_p = 0.8\,\mathrm{MA}$). On Fig. 4.18, a clear outgassing peak is vis-

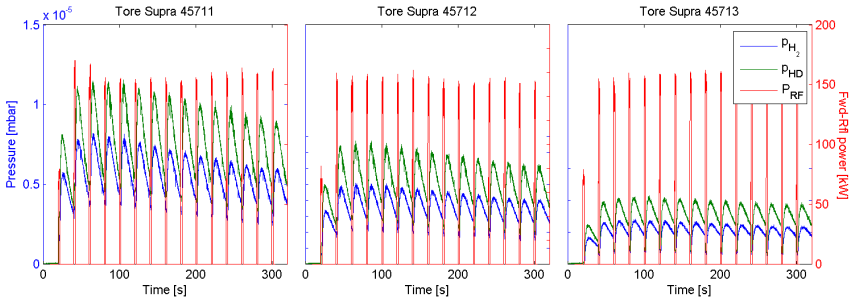

Figure 4.18: H_2 and HD partial pressure as a function of time for 3 identical subsequent He-ICWC discharges on TORE SUPRA: $15 \times 2\,\mathrm{s}$ pulses with $18\,\mathrm{s}$ between subsequent pulses, $p_{\mathrm{He}} = 2 \cdot 10^{-4}\,\mathrm{mbar}$ and $P_{\mathrm{RF,gen}} = 150\,\mathrm{kW}$

ible after every RF pulse, decreasing in height from pulse to pulse, which illustrates the progressing desaturation of the wall surfaces. Table 4.9 summarizes the total particle balances for each discharge. In total $9.1 \cdot 10^{20}$ H atoms could be recovered from the wall in the three discharges (~ 1 monolayer), which is about 5 to 10% of the short term retention accessible by plasma operation in TORE SUPRA, illustrating the effectiveness of He-ICWC[7]. The three subsequent ICWC discharges shown in 4.18, containing 45 RF pulses in total, were carried out without any occurring problems with respect to RF antenna operation, illustrating that this optimized He-ICWC scenario is ready for routine operation on TORE SUPRA.

Unlike for hydrogen RF discharges, in case of He-ICWC on TORE SUPRA, almost no helium is lost to the walls ($< 5\%$, see table 4.18). We will show further-on that during He-ICWC discharges on JET and ASDEX Upgrade a significant part of the injected helium is retained in the walls.

Table 4.9: Particle balances for the TORE SUPRA He-ICWC discharges 45711-45713 shown in Fig. 4.18. He injected: $N_{\mathrm{sv,He}}$, H recovered: $N_{\mathrm{p,H}}$

H+D wall	$N_{\mathrm{sv,He}}$	% He retained	$N_{\mathrm{p,H}}$
He-ICWC 45711	8.4e21	2.5	4.7e20
He-ICWC 45712	8.3e21	3.2	3.1e20
He-ICWC 45713	8.4e21	3.2	1.7e20

[7]The fact that the HD partial pressure is slightly higher than the H_2 partial pressure means that the amount of recovered deuterium is of the same order as the amount of recovered hydrogen, which puts the total number of removed hydrogen isotopes on 10-20% of the short term retention. In case of a wall isotopic ratio of $I = \mathrm{H}/(\mathrm{H}+\mathrm{D}) = 0.5$, one expects an identical partial pressure isotopic ratio: $I = [p_{\mathrm{H_2}} + 0.5 p_{\mathrm{HD}}]/[p_{\mathrm{H_2}} + p_{\mathrm{HD}} + p_{\mathrm{H_2}}]$, for which counts $p_{\mathrm{H_2}} = p_{\mathrm{D_2}}$ and $p_{\mathrm{HD}} = 2p_{\mathrm{H_2}}$.

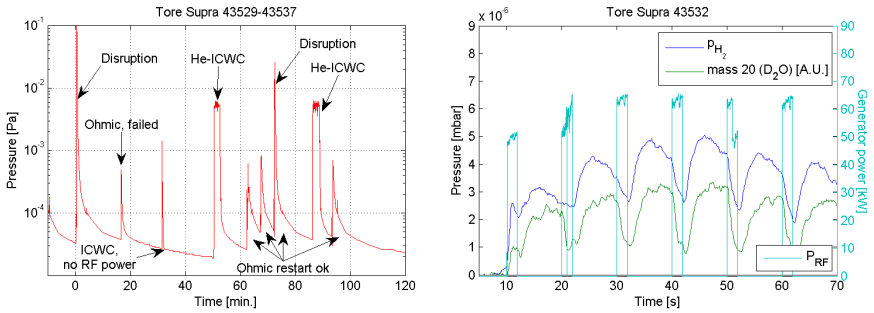

Figure 4.19: Left: Ion gauge pressure as a function of time in TORE SUPRA during recovery from disruption tests using He-ICWC ($p_{\mathrm{He}} \approx 5 \cdot 10^{-4}\,\mathrm{mbar}$, $p_{\mathrm{RF,gen}} \approx 60\,\mathrm{kW}$). Right: Hydrogen partial pressure and D_2O mass spectrometry signal for first recovery He-ICWC discharge.

4.2.2 Recovery from disruptions

After a tokamak plasma disruption event, the wall surfaces are often saturated with fuel and lots of impurities, produced as a result of the disruption, are present. After such an event it is generally difficult to restart a tokamak plasma due to too high plasma fueling by the walls, and to additional plasma cooling by impurities in the burn-through phase. To ensure tokamak start-up, conditioning procedures are employed to desaturate the walls and to remove the impurities (see section 1.5). In order to assess the efficiency of ICWC to recover to normal tokamak operation, two disruptions were provoked on the outboard poloidal limiter during ohmic discharges ($I_p = 1.2\,\mathrm{MA}$) on TORE SUPRA. Both disruptions had a similar strength ($\mathrm{d}I_p/\mathrm{d}t = 360\,\mathrm{MA/s}$). Fig. 4.19 (left) gives the total pressure in the vacuum chamber illustrating the chronology of the experiment. After the first disruption, an attempt to initiate an ohmic plasma failed due to the saturated vessel walls. At $t = 50\,\mathrm{min.}$, the walls are conditioned by He-ICWC ($p_{\mathrm{He}} \approx 6.0 \cdot 10^{-4}\,\mathrm{mbar}$). The pulsed He-ICWC discharge, consisting of ten 2 s RF pulses with 8 s of PT between the subsequent pulses, allowed to recover to normal tokamak operation (ohmic at $t = 62\,\mathrm{min}$). The hydrogen partial pressure and D_2O mass spectrometry signal for the first six RF pulses is given in Fig. 4.19 (right). One can clearly see the outgassing peak after each RF pulse, while during the pulse the hydrogen and D_2O pressure drop (particle consumption by wall). The after-shot partial pressure level increases in the first four pulses and starts to decrease from the fifth pulse on, illustrating the desaturation of the wall. To ensure that it was actually the He-ICWC discharge that successfully desaturated the walls, and not the failed ohmic discharge (at $t = 18\,\mathrm{min.}$), a second disruption was provoked

followed by He-ICWC. After this He-ICWC discharge, again it was possible to initiate a plasma, indicated by the last pressure increase on the figure, at $t = 95\,\text{min}$. During a later experimental campaign, a third test was successfully effectuated, putting the counter on 3/3. To gain more confidence in the ICWC technique, the number of tests should be increased in future. TORE SUPRA is the only (European) machine that can do this in a time efficient manner: its superconducting toroidal field system allows applying multiple RF pulses in one single discharge.

The efficiency of the discussed He-ICWC discharge can be improved by increasing the time in between pulses (e.g. 18 s PT instead of 8 s), so that more of the wall desorbed particles are removed by the pumps, to avoid re-implantation during the subsequent RF pulse.

4.2.3 Optimization of control parameters

Dedicated experiments have been carried out on TORE SUPRA to find the optimal discharge control parameters that maximize the He-ICWC efficiency. Below the effect of the pulse length and RF power will be discussed. No conclusive data was obtained on the effect of the neutral helium pressure, nor on the applied vertical magnetic fields.

4.2.3.1 Efficiency as a function of the RF pulse length

Fig. 4.20 (left) shows the hydrogen removal efficiency of TORE SUPRA He-ICWC pulses ($P_{\text{RF,gen}} = 250\,\text{kW}$, $p_{\text{He}} = 1.8 \cdot 10^{-4}\,\text{mbar}$) as a function of the pulse length, for a constant total pulse cycle of 40 s. The amount of removed hydrogen during one pulse cycle increases clearly on increasing pulse length. Continuous RF operation is however not advantageous since most of the hydrogen is recovered after the RF pulse, the hydrogen pressure during the discharge being very low. To optimize the discharge it is thus important to find the optimal combination of pulse and pulse cycle length. From previous section on H_2-ICWC we know that the re-implantation of wall desorbed species increases on increasing pulse length. In chapter 5 on the 0D modeling of ICWC discharges we will show that the contribution of wall desorbed hydrogen to the total wall flux in helium RF discharges is significant. The H^+ and He^+ ion flux are comparable, and the neutral H-atom flux is one order of magnitude higher than the ion fluxes. Re-implantation of wall desorbed hydrogen will thus likely also be important in He-ICWC discharges. It is therefore recommended to limit the discharge length also in He-ICWC, e.g. 2 s, and to foresee sufficient time between two discharge pulses, e.g. 18 s, as was successfully employed for the discharges in Fig. 4.18.

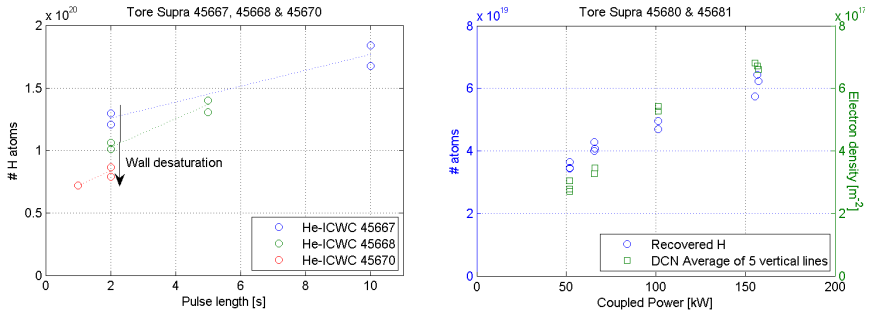

Figure 4.20: Hydrogen removal efficiency of TORE SUPRA He-ICWC discharges ($p_{\mathrm{He}} = 1.8 \cdot 10^{mbar}$ kW). Left: Efficiency per pulse as a function of the pulse length (constant total pulse cycle of 40 s and $P_{\mathrm{RF,gen}} = 250$ kW). Right: Efficiency per pulse as a function of the coupled power (2 s RF pulses and a total pulse cycle of 10 s).

4.2.3.2 Efficiency as a function of the RF power

Fig. 4.20 (right) shows the hydrogen removal efficiency of TORE SUPRA He-ICWC pulses ($p_{\mathrm{He}} = 1.8 \cdot 10^{-4}$ mbar) as a function of the coupled power, for 2 s RF pulses and a total pulse cycle of 10 s. On increasing the power, the mount of removed hydrogen increases. It is expected that this is due to an enhanced particle wall flux at increased coupled power. On the right axis the electron density is given as a function of the coupled power. In chapter 5 these particular discharges will be modeled, reproducing the measured densities as a function of the coupled power, and estimating the wall flux. From the model it is confirmed that the wall flux increases on increasing coupled power. In the case of H_2-ICWC we saw that the hydrogen implantation rate increased on increasing discharge power. As already mentioned, a large part of the wall flux during He-ICWC will consist of wall desorbed hydrogen, and thus it is expected that the re-implantation rate of wall desorbed species also increases with the RF power. If one intends to use very high powers for conditioning, the discharge length should thus be decreased.

4.2.4 Comparison with other techniques

The routine conditioning technique for inter-pulse conditioning on TORE SUPRA are the Taylor like 'TORE SUPRA cleaning discharges' (see section 1.5.2.2). The HD removal efficiency of these discharges (after disruptions) was previously compared with the efficiency of continuous He/H_2-ICWC discharges (see [126]). The efficiencies of both techniques were found to be comparable. Fig. 4.21 (top) shows a similar figure, comparing the HD removal efficiency of the optimized pulsed He-ICWC discharges dis-

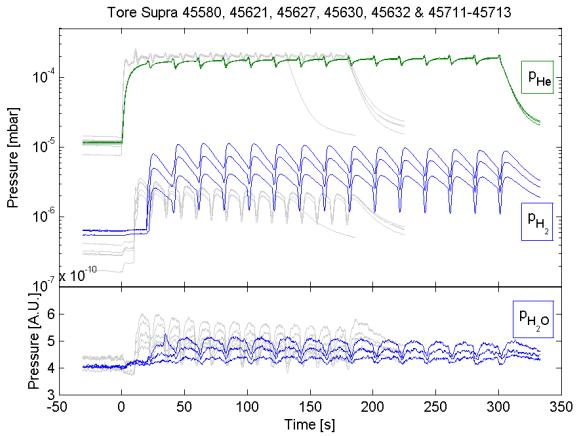

Figure 4.21: He, HD and H_2O partial pressures measured during Taylor like helium conditioning discharges (gray lines) and He-ICWC (blue and green lines) on TORE SUPRA.

cussed in section 4.2.1 (blue and green lines) to that of TDC discharges (gray lines). As mentioned, the He-ICWC discharges were preceded by a H_2-ICWC session, one non sustained tokamak plasma, and one ohmic D_2 plasma. Most of the TDC discharges were preceded by a plasma disruption. Both techniques operated in pulsed mode, at about the same helium pressure ($p_{\mathrm{He}} \approx 2 \cdot 10^{-4}$ mbar). The HD removal efficiency of ICWC is initially about five times higher than in the TDC discharges, and evolves during the 45 subsequent RF pulses to a removal rate that is about two times the maximum removal rate in the Taylor like discharges. Since TDC is successfully used for inter-pulse conditioning on TORE SUPRA, this result in principle indicates that also He-ICWC can be used for inter-pulse conditioning, at an at least equal efficiency.

The bottom figure shows that also the impurity removal rates (H_2O) are comparable. We will discuss impurity removal in more detail in section 4.3.

4.2.5 Helium retention

During He/D_2-ICWC discharges on JET and He/H_2-ICWC discharges on ASDEX Upgrade it was found that large amounts of helium were absorbed by the wall, as illustrated on Fig. 4.22. The red curve gives the expected helium pressure from the gas injection signals, the blue line is the measured helium partial pressure, and the green surface represents the amount of helium that went missing during the discharge. In the shown JET discharge this surface represents $2.0 \cdot 10^{20}$ helium particles or 80% of the injected

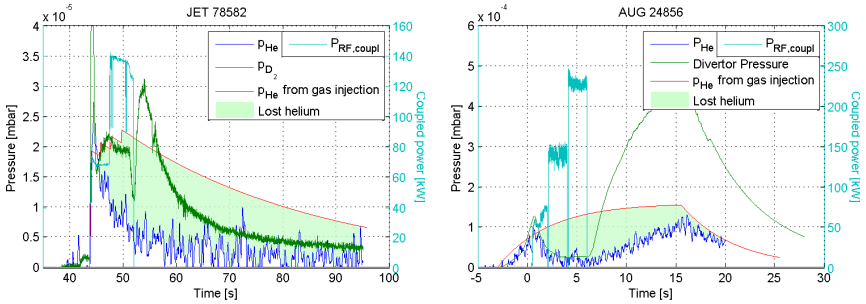

Figure 4.22: Illustration of helium loss during He/D_2-ICWC on JET (left) and He/H_2-ICWC on ASDEX Upgrade (right). Respectively the expected helium pressure (red, from the gas injection signals), the measured helium partial pressure (blue), and the consequently missing helium (green surface) are given.

atoms. In the ASDEX Upgrade discharge, $3.2 \cdot 10^{20}$ or 60% of the injected atoms were lost to the walls. For the total experimental session on JET consisting of 11 successive He-containing ICWC discharges, including the shown discharge, an average helium retention of 80% was found, good for about $2 \cdot 10^{21}$ He atoms in total. The He/D ratio[8] from visible spectroscopy and VUV He lines measured in during D_2 tokamak discharges right after the ICWC session was 4%. Before the RF session this ratio was practically zero ($\leq 0.2\%$), confirming the significant absorption of helium by the walls during the ICWC session. In total four tokamak discharges and 2 hours of D_2-GDC reduced the ratio again below $< 0.3\%$.

The cause of the helium retention it not well understood at this point. Similar strong helium losses were not observed on TORE SUPRA (see e.g. table 4.9), nor on TEXTOR, at any pressure or RF power. Since on JET the retention was found to be significant at any RF power, it is concluded that an explanation has to be sought in terms of the plasma facing components. As published in [127], the presence of beryllium in JET (on ICRF antennas) could explain the high helium retention on JET [128] and the helium losses to tungsten walls have also been reported for He-GDC [129]. Since ITER will have as main plasma facing components tungsten and beryllium, it is important to investigate this effect further in future. Conditioning in alternative inert gases could be envisaged if necessary, and if they do not feature the same problem.

[8]Thanks to dr. A. Kreter, IPP Juelich

4.3 Removal of impurities and codeposited layers

In previous sections we analyzed the efficiency of H_2 and He-ICWC for respectively isotopic exchange and wall desaturation. The removal rates of hydrogenic species and the additional induced hydrogen or helium retention could be accurately calculated thanks to the high partial pressures of the latter gases and the collected mass spectrometry and Penning gauge spectroscopy calibration data. An important question remains however to be treated, namely whether ICWC is able to reduce the impurity content in the vacuum vessel (to allow tokamak start-up and improve plasma performance), and whether it can remove codeposited layers together with the therein stored hydrogen (tritium removal). This section gives an overview of experimental results related to these two points.

4.3.1 Carbon removal

An accurate quantization of carbon removal by ICWC was obtained on JET. Gas chromatography analysis (see section B.1.3.2) of the pumped gas during the isotopic exchange experiment on JET, presented earlier in Fig. 4.5, evidenced a total of $4.1 \cdot 10^{20}$ carbon atoms in the form of CH_4 (98%), C_2H_4 (1.5%) and C_2H_6 (0.5%). This corresponds to 7.8 mg of carbon, or 0.13 monolayers, in eight RF pulses of 9 s. Taking the JET erosion and redeposition rates mentioned in section 1.4.1, one would need 90 similar ICWC pulses to remove the 90 mg of carbon, codeposited in an average 10 s JET discharge. This extrapolation holds of course only if the removed carbon stems from codeposited layers.

Fig. 4.23 (left) shows the impurity removal efficiency, represented by the time integrated mass spectrometry signal (including discharge and post discharge), as a function of the averaged coupled power for He/D_2-ICWC discharges on JET. The removal efficiency is clearly higher at higher discharge powers. Although the injected gas mixture was changed from discharge to discharge, no clear dependency was found on the discharge gas, which is likely due to the fact that most of the gas is consumed by the walls during the discharge.

In section 4.1.2 we investigated whether the presence of fast CX neutrals could improve the hydrogen removal efficiency, which turned out not to be the case. The same question can be posed for the impurity removal efficiency. Fig. 4.23 (right) gives estimated impurity partial pressures (mass 19 for HDO or CHD_3 and mass 20 for H_2O and CD_4, calibrated using mass 16 with CH_4), for the two TEXTOR discharges previously discussed in section

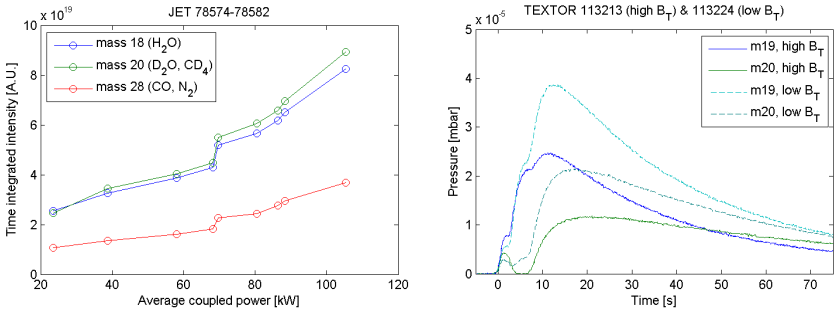

Figure 4.23: Left: Integrated mass spectrometry signal (including discharge and post discharge), as a function of the averaged coupled power for He/D_2-ICWC discharges on JET. Right: Estimated impurity partial pressures (mass 19 for HDO or CHD_3 and mass 20 for H_2O and CD_4, calibrated using mass 16 with CH_4), for two TEXTOR discharges operated respectively at $B_T = 2.3\,\mathrm{T}$ and $B_T = 0.23\,\mathrm{T}$.

4.1.2 (Fig. 4.8), operated respectively at high and low toroidal magnetic field. The presence of energetic CX neutrals in the high B_T discharge, due to resonant ion heating at the fundamental resonance layer, has clearly no major effect on the impurity removal efficiency. The outgassing peaks, visible on the partial pressures (t = 10 to 20 s), are 40% higher in the low B_T case than in the high B_T discharge. This is thought to be due to the better homogeneity of the discharge in case multiple harmonic resonances are present in the vessel. The idea that the fast CX neutrals might facilitate the removal of codeposited layers is thus either not correct, or that it cannot be shown from the partial pressures.

To test the ability of ICWC to erode codeposited layers, (deuterated-) carbon coated silicium samples were introduced into TEXTOR via the bottom limiter lock, during the previously presented isotopic exchange experiment consisting of 26 nearly identical He/H_2-ICWC discharges (Fig. 4.3). The sample holder was mounted on the Langmuir probe holder, described in section B.2.4 (dimensions: Fig. B.6). The plasma facing apertures of the sample holder (see photo: Fig. 4.24) are $\sim 2\,\mathrm{mm}$ smaller than the sample dimensions so that in the surface analysis after the ICWC session, the exposed sample area could be compared to the shadowed sample edge. The analysis[9] showed no significant thickness variation between the exposed and shadowed parts, illustrating that no net erosion or deposition occurred during the experiments at the location of the probe holder. In the first 10 nm of the exposed area, a significant increase of the hydrogen and oxygen concentration was observed (see Fig. 4.25). No clear decrease of the deuterium

[9]Thanks to dr. A. Litnovsky, IPP-Juelich

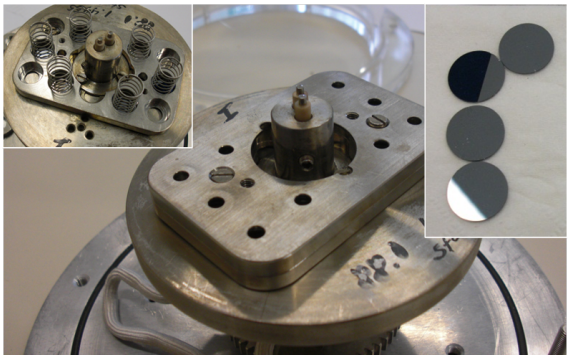

Figure 4.24: Sample holder to study PSI in situ on TEXTOR. From left to right: opened sample holder, sample holder mounted on the Langmuir probe holder and samples. The samples have to be placed on top of the springs, with the carbon coating facing the plasma.

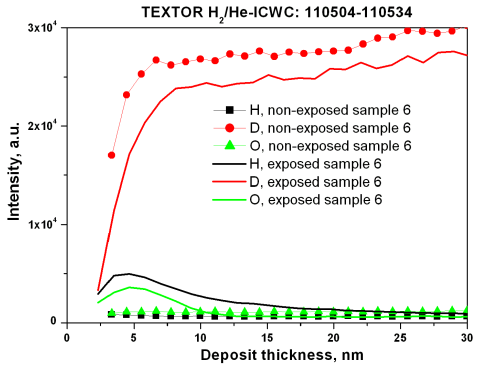

Figure 4.25: Surface analysis of deuterated carbon coatings exposed to 26 nearly identical He/H_2-ICWC discharges (see Fig. 4.3) on TEXTOR. Plasma exposed areas are compared to shadowed areas.

concentration could be seen. At larger depths the hydrogen and oxygen concentrations are less pronounced and at a depth of 30 nm the hydrogen concentration in the exposed area becomes equal to that of the non exposed area. One can conclude that by exposure to He/H_2-ICWC, mainly the first 10 nm of the deuterated-carbon coating is affected. Whereas the evidenced surface hydrogen concentration can be due to the H_2-RF discharges, the oxygen concentration is possibly built up after taking the samples out of the vacuum environment. If the latter is true, the fact that no oxygen is measured in the non-exposed area means that ICWC induces trapping sites for oxygen (or H_2O). In future, similar experiments should be carried out

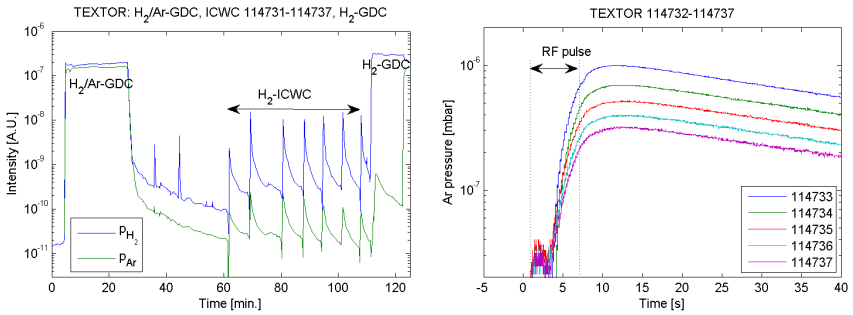

Figure 4.26: Left: H_2 and Ar partial pressure illustrating the chronology of the Ar removal experiment on TEXTOR. Right: Evolution of the Ar partial pressures for 5 subsequent H_2-ICWC discharges: 5 s long RF pulses, $P_{\mathrm{RF,gen}} = 2 \times 50\,\mathrm{kW}$, $p_{H_2} = 5 \cdot 10^{-4}$ mbar.

where one firstly has to aim at putting the samples as close as possible to the plasma. As we saw in chapter 3, the measured plasma densities at this location (Langmuir probe), are much lower than the evidenced plasma densities in the center of the vessel (interferometry), which reduces probably the removal, retention and erosion rates. Secondly, the cumulated discharge time has to be as high as possible[10].

4.3.2 Removal of marker gas: Argon

To compare the impurity removal efficiency of H_2-ICWC to that of standard H_2-GDC on TEXTOR, the TEXTOR wall was loaded with a marker gas, whereafter its removal efficiency by both techniques is recorded. For the marker gas argon was chosen. The advantage of argon is that it can be easily identified with mass spectrometry and that its presence in the vessel, if not injected on purpose, is negligible. Fig. 4.26 (left) shows the chronology of the experiment. A 15 min. Ar/H_2-GD was effectuated ($t = 10 - 25$ min.), followed by seven H_2-ICWC discharges (5 s long RF pulses, $P_{\mathrm{RF,gen}} = 2 \times 50\,\mathrm{kW}$, $p_{H_2} = 5 \cdot 10^{-4}$ mbar). Fig. 4.26 (right) gives the evolution of the argon partial pressures for five subsequent discharges. The argon release decreases from shot to shot, and most of the argon is recovered after the RF pulse. The total amount of argon removed in these discharges is $5.1 \cdot 10^{18}$ (integration over 60 s starting from discharge initiation). The H_2-GD at the end of this test removed another $1.4 \cdot 10^{19}$ argon atoms from the wall (partial pressure extrapolated by 10 min.), which allows to estimate the

[10] If one only wants to evidence erosion, long high power RF discharges are recommended, which will be at the price of high discharge gas retention. If the aims is to illustrate isotopic exchange, shorter RF pulses are recommended to limit the extra retention.

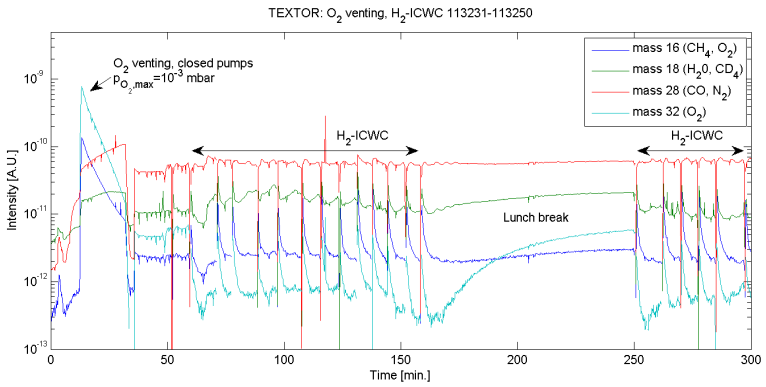

Figure 4.27: Mass spectrometer signals illustrating the chronology of the O_2 removal experiment by H_2-ICWC on TEXTOR.

total amount of retained argon by the Ar/H_2-GDC to $1.9 \cdot 10^{19}$. The seven ICWC discharges could thus remove $\sim 25\%$ of the introduced argon. To test whether ICWC reaches the same wall areas as GDC, more ICWC discharges should have been effectuated until no argon is recovered, estimated at ~ 15 discharges. Any extra argon removed by a subsequent GDC stems from areas that are not efficienctly reached by ICWC. The maximum recorded removal rate during the discharges in Fig. 4.26 (right) equals $Q_{\mathrm{p,ICWC}} = 2.1 \cdot 10^{16}$ /s (discharge 114733, $t = 12\,\mathrm{s}$). As the maximum argon partial pressure in the H_2-GD is about 3 to 5 times higher than in H_2-ICWC, the maximum removal rate of GDC will thus also be 3 to 5 times higher.

4.3.3 Reduction of vessel oxygen content

The most common or relevant tokamak vacuum vessel impurities are oxygen, carbon oxides and water. As stated in section 1.4.2 these impurities are highly radiative and can cause multiple unfavorable effects (e.g. hindering tokamak plasma initiation or causing disruptions). A wall conditioning technique used for inter-pulse conditioning has thus to be able to reduce the general oxygen impurity content, e.i. ICWC which is envisaged for inter-pulse and overnight conditioning on ITER.

On TEXTOR a small amount of oxygen was introduced into the vessel. During this injection, the pumping ducts were closed so that most of the injected gas is absorbed by the vessel walls ($t = 15 - 30\,\mathrm{min.}$ on Fig. 4.27), visible by the decreasing O_2-pressure signal. The simultaneous CO pressure increase stems both from wall desorption as from wall erosion by the injected oxygen. After reopening the valves to the pumps ($t = 30\,\mathrm{min.}$) a stable O_2,

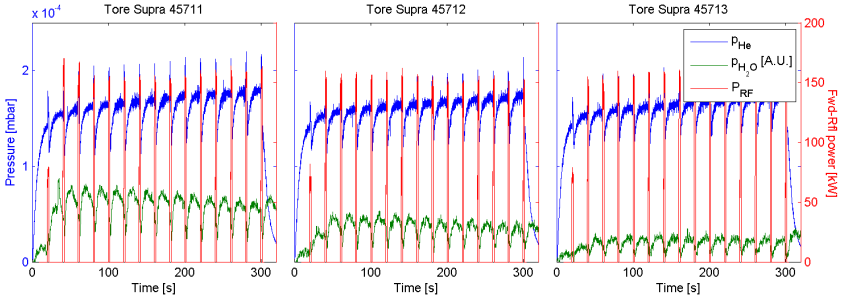

Figure 4.28: He and H_2O partial pressure as a function of time for 3 identical subsequent He-ICWC discharges on TORE SUPRA: $15 \times 2\,\mathrm{s}$ pulses with 18 s between subsequent pulses, $p_{\mathrm{He}} = 5 \cdot 10^{-4}\,\mathrm{mbar}$ and $P_{\mathrm{RF,gen}} = 150\,\mathrm{kW}$

H_2O and CO pressure level is formed in the vessel. Already after the first H_2-ICWC discharge ($t = 60\,\mathrm{min.}$), the O_2 pressure has decreased by 1 order of magnitude. The mass 16 signal becomes higher than mass 32, meaning that a significant amount of CH_4 is produced. At $t = 65\,\mathrm{min.}$ the Langmuir probe holder in limiter lock 1 is inserted into the plasma. The opening of the port causes a small rise of all the masses. In the subsequent H_2-ICWC discharges ($t = 60 - 160\,\mathrm{min.}$, short $0.15 - 1\,\mathrm{s}$ pulses of $2 \times 100\,\mathrm{kW}$ at generator, $p_{\mathrm{H_2}} = 5 \cdot 10^{-4}\,\mathrm{mbar}$) the partial pressures remain approximately at the same level. Only for the last three discharges at a reduced pressure of $p_{\mathrm{H_2}} = 1 \cdot 10^{-4}\,\mathrm{mbar}$ the O_2 level decreases by a factor 2 to 3. During the 1.5 hours lunch break, the O_2, H_2O and CO pressures rise back to their initial level. Already after the first H_2-ICWC pulse following this 1.5 hours period ($t = 250\,\mathrm{min.}$, pulse of 0.5 s with $2 \times 100\,\mathrm{kW}$ at generator, $p_{\mathrm{H_2}} = 1 \cdot 10^{-4}\,\mathrm{mbar}$) all signals have dropped again. One can conclude that ICWC reduces the oxygen content of the in-vessel neutral gas, although it is not very clear where the oxygen goes. Multiple options are possible, where in the less ideal case, ICWC puts the oxygen back in the wall and in the best case ICWC efficiently removes the oxygen from the vessel and vessel walls. Careful quantization of the impurity partial pressures is required to distinguish both mechanisms. Unfortunately it was not possible to quantify the amount of recovered oxygen after each discharge.

Fig. 4.28 shows the H_2O partial pressure as a function of time from the previously presented optimized TORE SUPRA He-ICWC discharge (Fig. 4.18). The wall release of H_2O is clearly visible after each RF pulse, and the outgassing peak decreases from pulse to pulse. The latter is likely due to both the decreasing hydrogen content of the wall and the decreasing oxygen level. As was the case for TEXTOR, also on TORE SUPRA it was not possible to estimate the total amount of recovered oxygen atoms in

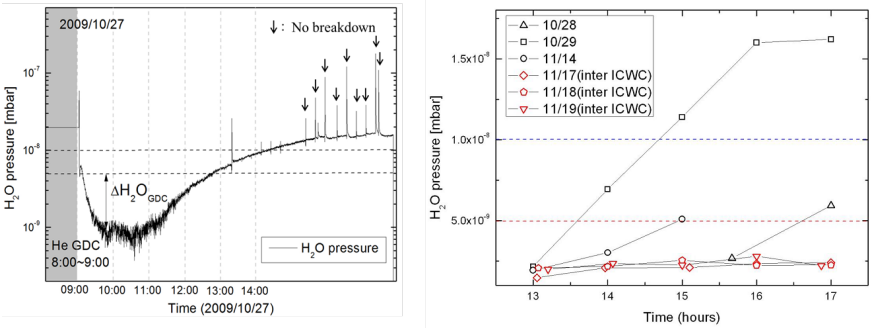

Figure 4.29: KSTAR [131]: Left: The p_{H_2O} time evolution after He-GDC, due to outgassing of the inboard graphite the H_2O pressure increases to levels $> 10^{-8}$ mbar at which tokamak plasma breakdown is prohibited. Right: The p_{H_2O} time evolution for resp. 3 operational days without, and 3 with inter-pulse He-ICWC.

these discharges.

4.3.4 H_2O removal on KSTAR

The presented results on carbon, O_2 and H_2O removal are mostly distilled from isotopic exchange experiments, where the walls were preloaded/cleaned by hours of GDC and the mass spectrometers were set up to record helium and hydrogenic species. Although the results show that it is possible to remove carbon, O_2 and H_2O from the vessel with ICWC, the question whether the removal efficiency is sufficient to ensure tokamak operation, remains. Promising results on this subject were reported by the KSTAR-team [130]. KSTAR, being a fully superconducting tokamak, employs He-ICWC to bring the H_2O partial pressure level below the operational limit. It is found that 30 min. of (lunch-time) He-ICWC is enough to reduce the water level down to $5 \cdot 10^{-9}$ mbar. Fig. 4.29 (left) shows the H_2O pressure as a function of time after a He-GD on KSTAR. Due to outgassing of the inboard graphite, the H_2O pressure increases slowly during the day to levels $> 10^{-8}$ mbar at which tokamak plasma breakdown is prohibited [131]. The right figure gives a similar H_2O pressure evolution for respectively three operational days without, and three with inter-pulse He-ICWC. It can be clearly seen that inter-shot ICWC suppresses the increase of water level completely. This results makes that inter-shot/lunch-time ICWC is essential for KSTAR operation [130].

4.4 Conclusion

In this chapter an overview was given of experimental results on the efficiency of ICWC, obtained on TORE SUPRA, TEXTOR, JET and ASDEX Upgrade. In the first part of the chapter the efficiency of H_2 and H_2/He discharges for isotopic exchange was analyzed. Hereafter the efficiency of He-ICWC for wall desaturation and recovery of normal tokamak operation after disruptions was presented. And finally also the efficiency of ICWC for impurity removal was discussed.

Isotopic exchange Table 4.10 gives an overview of the presented isotopic exchange results obtained on TORE SUPRA, TEXTOR, ASDEX Upgrade and JET (section 4.1.1), showing clearly that hydrogen ICWC is able to change the surface state within short time scales, but that the removal of wall isotopes can go at the price of a up to 10 times higher retention of the discharge gas. Studies to the causes of the high retention delivered

Table 4.10: Overview isotopic exchange results obtained on TORE SUPRA (TS), TEXTOR, ASDEX Upgrade (AUG) and JET (section 4.1.1). Change in isotopic ratio: IR-change, cumulated RF time: $\sum$ PL's, RF pulse lengths: PL, removed amount of monolayers [m-l]: N_p, ratio of retained over removed atoms: N_p/N_r.

	IR-change	$\sum$ PL's	PL	N_p	N_p/N_r
TS	$4 \rightarrow 40\%$	18 min.	~ 60 s	~ 2.5 m-l	10
TEXTOR	$7 \rightarrow 38\%$	3 min.	$6 - 8$ s	~ 9 m-l	2.6
JET	$30 \rightarrow 50\%$	1.2 min.	9 s	~ 6 m-l	2.9
AUG		0.85 min.	$0.05 - 10$ s	~ 12 m-l	4.8

important information but remained inconclusive. Firstly, no long-term saturation effects of the retention could be evidenced, even not after 15 min. of cumulated RF discharge time on TORE SUPRA. From this it was concluded that mechanisms such as retention in deeper layers, retention by codeposition and retention in remote areas might play an important role in ICWC discharges. From experiments on the tungsten machine ASDEX Upgrade, where the high retention rates were also observed, it was concluded that mechanisms other than codeposition with carbon have to be considered to explain the retention. By comparing the integrated total energetic CX atom flux on JET with the amount of retained isotopes it was concluded that direct implantation of these energetic particles is not the determining mechanism of the hydrogen retention. Additionally it was found that the fast CX atoms have also a limited contribution to the wall release. Both findings were confirmed by the particle balances for two TEXTOR isotopic

exchange discharges, resp. with and without fast particle population (high and low B_T). On ASDEX upgrade it was found that 11% of the retained hydrogen could be recovered by He-GDC illustrating that a significant part of the retained hydrogen is stored in layers accessible by GDC. As it was concluded that hydrogen retention is probably not due to codeposition, nor solely due to the fast particle fluxes, the remaining retained hydrogen (89%) must be stored differently. The hypothesis was made that ICWC discharges reach surface areas that are not accessible by glow discharges. Also the existence of a substantial non resonant ion wall flux component with energies above the typical GDC flux can at this point not be excluded. Both points require further investigation.

An extensive comparison of the isotope exchange efficiencies of ICWC and GDC on TORE SUPRA and TEXTOR learned that GDC can achieve 5 to 10 times higher removal rates of wall desorbed species than ICWC, although the wall release rate of particles during ICWC is about 10 times higher than in GDC. Both points are due to the higher electron density of ICWC discharges compared to GDC, which makes the reionization probability in ICWC discharges ($\sim 99.8\%$) is much higher than in GDC ($\sim 86\%$). Consequently the removal efficiency of wall desorbed species by the machine pumps is less efficient in ICWC than in GDC. It was found that also the measured high retention during the ICWC discharges can be understood as an effect of the high reionization probability. Even if the fraction of the wall flux that will be permanently retained is identical in GDC and in ICWC (e.g. 0.2%), the 10 times higher wall fluxes and the lower pumping probability in ICWC makes that the permanent retention rate in ICWC can be problematic, whereas the extra retention in GDC is negligible.

It was shown experimentally that the ratio of retained over recovered atoms can be significantly improved by optimizing the RF duty cycle. Since reionization and wall flux retention only occurs during the plasma discharge, and since it was shown that most of the wall desorbed gas is recovered after the RF pulse, the use of shorter RF pulses ($\sim 1\,\mathrm{s}$) separated by sufficient time between pulses to recover the wall desorbed particles by the machine pumps ($\sim 20\,\mathrm{s}$ on TORE SUPRA) significantly reduces the retention, without severely lowering the total amount of removed particles. Ratios of 1 have been achieved both on TORE SUPRA and on TEXTOR.

It was found that for H_2/He-ICWC discharges the conditioning efficiency improves on increasing the hydrogen concentration in the injected gas mixture (N_p increases and $N_\mathrm{p}/N_\mathrm{er}$ decreases) which motivated further isotopic exchange experiments in pure hydrogen. The absolute removal efficiency of wall desorbed particles is higher at higher feedback pressures (TEXTOR: $1 \cdot 10^{-4}\,\mathrm{mbar}$ vs. $5 \cdot 10^{-4}\,\mathrm{mbar}$). The efficiency increases also on increasing

the coupled RF power (although the pulse length has to be decreased at higher RF powers, since retention is more important at higher powers), but the gain is limited. The ideal RF power is the power at which the discharge can be established most reliably from point of view of antenna operation, and at which the discharge is most homogeneous. Whereas the toroidal field strength has a limited effect on the conditioning efficiency (at fixed coupled power), the ICWC conditioning efficiency can be improved by applying a vertical magnetic field. As charged particles are transported along the magnetic field lines, tilting the field lines can slightly increase or change the conditioned areas.

Wall desaturation He-ICWC discharges were successfully applied on TORE SUPRA to desaturate the wall from hydrogenic particles. In three discharges consisting each of 15×2 s RF pulses with 18 s PT between pulses ($p_{\mathrm{He}} = 2 \cdot 10^{-4}$ mbar and $P_{\mathrm{RF,gen}} = 150$ kW), 1 monolayer, or 5 to 10% of the short term retention accessible by plasma operation, could be removed illustrating the effectiveness of He-ICWC. The hydrogen is mostly recovered after the RF pulse. The removal efficiency is a clear function of the coupled power. For a same discharge length, the hydrogen removal efficiency increases with a factor two on increasing the coupled power form 50 kW to 150 kW. It is expected that redeposition of wall desorbed particles is as in the case of H_2-ICWC also important in He-ICWC. Therefore, although it was found that the amount of removed hydrogen from the wall improves on increasing pulse length (scanned range: $1 - 10$ s for constant total cycle time of 40 s), it is recommended to also limit the RF pulse length in He-ICWC.

On TORE SUPRA, He-ICWC was successfully applied to recover normal tokamak operation after plasma disruption events (3/3 attempts successful). It is found that the removal efficiency of He-ICWC is at least as efficient as that of the routinely operated TDC technique, both for hydrogen removal as for removal of H_2O, indicating that the optimized He-ICWC discharges can be used for inter-pulse conditioning during experimental campaigns on TORE SUPRA.

Both on JET and ASDEX Upgrade is was found that during helium containing ICWC discharges, a significant amount of the injected helium was consumed by the wall, resp. 80% and 60%. The beryllium elements on the ICRF antennas are thought to be responsible for this on JET. The helium losses are also reported for He-GDC on ASDEX Upgrade. Since ITER will have as main plasma facing components tungsten and beryllium it is important to investigate this effect further in future.

Impurity removal During the JET isotopic exchange experiments (included in table 4.10) 0.13 monolayers of carbon were removed from the vessel. This relatively high removal efficiency can however not be extrapolated to the removal efficiency of codeposited layers since the carbon source is not known. To evidence carbon erosion or deposition, samples were inserted in the TEXTOR ICWC plasmas. However no traces of erosion or deposition could be found on the plasma exposed areas. This might be due to the reduced plasma density at the location of the level sample holder, which was shadowed by a poloidal limiter. On JET it was found that the impurity removal efficiency improves on increasing the discharge power, and finally it was evidenced that there is no clear influence of the present energetic CX flux on the removal of impurities (TEXTOR experiments at high and low B_T).

The removal efficiency of the marker gas argon was tested on TEXTOR. In only seven 5 s H_2-ICWC pulses ($P_{\mathrm{RF,gen}} = 2{\times}50$ kW, $p_{\mathrm{H_2}} = 5{\cdot}10^{-4}$ mbar), 25% of the introduced argon by H_2/Ar-GDC could be removed. This illustrates that ICWC reaches a large part of the wall area affected by GDC.

Finally it was illustrated both on TEXTOR (H_2-ICWC) and TORE SUPRA (He-ICWC) that ICWC can reduce the oxygen content in the vacuum vessel. Whether this removal efficiency is sufficient to ensure tokamak operation could not be tested in the course of this PhD. For this ICWC has to be tested as routine conditioning technique during an experimental campaign. On TORE SUPRA this could be done in a time efficient manner because of its superconducting toroidal field system. Promising results on this subject were reported by the KSTAR-team [130]. The superconducting tokamak KSTAR employs He-ICWC routinely for inter-pulse and lunchtime conditioning, in order to keep the vessel H_2O pressure below the operational limit.

5 Kinetic Description of Hydrogen-Helium ICWC Plasmas

In this chapter the 0D kinetic description of hydrogen-helium plasmas implemented in TOMATOR-0D (0D Transport Oriented model for MAgnetized TOroidal Rf discharges) is outlined. The model is developed to describe the evolution of ICRF plasmas from discharge initiation to the steady state plasma stage. It allows to study ICRF plasmas in a wide density range, up to $n_e = 10^{12}\,\mathrm{cm}^{-3}$, and temperature range of $T_e = 1 - 100\,\mathrm{eV}$. It gives insight on ICRF plasma parameters, particle fluxes to the walls and main collisional processes, the latter being the fundamental mechanism for the build-up of a plasma. This is of particular importance since most standard tokamak plasma diagnostics (see section B.2) are not adapted to diagnose the low temperature and low density ICWC plasmas. Together with experimental data, the model can thus be used to obtain better understanding of the physics behind ICRF plasma production.

5.1 Model description

5.1.1 Overview of the balance equations

To describe numerically in a 0D approach the evolution of ICRF plasma parameters in tokamaks and stellarators, a set of transport equations, published previously by Moiseenko and others [84, 91, 132, 133], was adopted.

The equations are derived from the standard continuity and heat balance for simple plasmas, given by Braginskii [134], where all particle species are assumed to have a Maxwellian energy distribution. In the present model the transport equations are updated to include molecular hydrogen and helium, which is especially of importance for wall conditioning plasmas. The 0D plasma description is based on the energy and particle balance equations for nine species: H, H^+, H_2, H_2^+, H_3^+, He, He^+, He^{++} and e^-. It takes into account (1) elementary atomic and molecular collision processes, such as excitation/radiation, ionization, dissociation, recombination, charge exchange, etc. and elastic collisions, (2) particle losses due to the finite dimensions of the plasma volume and confinement properties of the magnetic configuration, and particle recycling, (3) active pumping and gas injection, (4) RF heating of electrons (and protons) and (5) a qualitative description of plasma impurities, as shown in eq. (5.1) and (5.2):

$$\frac{\mathrm{d}n_p}{\mathrm{d}t} = \sum_{j<k}\sum_{i} \epsilon^i_{jkp} k^i_{jk} n_j n_k - \frac{n_p}{\tau_p} + Q_{\mathrm{S},p} - Q_{\mathrm{L},p} \tag{5.1}$$

$$\begin{aligned}\frac{3}{2}\frac{\mathrm{d}\widetilde{n_p T_p}}{\mathrm{d}t} = & \sum_{j<k}\sum_{i} \epsilon^i_{jkp} E^i_{jkp} k^i_{jk} n_j n_k + \sum_{j} E_{jp} k^{\mathrm{el}}_j n_j n_p \\ & - \frac{3}{2}\frac{\widetilde{n_p T_p}}{\tau_{E,p}} + Q_{\mathrm{S}E,p} - Q_{\mathrm{L}E,p} + P_{\mathrm{RF},p}\end{aligned} \tag{5.2}$$

where n_p and T_p are the population density and Maxwellian temperature, k^i_{jk} is the reaction rate for reaction i between particles of population j and k, E^i_{jkp} the corresponding energy change for the involved populations and ϵ^i_{jkp} accounts the number of lost or gained particles for each population, τ_p and $\tau_{E,p}$ are the particle and energy confinement time, $Q_{\mathrm{S},p}$ and $Q_{\mathrm{L},p}$ are external particle sources and losses (gas injection, pumping and particle recycling) with corresponding energy sources $Q_{\mathrm{S}E,p}$ and losses $Q_{\mathrm{L}E,p}$, and finally E_{jp} is the energy transfer from population j to p due to elastic collisions, with k^{el}_j the elastic collision reaction rate. Many efforts have been put in rendering the 0D description of the hydrogen-helium plasmas as complete as possible, so that the major actors of the conditioning plasmas can be uncovered from the modeling.

The implemented balance equations are thoroughly discussed in the following subsections. For the sake of clarity we have chosen, instead of giving the balance equations as a whole, to separate the different terms of the equations and regroup them according to their relevant physical process. In section 5.1.2 the included elementary collisions are listed with in section 5.1.2.3 a description of the included elastic collision processes, in section 5.1.3 the included particle confinement times and edge conditions (particle

recycling) are outlined, in section 5.1.4 the balance equations for active gas throughput during RF discharges are explained, in section 5.1.5 the terms for the coupled RF power are introduced and finally in section 5.1.6 the balance equation adaptations to include impurities are given. Throughout these sections comments will be given on the effect of the different processes on the modeling results. In section 5.2 an overview of modeling results are given, including the comparison with experimental data. And finally, a discussion on the benefits and limitations of the 0D model approach is referred to the appendix: section C.1.

5.1.2 Elementary processes in hydrogen-helium plasmas

In this section all the included atomic and molecular collisions that are relevant for the model are described. For each reaction, a plot of the collision rate can be found in appendix C.2, and the collision rate source, expressed in [cm^3/s], will be given. The implemented inelastic processes are summarized in table 5.1. The model does not treat excited states as separate species, but treats them implicitly. Since cross sections are mostly dependent on the excited state of the involved particle, radiative-collisional (RC) models [135,136] are applied where possible to obtain effective rate coefficients[1]. To obtain these effective rate coefficients the population density of the excited states were calculated for a range of combinations of electron density (n_e) and temperature (T_e), whereafter the cross sections of each excited state are weighted by their population density.

5.1.2.1 Inelastic electron impact reactions

The general formula to determine the reaction rate in electron collisions is given by

$$k \text{ or } \langle \sigma v \rangle = \int f_e(v_e) \sigma(v_e) v_e \, \mathrm{d}v_e \tag{5.3}$$

with v_e the electron velocity, $f_e(v_e)$ the normalized velocity distribution of the electrons and $\sigma(v_e)$ the velocity dependent cross section. Here the ion or neutral 'heavy' particle velocity is neglected with respect to the electron velocity.

Electron collisions with H, H^+ (Table 5.1, 1-3) The effective reaction rates for these collisions are calculated taking into account excited states of the hydrogen atom up to $n = 5$, where n is the principal quantum number.

[1] Atomic and CX processes via dr. O. Marchuk (IPP-Juelich), molecular hydrogen processes via dr. D. Wünderlich (IPP-Garching)

The excitation rate coefficients are based on K-matrix calculations [137] and all the values used were compared with recommended close-coupling calculations [138]. The population of the hydrogen excited states $n = 2$ and $n = 3$ was found less than 0.5% relative to the ground state at the electron density of $10^{12}\,\mathrm{cm}^{-3}$. For this reason only the atomic processes involving the ground state of the hydrogen atom are of major importance for the present analysis.

Electron collisions with H_2, H_2^+ and H_3^+ (Table 5.1, 4-12) For electron collisions with the hydrogen molecule (reaction 5, 6 and 8) effective rate coefficient calculations were effectuated based on the Yacora model [135]. The RC model for molecular hydrogen includes the ground state and electronically excited states up to the principal quantum number $n = 10$. The individual electronic states are resolved up to $n = 3$ (e.g. $\mathrm{d}^3\Pi_\mathrm{u}$). For $n > 3$ this is not the case. The ground state, all states in $n = 2$ and the states $GK\,^1\Sigma_g^+$, $I\,^1\Pi_g$, $e\,^3\Sigma_u^+$ and $d\,^3\Pi_u$ in $n = 3$ are vibrationally resolved. The latter are the upper states of transitions in the visible wavelength range frequently used for diagnostic purposes. For additional reactions the reaction rates are taken from the Hydhel data file [108].

For excitation reaction (4), multiple final states are possible. The reaction rates for the most important reaction paths are given in the Hydhel data file [108] (plot of reaction rates on Fig. C.2). No effective cooling rate for the electrons in collisions with H_2 could be found. Although the different excited states of H_2 are not included explicitly in the model, we include each of these separate reactions in the energy balance since their effect on the energy balance was found to be important. It is realized that this is in principle not consistent because the excited particle remains in the group of H_2 and keeps thus contributing to the energy loss of the electrons via excitation.

The dissociative attachment reaction (formation of negative ions: $\mathrm{e} + \mathrm{H_2} \longrightarrow \mathrm{H^-} + \mathrm{H}$) needs not to be included separately in the model since it is included in the collisional radiative model for H_2 [135], hence the interesting structure for the effective dissociation rate (reaction 5) at $T_\mathrm{vib} = 4500\,\mathrm{K}$ and low electron temperature (Fig. C.3). The dissociative ionization of H_2^+ ($\mathrm{e} + \mathrm{H_2^+} \longrightarrow \mathrm{e} + \mathrm{H^+} + \mathrm{H^+} + e$) is not included since its reaction rate is negligible compared to other $\mathrm{e} + \mathrm{H_2^+}$ reaction paths ($k \ll 10^{-10}\,\mathrm{cm}^3/\mathrm{s}$ for $T_e < 5\,\mathrm{eV}$)

Electron collisions with He, He^+ and He^{++} (Table 5.1, 13-16) The effective reaction rates were obtained from the collisional radiative model NOMAD [136], using the recommended set of atomic data [142]. For He-atoms the singlet and triplet states up to $n = 4$ (19 states) are considered

Table 5.1: Summary of the included elementary inelastic processes in hydrogen-helium plasmas.

		Reaction	Refer.	Fig.
		Electron collisions with H, H^+		
1.)	Excit.	$e + H \longrightarrow e + H^*$	see text	C.1
2.)	Ioniz.	$e + H \longrightarrow e + H^+ + e$	see text	C.1
3.)	Recomb.	$e + H^+ \longrightarrow H + h\nu$	see text	C.1
		Electron collisions with H_2, H_2^+ and H_3^+		
4.)	Excit.	$e + H_2 \longrightarrow e + H_2^*$	[108]	C.2
5.)	Dissoc.	$e + H_2 \longrightarrow e + H + H$	see text	C.3
6.)	Ioniz.	$e + H_2 \longrightarrow e + H_2^+ + e$	see text	C.4
7.)	Dis. ion.	$e + H_2 \longrightarrow e + H^+ + H + e$	[108]	C.6
8.)	Recomb.	$e + H_2^+ \longrightarrow H_2 + h\nu$	see text	C.5
9.)	Dissoc.	$e + H_2^+ \longrightarrow e + H^+ + H$	[108]	C.6
10.)	Dis. rec.	$e + H_2^+ \longrightarrow H + H$	[108]	C.6
11.)	Dis. rec.	$e + H_3^+ \longrightarrow H + H + H$	[108]	
		$e + H_3^+ \longrightarrow H_2 + H$	[108]	C.6
12.)	Dissoc.	$e + H_3^+ \longrightarrow e + H^+ + H + H$	[108]	C.6
		Electron collisions with He, He^+ and He^{2+}		
13.)	Ioniz.	$e + He \longrightarrow e + He^+ + e$	see text	C.7
14.)	Recomb.	$e + He^+ \longrightarrow He + h\nu$	see text	C.7
15.)	Ioniz.	$e + He^+ \longrightarrow e + He^{2+} + e$	see text	C.7
16.)	Recomb.	$e + He^{2+} \longrightarrow He^+ + h\nu$	see text	C.7
		Ion impact reactions		
17.)	Char. ex.	$H^+ + H \longrightarrow H + H^+$	[139]	C.9
18.)	Char. ex.	$H^+ + H_2 \longrightarrow H + H_2^+$	[108]	C.9
19.)	Char. ex.	$H_2^+ + H_2 \longrightarrow H_2 + H_2^+$	[108]	C.9
20.)	Char. ex.	$He^+ + H \longrightarrow He + H^+$	[139]	C.9
21.)	Char. ex.	$He^+ + He \longrightarrow He + He^+$	[108]	C.9
22.)	Char. ex.	$He^{2+} + H \longrightarrow He^+ + H^+$	[140]	C.9
23.)	Char. ex.	$He^{2+} + He \longrightarrow He^+ + He^+$	[141]	C.9
24.)	Char. ex.	$He^{2+} + He \longrightarrow He + He^{2+}$	[108]	C.9
25.)	Form. H_3^+	$H_2^+ + H_2 \longrightarrow H_3^+ + H$	[108]	C.10
26.)	Excit.	$H^+ + H \longrightarrow H^+ + H^*$	[108]	C.10
27.)	Excit.	$H^+ + H_2 \longrightarrow H^+ + H_2^*$	[108]	C.10
28.)	Ioniz.	$H^+ + H \longrightarrow H^+ + H^+ + e$	[108]	C.10
29.)	Ioniz.	$H^+ + He \longrightarrow H^+ + He^+ + e$	[108]	C.10
30.)	Dis. ion.	$He^+ + H_2 \longrightarrow He + H^+ + H$	[108]	C.10

independently and for He^+-ions the calculations are extended up to the first $n = 6$ excited states. Electron energy losses for collisions with He, He^+ (and He^{2+}), including excitation, ionization and recombination, are implemented as cooling rates (Fig. C.8), and are approximately independent on the electron density. From radiative collisional theory, the determination of the correct cooling rate is a difficult matter due to existence of metastable helium states $1s2s3S$ and $1s2s1S$. The data, calculated based on [142], are in agreement with [143] (also given in the figure), at least for electron energies higher than 4 eV. At lower electron energies the data of [143] is about 10 times higher. To avoid rapid full ionization of the plasma at low RF power and so to better match the experimental data, the [143] data was used at lower energies ($T_e < 4$ eV). The cooling rates are implemented in the electron energy balance equation as

$$\dot{E}_e = ... - \Delta E^e_{\mathrm{He}}\, n_e\, n_{\mathrm{He}} - \Delta E^e_{\mathrm{He^+}}\, n_e\, n_{\mathrm{He^+}} - \Delta E^e_{\mathrm{He^{2+}}}\, n_e\, n_{\mathrm{He^{2+}}}. \quad (5.4)$$

The He-excitation and He^+-excitation reactions, leading only to electron energy losses are not numbered separately in table 5.1. Recombination reaction (14) includes both radiative recombination and dielectric recombination.

5.1.2.2 Inelastic ion impact reactions

The included inelastic ion impact reactions are listed in table 5.1 (17-30). The employed general formula to determine the reaction rate in (Maxwellian) particle collisions from the cross section is given by

$$k(T_1, T_2) = \sqrt{\frac{2}{\pi}} \left(\frac{m^*}{kT^*} \right)^{3/2} \int_0^\infty u^3 \sigma(u) e^{-\frac{m^* u^2}{2kT^*}} \mathrm{d}u \quad (5.5)$$

with T_1 and T_2 the Maxwellian temperatures of the interacting particles, $u = |\overrightarrow{v_1} - \overrightarrow{v_2}|$ is the impact velocity and $\sigma(u)$ the velocity dependent cross section [144]. All reaction rates are calculated using the reduced energy T^* and mass m^* of the system defined as

$$T^* = \frac{T_1 m_2 + T_2 m_1}{m_1 + m_2} \quad m^* = \frac{m_1 m_2}{m_1 + m_2}. \quad (5.6)$$

Differences in ionization potential between the colliding particles, e.g. H and He^+, have influence on the cross section of the reaction, which is implicitly taken into account in the calculation of the effective reaction rate. These differences are assumed not to interfere with the kinetic energy balance of the involved particles: the excited states of the particles are not considered as separate species in this model and also the electrons are not involved in most of the following reactions.

Inelastic collisions between ions, for example the charge exchange reaction $H^+ + He^+ \longrightarrow H + He^{++}$, can be neglected because of the repulsive coulomb force. Charge exchange reactions that have no effect on particle balances (reactions 17, 19, 21 and 24) are included since they are important for temperature equalization between ions and atoms or molecules.

Reactions (25-30) give only minor corrections to the final particle densities and temperatures and therefore can be switched off in the model calculation. The cross sections for these reactions are taken from the Hydhel data file [108]. The ionization on proton impact reactions (reaction 28 and 29) are included in this document to show that they can safely be neglected in the model for reduced temperatures below 100 eV. For the excitation on proton impact reaction (26), only excitation from the ground state is considered. The reaction rate is negligible for reduced temperatures of $T^* < 100\,\text{eV}$. The reaction rate for excitation reaction (27) is considerably high at lower reduced temperatures $T^* \approx 1\,\text{eV}$ (see Fig. C.10). The energy loss in each collision is however limited ($\approx 0.1\,\text{eV}$).

5.1.2.3 Elastic processes

Elastic collisions have a direct effect on the energy balance of the involved particles. Indirectly also the particle densities will be affected due to the energy dependent reaction rate coefficients. Since we require the model to predict the temperature and density of the plasma species in a self consistent manner, both the elastic Coulomb collisions between the charged particles and elastic neutral-neutral and ion-neutral collisions are included.

Coulomb collisions Energy transfers through Coulomb collisions between the charged particles are based on the derivation of Sivukhin [145]. Here the 'binary-collision' approximation is used in which the many body interaction between plasma particles is reduced to an isolated and instantaneous interaction between a pair of plasma particles. For the interaction potential a Coulomb potential is used which is cut off at the Debye radius to account for the shielding of the localized charge by the plasma as a whole. The latter also allows to tackle divergences that appear in the calculations for the mean energy exchange rate, and can be found in the equations below as the Coulomb logarithm λ. In the book of Sivukhin first the mean energy transfer per unit of time from one particle of a first group to all the particles of a second particle group, having a Maxwellian energy distribution, is considered. Secondly this energy transfer is averaged over the Maxwellian energy distribution of the first group. The resulting averaged energy transfer Q_c^{12} from population 1 to 2 is proportional to the difference of the Maxwellian temperatures of the two groups and the Coulomb collision

frequency ν_{12}. It is implemented into the energy balance as:

$$\dot{E}_1 = ... - Q_c^{12} = ... - 3/2(T_1 - T_2)\nu_{12} n_1 \tag{5.7}$$

with n_1 and T_1 the particle density and temperature of the first group. The collision frequency (eq. 5.8) depends on the particle density of the second group n_2, the temperature T and mass m of the involved particles, and the Coulomb logarithm (eq. 5.9):

$$\nu_{12} = n_2 \frac{8}{3} \sqrt{2\pi}\, q^4 Z_1^2 Z_2^2 \frac{\lambda_{12}}{m_1\, m_2\, (T_1/m_1 + T_2/m_2)^{1.5}} \tag{5.8}$$

with q, m and T in Gaussian units;

$$\lambda_{12} = 23 - \log\left[\frac{Z_1 Z_2 (m_1 + m_2)}{m_1\, T_2 + m_2\, T_1}\left(\frac{Z_1^2 n_1}{T_1} + \frac{Z_2^2 n_2}{T_2}\right)^{0.5}\right] \tag{5.9}$$

with Z the particle charge. For electrons the Coulomb logarithm simplifies to

$$\lambda_{e2} = \begin{cases} 23 - \log(\sqrt{n_e}\, Z\, T_e^{-3/2}) & \text{if } T_e < 10\, Z^2\, \text{eV} \\ 24 - \log(\sqrt{n_e}\, T_e^{-1}) & \text{otherwise.} \end{cases} \tag{5.10}$$

and the collision frequency to

$$\nu_{e2} = n_2 \frac{8}{3} \sqrt{2\pi}\, q^4 Z_2^2 \frac{\sqrt{m_e}\lambda_{e2}}{m_2\, T_2^{1.5}} \tag{5.11}$$

The equivalent reaction rates, obtained by dividing the collision frequency by n_2 is given for electron-ion collisions on Fig. C.11 and for ion-ion collisions on Fig. C.12.

Elastic ion-neutral and neutral-neutral collisions The relevancy of elastic ion-neutral and neutral-neutral collisions was already shown for fusion edge plasmas for temperatures below 10 eV [146–148], and can be illustrated by comparing elastic collisions with their mutually related charge exchange collisions. The relation between the cross section for momentum transfer via elastic collisions σ_{mt} and charge exchange reactions σ_{cx} in homonuclear systems for the low energy region is approximately given by $\sigma_{\text{mt}} = 2.21\sigma_{\text{cx}}$ [149]. (The comparison of the energy dependent reaction rate figures for momentum transfer collisions (Fig. C.12) and charge exchange collisions (Fig. C.9) leads to the same conclusion.) The reaction rates for elastic collisions are obtained via eq. (5.5), using cross sections from [150–152].

The determination of the average energy transfer in ion-neutral and neutral-neutral elastic collisions is a difficult matter. It depends on the

interaction potential between the particles for which no simple general formula can be defined that is valid for all the elastic collisions that we need to consider in the model. In the references mentioned above multiple cross sections are listed for each reaction: the elastic (or total) cross section Q^{el}, the momentum transfer (diffusion) cross section Q^{mt} and the viscosity cross section Q^{vis}:

$$Q^{\mathrm{el}} = 2\pi \int_0^{\pi} \frac{\partial \sigma^{\mathrm{el}}}{\partial \Omega} \sin(\theta) \mathrm{d}\Omega \tag{5.12}$$

$$Q^{\mathrm{mt}} = 2\pi \int_0^{\pi} (1 - \cos(\theta)) \frac{\partial \sigma^{\mathrm{el}}}{\partial \Omega} \sin(\theta) \mathrm{d}\Omega \tag{5.13}$$

$$Q^{\mathrm{vis}} = 2\pi \int_0^{\pi} (1 - \cos^2(\theta)) \frac{\partial \sigma^{\mathrm{el}}}{\partial \Omega} \sin(\theta) \mathrm{d}\Omega \tag{5.14}$$

where θ is the scattering angle, Ω the solid angle and $\partial\sigma^{\mathrm{el}}/\partial\Omega$ the differential elastic cross section. Not to overestimate the importance of elastic collisions, we decided for our model to use the momentum transfer cross section. This cross section is weighted by a factor $(1 - \cos(\theta))$ which accounts for the fact that when the incident particle is deflected only by a small angle, the momentum transfer is small, if the deflection is large, the momentum transfer is large as well. The resulting cross section is generally smaller than the total cross section. The averaged energy transfer from group 1 to 2, Q_c^{12}, is taken similarly as for Coulomb collisions proportional to the difference of the Maxwellian temperatures of the two groups, and is thus implemented into the energy balance as eq. (5.7).

The implemented collisions are given below. Their collision rates are plotted in Fig. C.13 as a function of the reduced temperature. Elastic collisions between He and H_2 are presently not included in the model.

31.) H^++H [150]: For elastic collisions between ${H_2}^+$+H, ${H_3}^+$+H and He^++H we assume a similar interaction potential and thus approximately equal cross section.

32.) H^++H_2 [150]: The cross sections for elastic collisions between ${H_2}^+$+H_2 [152] and ${H_3}^+ + H_2$ [150,152] are approximately equal to the cross section of this reaction (within the error bar). In the model the same cross section is used for these three reactions. Also for the reaction $He^+ + H_2$ we assume a similar interaction potential and thus an approximately equal cross section.

33.) $H^+ + He$ and $He^+ + He$ [151]

34.) $H + H_2$ [150]

35.) H + He: The cross section for this reaction is an average total cross section for elastic collisions given in [150]. The momentum transfer cross section could not be found.

5.1.3 Particle residence times and edge conditions

5.1.3.1 Neutral wall fluxes

To estimate the flux of neutrals (H, H_2, He) striking the walls, their mean free path, thermal velocity and approximate average distance the particles need to travel to reach the walls of the toroidal chamber, are required. For the latter we take an approximate distance of 2 times the minor radius a, accounting for the fact that for all lines of sight that have a toroidal component the average distance is larger than a. The mean free path λ_n of neutral particle 'n' is defined as

$$\lambda_n = v_{T,n} / \sum_{ij} k^i_{jn}\, n_j \tag{5.15}$$

where $v_{T,n} = \sqrt{\frac{k_b T_n(\mathrm{K})}{m_n}} = \sqrt{\frac{e T_n(\mathrm{eV})}{m_n}}$ is the thermal velocity and the sum goes over the different species j in the plasma and over the possible reactions i between neutral n and particle j. The wall flux, or neutral particle loss term, is then estimated by defining their effective confinement time

$$\tau_n = \frac{2a}{v_{T,n}} e^{2a/\lambda_n} \tag{5.16}$$

which is in the 0D approach weighted by the probability that the particles will travel a distance of $2a$ without undergoing a collision (e^{-2a/λ_n}).

The general expressions for the particle and energy balance are

$$\frac{\mathrm{d}n_n}{\mathrm{d}t} = ... - \frac{n_n}{\tau_n} \tag{5.17}$$

$$\frac{\mathrm{d}E_n}{\mathrm{d}t} = ... - \frac{E_n}{\tau_n} \tag{5.18}$$

where we thus consider that the particle confinement time equals the energy confinement time (see appendix C.3).

5.1.3.2 Ion wall fluxes

The ion wall fluxes are constrained by the magnetic field and were thoroughly discussed in chapter 3. The charged particle loss mechanisms are summarized in the following general formula for the ion confinement time:

$$\tau_p = \frac{a}{(v_{Dz,p} + v_{DR,p} + v_{\mathrm{Bohm},p}) e^{-a/\lambda_p} + v_{T,p} B_z / B_\phi e^{-a B_\phi / B_z \lambda_p}} \tag{5.19}$$

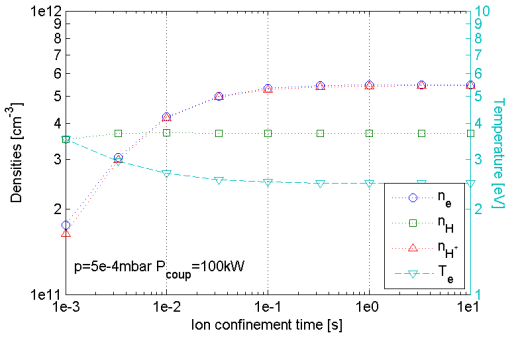

Figure 5.1: Modeled influence of the ion confinement time on plasma parameters for a partially ionized TEXTOR H_2-RF discharge with $p_{H_2} = 5 \cdot 10^{-4}$ mbar and $P_{RF} = 100$ kW. Above confinement times of 0.01 s the influence on the plasma density is minor. Typical confinement times are ~ 0.1 s for 3 eV ions.

where a is the minor radius, B_ϕ and B_z the toroidal and vertical field, λ_p the mean free path of the ion, $v_{Dz,p}$ is the '$\vec{B} \times \nabla B$' drift velocity, $v_{DR,p}$ is the radial outward '$\vec{E} \times \vec{B}$' drift velocity, $v_{\mathrm{Bohm},p}$ is the cross field diffusion velocity and $v_{T,p}$ the thermal velocity. The expressions for the energy and particle balances are similar as those for the neutrals.

Fig. 5.1 shows the modeled influence of the ion confinement time on TEXTOR plasma parameters. Both the density and temperature are plotted for the electrons, H^+-ions and H-atoms in a H_2-RF discharge with $p_{H_2} = 5 \cdot 10^{-4}$ mbar and $P_{RF} = 100$ kW. It is found that ion confinement times above 0.1 s have a minor influence on the plasma parameters. For smaller confinement times, the electron density will start to decrease leading, in this example, to a 3 times lower electron density in case of $\tau_p = 1$ ms. At the same time the electron temperature will increase. The typical values for vertical drifts and Bohm diffusion found in chapter 3 make that for partially ionized plasmas, the ion confinement time has only a minor influence on the plasma parameters. However in the plasma edge, the confinement time is very low due to the unrestricted charged particles transport along the (limited) magnetic field lines, which might explain the high electron temperatures measured in the TEXTOR RF plasma edge by Langmuir probes (Fig. 3.17).

5.1.3.3 Electron losses

In the model the electron losses are set to account for charge neutrality in the plasma. It is sometimes argued that electrons lose their energy faster than ions. To account for this, one should include an energy confinement

time that is smaller than the particle confinement time: $\tau_{p,e} \approx \chi \tau_{E,e}$, with $\chi > 1$. In the model we use $\chi = 3$ based on [84, 91, 153]. When the neutral gas is partially ionized, e.g. 20%, a change of χ from 1 to 3 decreases the plasma density only by 0.5%.

$$\dot{n}_e = ... - \frac{n_{H^+}}{\tau_{H^+}} - \frac{n_{H_2^+}}{\tau_{H_2^+}} - \frac{n_{H_3^+}}{\tau_{H_3^+}} - \frac{n_{He^+}}{\tau_{He^+}} - 2\frac{n_{He^{2+}}}{\tau_{He^{2+}}} \quad (5.20)$$

$$\dot{E}_e = ... - \chi \frac{3}{2} T_e \left(\frac{n_{H^+}}{\tau_{H^+}} + \frac{n_{H_2^+}}{\tau_{H_2^+}} + \frac{n_{H_3^+}}{\tau_{H_3^+}} + \frac{n_{He^+}}{\tau_{He^+}} + 2\frac{n_{He^{2+}}}{\tau_{He^{2+}}} \right) \quad (5.21)$$

5.1.3.4 Particle recycling

Neutrals, not affected by the magnetic field will be in constant interaction with the vessel walls. Also charged particles, due to their collective drifts, diffusion across the magnetic field, and transport along the field lines will interact with the walls. To describe the wall interaction in the model, the exchange of particles between wall and plasma is represented by the recycling coefficient R. From analysis of TEXTOR and TORE SUPRA mass spectroscopy data it is found that particle recycling in ICWC plasmas can be up to $R \geq 0.99$ (see section 4.1.3 [154]). The recycling in the model is assumed to be immediate. The particles that leave the plasma will be immediately re-injected into the plasma (weighted by recycling coefficient R). To properly add particle recycling in the balance equations the main PSI mechanisms have been considered. To ensure clear interpretations of the modeling results it was decided to simplify these source terms as much as possible:

1. In an ICWC plasma the high recycling comes partly from reflection of impinging particles. The reflection probability depends on the type of particle, its energy and incident angle, and the target material. An extensive overview of these dependencies is tabulated in [122]. A selection is given in tables 5.2-5.5, with R_N and R_E respectively the particle and energy reflection coefficient.

Table 5.2: Particle and energy reflection coefficient of H backscattered from C

E_0		0°	85°
10	R_N	0.48	0.97
eV	R_E	0.24	0.84
100	R_N	0.28	0.99
eV	R_E	0.12	0.94

Table 5.3: Particle and energy reflection coefficient of He backscattered from C

E_0		0°	85°
10	R_N	0.41	1.0
eV	R_E	0.95	0.96
100	R_N	0.15	1.0
eV	R_E	0.33	0.98

Table 5.4: Particle and energy reflection coefficient of H backscattered from W

E_0		0°	85°
10	R_N	0.76	0.98
eV	R_E	0.56	0.92
100	R_N	0.63	0.99
eV	R_E	0.41	0.97

Table 5.5: Particle and energy reflection coefficient of He backscattered from W

E_0		0°	85°
10	R_N	0.81	1.0
eV	R_E	0.60	0.99
100	R_N	0.64	1.0
eV	R_E	0.41	0.99

2. The wall surfaces in a tokamak contain large amounts of hydrogen. On high hydrogen concentrations, the formation of neutral molecules by the collision of low energy (plasma) hydrogen neutrals or ions with hydrogen atoms weakly bounded on the wall surface can become dominant as explained by Rutigliano [155]. The recombination probability is especially high for incident particles with energies between 0.05 and 1.5 eV (60% at 500 K on graphite), and increases on decreasing wall temperature. The geometrical probability for picking up a particle is not negligible; for a homogeneous hydrogen atom wall flux of $\Phi = 10^{20}\,\mathrm{H/m^2s}$ ($r_H \approx 0.1\,\mathrm{nm}$) the whole wall area can be touched by the impinging particles every $1/(\Phi\pi r_H^2) = 0.3\,\mathrm{s}$.

3. A third part of the recycling flux comes from the release of stored hydrogen. Unlike reflection, desorption occurs with a time delay with respect to the particle impact. This time delay is determined by for example the penetration depth of the particle, the wall diffusion coefficient and bulk or surface recombination coefficient [38]. From the wall reservoir model (see chapter 6) we will learn that the characteristic time for particle release is of the order of $1 - 3\,\mathrm{s}$. This characteristic time is not included in the balance equations of the model. All particles that are absorbed by the wall are in the model immediately released again as a neutral molecules (H_2), or atoms (He). The energy of these released neutral particles part will generally have a Maxwell-Boltzmann velocity distribution determined by the temperature of the wall materials [156].

The above considerations led to the determination of the implemented edge conditions. In the balance equations for neutral He and H_2 (T_{He}, $T_{\mathrm{H_2}} < 10\,\mathrm{eV}$), the particle and energy reflection coefficient are set equal to one, in close agreement with [122, 156]. (An energy reflection coefficient smaller than one will lower the final gas temperature and set a minor variation in the final plasma density.) Hydrogen atoms and ions in interaction with the

wall either pick up a bounded H-atom on the wall surface to form directly H_2 [155], or either penetrate into the wall to be desorbed later as H_2. Also the helium ions are neutralized by the wall and released with an energy equal to the wall temperature. The ions H_2^+ and H_3^+, having generally very low densities, are recycled as H_2. The implemented edge conditions appear as source terms in particle ($Q_{S,p}$, eq. (5.1)) and energy ($Q_{SE,p}$, eq. (5.2)) balance. The implemented source terms can be summarized by following equations:

$$\dot{n}_{H_2} = ... + R_{H_2}\left(\frac{1}{2}\frac{n_H}{\tau_H} + \frac{1}{2}\frac{n_{H^+}}{\tau_{H^+}} + \frac{n_{H_2^+}}{\tau_{H_2^+}} + \frac{3}{2}\frac{n_{H_3^+}}{\tau_{H_3^+}}\right) \quad (5.22)$$

$$\dot{E}_{H_2} = ... + R_{H_2}\frac{3}{2}T_{wall}\left(\frac{1}{2}\frac{n_H}{\tau_H} + \frac{1}{2}\frac{n_{H^+}}{\tau_{H^+}} + \frac{n_{H_2^+}}{\tau_{H_2^+}} + \frac{3}{2}\frac{n_{H_3^+}}{\tau_{H_3^+}}\right) \quad (5.23)$$

$$\dot{n}_{He} = ... + R_{He}\left(\frac{n_{He^+}}{\tau_{He^+}} + \frac{n_{He^{2+}}}{\tau_{He^{2+}}}\right) \quad (5.24)$$

$$\dot{E}_{He} = ... + R_{He}\frac{3}{2}T_{wall}\left(\frac{n_{He^+}}{\tau_{He^+}} + \frac{n_{He^{2+}}}{\tau_{He^{2+}}}\right) \quad (5.25)$$

5.1.4 Gas injection and active pumping

For the injection of gas into the vessel we distinguish two regimes: feedback and feed forward gas injection. Both regimes can be studied in the frame of the 0D model. In feedback gas injection, the injection is regulated to keep the total pressure in the vessel constant. A pressure drop due to ionization will be compensated by extra injection of gas. Similarly, losses to wall ($R < 1$) will also be compensated by extra injection and, when the wall has a net release rate, the gas injection rate will be lowered. In the feed forward gas injection scheme, the injection rate is pre-programmed. In this regime, in the absence of a plasma, the removal rate by the pumps will be equal to the injection rate. Due to the pressure drop by ionization, the removal rate by the pumps ($\propto pS$) will be lower. This effect, combined with the constant injection will give rise to an accumulation of particles in the vessel. Eventual losses to the walls will not be compensated by extra gas injection.

The model includes both the feed forward and feedback gas injection option, and can be ran with or without active gas throughput. Terms for the removal rate of particles by the pumps and the injection rate appear in the particle balance as (Q_S and Q_L in eq. (5.1))

$$\dot{n}_{H_2} = ... + Q_{H_2,valve} - n_{H_2}S_{H_2}/V_{pl} \quad (5.26)$$

$$\dot{n}_{He} = ... + Q_{He,valve} - n_{He}S_{He}/V_{pl} \quad (5.27)$$

with Q_{valve} the gas injection rate [$\mathrm{cm^{-3}s^{-1}}$], S the pumping speed [$\mathrm{cm^3s^{-1}}$] and V_{pl} the vessel volume [$\mathrm{cm^3}$]. In feedback regime the source term Q_{valve} is changed proportional to the difference between set value and actual pressure. A gain factor is included representing the response time of the feedback control, τ_r.

$$Q_{\mathrm{H_2,valve}}(t) = \frac{n_{\mathrm{H_2,set}} - n_{\mathrm{H_2}}(t)}{\tau_r} \tag{5.28}$$

The same terms come back in the energy balance, included in $Q_{SE,p}$ and $Q_{\mathrm{L}E,p}$ in eq. (5.2):

$$\dot{E}_{\mathrm{H_2}} = ... + 3/2 Q_{\mathrm{H_2,valve}} T_{\mathrm{H_2,valve}} - E_{\mathrm{H_2}} S_{\mathrm{H_2}}/V_{\mathrm{pl}} \tag{5.29}$$

$$\dot{E}_{\mathrm{He}} = ... + 3/2 Q_{\mathrm{He,valve}} T_{\mathrm{He,valve}} - E_{\mathrm{He}} S_{\mathrm{He}}/V_{\mathrm{pl}} \tag{5.30}$$

where T_{valve} is the temperature of the injected gas [eV].

5.1.5 Coupled power

5.1.5.1 RF power coupling

TOMCAT simulations show that the RF power coupled from the ICRF antenna to the RF plasma is absorbed mainly collisionally by electrons (typically $x \approx 75 - 90\%$) [157]. Most of the remaining fraction $(1 - x)$ is coupled to ions by collisional absorption. The electrons, accelerated by the parallel electric RF field, absorb RF power either due to collisional damping (collisions with neutrals and ions), which is the typical damping mechanism in low T_e ICWC plasmas, or due to collision-free Landau damping which is less probable but still a possible damping mechanism, especially in warm (several tens eV) ICWC plasmas like in JET [127]. Non-resonant ions absorb energy mostly non-directly via collisions with the electrons. Resonant ions absorb energy directly from the RF field due to cyclotron absorption (collision free damping). The coupling of RF power P_{RF} is included in the model by adding a coupled power density $P_{\mathrm{RF}}/V_{\mathrm{pl}}$ to the energy balance equations of the electrons ($xP_{\mathrm{RF}}/V_{\mathrm{pl}}$) and protons ($(1-x)P_{\mathrm{RF}}/V_{\mathrm{pl}}$):

$$\frac{\mathrm{d}E_e}{\mathrm{d}t} = ... + x\frac{P_{\mathrm{RF}}}{V_{\mathrm{pl}}} \tag{5.31}$$

$$\frac{\mathrm{d}E_{\mathrm{H^+}}}{\mathrm{d}t} = ... + (1-x)\frac{P_{\mathrm{RF}}}{V_{\mathrm{pl}}} \tag{5.32}$$

where P_{RF} is the power coupled to the plasma, x is the fraction of this power which is coupled to the electrons and V_{pl} is the plasma volume.

Fig. 5.2 shows modeled plasma densities and Maxwellian energies for a TORE SUPRA hydrogen ICWC plasma, $p_{\mathrm{H_2}} = 5 \cdot 10^{-4}$ mbar and $P_{\mathrm{RF}} =$

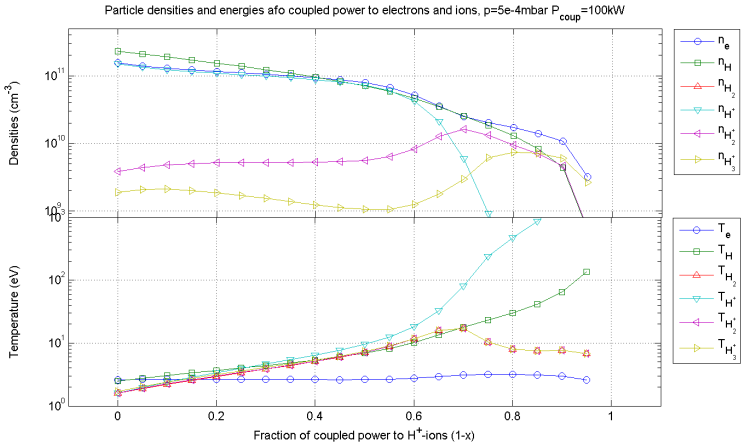

Figure 5.2: Modeled plasma densities (top) and Maxwellian energies (bottom) for a TORE SUPRA hydrogen ICWC plasma, $p_{\mathrm{H_2}} = 5 \cdot 10^{-4}$ mbar, $B_T = 3.8\,\mathrm{T}$ and $P_{\mathrm{RF}} = 100\,\mathrm{kW}$. The electron density decreases when the fraction of coupled power to the electron decreases while the ion temperature increases.

100 kW. The figure shows clearly that the electron density decreases when the fraction of coupled power to the electron decreases. This can be understood from the fact that electron impact ionization reactions are much more efficient than ionization on proton impact. Likewise the generally lower collisionality of the ions allow them to reach Maxwellian temperatures higher than 10 eV on increasing coupled power fraction ($1 - x > 0.5$). Higher ion energies might increase the wall conditioning efficiency of RF discharges. In the present understanding of ICWC discharges it is stated that most of the ICRF power is coupled to the electrons. In further modeling results we assumed $x = 1$.

5.1.5.2 Breakdown phase and α-scaling

Before plasma breakdown, electrons will move quasi freely around the torus, accelerated and decelerated by the antenna electric field. The RF-power that is coupled in this situation is proportional to the electron density. After a certain degree of ionization the maximum RF power will be coupled. To simulate plasma breakdown with the 0D model the coupled power is likewise set proportional to the electron density in the initial plasma phase. The nominal RF power will only be partially coupled when the electron density is low compared to the neutral density. For this the α-scaling, previously adopted by Moiseensko [132] and successfully used in the 0D model version

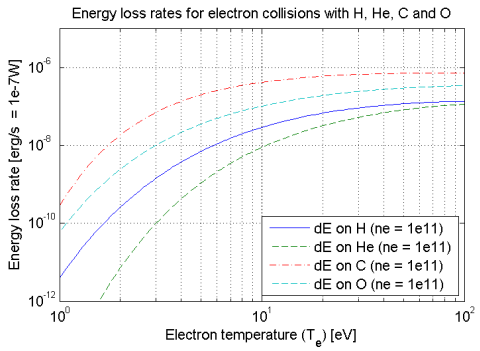

Figure 5.3: Total electron cooling rate for electron collisions with H, He, C and O as a function of the electron temperature, T_e ([143] = [INDC1995])

for atomic hydrogen [91, 95], was expanded for hydrogen-helium plasmas:

$$P_{\mathrm{RF,coup}} = \begin{cases} P_{\mathrm{RF,max}} f_\alpha/\alpha & \text{if } f_\alpha < \alpha \\ P_{\mathrm{RF,max}} & \text{if } f_\alpha \geq \alpha \end{cases}, \tag{5.33}$$

$$\text{where } f_\alpha = \frac{n_e}{n_e + n_{\mathrm{H}} + n_{\mathrm{H_2}} + n_{\mathrm{He}}}.$$

Above a degree of ionization represented by α, the total RF power will be coupled.

To compare modeled breakdown times with experimental data it is important to define the breakdown moment mathematically. Several hypothesis exist [158]: it is considered that the transition from single ionization event to an avalanche (gas breakdown moment) is related to strongly developed electron-ion collisions. Therefore the following definitions for gas breakdown are formulated as the moment when (1) the electron energy losses between ionization reactions and electron-ion collisions become equal or (2) when the frequencies for these reactions become equal. In case of the simulation shown at the end of this chapter (Fig. 5.14), both definitions result in the same breakdown time.

5.1.6 Impurities

Impurities in wall conditioning plasmas, either liberated by plasma wall interactions or from background neutral pressure in the vacuum vessel, strongly affect the plasma parameters. Fig. 5.3 shows electron cooling rates on neutral hydrogen, helium, carbon and oxygen as a function of the electron temperature, for a plasma with an electron density of $n_e = 10^{11}\,\mathrm{cm}^{-3}$, illustrating the importance of impurities. To obtain the actual energy loss

per unit density one has to multiply with the density of the involved atom. The electron cooling rate on carbon is two orders of magnitude higher than that of hydrogen, and almost three orders of magnitude than that of helium. The contributions of hydrogen and carbon to the total electron cooling in a low temperature hydrogen plasma ($< 10\,\mathrm{eV}$) with 1% carbon impurities are thus of the same order of magnitude. In conditioning plasmas on machines with carbon facing components one expects mainly hydrocarbons, carbonoxides, and water as impurities. Not only neutral impurities play a role, also their ions. Table 5.6 gives ionization potentials of H_2O, CH_4 and CO in comparison with the ionization potentials of H, H_2 and He, illustrating that also the presence of impurity ions in hydrogen-helium wall conditioning plasmas can not be neglected.

Table 5.6: Ionization potentials for relevant hydrogen-helium wall conditioning plasma species [159].

C	H_2O	H	O
11.26 eV	12.61 eV	13.60 eV	13.62 eV
CO	CH_4	H_2	He
14.01 eV	14.25 eV	15.37 eV	24.59 eV

A proper consideration of the plasma impurities requires including particle and energy balance equations, containing elementary collisions, elastic collisions, particle residence times, edge conditions and pumping of neutral molecules, for all the relevant impurity species and their ions. To enable a qualitative analysis on the effect of impurities, the 0D model includes three extra particle balance equations, one for atomic carbon and two for its ionized states C^+ and C^{2+}. The energy balance for the carbon species is not included. The electron energy balance is completed with cooling rates including excitation, ionization and recombination of carbon atoms and ions, in the same manner as was done for helium (eq. 5.4). Fig. C.14 shows the implemented electron cooling rates on carbon atoms and ions, obtained from [143]. Also electron-ion Coulomb collisions are included in the electron energy balance equation. The electron particle balance is completed with carbon ionization reactions, that contribute to the electron density. Fig. C.15 shows the implemented electron impact ionization rates for C and C^+, obtained from [151]. The actual production rate for carbon ions is however estimated to be lower than the given atomic carbon ionization rate. In the initial plasma phase, carbon will not be present as atoms, but rather as molecules due to its chemical reactiveness. For this same reason the electron cooling rate is estimated to be higher due to the existence of numerous molecular excitational states and to molecule dissociation energies. Finally,

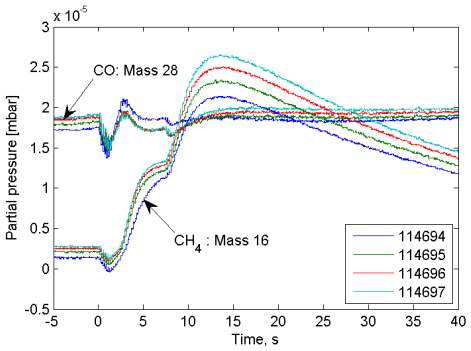

Figure 5.4: CO and CH_4 partial pressures from mass spectrometry for 4 subsequent H_2-ICWC discharges (RF pulse from 2 to 7 s) in TEXTOR with feedback hydrogen pressure of $p_{H_2} = 5 \cdot 10^{-4}$ mbar and $P_{RF} \sim 60$ kW.

the impurity ion confinement time is set to a constant value in accordance with [85].

Modeling results show indeed that even small amounts of impurities can have a large influence on the final electron density. For example a carbon impurity content of 1% of the total hydrogen pressure in a TEXTOR discharge of $p_{H_2} = 5 \cdot 10^{-4}$ mbar and $P_{RF} = 100$ kW (Fig. 5.2, $x = 1$) decreases the final electron density at least by a factor 2. Impurity contents of 1% are easily obtainable on TEXTOR. Fig. 5.4 shows CO and CH_4 partial pressures for four subsequent H_2-ICWC discharges in TEXTOR with feedback hydrogen pressure of $p_{H_2} = 5 \cdot 10^{-4}$ mbar and $P_{RF} \sim 60$ kW. According to the mass spectrometry data, and in accordance to baratron pressure data, there is a background CO pressure of approximately 4% of the feedback pressure. During the RF discharge (RF discharge initiation at 2 s, discharge ending at 7 s) the CH_4 partial pressure increases to approximately 2% of the feedback pressure. To be able to reproduce RF plasma parameters the plasma impurity content has to be known and their elementary collisions have to be accurately described in the balance equations. Unfortunately it is often difficult to estimate the exact impurity content and even the elementary collision data of molecules such as H_2O, CH_4 and CO is scarce. Nevertheless in the next section on modeling results we will show that the 0D model with carbon impurities is able to reproduce, at least qualitatively, the experimental data.

It is important to mention that ITER will not be a carbon machine.

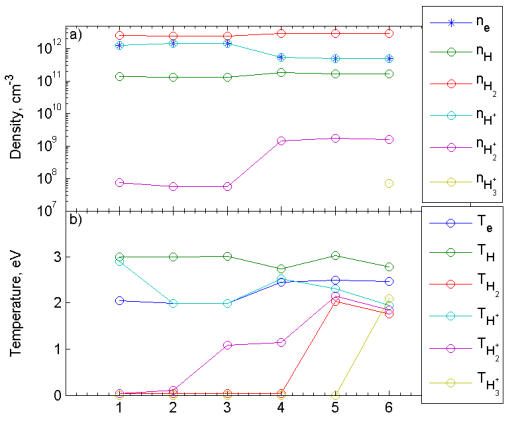

Figure 5.5: Plasma parameters as a function of elementary collisions: a) densities, b) temperatures; 1) electron collisions only, 2) + electron-ion Coulomb collisions, 3) + ion-ion Coulomb collisions, 4) + charge exchange, 5) + elastic collisions, 6) + additional heavy particle collisions.

5.2 Modeling results

5.2.1 Discussion on elementary reactions

Here we illustrate for a typical TORE SUPRA hydrogen ICWC plasma ($P_{\mathrm{RF}} = 100\,\mathrm{kW}$, $B_T = 3.8\,\mathrm{T}$, $B_V = 0\,\mathrm{T}$, $p_{\mathrm{H_2}} = 1.8 \cdot 10^{-4}\,\mathrm{mbar}$, $x = 1$) the influence on the plasma parameters of the different groups of particle collisions. The code was run six times with the same input values, while adding on each run an elementary collision group:

1. Only electron impact reactions
2. + electron-ion Coulomb collisions
3. + ion-ion Coulomb collisions
4. + charge exchange
5. + elastic ion-neutral and neutral-neutral collisions
6. + additional heavy particle collisions

The summary of the plasma parameters is given in Fig. 5.5. In case only electron collisions are considered (1) the equilibrium electron temperature is $\sim 2\,\mathrm{eV}$, the H-atom temperature is $3\,\mathrm{eV}$ as a result of the average energy

obtained on the dissociation of H_2 [160], the H^+-ion temperature is approximately equal to T_H due to the ionization of the atoms. All other particles will have the background energy (0.035-0.1 eV) since no energy transport to them is included in the first calculation. For this same reason the ionization degree is quite high (32%) since all the coupled RF power can be used for excitation and ionization on electron impact.

On inclusion of electron-ion coulomb collisions (2) it is clear that the H^+-ions have transferred their excess energy to the electrons leading to energy equalization. The extra electron energy results in a slightly higher ionization degree (n_e increases by 15%).

On inclusion of ion-ion coulomb collisions (3) the H_2^+-ions gain energy. H_2^+-ions have short lifetimes which makes that the energy equalization is not complete. The transfer of energy to the H_2^+-ions does not change the final electron density or temperature much, due to their small concentration.

On inclusion of charge exchange reactions (4) we see that the neutral H-atom and H^+-ion temperature approach each other. The higher ion temperature (T_{H^+}) increases simultaneously the electron temperature via Coulomb collisions. The concentration of H_2^+-ions increases significantly due to the charge exchange reaction of H^+ and H_2, of which the reaction rate at the involved temperatures is higher than that of the ionization of H_2 and H, and approximately equal to the dissociation of H_2. This charge exchange reaction has as additional consequence that the ionization degree is clearly lower: the formation of H^+-ions by ionization on electron impact, and the loss of H^+-ions via charge exchange with H_2-molecules are strongly competing processes. The formed H_2^+ ions have as most important reaction dissociation into H^+ and H, which will happen almost instantly due to its high reaction rate. Whereas in result (3) the H^+-ion could be considered as a final state, on inclusion of CX reactions, a H^+ ion will very likely produce two H-atoms and one other H^+-ion in the subsequent CX reaction with H_2 and dissociation of H_2^+. As a result, which can be seen in the graph, the neutral H density increases slightly. Finally, since neutral atoms have smaller confinement times than ions, and as they will recombine to molecules at the vessel walls, the concentration of H_2 increases also.

On inclusion of elastic ion-neutral and neutral-neutral collisions (5) we see that all particle energies approach each other. Since we set the wall energy reflection coefficient of H_2 equal to one, the molecules are able to obtain energy in elastic collisions with H-atoms and H^+-ions. In turn also the H_2^+-ions obtain extra kinetic energy, either directly by elastic collisions, or as a consequent of CX or ionization reactions. The energy changes make the ionization degree decrease by 15%.

On inclusion of additional heavy particle collisions (6) we see as major change the presence of H_3^+-ions which are created by collision of H_2^+ and H_2.

5.2.2 Plasma characteristics as a function of the electron temperature

Plots of plasma parameters as a function of the electron temperature are especially interesting since they allow to understand, independently of the pressure and input power, the role of the electron temperature. In an equilibrium situation for pure gases, the plasma parameters can be brought back to the electron temperature. In case of gas mixtures, there will be a clear influence of the mixture on the plasma parameters, especially in the temperature range where the plasma is partially ionized. Below we will discuss ion fraction data for a pure hydrogen plasma, a pure helium plasma, and a 50/50 H_2/He plasma. The analysis is done for a perfectly confined plasma ($\tau_{\text{ion}} = 1000\,\text{s}$).

5.2.2.1 Pure hydrogen plasma

Fig. 5.6 (left, full lines) gives the hydrogen ion fractions as a function of the electron temperature. To obtain sufficient ionization, the electron temperature needs to be above 2 eV. The transition from no ionization to full ionization happens completely in the electron temperature range of 2 to 2.8 eV. Steady state electron temperatures between these values can keep partially ionized plasmas. The presence of H_2^+ and H_3^+ is important below 2.7 eV. In this example considering a perfectly confined plasma the H_3^+ density is almost equal to the electron density. In partially ionized plasmas the presence of H atoms is significant ($\sim 10\%$ of n_e). In fully ionized plasmas, the presence of H atoms is more important than H_2 molecules, and both their concentrations decrease on increasing electron energy. The ratio of H ions and atoms is found to be in agreement with [161].

On taking into account the confinement properties of the plasma, the full ionization threshold temperature will shift to slightly higher values. Since ions and atoms are recycled as neutral molecules, the presence of neutrals at high temperatures will be more important in the case of the real ion confinement.

5.2.2.2 Pure helium plasma

Fig. 5.6 (right, full lines) gives the helium ion fractions as a function of the electron temperature. From electron temperatures of 2.2 eV on, the plasma attains a significant degree of ionization. The transition from no ionization

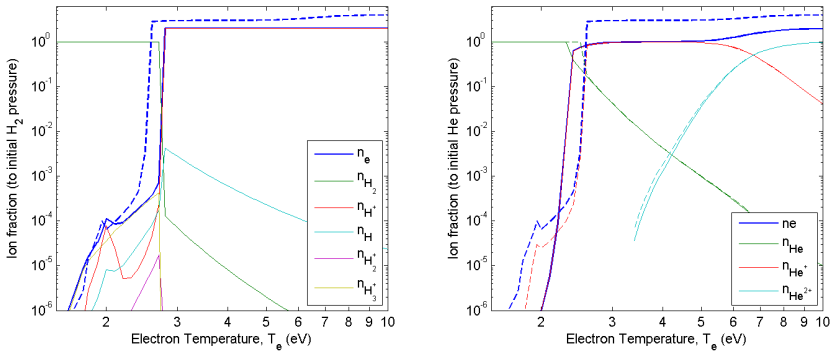

Figure 5.6: Ion fractions as a function of the electron temperature (T_e). Left: pure H_2 plasma (full lines) and 50/50 He/H_2 plasma (dashed, only electron density). Right: Pure He plasma (full lines) and 50/50 He/H_2 plasma (dashed).

to full ionization happens in the electron temperature range from 2 to 3 eV. Like for hydrogen, steady state electron temperatures between these two values can keep partially ionized plasmas. An ionization degree of 50% is obtained at an electron temperature of ≈ 2.4 eV. A second transition, from the single ionized state to double ionized state, happens in the electron temperature range of 4 to 10 eV where, as the electron temperature increases, the electron density increases likewise. A simultaneous presence of He and He^{2+} appears negligible: the maximum simultaneous presence of both double ionized helium and neutral helium is at $T_e = 4.2$ eV and will only make $\approx 0.25\%$ each of the He^+ concentration. The modeled ion fractions are found to be in agreement with [161].

Similar as for the hydrogen case, by taking into account the confinement properties of the plasma, the full single ionization and double ionization threshold temperatures will shift to slightly higher values. Since ions are recycled as neutrals, the presence of neutrals at high temperatures will be more important when we take into account the real ion confinement.

5.2.2.3 Hydrogen-helium mixtures

On Fig. 5.6 also the electron density (resp. normalized to the initial hydrogen and helium density) and ion fractions (only for helium, right figure) for a neutral gas mixture of 50/50 H_2/He (dashed line) is plotted as a function of the electron temperature. The increased electron density in the temperature range of 2.1 to 2.5 eV due to ionized helium results in additional ionization of hydrogen. Consequently the full ionization state of hydrogen is reached somewhat earlier. On the other hand, the full ionization state of helium is

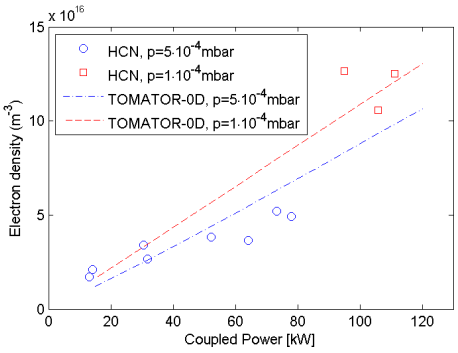

Figure 5.7: Modeled and experimental TEXTOR ICRF plasma densities as a function of the coupled RF power to the electrons (feed back controlled pressures, $B_T = 2.3\,\mathrm{T}$, $B_V = 0.04\,\mathrm{T}$).

reached later than for a pure helium plasma.

5.2.3 Plasma characteristics as a function of the discharge pressure, coupled power and H_2/He gas mixture

To benchmark the 0D model a comparison follows between model results, using experimental partial pressures and coupled RF power as model inputs, with experimental electron density data obtained from interferometry measurements. Once the density is modeled, additional information on the particle energies and principle wall bombarding particle fluxes can be obtained. We will discuss TEXTOR H_2-ICWC discharge densities as function of RF power and pressure, TORE SUPRA He-ICWC discharge densities as function of RF power and TEXTOR H_2/He-ICWC discharge densities as function of the gas mixture.

5.2.3.1 TEXTOR H_2-ICWC discharges

Fig. 5.7 shows modeled and experimental TEXTOR ICRF plasma densities as a function of the coupled RF power to the electrons. The plots contain experimental data for RF discharges with a toroidal magnetic field of $B_T = 2.3\,\mathrm{T}$ and vertical field of $B_V = 0.04\,\mathrm{T}$. The pressure during these discharges was feedback controlled at $p_{\mathrm{H_2}} = 5 \cdot 10^{-4}\,\mathrm{mbar}$ or $p_{\mathrm{H_2}} = 1 \cdot 10^{-4}\,\mathrm{mbar}$. At a pressure of $p_{\mathrm{H_2}} = 5 \cdot 10^{-4}\,\mathrm{mbar}$ the measured electron density is of the order of $n_e = 4 \cdot 10^{10}\,\mathrm{cm}^{-3}$ ($P_{\mathrm{RF}} = 50\,\mathrm{kW}$). For the same pressure and power, in absence of impurities, the 0D model predicts a ICWC plasma density of $n_e = 2.5 \cdot 10^{11}\,\mathrm{cm}^{-3}$. To match the experimental data the impurity

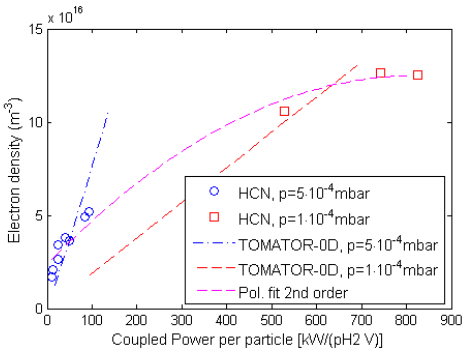

Figure 5.8: Modeled and experimental TEXTOR ICRF plasma densities as a function of the coupled RF power per particle ($P_{\mathrm{RF}}/p_{\mathrm{H}_2}V$) (feed back controlled pressures, $B_T = 2.3\,\mathrm{T}$, $B_V = 0.04\,\mathrm{T}$).

content of the discharge was set to 1.5% for the high pressure case and 7.5% for the 5 times lower feedback pressure case (same absolute impurity content). These high impurity concentrations are realistic on TEXTOR, considering the evidenced high background CO pressure and increasing CH_4 pressure during the discharge (Fig. 5.4). The figure shows clearly that the density increases with increasing power. For the high pressure case one can recognize a linear trend, which could be reproduced by the 0D model qualitatively. Fig. 5.8 contains the same density data plotted as function of the power per particle, here defined as the coupled RF power divided by the neutral pressure and the plasma volume. A second order polynomial fit shows an apparent tendency for the density as a function of the coupled power per particle, which is independent of the discharge pressure. A similar tendency could be reproduced with the 0D model in absence of impurities, however the predicted density in this case is too high. On inclusion of impurities the densities can be brought in the range of the experimental data, however the density dependency on the power per particle could not be found back in this case, as is clear from the figure, which might indicate that a more accurate description of the plasma impurities is required.

Fig. 5.9 shows the modeled neutral and ion fluxes to the wall as a function of the coupled RF power, for both the high pressure case and low pressure case. For the high pressure case the ion flux is negligible compared to the neutral atom flux. On decreasing the feedback pressure to $p_{\mathrm{H}_2} = 1 \cdot 10^{-4}\,\mathrm{mbar}$, the neutral wall flux becomes comparable to the ion wall flux. The neutral flux has decreased due to the smaller mean free path of the neutrals (higher electron density), and the lower neutral hydrogen pressure. The ions on the other hand will have a larger mean free path, due to their

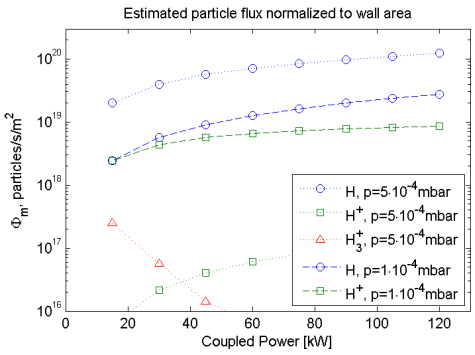

Figure 5.9: Modeled neutral and ion fluxes to the wall as a function of the coupled RF power, for the TEXTOR H_2-ICWC discharges given in Fig. 5.7.

lower collisionality in the low pressure plasma, which significantly increases the number of particles reaching the vessel walls via transport along the magnetic field lines. The predicted temperature of these ions is in case of a partially ionized plasma around 2 to 3 eV. This temperature is not necessarily the impact energy on the wall since sheath effects can increase the energy significantly. The ion wall flux consists mainly of H^+. Both the neutral H and H^+ flux increase close to linear with the coupled RF power. When the plasma becomes fully ionized the neutral flux will drop to zero, while the ion flux will increase drastically. The energy of the wall bombarding neutrals is about 3 eV, equal to the assigned average energy to the atoms on dissociation of hydrogen molecules. To obtain high ion fluxes to the wall one should aim at high RF powers, or low neutral gas pressures (high P/N, see JET result Fig. 4.16).

The modeled neutral flux is in the range of the neutral flux that was predicted from partial H_2, HD and D_2 pressures, gas injection data and machine pumping speeds on TEXTOR (see table 4.8). Also on TEXTOR the charged particle flux on a toroidal limiter blade, with a 0.5 m^2 surface, was measured. For a grounded ALT limiter, the measured ion current was $9.3 \cdot 10^{17} \pm 1.3 \cdot 10^{17}$ /m^{2}s in case of hydrogen feedback pressure $p_{H_2} = 5 \cdot 10^{-4}$ mbar and $16.5 \cdot 10^{17} \pm 0.5 \cdot 10^{17}$ /m^{2}s for $p_{H_2} = 1 \cdot 10^{-4}$ mbar, both for a coupled RF power of $P_{RF} \approx 100$ kW. The predicted ion flux in the low pressure case is too high by a factor 4, and the predicted ion flux in the high pressure case is one order of magnitude too low.

Fig. 5.10 shows the pumping probability $(1 - f)$, with f the ionization probability, of neutral H_2 as a function of the electron density. The ionization probability is the probability that a neutral molecule will be ionized or dissociated instead of pumped out of the machine [85]. The evacuation

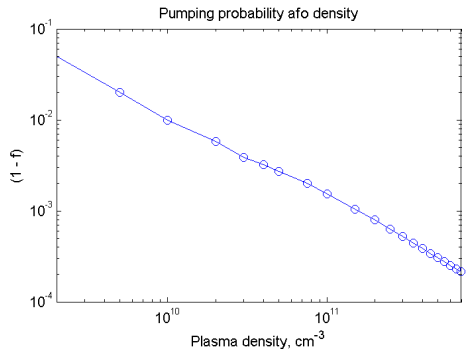

Figure 5.10: Pumping probability $(1 - f)$ of neutral H_2 as a function of the electron density for TEXTOR discharges.

of wall desorbed particles is very inefficient in a plasma with high ionization probability. From the figure it is clear that the pumping probability of H_2 for typical ICWC plasma densities of order $n_e \approx 10^{11}\,\mathrm{cm}^{-3}$ is very low, in the range of 0.1%. Experimentally these low values are confirmed (see section 4.1.1.2). To optimize the conditioning efficiency it is clear that a compromise has to be sought between the high wall fluxes on one side (neutrals: high power, high pressure; ions: high power, low pressure) and the reionization probability on the other. An alternative solution is to operate the discharges in pulsed mode: $\sim 1\,\mathrm{s}$ discharges followed by sufficient pumping time (order of a few times the characteristic pumping time, see section 4.1.4).

5.2.3.2 TORE SUPRA He-ICWC discharges

Fig. 5.11 shows both experimental and modeled helium plasma densities as a function of the coupled power for TORE SUPRA He-ICWC discharges at pressure $p_{\mathrm{He}} = 1.8 \cdot 10^{-4}\,\mathrm{mbar}$, $B_T = 3.8\,\mathrm{T}$ and $B_V = 0\,\mathrm{T}$. The neutral hydrogen content during these discharges stemming from plasma wall interaction is set constant to $p_{\mathrm{H_2}} = 8 \cdot 10^{-6}\,\mathrm{mbar}$ (implemented in the calculation as a feedback controlled particle source) in accordance with experimental partial pressures. To match the experimental data a reasonable impurity content of 0.35% is added to the neutral pressure (the impurity content during TORE SUPRA ICWC discharges is found to be much lower than on TEXTOR). A helium plasma has generally a higher plasma density ($n_e \approx 4 \cdot 10^{11}\,\mathrm{cm}^{-3}$) than a hydrogen plasma ($n_e \approx 4 \cdot 10^{10}\,\mathrm{cm}^{-3}$) for the same coupled power at a given pressure. The density in He-plasmas is linear with the coupled RF power. Fig. 5.12 shows the modeled particle fluxes to the wall as a function of the coupled RF power. As in case of pure hydrogen

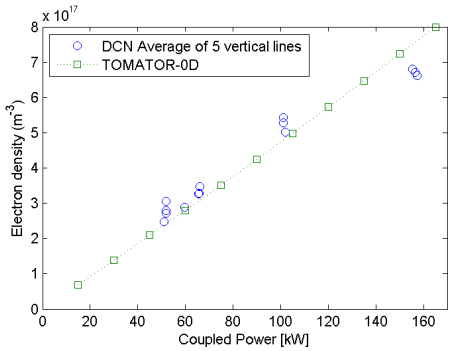

Figure 5.11: Experimental and modeled helium plasma densities as a function of the coupled power for TORE SUPRA He-ICWC discharges at pressure $p_{\mathrm{He}} = 1.8 \cdot 10^{-4}$ mbar, $p_{\mathrm{H_2}} = 8 \cdot 10^{-6}$ mbar (stemming from wall interaction), $B_T = 3.8\,\mathrm{T}$ and $B_V = 0\,\mathrm{T}$.

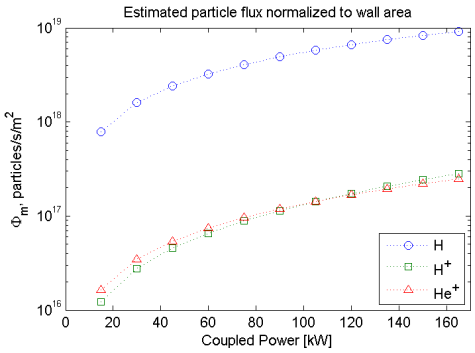

Figure 5.12: Modeled particle fluxes to the wall as a function of the coupled RF power, for the TORE SUPRA He-ICWC discharges given in Fig. 5.11.

discharges, also in helium RF discharges the fluxes increase with power and with density (and also the conditioning efficiency as shown on Fig. 4.20). Interestingly it is found that the main wall bombarding species are neutral H-atoms. The He^+-ion flux is approximately equal to the H^+-ion flux. The 0D model reveals thus clearly that in case of helium wall conditioning discharges, the wall released hydrogen particles will largely contribute to the wall bombarding flux. For the typical low temperature ICWC plasmas, the presence and wall flux of double ionized He^{2+}-ions is negligible.

5.2.3.3 TEXTOR H_2/He-ICWC discharges

Fig. 5.13 shows the influence of the neutral gas mixture on the electron density for a series of TEXTOR discharges with constant helium injection

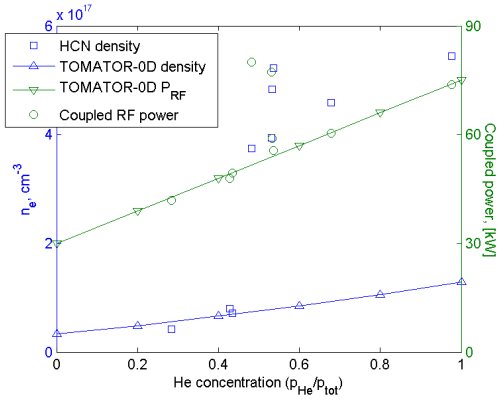

Figure 5.13: Influence of the neutral gas mixture on the electron density for a series of TEXTOR discharges with constant helium injection and feedback hydrogen injection ($p_{\mathrm{tot}} = 5 \cdot 10^{-4}$ mbar). The RF coupling efficiency increases linearly with increasing helium concentration. The plasma density shows a discontinuous increase around He/H_2-concentrations $\approx 50/50$ which is presently not reproducible with the 0D model.

and feedback hydrogen injection ($p_{\mathrm{tot}} = 5 \cdot 10^{-4}$ mbar). For a helium concentration below 50% the electron density is as in previous examples lower than $10^{17}\,\mathrm{m}^{-3}$ (HCN interferometer density, blue rectangles). On higher helium concentrations the electron density increases abruptly to values around $(3.5 - 5.5) \cdot 10^{17}\,\mathrm{m}^{-3}$. On the right axis, the coupled power during these discharges is given. Except for two discharge with a helium concentration of $50 - 55\%$, the coupled power (green dots) in the discharges increases monotonically with the helium concentration, although the RF generator power was kept constant for all discharges, which means that the RF coupling efficiency increases with increasing helium concentration. From RF physics point of view one would expect that the coupling efficiency is firstly dependent on the electron density rather than on the gas mixture. Since the coupling efficiency doesn't show the same discontinuity as the plasma density, it is expected that the increase of density is due to collisional processes. On the figure also modeled densities are given (blue triangles). The densities are modeled by adjusting the input coupled power proportional to the gas mixture, according to the experimental coupled powers. The model input powers are given by the green rectangles. The hydrogen injection in the modeling is like in the experiment controlled to keep the total pressure constant, while the helium injection is kept continuously constant. In accordance with previous TEXTOR example, the impurity concentration is set to 1.5% of the total pressure. It is clear from the figure that the model

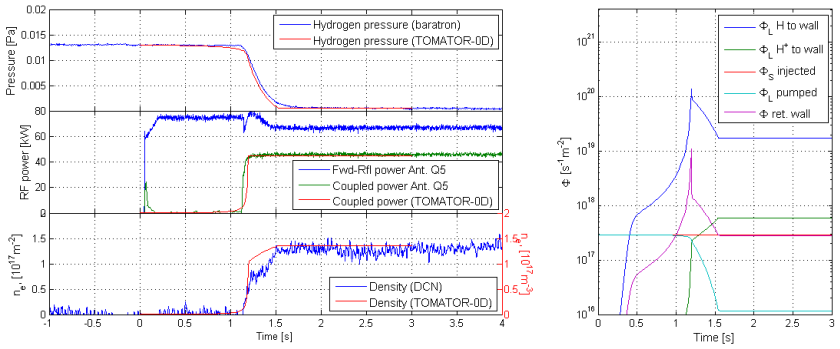

Figure 5.14: TORE SUPRA H_2-ICWC discharge ($P_{\mathrm{RF,gen}} = 75\,\mathrm{kW}$, $p_{H_2} = 1.3 \cdot 10^{-4}\,\mathrm{mbar}$). Right, top to bottom: exp. and modeled (red lines) hydrogen pressure, forward minus reflected power and coupled RF power, and plasma density. Left: Modeled particle wall flux, sources (injection and wall recycled) and retention rate.

is able to reproduce the density in case of a hydrogen like plasma (helium concentration lower than 50%). However it does not reproduce the sudden density increase observed on higher helium concentration. The non-perfect description of plasma impurities in the model is thought to lie at the origin of this, but in this stage of the model also the influence of RF coupling properties can't be ruled out. It should therefore be envisaged to upgrade the 0D model to include a RF power coupling module based on full wave code TOMCAT, which should preferentially be done in a 1D context.

5.2.4 Time dependent simulation of a TORE SUPRA H_2-ICWC discharge

Fig. 5.14 (left) shows modeling results (red lines) for a TORE SUPRA H_2-ICWC discharge with $P_{\mathrm{RF,gen}} = 75\,\mathrm{kW}$ and $p_{H_2} = 1.3 \cdot 10^{-4}\,\mathrm{mbar}$. The employed model inputs are the neutral gas injection rate (constant during the whole discharge), the impurity content (0.8% of the neutral pressure before breakdown), the vessel volume and pumping speed, the wall recycling coefficient R and the maximum coupled RF power. The hydrogen pressure (baratron), coupled RF power and plasma density (averaged over five central vertical DCN interferometry lines, $\sim 1\,\mathrm{m}$) are plotted separately. Two main phases can be distinguished from the figure. During the breakdown phase ($0 - 1.2\,\mathrm{s}$), the neutral pressure remains unchanged and the plasma density is out of measurement range although the RF antenna is powered, until a sudden increase of the plasma density and RF coupling efficiency is

noticeable together with a drop in pressure. Electron collisional processes, well described in the model, are the fundamental mechanism for the build-up of the ICRF plasma. The plasma breakdown moment is generally indicated by a sudden drop in antenna voltage (not shown on the figure). During the plasma phase ($> 1.2\,\mathrm{s}$) the density remains practically unchanged around $n_e = 1.3 \cdot 10^{17}\,\mathrm{m}^{-3}$. The electron, hydrogen atom and hydrogen ion temperatures during the steady state phase equal $T_e = 3.5\,\mathrm{eV}$, $T_\mathrm{H} = 3.7\,\mathrm{eV}$ and $T_{\mathrm{H}^+} = 3.0\,\mathrm{eV}$, respectively.

The hydrogen RF plasma was simulated using $\alpha = 0.044$. The sudden coupled power increase during plasma breakdown obtained from the antenna resistance is reproduced by the 0D model. The simultaneous pressure drop is mainly due to the consumption of particles by the walls. Upon discharge initiation a transient storage of particles is observed, governed by a low recycling coefficient of $R = 0.92$. An equilibrium between the particle flux to the wall and the wall release rate is reached rapidly, resulting in a much higher recycling coefficient during the plasma phase $R = 0.984$, which is about 1% lower as found in section 4.1.3, table 4.8. The latter recycling coefficient is calculated from the modeling results by comparing the particle fluxes to the wall with the required hydrogen source (injection and wall release) to obtain the steady state pressure of $p_{\mathrm{H}_2} \approx 5 \cdot 10^{-6}\,\mathrm{mbar}$ after the plasma breakdown.

Fig. 5.14 (right) summarizes the particle fluxes to the walls (mainly H and H^+, resp. blue and green lines), the injection rate of hydrogen molecules (normalized to wall surface and number of atoms, red line), the removal rate of hydrogen molecules by the pumps (cyan line), and the retention rate of hydrogen into the wall (purple line). Before plasma breakdown, the hydrogen evacuation rate by the machine pumps equals the gas injection rate, leading to a stable vessel pressure of $p_{\mathrm{H}_2} = 1.3 \cdot 10^{-4}\,\mathrm{mbar}$. At the plasma breakdown moment ($t \approx 1.2\,\mathrm{s}$) the atomic hydrogen wall flux peaks to a value of the order of $\Phi_\mathrm{H} \approx 10^{20}\,/\mathrm{m}^2\mathrm{s}$, whereafter due to the decreasing pressure the atom flux decreases to $\sim 1.8 \cdot 10^{19}\,/\mathrm{m}^2\mathrm{s}$. These modeled values are in agreement with estimated total wall fluxes from particle balance analysis [154]. The ion wall flux is much lower, and behaves proportional to the electron density. The steady state value during the plasma phase is of the order of $Q_{\mathrm{H}^+} \approx 6.0 \cdot 10^{17}\,/\mathrm{m}^2\mathrm{s}$, in agreement with ion currents collected on the ALT limiter blades in TEXTOR during hydrogen ICWC discharges (see section 5.2.3.1). The retention at the start of the discharge accounts for a total of $\sim 5 \cdot 10^{19}$ particles. It is expected that a large part of these particles are transiently stored and are retrieved from the wall after the RF pulse, which causes the typical outgassing peak. The retention rate during the steady state plasma phase ($t > 1.5\,\mathrm{s}$) equals the injection rate minus the

removal rate by the pumps, and is approximately equal to the injection rate of particles into the vessel ($\sim 2.9 \cdot 10^{17}$ /m^{2}s) due to the low pressure during this phase ($p_{H_2} \approx 5 \cdot 10^{-6}$ mbar). It is expected from the stable density and pressure time traces (Fig. 5.14) that these particles are permanently stored in the vessel, which corresponds for this ≈ 4 s RF discharge to a permanent retention of $\sim 8 \cdot 10^{19}$ particles, which is of the same order as the values given on Fig. 4.13. ICWC isotope exchange experiments on both TEXTOR and TORE SUPRA revealed indeed that the total amount of permanently retained particles increases on increasing RF pulse length.

From the modeled temporal pressure, density and coupled power dependencies shown in Fig. 5.14 it can be concluded that the wall interaction has a major influence on the neutral hydrogenic pressure and plasma density in case of constant injection. During the breakdown phase particles are transiently stored in the wall causing a steep pressure drop while during the plasma phase an equilibrium pressure is formed where the permanent hydrogen retention rate is of the order of the gas injection rate. In chapter 4 we saw already that in order to minimize retention it is recommended to employ shorter RF pulses ($1 \sim 2$ s), which at the same time maximizes the recovery of transiently stored particles.

5.3 Conclusion

In this chapter the 0D kinetic description of magnetized toroidal hydrogen-helium RF discharge was outlined. The model is developed to obtain insight on ICRF plasma parameters, particle fluxes to the walls and the main collisional processes, the latter being the fundamental mechanism for the build-up of a plasma. This is of particular importance since most standard tokamak plasma diagnostics are not adapted to diagnose the typical low temperature and low density RF plasmas.

The 0D plasma description is based on the energy and particle balance equations for nine principal species: H, H^+, H_2, H_2^+, H_3^+, He, He^+, He^{++} and e^-. It takes into account (1) elementary atomic and molecular collision processes, such as excitation/radiation, ionization, dissociation, recombination, charge exchange, etc... and elastic collisions, (2) particle losses due to the finite dimensions of the plasma volume and confinement properties of the magnetic configuration, and particle recycling, (3) active pumping and gas injection, (4) RF heating of electrons (and protons) and (5) a qualitative description of plasma impurities.

Many efforts have been put in rendering the 0D description of the hydrogen-helium plasmas as complete as possible. The 0D model predicts however plasma densities that are 2 to 10 times higher than the experi-

mental densities, obtained from interferometry measurements on TEXTOR and TORE SUPRA. The main physical actors that can reduce the modeled densities were investigated. (1) Firstly on inclusion of small charged particle confinement times ($< 1\,\mathrm{ms}$), the plasma densities are found to be smaller by a factor 3 compared to a perfectly confined plasma. In the model the charged particle confinement times ($\sim 0.1\,\mathrm{s}$) are estimated from particle drifts in the magnetic field configuration, diffusion across the magnetic field and losses along the magnetic field lines. It was concluded from numerical experiments that the confinement times play only a minor role on the final plasma parameters. (2) Secondly, in case a large fraction of the RF power would be coupled to ions the plasma density decreases by a factor of 2 to 5 (50%-60% coupled to ions), while the ion temperature increases, which could be beneficial with respect to the wall conditioning efficiency of the RF discharges. However such large coupled power fractions are not in agreement with the present understanding of RF plasma production, mainly obtained from the full wave code TOMCAT (typically ∼80-90% coupled to electrons). (3) Finally it was found that on inclusion of limited amounts of plasma impurities (∼0.1-1%) the plasma density can decrease by a factor of 2 to 10 times. Impurities have thus an important impact on the plasma parameters. It is found from mass spectrometry that these small impurity concentrations are in agreement with experiments, (e.g. CH_4 and CO on TEXTOR). Unfortunately it is often difficult to estimate the exact impurity content of RF plasmas and the elementary collision data of molecules such as H_2O, CH_4 and CO is scarce. The effect of impurities on the plasma parameters is simulated by including balance equations for C, C^+ and C^{2+}.

On inclusion of plasma impurities the model reproduces experimental plasma density dependencies on discharge pressure and coupled RF power, both for hydrogen RF discharges ($n_e \approx (1-5)\cdot 10^{10}\,\mathrm{cm}^{-3}$) as for helium discharges ($n_e \approx (1-5)\cdot 10^{11}\,\mathrm{cm}^{-3}$). The modeled wall fluxes of hydrogen discharges are in the range of what is estimated experimentally: $\sim 10^{19} - 10^{20}\,/\mathrm{m}^2\mathrm{s}$ for H-atoms, and $\sim 10^{17} - 10^{18}\,/\mathrm{m}^2\mathrm{s}$ for H^+-ions. In case of helium RF discharges it is found that the wall desorbed particles contribute largely to the wall flux. The main wall bombarding species are hydrogen neutrals. The helium and hydrogen ion flux are approximately of the same order of magnitude although the hydrogen neutral pressure, stemming from wall desorption, is in accordance to mass spectrometry data less than 5% of the helium neutral pressure.

The sudden increase of plasma density on increasing the discharge helium concentration, while keeping the total pressure constant could not be reproduced by the 0D model. Since the coupled power, and thus the coupling efficiency does not show a similar discontinuity, it is nevertheless

expected that collisional processes lie at the basis of this effect. A future upgrade of the 0D model to 1D, including a self consistent description of the coupled RF power, and reconsideration of the inclusion of plasma impurities is required to evidence this.

The presented 0D ICWC plasma model allows to reproduce experimental pressure, density and coupled power temporal dependencies of a TORE SUPRA H_2-ICWC discharge from discharge initiation to steady state plasma, and gives insight into the particle wall fluxes and retention rates. The wall interaction, represented in the model by a particle recycling coefficient, has a major influence on the neutral pressure and plasma density in H_2-ICWC discharges (in case of constant injection). During the breakdown phase, particles are transiently stored in the wall causing a steep pressure drop while during the plasma phase an equilibrium pressure is formed where the permanent hydrogen retention rate approximately equals the gas injection rate. Employing shorter RF pulses ($1 \sim 2\,\mathrm{s}$) is favored to limit retention, while maximizing the recovery of transiently stored particles.

6

Simulation of wall interaction

In chapter 4 we discussed the efficiency of ICWC for isotopic exchange. We saw that hydrogen ICWC is able to remove monolayers of wall isotopes within short time scales ($\sim$ minutes), and that pulsed RF conditioning is recommended to limit the observed retention during the conditioning procedure. The presented experimental particle balances delivered however only information on the overall wall conditioning efficiency. The purpose of this chapter is to investigate the evidenced efficiencies into deeper detail by determining a minimum structure for a 0D reservoir model of the wall. This model, together with experimental data, could allow for a first physical interpretation of the observed conditioning effect, e.g. on the sources of the removed wall isotopes and on the retention mechanisms during ICWC, and to propose improvements on wall conditioning efficiency. Determining the sources of the removed wall isotopes is of particular importance for evidencing the hydrogen ICWC efficiency for tritium removal, and is required for assessing the applicability of ICWC for removing tritium-rich codeposited layers on ITER.

The hypothesis used to build up the model is that the same model structure should be able to describe the wall behavior during normal plasmas and conditioning procedures. We will base the structure of the model on robust experimental facts observed during normal plasmas. In a first section the model will be presented, including a plasma description and a wall description derived from experimental facts. In a second section the model equations are given. The third section shows the capability of the model to

reproduce the experimental facts in normal plasma discharges. In the final section, TORE SUPRA H_2-ICWC discharges are modeled, and proposals for ICWC optimization in terms of discharge timing are worked out.

6.1 Model description

6.1.1 Plasma description

The plasma included in this plasma wall interaction simulation is based on the 0D model presented in chapter 5. The plasma balance equations are very much simplified and only the particle balances are retained. The neutral gas consists of a mixture of H_2, HD and D_2. The included elementary collisions are dissociation of molecules, ionization of atomic hydrogen and recombination of ions. At the start of the RF pulse we consider a high electron temperature ($T_e > 10\,\mathrm{eV}$), so that the electron density is built up quickly, in accordance with 0D model results. When sufficient electron density is attained ($n_e > 10^9\,\mathrm{cm}^{-3}$) the electron temperature reaches the steady state value of $T_e \approx 2 - 3\,\mathrm{eV}$, and the density stabilizes around $n_e \sim 10^{10} - 10^{11}\,\mathrm{cm}^{-3}$. The plasma confinement times are set to constant steady state values, obtained from 0D model calculations. The resulting particle fluxes to the wall from these confinement times are used as source terms in the balance equations of the wall description. The included plasma parameters are:

- electron temperature: T_e
- population of hydrogen ions in the plasma: N_{H}^{+}
- population of deuterium ions in the plasma: N_{D}^{+}
- population of hydrogen atoms in the plasma: N_{H}
- population of deuterium atoms in the plasma: N_{D}
- populations of neutral molecules in the plasma: $N_{\mathrm{H_2}}$, N_{HD} and $N_{\mathrm{D_2}}$
- plasma volume: V_{pl}
- molecule dissociation reaction rate: $k^{\mathrm{dis}}(T_e)$
- atom ionization reaction rate: $k^{\mathrm{ion}}(T_e)$
- ion recombination reaction rate: $k^{\mathrm{rec}}(T_e)$
- atom confinement time: τ_p

- ion confinement time: τ_i
- characteristic neutral molecule pumping time: τ_S
- neutral pressure of the injected gas: p_{H_2}
- discharge timing (number and length of pulses, and pumping time between pulses)

The electron density n_e is calculated by the model ($(N_{\mathrm{H}}^+ + N_{\mathrm{D}}^+)/V_{\mathrm{pl}}$) and the injection rate of neutral gas is either continuously constant, calculated from the requested neutral pressure, or either feedback controlled to obtain a constant electron density (to simulate the SOL in normal plasma operation, $T_e \approx 100\,\mathrm{eV}$, $n_e \approx 4 \cdot 10^{12}\,\mathrm{cm}^{-3}$).

6.1.2 Wall description

The wall description is based on robust experimental facts observed on the carbon machine TORE SUPRA during standard tokamak discharges with plasma current. This is motivated by the fact that the wall properties are essentially the same in discharges with plasma current and in RF discharges. One PSI model should thus be able to explain the wall interaction in both types of discharges. In this section we will first summarize the experimental facts. Hereafter we will, based on these facts, propose a wall model consisting of communicating particle reservoirs.

6.1.2.1 Experimental facts

Permanent retention One observes a permanent retention even after 5 hours of cumulated plasma time [40]. It is concluded that there exists an infinite reservoir N^t which corresponds to atoms trapped in deposits in remote areas of the vacuum chamber or in deep pores of the CFC. At a first approximation, the particles entering this reservoir are definitely lost. On ITER, the tritium inventory build-up in similar infinite reservoirs is a severe problem, as shown in section 1.4.4, and has to be mitigated by wall conditioning. At this point it is not certain that this reservoir can be emptied during conditioning procedures, although it is expected that it is at least very partially emptied due to the different geometries of such discharges with respect to normal plasmas. (This chapter aims at investigating this into deeper detail.)

Diffusive particles - transient retention One observes an equality for long discharges between the overshoot of retention at the beginning of the plasma and the post-discharge outgassing [36, 41, 162]. There exists a

reservoir of diffusive particles, N^d, which are recovered at the end of the plasma. Since the outgassed amount of gas saturates for long discharges, the size of this reservoir is limited $N^{d,\max} \approx 5 \cdot 10^{21}$ H and D.

Accessible retention One observes a 'natural' plasma density which depends only on the plasma current and/or total power. In this case the wall features a net release of particles. In the opposite case the wall continuously 'pumps' particles in which case the injected gas flux has to be high enough for maintaining the plasma density [41]. It is concluded that there exists an accessible reservoir of trapped particles, N^a, whose maximum size $N^{a,\max} \approx 10^{22} - 10^{23}$ depends on the power in the discharge (i.e. on the energy of the ions impinging the wall). It is essentially this reservoir that governs the exchange of particles between plasma and wall. In tokamak discharges, both the gas injection flux and the release/pumping by the wall determine whether the discharge density can be controlled:

- if the gas flux is not high enough and $N^a \approx 0$, one cannot sustain the plasma;
- if the gas flux is not high enough and $N^a \neq 0$, the wall outgases;
- if the gas flux is too high and $N^a < N^{a,\max}$, the wall pumps;
- if the gas flux is too high and $N^a \approx N^{a,\max}$, the wall flux will return into the plasma, yielding a disruption by limit in density.

Slowly varying wall status During 'wall saturation-desaturation' experiments, several discharges (~ 10) are required for modifying the wall status [163]. During a plasma discharge, the majority of the impinging ion flux recycles immediately without entering the wall. Typically, one has:

- proportion of the recycling flux for permanent retention in N^t: $\eta_t \sim 0.1 - 1\%$;
- proportion of the recycling flux in N^a: $\eta_a \sim 1 - 10\%$;
- proportion of the recycling flux immediately re-injected in the plasma: $(1 - \eta_a - \eta_t)$.

Diffusion into micro-voids In long plasma discharges the wall retention features a peak at the start of the discharge, representing the already mentioned filling of the transient reservoir (see Fig. 6.4 on page 6-13), whereafter a slower decrease of the wall retention is observed, while at $t \sim 100\,\mathrm{s}$ a constant retention is attained [36]. It is acknowledged that a model with only

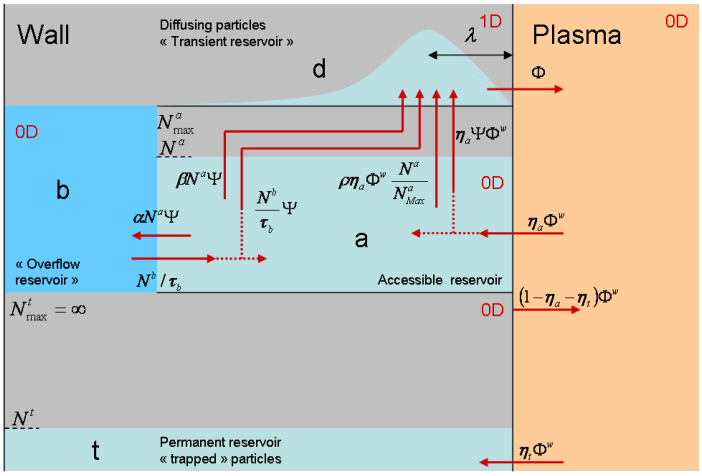

Figure 6.1: Schematic representation of the included wall reservoirs.

one accessible reservoir is too limited to explain this effect. The carbon subsurface representing the accessible reservoir consists of different types of trapping sites. It is proposed that the time constant of 100 s originates from the diffusion of particles from macro-voids (accessible reservoir) into micro-voids in the CFC pores [36]. The latter effect becomes important when the concentration of particles in the accessible reservoir is high. This can be interpreted as an equivalent of enhanced diffusion deeper into the carbon layers due to 'elevated pressures'. Also, when the common trapping sites are saturated the hydrogen can travel further through the carbon structure where it can be trapped in the second type of traps. In the model we will call this reservoir the overflow reservoir.

6.1.2.2 Formulation of reservoir model

Based on the listed experimental facts the following wall model was proposed, represented in Fig. 6.1. It consists of four different reservoirs: an accessible reservoir which is thus accessible for implantation, removal and exchange of particles, a permanent reservoir in which only storage is possible (implantation or codeposition), a diffusive (transient) reservoir that represents diffusing particles in the wall subsurface, and an overflow reservoir to account for effects that occur when the particle concentration in the accessible reservoir becomes large. The related wall variables are:

- population of accessible hydrogen atoms in the wall: N^a_{H}
- population of accessible deuterium atoms in the wall: N^a_{D}

- isotopic ratio of the wall: $I^a_{\mathrm{H}/(\mathrm{H+D})} = N^a_{\mathrm{H}}/(N^a_{\mathrm{H}} + N^a_{\mathrm{D}})$
- maximum possible amount of atoms in the accessible reservoir: $N^{a,\max}$ $(10^{22} - 10^{23})$
- population of hydrogen atoms in the permanent reservoir: N^t_{H}
- population of deuterium atoms in the permanent reservoir: N^t_{D}
- population of hydrogen atoms in the overflow reservoir: N^b_{H}
- population of deuterium atoms in the overflow reservoir: N^b_{D}
- 'transient' population of diffusing hydrogen atoms: N^d_{H}
- 'transient' population of diffusing deuterium atoms: N^d_{D}

The included wall parameters are:

- proportion of recycling flux $\Phi^{w(1)}$ going into the accessible reservoir: η_a (typically from the order of 1 to 10%)
- proportion of recycling flux Φ^w going into the permanent reservoir: η_t (typically from the order of 0.1 to 1%)
- efficiency for an impinging particle to detrap a particle from the accessible reservoir (which will then be accounted to the transient reservoir): detrapping rate ρ. In the model we will use a geometric interpretation of the detrapping coefficient. The hydrogen trap concentration in carbon is of the order of $C_t = 4{\cdot}10^{28}\,\mathrm{m}^{-3}$, while the detrapping cross section is of the order of $\sigma = 8 \cdot 10^{-21}\,\mathrm{m}^2$ (for helium) [38]. For a typical hydrogen penetration depth of into carbon of $\lambda = 5\,\mathrm{nm}$ ($\sim 100\,\mathrm{eV}$), the line integrated trapping site density is $2 \cdot 10^{20}\,\mathrm{m}^{-2}$. In case we consider that only collisions with trapped hydrogen atoms are possible, the detrapping rate by an impinging particle equals $\rho = \sigma C_t \lambda = 1.6$.
- diffusion coefficient: D ($\sim 7.5 \cdot 10^{-19}\,\mathrm{m}^2/\mathrm{s}$ [38])
- penetration depth for impinging particles: λ (normal impact on carbon: $\sim 0.6\,\mathrm{nm}$ for 10 eV H-ions, $\sim 3.4\,\mathrm{nm}$ for 100 eV H-ions [122])
- characteristic diffusion time: τ_d ($\sim 2\,\mathrm{s}$, see further)
- efficiency for diffusion into micro-voids: α

[1] The particle flux to the wall Φ^w was in previous chapters called Q_{ftw}.

- efficiency for spontaneous detrapping: β, where we assume a similar 'pressure' dependent effect as for diffusion into micro-voids. In case the concentration of particles in the accessible reservoir is small, spontaneous detrapping is only determined by thermal detrapping (not included in the model).
- characteristic residence time of particles in the overflow reservoir: τ_b

6.1.3 Diffusion in wall

In the model a simplification is introduced to describe the release of particles from the transient reservoir into the vessel, that is acknowledged to be in disagreement with the present understanding that can be found in the literature. It is known that the release rate of gas controlled by a diffusion process follows a t^{-n} dependency [38, 124, 164]. The theoretical value for n varies from 1.5 for a pure diffusion process, to 0.5 for a diffusion-recombination controlled process [124]. Experimentally, for example after JET low power ohmic cleaning discharges [164] values between 0.5 and 0.8 are recorded. For TORE SUPRA, $n \approx 0.5$ after He-GDC cleanings and $n \approx 0.7$ after normal tokamak discharges [38]. To properly include this effect in the model, the original aim was to include a 1D diffusion description for the transient reservoir. In the final version of the model the 1D diffusion module is replaced by a 0D description where the particle release is described by an exponential decay of the transient reservoir content. The advantage of this approach is that the code becomes much faster, while the final modeling results are not significantly influenced. The characteristic decay time employed in the model is chosen from calculated diffusion release rates, as illustrated on Fig. 6.2. In the calculation we assume the simplest situation where the release of particles from the wall is controlled by diffusion alone. The figure shows calculated D_2 release rates (blue) for a 5 s discharge and a constant arbitrary wall flux of 10^{21} D/s. The particles are assumed to be deposited in the wall at a depth of $\lambda = 1$ nm and the diffusion coefficient equals $D = 7.5 \cdot 10^{-19}\,\mathrm{m}^2/\mathrm{s}$ [38]. The left and right plot contain the same data, given respectively in a logarithmic and linear scale. The release rate decreases rapidly right after the discharge, and after some time the decrease becomes linear on the logarithmic plot, and thus follows a t^{-n} dependency. The calculated release rate is found to be very sensitive to the chosen particle deposition profile (λ). Information on the deposition profile is however not available.

To both plots an approximate exponential ($\tau_d = 1.5$ s, red) and t^{-n} ($n = 1.6$, green) fit is given. It is clear from the figure that the 'exponential fit'-approach does not perfectly describe the actual release rate, especially for

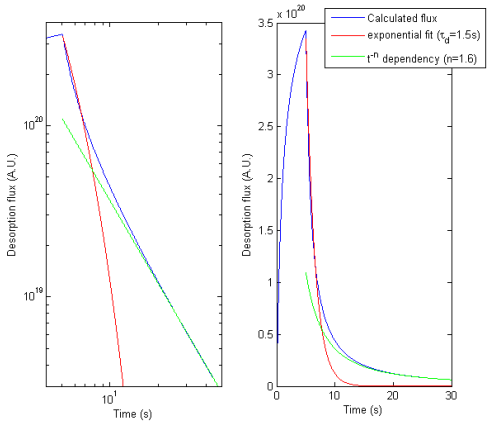

Figure 6.2: Calculated typical wall release rate governed by bulk diffusion (blue line), fitted exponential release rate (red line) and general accepted t^{-n} dependency (green line). Right after the discharge pulse ($t = 5\,\mathrm{s}$) the exponential fit best describes the desorption rate, whereafter it quickly evolves to the t^{-n} fit.

$t > 10\,\mathrm{s}$. And when calculating the exponential release rate also during the discharge, the result deviates even more from the actual rate. Nevertheless it was still chosen to adopt this approach in the model. This choice might be justified by the fact that the particle deposition profile in the wall is not known, which makes that the completer 1D approach taking into account diffusion and eventually surface recombination is not necessarily correcter.

It is also clear from the figure that including the t^{-n} fit in the model to simulate the wall release is also not an option since the slope of release rate in the logarithmic plot becomes only linear about 10 s after the discharge. Furthermore this approach requires choosing an universal $t = 0\,\mathrm{s}$ point, which is not possible when one intends to model multiple subsequent RF pulses.

6.2 Summary of the model equations

6.2.1 Plasma equations

6.2.1.1 Molecules in plasma

$$\frac{\mathrm{d}N_{\mathrm{H}_2}}{\mathrm{d}t} = \Phi_{\mathrm{H}_2} + O_{\mathrm{H}_2}\frac{N^d}{2\tau_d} - \gamma N_{\mathrm{H}_2} n_e k^{\mathrm{dis}} - \frac{N_{\mathrm{H}_2}}{\tau_S} + R_{\mathrm{H}_2}\frac{\Phi^w}{2}(1-\eta_a-\eta_t) \quad (6.1)$$

$$\frac{\mathrm{d}N_{\mathrm{HD}}}{\mathrm{d}t} = 0 + O_{\mathrm{HD}}\frac{N^d}{2\tau_d} - \gamma N_{\mathrm{HD}} n_e k^{\mathrm{dis}} - \frac{N_{\mathrm{HD}}}{\tau_S} + R_{\mathrm{HD}}\frac{\Phi^w}{2}(1-\eta_a-\eta_t) \quad (6.2)$$

$$\frac{\mathrm{d}N_{\mathrm{D}_2}}{\mathrm{d}t} = \Phi_{\mathrm{D}_2} + O_{\mathrm{D}_2}\frac{N^d}{2\tau_d} - \gamma N_{\mathrm{D}_2} n_e k^{\mathrm{dis}} - \frac{N_{\mathrm{D}_2}}{\tau_S} + R_{\mathrm{D}_2}\frac{\Phi^w}{2}(1-\eta_a-\eta_t) \quad (6.3)$$

The first term on the rhs is the injection flux of neutral hydrogen gas by the valves (continuously constant), the second term on the rhs is the release of molecules from the walls, with the factors O_{H_2}, O_{HD} and O_{D_2} representing the probability that an outgassed hydrogen atom recombines to H_2 or HD, and an outgassed deuterium atom to HD or D_2:

$$O_{\mathrm{H}_2} = \frac{{N_{\mathrm{H}}^d}^2}{{N^d}^2} \quad O_{\mathrm{HD}} = 2\frac{N_{\mathrm{H}}^d N_{\mathrm{D}}^d}{{N^d}^2} \quad O_{\mathrm{D}_2} = \frac{{N_{\mathrm{D}}^d}^2}{{N^d}^2},$$

with $N^d = N_{\mathrm{H}}^d + N_{\mathrm{D}}^d$, and τ_d the characteristic time for release of a diffusing particle from the wall into the vessel. The third term represents the loss of neutral molecules due to dissociation on electron impact, with

$$\gamma = \begin{cases} 1, & \text{during RF pulse} \\ 0, & \text{else,} \end{cases}$$

n_e the plasma electron density and k^{dis} the dissociation reaction rate for hydrogen molecules. The fourth term represents the evacuation of neutral gas by the machine pumps with τ_S the characteristic pumping time. The last source term on the rhs represents particle surface recombination and reflection at the walls. The factors R_{H_2}, R_{HD} and R_{D_2} are the probability that a reflected hydrogen atom/ion recombines to H_2 or HD, and a reflected deuterium atom/ion to HD or D_2:

$$R_{\mathrm{H}_2} = \frac{{\Phi_{\mathrm{H}}^w}^2}{{\Phi^w}^2} \quad R_{\mathrm{HD}} = 2\frac{\Phi_{\mathrm{H}}^w \Phi_{\mathrm{D}}^w}{{\Phi^w}^2} \quad R_{\mathrm{D}_2} = \frac{{\Phi_{\mathrm{D}}^w}^2}{{\Phi^w}^2},$$

Φ^w is the total wall flux (neutrals and ions, H (Φ_{H}^w) and D (Φ_{D}^w)), η_a is the probability that an impinging particle enters the accessible reservoir, and finally η_t is the probability that an impinging particle is implanted in the permanent reservoir.

6.2.1.2 Atoms in plasma

$$\frac{\mathrm{d}N_{\mathrm{H}}}{\mathrm{d}t} = \gamma(2N_{\mathrm{H}_2} + N_{\mathrm{HD}})n_e k^{\mathrm{dis}} + N_{\mathrm{H}^+} n_e k^{\mathrm{rec}} - \gamma N_{\mathrm{H}} n_e k^{\mathrm{ion}} - \frac{N_{\mathrm{H}}}{\tau_{\mathrm{H,D}}} \quad (6.4)$$

$$\frac{\mathrm{d}N_{\mathrm{D}}}{\mathrm{d}t} = \gamma(2N_{\mathrm{D}_2} + N_{\mathrm{HD}})n_e k^{\mathrm{dis}} + N_{\mathrm{D}^+} n_e k^{\mathrm{rec}} - \gamma N_{\mathrm{D}} n_e k^{\mathrm{ion}} - \frac{N_{\mathrm{D}}}{\tau_{\mathrm{H,D}}} \quad (6.5)$$

The first term on the rhs is the atom source following from molecule dissociation, the second term is an atom source following from the recombination of ions and electrons, with k^{rec} the recombination reaction rate for hydrogen

ions. The third term represents the ionization of neutral atoms, with k^{ion} the ionization reaction rate for hydrogen atoms. The last term contains the neutral particle confinement time $\tau_{\text{H,D}}$, and represents as such the flux of neutral particles to the walls.

6.2.1.3 Ions in plasma

$$\frac{\mathrm{d}N_{\text{H}^+}}{\mathrm{d}t} = \gamma N_{\text{H}} n_e k^{\text{ion}} - N_{\text{H}^+} n_e k^{\text{rec}} - \frac{N_{\text{H}^+}}{\tau_{\text{H}^+,\text{D}^+}} \tag{6.6}$$

$$\frac{\mathrm{d}N_{\text{D}^+}}{\mathrm{d}t} = \gamma N_{\text{D}} n_e k^{\text{ion}} - N_{\text{D}^+} n_e k^{\text{rec}} - \frac{N_{\text{D}^+}}{\tau_{\text{H}^+,\text{D}^+}} \tag{6.7}$$

The first term on the rhs is the ion source following from the ionization of neutral atoms, the second term is a loss term following from the recombination of ions and electrons. The last term contains the ion confinement time $\tau_{\text{H}^+,\text{D}^+}$, and represents as such the flux of ions to the walls. The total flux of particles Φ^w given in eq. (6.1-6.3) is thus

$$\Phi^w = \Phi^w_{\text{H}} + \Phi^w_{\text{D}} = \frac{N_{\text{H}}}{\tau_{\text{H,D}}} + \frac{N_{\text{H}^+}}{\tau_{\text{H}^+,\text{D}^+}} + \frac{N_{\text{D}}}{\tau_{\text{H,D}}} + \frac{N_{\text{D}^+}}{\tau_{\text{H}^+,\text{D}^+}}$$

6.2.2 Wall equations

6.2.2.1 Atoms in accessible reservoir

$$\begin{aligned}\frac{\mathrm{d}N^a_{\text{H}}}{\mathrm{d}t} = \; & [1-\Psi(N^a/N^{a,\max})][\eta_a \Phi^w_{\text{H}} + \frac{N^b_{\text{H}}}{\tau_b}] - \rho I^a_{\text{H}/(\text{H+D})} \frac{N^a}{N^{a,\max}} \eta_a \Phi^w \\ & -(\alpha+\beta)\Psi(N^a/N^{a,\max}) I^a_{\text{H}/(\text{H+D})} N^a \end{aligned} \tag{6.8}$$

$$\begin{aligned}\frac{\mathrm{d}N^a_{\text{D}}}{\mathrm{d}t} = \; & [1-\Psi(N^a/N^{a,\max})][\eta_a \Phi^w_{\text{D}} + \frac{N^b_{\text{D}}}{\tau_b}] - \rho(1 - I^a_{\text{H}/(\text{H+D})}) \frac{N^a}{N^{a,\max}} \eta_a \Phi^w \\ & -(\alpha+\beta)\Psi(N^a/N^{a,\max})(1 - I^a_{\text{H}/(\text{H+D})}) N^a \end{aligned} \tag{6.9}$$

The first term on the rhs represents the source of particles into the accessible reservoir. It contains the plasma wall flux, with η_a the fraction of this flux that enters the wall, and a source of particles released from the overflow reservoir that represents the temporarily trapping of particles in denser carbon structures. The second term represents the particle induced detrapping of particles in the accessible reservoir, with ρ the detrapping rate ($\sim$ cross section), $I_{\text{H}/(\text{H+D})}$ the isotopic ratio of the reservoir, and $N^a/N^{a,\max}$ the filling degree of the reservoir ($N^a = N^a_{\text{H}} + N^a_{\text{D}}$). The third term represents particle transfers into the overflow reservoir and spontaneous detrapping, which are both expected to become more important on higher filling degree, represented by Ψ. The latter effect is thus non linear. The value for

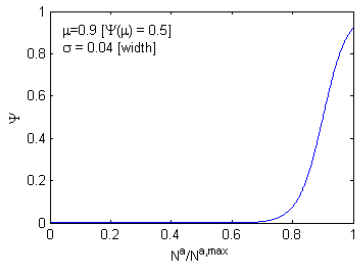

Figure 6.3: The highly speculative function $\Psi(N^a/N^{a,\max})$, to account for observed effects that are only important at high $N^a/N^{a,\max}$-values.

Ψ needs to remain small for small and intermediate filling degrees, and to increase steeply for higher filling degrees. It was chosen to employ the Fermi function $f(N^a/N^{a,\max})$:

$$\Psi(N^a/N^{a,\max}) = 1 - f(N^a/N^{a,\max}) = \frac{\exp(\frac{N^a/N^{a,\max}-\mu}{\omega})}{1+\exp(\frac{N^a/N^{a,\max}-\mu}{\omega})} \tag{6.10}$$

with μ the value for which $f(\mu) = 0.5$ and ω the width. An example of this function with $\mu = 0.9$ and $\omega = 0.04$ is given in Fig. 6.3.

6.2.2.2 Atoms in trapped reservoir

$$\frac{\mathrm{d}N^t_{\mathrm{H}}}{\mathrm{d}t} = \eta_t \Phi^w_{\mathrm{H}} \tag{6.11}$$

$$\frac{\mathrm{d}N^t_{\mathrm{D}}}{\mathrm{d}t} = \eta_t \Phi^w_{\mathrm{D}} \tag{6.12}$$

The only source term for this reservoir is the fraction η_t of the wall flux that will be permanently retained. In the present model there is no loss term included for particles in this reservoir, in agreement with the experimental facts presented in section 6.1.2.1. Including removal out of this reservoir appeared also not necessary to model the experimental ICWC data (see further) meaning that the hydrogen removal rate out of the trapped reservoir is likely much lower than out of the other reservoirs.

6.2.2.3 Atoms in overflow reservoir

$$\frac{\mathrm{d}N^b_{\mathrm{H}}}{\mathrm{d}t} = \alpha \Psi(N^a/N^{a,\max}) I^a_{\mathrm{H}/(\mathrm{H+D})} N^a - \frac{N^b_{\mathrm{H}}}{\tau_b} \tag{6.13}$$

$$\frac{\mathrm{d}N^b_{\mathrm{D}}}{\mathrm{d}t} = \alpha\Psi(N^a/N^{a,\max})(1 - I^a_{\mathrm{H}/(\mathrm{H+D})})N^a - \frac{N^b_{\mathrm{D}}}{\tau_b} \tag{6.14}$$

The first term on the rhs represents the transfer of particles from the accessible reservoir to the overflow reservoir, which becomes important in case the filling factor of the transient reservoir is high, represented by Ψ. The last terms represents the fact that these particles are completely released with slow time constant τ_b.

6.2.2.4 Diffusing atoms

$$\begin{aligned}\frac{\mathrm{d}N^d_{\mathrm{H}}}{\mathrm{d}t} = \quad & \rho I^a_{\mathrm{H}/(\mathrm{H+D})}\frac{N^a}{N^{a,\max}}\eta_a\Phi^w + \Psi(N^a/N^{a,\max})[\eta_a\Phi^w_{\mathrm{H}} + \frac{N^b_{\mathrm{H}}}{\tau_b}] \\ & +\beta\Psi(N^a/N^{a,\max})I^a_{\mathrm{H}/(\mathrm{H+D})}N^a - \frac{N^d_{\mathrm{H}}}{\tau_d}\end{aligned} \tag{6.15}$$

$$\begin{aligned}\frac{\mathrm{d}N^d_{\mathrm{D}}}{\mathrm{d}t} = \quad & \rho(1 - I^a_{\mathrm{H}/(\mathrm{H+D})})\frac{N^a}{N^{a,\max}}\eta_a\Phi^w + \Psi(N^a/N^{a,\max})[\eta_a\Phi^w_{\mathrm{D}} + \frac{N^b_{\mathrm{D}}}{\tau_b}] \\ & +\beta\Psi(N^a/N^{a,\max})(1 - I^a_{\mathrm{H}/(\mathrm{H+D})})N^a - \frac{N^d_{\mathrm{D}}}{\tau_d}\end{aligned} \tag{6.16}$$

The first term on the rhs is the particle source to the diffusing reservoir stemming from particle induced detrapping from the accessible reservoir. The second term represents the fact that free particles in the wall, either stemming from the wall flux or from the overflow reservoir, can not all be trapped in the accessible reservoir. A part, dependent on the filling degree Ψ, will enter the transient reservoir and thus diffuse back out of the wall. The third term accounts for spontaneous detrapping of particles, which is more important in case the filling degree of the transient reservoir is high, again represented by Ψ. The last term is the flux of particles from the wall into the vessel. On including a 1D diffusion module in the model the whole equation can be conserved, while an additional calculation is required to account for the changing 1D particle profile in the subsurface. The last term of the rhs of eq. (6.15) and (6.16) needs to be replaced by the wall release rate obtained from the diffusion module.

6.3 Simulation of TORE SUPRA discharges with plasma current

In this section we will show the capability of the wall reservoir model to reproduce experimental observations during normal tokamak discharges. This

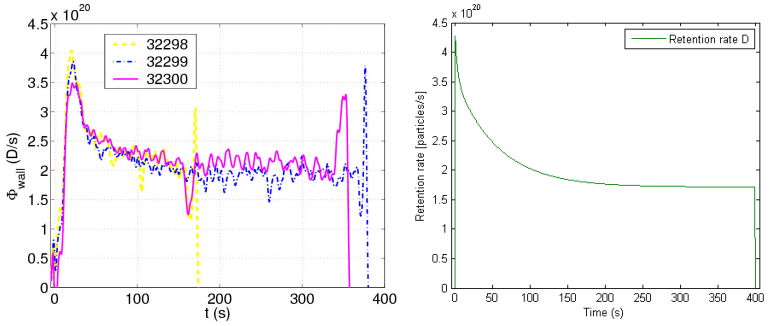

Figure 6.4: Left: Wall retention rate calculated from particle balance during 3 consecutive long discharges [36]. Right: Wall retention rate simulated by reservoir model.

is important to gain confidence in the reservoir model approach, although there is no doubt that the balance equations can still be further optimized, for example by including more PSI physics or by limiting the number of free parameters. We will give two examples of modeling results. First the 400 s long TORE SUPRA discharges 32298-32300, published in [36] will be discussed, then we show the capability of the model to simulate natural density.

6.3.1 Long plasma discharges: TORE SUPRA 32298-32300

Fig. 6.4 (left) shows experimental retention rates obtained from the particle balance for three consecutive long TORE SUPRA discharges. On the figure two phases are separable. During the first phase ($t = 0-100$ s) the retention rate decreases from $4 \cdot 10^{20}$ D/s to $2 \cdot 10^{20}$ D/s, whereafter in the second phase the retention remains constant. The behavior is identical in each shot and shows no sign of wall saturation. It was possible to reproduce these discharges with the reservoir model. Fig. 6.4 (right) shows the simulated retention rate Φ^{ret}, defined as the injection rate from the valves minus the time derivative of the vessel total particle content (neutrals and ions).

$$\Phi^{\mathrm{ret}} = 2\Phi^{\mathrm{injected}}_{\mathrm{H_2,D_2}} - \frac{\mathrm{d}}{\mathrm{d}t}(2N_{\mathrm{H_2}} + 2N_{\mathrm{HD}} + 2N_{\mathrm{D_2}} + N_{\mathrm{H}} + N_{\mathrm{D}} + N_{\mathrm{H^+}} + N_{\mathrm{D^+}}) \quad (6.17)$$

In the simulation we included a typical SOL plasma ($T_e = 100$ eV, $n_e = 4 \cdot 10^{18}\,\mathrm{m}^{-3}$ [36] and $V_{\mathrm{pl}} = 12\,\mathrm{m}^3$). The gas injection ($D_2$) was feedback controlled on the electron density in the SOL. To reproduce the typical ion flux to the wall ($\sim 10^{22}\,/\mathrm{m}^3\mathrm{s}$ [36]), the ion confinement time is set to $\tau_{\mathrm{H^+,D^+}} = n_e V_{\mathrm{pl}}/10^{22} = 5$ ms (the neutral confinement time is set to

a large value, $\tau_{\mathrm{H,D}} = 1\,\mathrm{s}$). The confinement times mentioned here are the 'confinement time components' representing the flux to the wall. The actual typical residence time of a neutral atom in the plasma taking into account the rapid ionization process is of course much smaller. Since it is expected that the constant retention in the second discharge phase ($t > 100\,\mathrm{s}$) results from retention in the permanent reservoir, the fraction of the wall flux that enters this reservoir is set to $\eta_t = 2{\cdot}10^{20}/10^{22} = 0.02$. Table 6.1 summarizes the used discharge parameters. The peak in the retention at the start of

Table 6.1: Wall parameters for tokamak discharges

parameter	value
$N^{a,\max}$	10^{23}
N^a_{D}	$7.5 \cdot 10^{22}$
η_a	0.12
η_t	0.02
ρ	0.7
α	1.5
β	2.5
τ_b	12.5 s
τ_d	1.5 s
μ (Ψ)	1
ω (Ψ)	0.04

the discharge results from the filling of the transient 'diffusive' reservoir ($\sim 1.5 \cdot 10^{21}$ D). The slow decrease in the first phase results from the filling of the overflow reservoir ($\sim 9.7 \cdot 10^{21}$ D). At the end of the discharge, all the particles from these two reservoirs are recovered from the wall. The total additional retention of deuterium in the permanent reservoir is about $6.4 \cdot 10^{22}$ D. The total number of particles stored in the accessible reservoir remains stable around the initial value $7.5 \cdot 10^{22}$ D.

When the model is ran taking into account a saturated hydrogen wall ($I^a_{\mathrm{H/(H+D)}} = 1$) while the valves inject deuterium molecules, it is found that the isotopic ratio decreases from 1 to 0.64 in one 400 s discharge. After 10 similar discharges the isotopic ratio has decreased to 0.27. This is in agreement with the experimental observation that multiple discharges are required to change the wall state. During the discharges the plasma isotopic ratio is approximately equal to the wall isotopic ratio.

6.3.2 Natural plasma density

As mentioned above, natural plasma density means that the plasma is completely fueled by the wall. The discharge is still initiated by injected gas, but

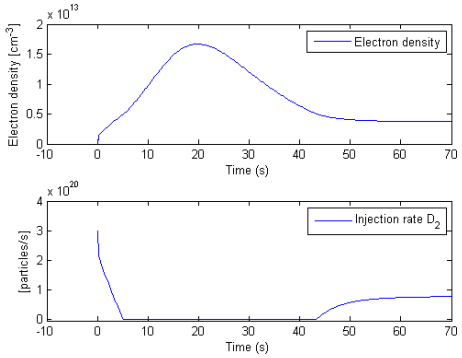

Figure 6.5: Simulated SOL density and injection rate by reservoir model, in case of natural density ($\rho = 2$).

after discharge initiation the wall releases more particles than it absorbs. Under the assumption that the particle release is induced by impinging plasma ions on the walls, the situation of natural density requires that for each impinging particle on the wall at least one particle is released. The condition $\rho = 1$ is not sufficient since a part of the impinging wall flux is permanently trapped. Fig. 6.5 shows a simulation using the same wall parameters as given in table 6.1, but taking $\rho = 2$. A changing ρ-value from discharge to discharge can be defended by the dependency of ρ on the wall flux energy. As such ρ might be dependent on the discharge power. On the figure, both the electron density in the SOL as the deuterium injection rate are given. The gas injection starts at discharge initiation. Although the gas injection is feedback controlled on the plasma density ($n_e = 4 \cdot 10^{18}\,\mathrm{m}^{-3}$), the actual plasma density quickly exceeds the set value by a factor 4, while the gas injection rate at this time is zero. The plasma density is in this case thus not controllable. During experiments this might lead to unstable plasma operation or even disruptions (density limit). Interestingly after some time (50 s) the accessible reservoir attains a new equilibrium value of $N^a = 5 \cdot 10^{22}\,\mathrm{D}$ instead of the initial $7.5 \cdot 10^{22}\,\mathrm{D}$, which corresponds to the experimental observation that the maximum concentration in the accessible reservoir depends via the parameter ρ on the power of the discharge. A subsequent similar shot will feature no natural density.

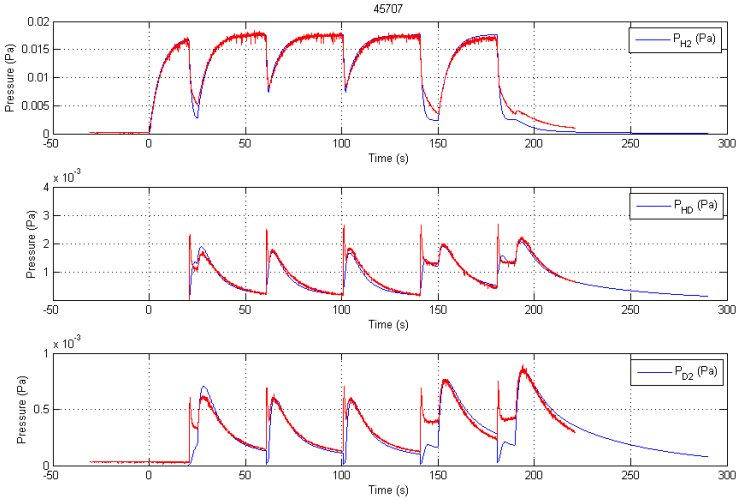

Figure 6.6: Experimental (red, from mass spectrometry) and modeled (blue) partial pressures (H_2, HD and D_2) for TORE SUPRA discharge 45707, consisting of 5 RF pulses ($P_{\mathrm{RF}} = 60\,\mathrm{kW}$) with different pulse lengths (5 s, $2 \times 2\,\mathrm{s}$, and $2 \times 10\,\mathrm{s}$), starting at [$t = 20$, 60, 100, 140 and 180 s] and constant H_2 injection ($p_{\mathrm{H_2}} = 1.75 \cdot 10^{-4}\,\mathrm{mbar}$)

6.4 Simulation of TORE SUPRA H_2-ICWC discharges

6.4.1 Isotopic exchange experiment with pulsed discharges

The model was used to simulate TORE SUPRA H_2-ICWC discharges where the wall was preloaded with D_2. Fig. 6.6 shows experimental (red) and modeled (blue) partial pressures (H_2, HD and D_2) for discharge 45707, consisting of 5 RF pulses ($P_{\mathrm{RF}} = 60\,\mathrm{kW}$) with different pulse lengths (5 s, $2 \times 2\,\mathrm{s}$, and $2 \times 10\,\mathrm{s}$), starting at $t = 20$, 60, 100, 140 and 180 s, and constant H_2 injection ($p_{\mathrm{H_2}} = 1.75 \cdot 10^{-4}\,\mathrm{mbar}$). The choice for this particular discharge is motivated by the fact that all discharge parameters are kept constant except for the changing discharge length from pulse to pulse. The figure shows that the partial pressure time traces can be accurately modeled, with minor deviations to the real pressure (from mass spectrometry) during the discharge itself. Respecting the premise of the model, the wall parameters are identical as those used in the simulations above (table 6.1), except for $\eta_a = 0.0175$ and $\eta_t = 0.015$, which might be explained by different wall flux

characteristics (the ICWC wall flux consists mostly of low energy neutrals, see chapter 5). The initial accessible wall reservoir content was set equal to $N_{\mathrm{H}}^{a} = 1.4 \cdot 10^{22}$ and $N_{\mathrm{D}}^{a} = 1.6 \cdot 10^{22}$. It is found that the modeled partial pressures are not very sensitive to the absolute values of N_{H}^{a} and N_{D}^{a}, as long as their ratio to the maximum value $N^{a,\max}$ is kept constant. In the simulation, the maximum value is set equal to $N^{a,\max} = 4 \cdot 10^{22}$, which is smaller than in normal discharges, motivated by the fact that the likely lower flux energy might not efficiently condition deeper carbon layers, although no clear experimental proof is available for this (see chapter 4.1.2).

Table 6.2 gives the changes that were effectuated in each reservoir. According to the developed reservoir model, ran with the mentioned discharge and wall parameters, the removed deuterium from the wall stems from the accessible reservoir. The removed deuterium from the accessible reservoir is completely replaced by hydrogen. Due to the continuous particle recycling, a part of the wall released deuterium is lost in the permanent reservoir. Additionally, also hydrogen is stored in the permanent reservoir. The total particle balance is found to be in close agreement with the experimental one.

Table 6.2: Particle balance of TORE SUPRA H_2-ICWC discharge 45707 separated in terms of accessible and permanent reservoir

	hydrogen	deuterium
accessible	$3.3 \cdot 10^{20}$	$-3.3 \cdot 10^{20}$
permanent	$6.2 \cdot 10^{20}$	$0.8 \cdot 10^{20}$
total	$9.5 \cdot 10^{20}$	$-2.5 \cdot 10^{20}$
total exp.	$9.1 \cdot 10^{20}$	$-2.1 \cdot 10^{20}$

6.4.2 Optimization of TORE SUPRA pulsed H_2-ICWC discharges

The reservoir model allows to assess the effect of the discharge pulse length and pumping time on the conditioning efficiency of the TORE SUPRA H_2-ICWC discharges, which will be shown below. A comparison of these results to other machines is not straightforward since the choice of the ideal discharge timing (see Fig. 6.7) depends on the outgassing rate of the wall (and thus of the wall materials), and on the device's pumping speed. The dependency on the pumping speed is very illustrative and will be shown below as well. Discharge optimization via the wall model with respect to the pressure and RF power are at this point not carried out.

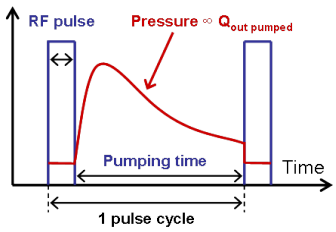

Figure 6.7: Schematic of ICWC operation in pulsed mode. One pulse cycle consists of the RF pulse length and the pumping time. Generally, right after the RF pulse during the pumping time, a typical partial pressure increase of wall desorbed particles can be observed.

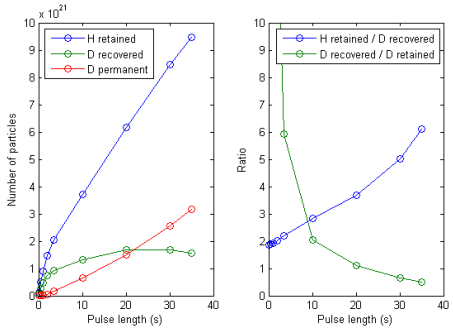

Figure 6.8: Modeled amounts of retained hydrogen, recovered deuterium and permanently stored deuterium as a function of the discharge pulse length for ten 40 s pulse cycles.

6.4.2.1 Pulse length

Fig. 6.8 shows for the same wall and discharge parameters as in the ICWC simulation above, and for a saturated deuterium wall, the amount of retained hydrogen (into the accessible and permanent reservoir), the amount of recovered deuterium and the amount of retained deuterium in the permanent reservoir, as a function of the pulse length. Each plotted data point represents the effect of 10 subsequent RF pulses, including sufficient pumping time (150 s) after the last cycle to ensure complete recovery of the particles from the overflow reservoir, the transient reservoir and the vessel. The total time of one pulse cycle (see Fig. 6.7) is kept constant to 40 s. It is clear from the figure that on longer pulse lengths, while keeping the total cycle period constant, the amount of retained particles increases. This is true both for the injected hydrogen as for deuterium stemming from the accessible reservoir and being transferred via the plasma to the permanent

reservoir. The amount of deuterium released from the accessible reservoir and pumped out of the vessel increases first also on increasing pulse length, reaches a maximum at a pulse length of 20 s, and decreases again on applying even longer pulses. The latter is explained by the fact that the pumping probability of a particle during the discharge is small. A wall desorbed particle is thus very likely sent back to the wall, as was discussed into detail in chapter 4. In this continuous recycling process most of the particles end up in the permanent reservoir. The right figure shows the ratio of retained hydrogen to recovered deuterium. The ratio is always higher than one, and in that respect thus contradicts the experimental result on Fig. 4.13 discussed in section 4.1.4. It is explained by the choice of a fixed value for η_a and η_t given in table 6.1. It is thus logically not possible to obtain a better ratio than $\eta_a/\eta_t \approx 1.2$. The shorter the pulse length, the better the ratio. On the other hand, by employing very short pulses the amount of recovered deuterium remains limited (green line on left figure). The ideal pulse length is 2 s long. For this length the amount of removed deuterium is about one half of the maximum achievable amount (at 20 s), while both the implantation of hydrogen (blue line on left figure), and the re-implantation of wall desorbed deuterium into the permanent reservoir (red line on left figure) remain limited.

6.4.2.2 Pumping time

Fig. 6.9 shows a similar analysis as above. Cases were ran for the same plasma and wall parameters as above and again for a saturated deuterium wall, to determine the amount of retained hydrogen (into the accessible and permanent reservoir), the amount of recovered deuterium and the amount of retained deuterium in the permanent reservoir, as a function of the total cycle period for each of the 2 s RF pulses (see Fig. 6.7). The length of the total conditioning procedure is kept constant to 420 s, including 20 s before the first pulse to build up the required gas pressure. In the simulation sufficient pumping time (150 s) after the last cycle is included. Each plotted data point represents thus the effect of a 420 s conditioning procedure and the number of 2 s RF pulses varies as a function of the requested pumping time. The figure shows clearly that, similar as the above analysis, the more RF time that is included in the conditioning procedure, the more of the injected hydrogen gas is retained into the wall (blue line left figure) and the more of the recovered deuterium from the accessible reservoir will be transferred via the plasma into the permanent reservoir (red line left figure). The maximum amount of recovered deuterium (green line left figure) is at a cycle period of 7 s (2 s pulse + 5 s pumping time). The ratio of retained hydrogen over recovered deuterium (blue line right figure) does not improve

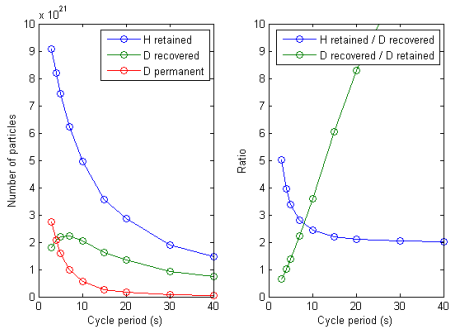

Figure 6.9: Modeled amounts of retained hydrogen, recovered deuterium and permanently stored deuterium as a function of the pulse cycle length with 2 s long RF pulses and a total conditioning procedure length of 420 s.

further for larger cycle periods than 20 s. The amount of removed deuterium for this cycle is about one half of the maximum achievable value (7 s). For shorter cycle periods the hydrogen retention and transfer of deuterium from the accessible to the permanent reservoir becomes too severe, and thus 2 s RF pulses every 20 s seems to be the ideal pulsed ICWC scenario, for these plasma and wall parameters. The pumping time interval of 18 s corresponds to three times the characteristic removal time related to the pumping speed, $3\tau_S$.

6.4.2.3 Pumping speed

The ideal scenario defined above was derived for a TORE SUPRA H_2-ICWC discharge with neutral pressure of $p_{H_2} = 1.75 \cdot 10^{-4}$ mbar (injection continuously constant) and RF generator power of $P_{RF} = 60$ kW. It is thus characteristic for these discharge parameters, the TORE SUPRA wall (outgassing rate) and the TORE SUPRA pumping speed. Fig. 6.10 shows the influence of the pumping speed (characteristic time) on the conditioning efficiency. Cases were ran for the same plasma and wall parameters as above and again for a saturated deuterium wall, to determine the amount of retained hydrogen (into the accessible and permanent reservoir), the amount of recovered deuterium and the amount of retained deuterium in the permanent reservoir. The total conditioning procedure is 420 s long with 2 s RF pulses every 20 s. As the pumping speed decreases (larger τ) the amount of retained hydrogen decreases as well (blue line left figure). This is due to the lower required gas injection rate needed to obtain the pressure of $p_{H_2} = 1.75 \cdot 10^{-4}$ mbar when the pumping speed is lower. The amount of recovered deuterium decreases as well (green line left figure), while the ra-

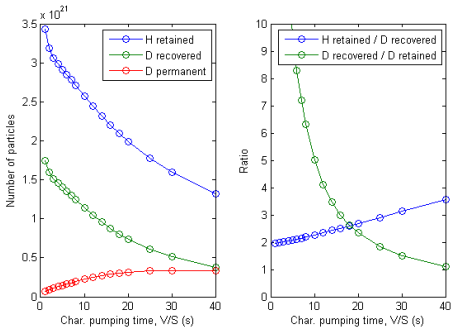

Figure 6.10: Modeled amounts of retained hydrogen, recovered deuterium and permanently stored deuterium as a function of the pumping speed (represented by the characteristic pumping time constant $\tau = V/S$) for 20 s long pulse cycles with 2 s RF pulses and a total conditioning procedure length of 420 s.

tio of retained hydrogen over recovered deuterium increases (blue line right figure). The amount of deuterium stemming from the accessible reservoir and being retained in the permanent reservoir (red line left figure) is lowest for large pumping speeds. In the extreme case of very slow pumping speed ($\tau = 40$ s) the half of the removed deuterium from the accessible reservoir is permanently retained: ratio of recovered deuterium over retained deuterium in the permanent reservoir equals one (green line right figure). A high pumping speed is thus required so that all the released deuterium can be removed from the vessel by the machine pumps between two subsequent RF pulses. The amount of deuterium that is not removed before the start of the next pulse, will become part of the wall flux during this discharge, with a large probability to be retained in the permanent reservoir.

6.5 Discussion

Although the presented model reproduces the experimental facts, both in tokamak discharges as in RF discharges, the question may rise on how robust the presented minimum structure of the reservoir model is. In this final section we will look for differences and similarities of the developed rather phenomenological reservoir model with a physically more profound model describing the hydrogen isotope inventory in porous materials, recently presented in [165].

The latter model considers carbon based materials made of granules and voids. The wall surface is represented by two sets of two layers, each consisting of internal surface layers surrounding the carbon bulk layers. The first set represents codeposited layers, while the second set represents

the actual wall material. The four layers are resolved in one dimension, whereas in our model we considered a 0D representation. Compared to our model the two sets correspond respectively to the permanent reservoir (permanent storage in codeposited layers), and the accessible (surface) and overflow (bulk) reservoir. Transport of particles inside a region is governed by diffusion. Diffusion is in our model only included in the 'surface' layer of the actual wall material (so not in the codeposited layers, nor in layer bulk), and additionally it was chosen to represent the residence time of diffusing particles inside the surface layer by an exponential factor, instead of resolving the 1D diffusion equation explicitly. The trapping site density in all regions is in [165] pre-defined, and no dynamic trapping site production is included in the model, nor in our model. A maximum trapping level in our model is however only included in the accessible reservoir (surface layer of the actual wall material).

For each layer specific physical mechanisms are included. These reactions are all thermally activated which is not the case in our model. (The model even includes a time dependent description of the wall temperature, which is also not the case in our model. It might be interesting to estimate the wall heating during RF discharges, although the short and low energy RF pulses probably don't significantly heat up the entire wall. Fig. 3.13 (JET IR camera image) showed however that wall elements close to the plasma, intersecting the magnetic field lines, do heat up during RF discharges.) For the surface regions seven reactions are considered:

1. volume recombination: not included in our model
2. surface recombination: included in our model, and is assumed to be much faster than the diffusion of particles so that wall release is dominated by diffusion.
3. spontaneous desorption: included in our model and is as in [165] dependent on the filling rate. A dependency on the trapping site energy however is not included in our model.
4. trapping: the trapping of particles in the accessible reservoir and permanent reservoir is included in our model. Only for the accessible reservoir trapping is dependent on the filling rate.
5. detrapping: detrapping of particles is in our model only included for the accessible reservoir and is also dependent on the filling rate, the trapping site density ($N^a_{\max}$) and the detrapping cross section (via ρ).
6. inter-region transport between surface and bulk: see below

7. inter-region transport between bulk and surface: see below

For the bulk regions three reactions are considered:

8. volume recombination: not included in our model
9. inter-region transport between surface and bulk: see below
10. inter-region transport between bulk and surface: see below

Inter-region transport (6 & 7, 9 & 10) is included only for the 'actual wall material' (thus not for the permanent reservoir, corresponding to codeposited layers). Transport from the surface to the bulk in the 'actual wall material' (thus from reservoir 'a' to 'b') is as in [165] also in our model dependent on the filling rate of the accessible reservoir. The bulk material in our model releases particles with a time constant (τ_b), for which no explicit physical representation is found in the paper of [165]. There the exchange of particles depends on the hydrogen concentration and the difference in diffusivity between the two regions.

The elements in the developed phenomenological model correspond fairly well to the physically more profound model presented in [165], albeit in much simplified form. Ideas for model upgrades can be distilled from this last section, were firstly a release of particles from the permanent reservoir should be considered (additional dedicated experiments are probably required). Secondly the exchange of particles between reservoir 'a' and 'b', which is presently dependent on the postulated phenomenological function Ψ should be reconsidered. Thirdly also the spontaneous desorption, in our model likewise dependent on the filling rate expressed by Ψ should receive an equivalent physical process. Once this is achieved the model, or in a first phase only for reservoir 'a' and the diffusing particle reservoir 'd', an upgrade to 1D might be interesting (for this the energy of the wall bombarding species and the particle deposition profile into the wall has to be known).

It must be kept in mind there will always be reasons to implement improvements to these kinds of models. What counts is that what can be learned from the model, while taking into account its limitations.

6.6 Conclusion

In this chapter a minimum structure for a 0D reservoir model of the TORE SUPRA (carbon) wall was determined to obtain more insight in experimental isotopic exchange particle balances. The hypothesis used to build up the model is that the same model structure should be able to describe

the wall behavior during normal plasmas and conditioning procedures. The model consists of a reduced plasma model based on the 0D model described in chapter 5, coupled (via wall fluxes and wall release rates) to the wall description. The wall description is based on four reservoirs: an accessible reservoir in which trapping, detrapping and exchange of particles is possible, a permanent reservoir in which only retention is possible, a transient reservoir representing diffusing particles in the wall and an additional reservoir accounting for effects that become important on high filling degrees of the accessible reservoir. The formulated balance equations are able to describe the time evolution of retention rates in long TORE SUPRA discharges, to reproduce the slow change-over of the wall isotopic ratio, to illustrate the dependency of the maximum concentration of accessible particles in the wall on discharge power and to simulate natural plasma density.

Using the same wall parameters, the model also allows to simulate the H_2, HD and D_2 partial pressures during ICWC isotope exchange discharges. It is found that there is a strong interaction with the typical accessible hydrogen reservoir in carbon and that hydrogen removal from the permanent reservoir is not needed to be included in the model to reproduce the experimental ICWC data. At the same time, the fraction of the wall flux that enters into the permanent reservoir and that is thus permanently lost in the walls is significant ($\sim 1.5\%$). Moreover, the model illustrates also that the wall flux consists both of injected hydrogen isotopes and wall desorbed hydrogen isotopes, stemming from the accessible reservoir. If not optimizing the RF duty cycle, this recycling proces will make that a large part of the desorbed wall isotopes will be retained in the permanent reservoir. At this point it is not clear whether the permanently stored particles can be retrieved, and thus whether hydrogen ICWC can be effectively applied for mitigating the tritium inventory build-up in ITER. Additional experimentation will be required to study this further.

The model is used to study the isotopic exchange efficiency as a function of the discharge timing (RF pulse length and interval between subsequent RF pulses) and the machine pumping speed. It is possible from the wall model to identify the ideal RF pulse length and pumping time between subsequent pulses to maximize the amount of recovered particles from the wall, while minimizing firstly the retention of injected gas, and secondly the loss of wall desorbed particles into the permanent retention reservoir. The optimal discharge timing depends on the wall parameters (materials) and discharge parameters, and additionally to allow for achieving high conditioning efficiencies it is very important that the vacuum pumping speed is high. For a TORE SUPRA H_2-ICWC discharge with $p_{H_2} = 1.75{\cdot}10^{-4}$ mbar, $P_{RF,gen} = 60$ kW and pumping speed of $\tau_S = 6$ s, the ideal discharge timing

consists of 2 s RF pulses every 20 s, respecting a pumping time interval of $3\tau_S = 18$ s.

In a final discussion the developed phenomenological model was compared to a recently presented physically more profounded model [165], from which it is concluded that both models correspond fairly well, although our model features a much more simplified wall representation. Principal ideas for model expansions could be identified.

7 Extrapolation to ITER

In this final chapter an assessment is made on the applicability and the implementation of ICWC on ITER, based on what was learned from the previous chapters. In the first section the envisaged wall conditioning aims of helium and hydrogen ICWC for ITER are summarized. In the second section, the experimental results are extrapolated to ITER, treating the discharge and wall flux homogeneity, and the extrapolated efficiencies of both helium and hydrogen ICWC. In the last section the implementation of ICWC into the ITER operation cycles is discussed.

7.1 ITER ICWC aims

In section 1.5.3 the envisaged wall conditioning techniques for ITER were summarized from [42]. It was concluded that ICWC is a good candidate technique to be applied on ITER during the two weeks long operational cycles, i.e. when the toroidal magnetic field is present, for inter-pulse and overnight conditioning. The conditioning aims for ICWC during the operational cycles cover the three main aims that were summarized in section 1.5, namely: controlling the in-vessel impurity content, controlling the recycling of hydrogenic fluxes and reducing the tritium inventory. The given list of aims from operational point of view is only slightly reduced: in accordance to section 1.5, these conditioning aims can be regrouped according to the discharge gas. The preferred conditioning gases are presently hydrogen (H_2

or D_2) and helium (the use of oxygen to remove tritiated codeposited layers is not allowed due to the resulting formation of highly corrosive tritiated water [42]). The conditioning aims for He-ICWC are:

- recovering plasma start-up after disruptions,
- desaturating the wall from hydrogen isotopes to ensure plasma start-up, and
- improving the plasma performance by impurity removal,

which consequently should be applied before the start of a tokamak plasma, thus for inter-pulse conditioning. The conditioning aims for H_2-ICWC (or D_2-ICWC) are:

- changing the wall isotopic ratio to control the plasma isotopic ratio,
- improving the plasma performance by impurity removal, and
- removing tritium,

which could be adopted for overnight conditioning, followed by He-ICWC to ensure low recycling in the subsequent tokamak plasma.

7.2 Extrapolation of experimental results

7.2.1 General considerations

The presented experiments and modeling efforts in this manuscript are carried out to study and to optimize the efficiency of ICWC. From the analysis it can be concluded that optimal ICWC discharges need to fulfill the following intercorrelated points, which can vary according to the specific conditioning needs:

- optimal discharge control parameters (pressure, RF power, antenna strap phasing, poloidal magnetic field),
- optimal plasma parameters (homogeneous plasma, partially ionized),
- optimal particle fluxes to the wall (high homogeneous wall flux),
- optimal liberation of fuel or impurity particles and low retention of discharge gas (reduce RF pulse length),
- optimal removal of the outgassed particles by the vacuum pumps (foresee pumping time and high pumping speed),

Restrictions in the optimization of ICWC are given by

- the presence of the nominal toroidal magnetic field: either 5.3 T or 2.65 T),
- the available RF frequencies: 40 to 55 MHz, and
- the reliable and safe operation of the RF antenna.

The presented experimental data was obtained on TORE SUPRA, TEXTOR, ASDEX Upgrade and JET, and the modeling efforts have been concentrated mostly on TORE SUPRA and TEXTOR. Limitations in extrapolating the efficiency of ICWC to ITER are consequently given by

- machine size and shape,
- available f_{RF}/B_T values,
- limiter or divertor configuration, and
- most importantly the wall materials,

summarized for the concerned tokamaks in table 7.1. Regarding the last point, future experimentation on the JET device with its recently finalized ITER-like wall can bring closing information on the conditioning efficiency of ICWC.

Table 7.1: Comparison of the relevant machine parameters of ITER, JET, TORE SUPRA, TEXTOR and ASDEX Upgrade (AUG) for the extrapolation of ICWC results to ITER.

	R (m)	a (m)	Shape	Wall mat.	f/B
ITER	6.2	2	D	Be/W	7.5
JET	2.96	1.25	D	Carbon	7.5
TORE SUPRA	2.4	0.72	O	Carbon	12.6
TEXTOR	1.75	0.47	O	Carbon	15.1
AUG	1.65	0.5	D	Tungsten	12.5

7.2.2 Discharge and wall flux homogeneity

7.2.2.1 Plasma homogeneity

The ICRF discharges were found to be toroidally homogeneous on present machines, and can be poloidally inhomogeneous. Vertical inhomogeneities stem from plasma drifts and are more severe at higher RF powers. The vertical homogeneity can be improved by applying a small vertical magnetic

field, which should be typically of the order of $1 - 1.5\%$ of the toroidal field strength (40 mT on TEXTOR for $B_T = 2.3$ T and 30 mT on JET for $B_T = 3.3$ T). Radial inhomogeneities stem from inhomogeneous RF absorption. The employed ICRF heating antennas are designed to couple RF power to dense target plasma ($> 10^{19}\,\mathrm{m}^{-3}$) via excitation of the fast wave (FW). The antenna vacuum RF field is evanescent on present size devices and the standard cut-off density for FW excitation is too high to obtain FW propagation in the typically low density ICWC plasmas ($10^{16} - 10^{18}\,\mathrm{m}^{-3}$). However, antenna operation schemes were found that allow to excite the FW also in low density ICWC plasmas [94] (see section 2.3). These consist either of decreasing the cut-off density for FW propagation, namely operation at close to monopole strap phasing, and/or operation at high cyclotron harmonic numbers (e.i. at strongly reduced toroidal magnetic field values), or rely either on mode conversion (MC) scenarios of the evanescent FW into the slow wave or ion Bernstein wave in plasmas with multiple ion species (which is the case in ICWC plasmas). The JET D_2-ICWC experiments, simulating the ITER full field situation (ITER: $B_T = 5.3$ T, $f_{\mathrm{RF}} = 40$ MHz; JET: $B_T = 3.3$ T, $f_{\mathrm{RF}} = 25$ MHz) with on axis location of the fundamental D^+-ICR layer, while operating the antenna with monopole antenna strap phasing, evidenced the feasibility of filling the entire JET vacuum vessel with plasma. On application of a small vertical field of 30 mT, bright recycling radiation was observed both at the central column on the HFS and in the divertor area.

The ITER plasma volume will be significantly larger than that of present devices (see table 7.1). The LFS torus circumference equals about 50 m and the height of the tokamak chamber will be about 8 m, which might affect the toroidal and vertical plasma homogeneity. The distance from the antenna to the on axis resonance layer will be 2 m, i.e. ~ 1 m longer than on JET, the present largest machine. This means that to ensure the presence of plasma at the HFS, in case the operation is based on mode conversion schemes, RF power has to be transported to the antenna distant (> 2 m) conversion layer [94], requiring the excited FW to have a very long toroidal wavelength. To improve the radial homogeneity via MC schemes, it is proposed based on TOMCAT code predictions to employ the dual frequency mode of operation at intermediate toroidal field[1] to improve the radial homogeneity [94]. Also antenna operation with monopole strap phasing, shifting the wave spectrum to longer wavelengths and bringing the cut-off density for FW propagation closer to the antenna surface in the typical ICWC plasma densities, looks

[1] Utilization of two ICRF antennas at resp. $f = 40$ MHz and 48 MHz, $B_T = 3.6$ T and with He/H_2-mixture: the fundamental H^+-ion resonance for $f = 40$ MHz is located at the LFS (antenna side, $r = 2.3$ m), fundamental H^+-ion resonance for $f = 48$ MHz is located at $r = 0.9$ m from axis.

very promising to ensure radial homogeneous ICWC plasmas on ITER.

Recent papers of Lyssoivan [157, 166] propose that due to the large ITER vacuum vessel dimensions, a vacuum cavity RF Eigen-mode can be excited if the ICRF system is tuned to ITER torus Eigen-frequencies: $f_{\mathrm{TM010}} = 42.98\,\mathrm{MHz}$, TM-mode with on-axis maximum for the E_z-field (parallel to magnetic field). As a result initial ionization and plasma breakdown may occur simultaneously over the whole torus which could facilitate the operation of the ITER antenna in the ICWC mode, and even make the operation safer.

7.2.2.2 Wall flux homogeneity

Section 2.5 summarized the evidenced wall fluxes in hydrogen and helium ICWC discharges. Both in hydrogen ICRF discharges as in helium ICRF discharges the wall flux consists predominantly of low energy neutral hydrogen atoms ($\sim 3\,\mathrm{eV}$): $10^{19} - 10^{20}\,/\mathrm{m^2s}$ in hydrogen discharges, and $10^{18} - 10^{19}\,/\mathrm{m^2s}$ in helium discharges, stemming from wall desorbed hydrogen. The latter fluxes are considered homogeneous. The H^+-ion flux in hydrogen ICRF discharges is estimated to be $10^{17} - 10^{18}\,/\mathrm{m^2s}$, and the He^+-ion flux in helium ICRF discharges is of the order of $5 \cdot 10^{16} - 5 \cdot 10^{17}\,/\mathrm{m^2s}$, with an equal important contribution of wall desorbed hydrogen. Due to ion transport along the magnetic field lines the latter ion fluxes are expected to be received predominantly by limiting surfaces. At the top, HFS and LFS of the vessel of present devices, these limiting surfaces consist of poloidal structures, employed to localize the plasma wall interaction and to protect the plasma facing components from high plasma fluxes. On the bottom of the vessel either the toroidal belt limiter or the divertor receives the ion flux. An important difference between ITER and the present devices is that the ITER first wall will be completely shaped [125]. This makes that the plasma edge behind the limiting surfaces, evidenced on TORE SUPRA, TEXTOR and JET, will be inexistent on ITER. A homogeneous ICWC discharge on ITER will thus effectively reach the whole inner wall area, and thus condition the whole wall.

For present devices it was proposed to inverse the vertical magnetic field between two sets of RF pulses to increase the effective total conditioned surface area. Although the ITER first wall is shaped, adopting this method might be beneficial for ITER as well. The application of an oscillating poloidal magnetic field is however not recommended (see section 3.1).

7.2.3 He-ICWC

On TORE SUPRA, He-ICWC was successfully used to recover tokamak operation after disruptions, and was found to be at least as efficient as the standard applied Taylor like conditioning technique for removing hydrogenic species and H_2O, indicating that the optimized He-ICWC discharges can be effectively employed for inter-pulse conditioning. A 300 s long He-ICWC conditioning procedure (15×2 s RF pulses with 18 s of pumping time (PT) between subsequent pulses, $p_{\mathrm{He}} = 2{\cdot}10^{-4}$ mbar and $P_{\mathrm{RF,gen}} = 150$ kW) could remove on average $3.2 \cdot 10^{20}$ H-atoms from the first wall, or an equivalent of 0.3 monolayers (averaged over three subsequent procedures). Respecting three characteristic pumping times between two subsequent RF pulses, the required ITER pumping time can be estimated at 27 s ($\tau_S \approx 9$ s, see section 2.4.2.3), expanding the conditioning procedure length to 435 s. The plasma density was estimated by the 0D model to be $7 \cdot 10^{17}\,\mathrm{m}^{-3}$ (chapter 5, including $p_{\mathrm{H_2}} = 8 \cdot 10^{-6}$ mbar during plasma and 0.35% of impurities), with a He^+-ion wall flux of $\sim 3 \cdot 10^{17}\,/\mathrm{m}^2\mathrm{s}$. Producing a similar plasma density on ITER requires a coupled power of 4 to 5 MW. The required gas injection rate is estimated to be $Q_{\mathrm{sv}} = 3.1\,\mathrm{Pa.m}^3/\mathrm{s}$, which will cause a gas load of $Q_{\mathrm{sv}} = 1.4\,\mathrm{kPa.m}^3$ to the cryopanels in case of continuous gas injection, or $Q_{\mathrm{sv}} = 0.34\,\mathrm{kPa.m}^3$ per pump, i.e. less than 1% of the pump capacity.

During He-ICWC experiments on ASDEX Upgrade and JET, 60 to 80% of the injected helium was retained in the wall, which is thought to be due respectively to retention in tungsten and retention in beryllium. Since ITER will employ these materials for its main plasma facing components, this point needs to be further investigated in future, e.g. on JET which is presently equipped with an ITER like wall. The pulse cycle optimization criteria in terms of the ratio of retained discharge gas over recovered wall desorbed particles, used for hydrogen ICWC, might be adopted for He-ICWC as well. The ideal ratio for He-ICWC, and moreover for any He-based conditioning discharge, equals 'zero'. In case the (eventual) helium retention rates in beryllium and/or tungsten PFC's during helium discharge conditioning are unacceptable for ITER operation, conditioning discharges in other (noble) gases may need to be developed for the above mentioned aims.

The statement that the optimized TORE SUPRA He-ICWC discharges could be used for routine operation is supported by encouraging results from KSTAR. On KSTAR He-ICWC is routinely operated for inter-pulse and lunchtime conditioning to suppress the H_2O base pressure during the experimental operation campaigns, providing the required conditions for tokamak operation.

7.2.4 D_2-ICWC

In chapter 4 we concluded that hydrogen-ICWC is able to change the wall surface state within short time scales ($\sim$ minutes), both on carbon machines JET, TORE SUPRA and TEXTOR, and on the tungsten machine ASDEX Upgrade. On JET ($170\,m^2$), $8 \times 9\,s$ D_2-ICWC pulses were able to remove in total $1.8 \cdot 10^{22}$ H-atoms from the JET first wall (6 monolayers). This number corresponds on ITER ($900\,m^2$, wall isotopic ratio 50:50 D:T) to $4.8 \cdot 10^{22}$ T-atoms, or 240 mgT, which is of the same order of magnitude than the expected tritium retention in one 400 s (burning time) D-T ITER discharge, estimated at $140 - 500$ mgT/shot [42], illustrating the high isotopic exchange efficiency of D_2-ICWC. From chapter 6 it was however concluded that ICWC predominantly exchanges particles with the subsurface hydrogen reservoirs that are responsible for the short term hydrogen retention in normal tokamak discharges. The removal of tritium-rich codeposited layers is expected to occur at much slower rates: 0.13 monolayers of carbon, possibly stemming from codeposited layers, were removed during these JET D_2-ICWC discharges. The utility of D_2-ICWC for inter-pulse conditioning to mitigate the expected in-vessel tritium inventory build-up, which is mainly due to storage by codeposition [34] is thus not clear at this point. D_2-ICWC for codeposited layer removal will likely require long conditioning procedures for which reason, in section 7.1, the technique was proposed for overnight conditioning.

The high removal rate of wall desorbed atoms in the JET experiments was achieved at the price of an important retention of discharge gas. It is shown that this discharge gas retention can be minimized by applying shorter RF pulses, which has only a minor influence on the total amount of removed wall desorbed atoms. On TORE SUPRA, the ideal 'retained over removed'-ratio of 1 was obtained by applying 2 s long RF pulses with $p_{H_2} = 2 \cdot 10^{-4}$ mbar and $P_{RF,gen} = 60$ kW, where each pulse cycle removed about $1.5 \cdot 10^{20}$ of wall desorbed D-atoms from the vessel (0.11 monolayers). When extrapolating this number to a D_2-ICWC procedure on ITER, e.g. 15×2 s RF pulses with 27 s PT between subsequent pulses, an amount of 1.7 monolayers of hydrogenic particles (68 mgT) can be removed from the first wall in this 435 s procedure.

The removal efficiency is found to increase on increasing coupled RF power. However, on increasing the discharge power, the optimal discharge length decreases (see section 4.1.4). In case of continuous gas injection, the ideal pulse length can be found experimentally as the time instance where the wall desorbed hydrogenic partial pressures reaches a maximum (see Fig. 4.15). The plasma density in hydrogen RF discharges is typically one order of magnitude lower than in helium RF discharges. Reproducing

the TORE SUPRA hydrogen ICWC plasma density or the JET coupled power on ITER requires a coupled power of 1.5 to 2 MW. In chapter 4 it was concluded that the ideal coupled power is the (highest) power at which the plasma can be produced homogeneously, while assuring reliable and safe antenna operation.

7.3 Implementing ICWC in the ITER operation cycles

As stated in section 2.1, ICWC makes use of several main tokamak systems: the RF antennas, the gas injection valves, the machine pumps, the poloidal magnetic field system and the present toroidal magnetic field. Additionally neutral gas and plasma diagnostics are required to monitor the discharge and the conditioning efficiency: namely high resolution mass spectrometry and Penning gauge spectroscopy to distinguish hydrogen, deuterium, tritium and helium partial pressures, and plasma diagnostics adapted to diagnose low temperature ($\sim$ eV) low density ($10^{16} - 10^{18}\,\mathrm{m}^{-3}$) plasmas (see appendix B). The ICWC mode of operation of the tokamak systems needs to be preparable in a reliable and time efficient manner, the latter especially in case of inter-pulse conditioning: respecting the tight tokamak discharge frequency of one D-T discharge every 30 minutes, maximum 20 minutes will be available to prepare and perform an inter-pulse ICWC discharge, including the preparation of the subsequent tokamak discharge. It should therefore be considered to automate the preparations, requiring a minimum of manual interventions, and to simplify the ICWC technique as much as possible, employing the minimum of tokamak systems (only one ICRH antenna and no assistance of additional heating systems such as ECRH for discharge homogenization, if possible).

In the ITER project requirements [68] it is stated that the IC heating and current drive system should be capable of providing heating and current drive, and producing ICWC plasmas. This means that either the full antenna, or a subset of strap arrays needs to be able to operate in monopole phasing, at a frequency of 40 MHz, coupling in the range of 1.5 to 5 MW of ICRH power to the plasma (coupling efficiency ≥ 0.5 [94]). Operating the antenna in ICWC mode requires furthermore that the strap phasing and antenna matching needs to be controllable at the typical low ICWC powers. The strap voltages in ICWC need to be high enough so that the vacuum parallel electric field in front of the antenna is sufficiently high for producing an ionization cascade (order of $4 - 5\,\mathrm{kV/m}$ in hydrogen at 40 MHz). Deleterious effects such as the presence of plasma inside the antenna box, multipactoring and high voltage arcs need to be detectable at the typical

low ICWC powers, and distinguishable from the actual ICRF plasma breakdown. The foreseen RF pulse durations range from 0.25 to 5 s, depending on the applied discharge power and discharge gas. Operation at torus pressures above 10^{-3} mbar has to be avoided for antenna safety considerations (see section 2.3.4.2), and of course, ICRF operation at ICWC pressures but in absence of the toroidal magnetic field has to be prohibited as well.

For the gas injection a continuously constant injection rate is preferable, using multiple injection valves equally divided over the torus wall. The foreseen neutral gas pressures ranges from $(1-5)\cdot 10^{-4}$ mbar (in absence of plasma). On JET, the gas injection was activated after the application of the RF power to limit the neutral gas pressure in the vacuum transmission lines, limiting the risks for arcing generation. Due to the preferred multi-pulse ICWC procedures on ITER it is however not time efficient to await the complete evacuation of the neutral gas before the application of a next RF pulse. Partial suppression of the neutral pressure, by stopping the gas injection at the end of each RF pulse, is however possible.

The foreseen cycling of the eight ITER torus cryopumps, ensuring the operation of four cryopumps at all time, needs to be maintained also during the ICWC procedures. To obtain a high discharge conditioning efficiency, high pumping speeds are required. For an optimal removal efficiency the foreseen pumping time between two RF pulses needs to respect three characteristic pumping times (e.g. 3×9 s)[2].

A static vertical magnetic field of $1 - 1.5\%$ of the toroidal magnetic field is recommended to improve the discharge homogeneity. On present devices, the inversion of the vertical magnetic field between two sets of RF pulses increases the effective plasma wetted area. The latter might also be beneficial on ITER.

[2]The ITER pumping system is currently re-designed, featuring a lower pumping speed, which is disadvantageous with respect to the conditioning efficiency of discharge conditioning techniques. For an optimal conditioning efficiency, the pumping speed needs to be high. The optimal duty cycle needs to be adapted to the final design.

8 Conclusion

The discharge wall conditioning techniques foreseen to be employed during the two weeks long operational cycles of ITER require to operate in presence of the toroidal magnetic field. The presence of the latter magnetic field prevents the use of standard glow discharge conditioning (GDC). Alternative discharge conditioning methods are: the use of tokamak discharges for inter-pulse conditioning (separatrix scanning or controlled disruptions), and ion cyclotron wall conditioning (ICWC) and/or pulsed glow discharge conditioning (P-GDC[1]) for inter-pulse and overnight conditioning. The qualification of wall conditioning discharges applicable in presence of the toroidal magnetic field for inter-shot and overnight conditioning during ITER operation cycles is considered a high priority task. The conditioning discharges need to mitigate the tritium inventory build-up, to achieve the required low recycling levels at plasma start-up and to reduce impurity (and fuel) levels after plasma disruptions. This manuscript focused on the study and optimization of the very promising ICWC technique and assessed its efficiency and applicability to ITER.

The 1st chapter of this manuscript presented the general frame of the PhD subject, covering the motivation for developing magnetic fusion, the tokamak principle, a presentation of the European tokamaks TORE SUPRA, TEXTOR, ASDEX Upgrade and JET, the ITER project, the important influence of plasma wall interaction on tokamak plasma performance, the

[1]The applicability of P-GDC on ITER still needs to be assessed.

resulting need for wall conditioning and the presently employed wall conditioning techniques. The first part of the 2nd chapter explained the principle of ICWC and summarized the state of the art before the start of this PhD, from which the aims of this PhD work were distilled. Hereafter the RF physics aspects of ICWC, the neutral gas cycle in the vacuum vessel (gas injection and vacuum pumps), and an overview of the during this manuscript evidenced plasma wall fluxes were presented. The main results of this PhD were presented in chapters 3 to 6. The emphasis in these chapters is put on discharge characterization, and the study and optimization of the conditioning efficiency. The material of these chapters is obtained during dedicated experiments on the mentioned four European tokamaks, and from the developed 0D plasma model and plasma wall interaction model. Finally, in the last chapter of this manuscript (chapter 7), an assessment was made on the applicability and the implementation of ICWC on ITER, based on what was learned from the previous chapters.

The first part of this conclusive chapter gives a review of the obtained results, covering RF physics aspects, discharge and wall flux homogeneity, the wall conditioning efficiency, the modeling of hydrogen-helium plasmas and the simulation of the plasma wall interaction. The second part of this conclusive chapter represents the general conclusion of this manuscript, containing a review of the ICWC discharge and plasma parameters, and the envisaged aims and obtainable efficiencies of ICWC on ITER.

Overview results

RF physics aspects

The RF physics aspects of ICWC were summarized in section 2.3, starting with an overview of important RF terms, the employed ICRF antennas of the four tokamaks and the experienced deleterious effects on the TORE SUPRA antennas, which remain presently not fully understood. ICRF discharge production (in the present-size fusion machines and frequency band of 20 to 60 MHz) can be divided into the pre-wave stage, where the electron plasma frequency is smaller than the RF generator frequency ($\omega_{pe} < \omega_{\mathrm{RF}}$), and the plasma wave stage ($\omega_{pe} > \omega_{\mathrm{RF}}$). The initial breakdown phase corresponds to the pre-wave phase. The plasma density build-up in the initial breakdown phase is due to collisional ionization by electrons accelerated in the near antenna parallel electric field. Two models were presented that describe this phase. They provide criteria for obtaining plasma breakdown and to avoid spurious plasma formation inside the antenna box. The first model, developed by Dr. A. Lyssoivan, describes the plasma breakdown in front of

the antenna as a function of the toroidal geometry of the parallel electric field, the electric field strength, and the RF frequency. For a given antenna voltage, lowering the RF frequencies moves the radial breakdown region away from the antenna. A longer decay length of the evanescent vacuum RF field expands the breakdown region. The second model, developed by Prof. C. Schüller, takes into account electron multiplication reactions along the whole torus, and includes a breakdown dependency on the discharge pressure, providing a safety criteria on the maximum tolerable discharge pressure to avoid plasma formation at the level of the antenna Faraday screen: $p_{H_2} < 10^{-1}$ Pa. The contribution of this PhD work to the description of the initial breakdown phase consists of a numerical study of the evolution of the electron spatial energy distribution in the initial discharge phase. For this the Vlasov equation is solved for a 1D electron distribution along a toroidal magnetic field line, and a 1D parallel RF electric field distribution, respecting the TEXTOR antenna and torus dimensions. The modeling is carried out to obtain information on whether the plasma builds up mainly in front of the antenna on present devices, or whether electron multiplication along the torus significantly contributes. Only a limited number of RF periods could be simulated due to divergence problems, rendering the analysis fruitless at this point.

In the wave phase, the electromagnetic field expands in the vessel volume causing further space ionization. In this phase the RF power is absorbed mainly collisionally by electrons. Antenna operation schemes were presented that improve the plasma breakdown time, the efficiency for RF power coupling to the plasma and the plasma homogeneity [94]. These consist either of decreasing the cut-off density for FW propagation, namely operation at close to monopole strap phasing and/or operation at high cyclotron harmonic numbers (e.g. at strongly reduced toroidal magnetic field values), or rely on mode conversion scenarios of the evanescent FW into the slow wave and ion Bernstein wave in plasmas with multiple ion species (which is the case in ICWC plasmas). It was concluded that for ICRF plasma production, monopole strap phasing of the ICRF antennas, is the optimal mode of operation.

Chapter 3: Discharge and wall flux homogeneity

In chapter 3 experimental facts on the discharge homogeneity were presented and the contributions of the confinement properties of the ICWC magnetic configuration to the inhomogeneities were analyzed. Achieving homogeneous RF conditioning discharges is important to ensure the effective conditioning of the maximum vessel wall area. It is found that the observed radial inhomogeneities can be explained in terms of RF power

absorption properties, and that vertical inhomogeneities are due to the confinement properties of the magnetic configuration. Close to the vessel walls, in regions where the magnetic field lines are limited by wall structures such as poloidal limiters, the plasma density is observed to decrease exponentially, which evidences the existence of a plasma edge in ICRF discharges. The exponential decrease is characterized by Bohm diffusion. Due to the existence of this edge plasma, the ion wall flux is concluded to be largest on the first limiting surfaces. On ITER the ion wall flux is expected to be homogeneous since no dedicated limiting structures will be present in the vessel, other than the shaped first wall itself.

In order to obtain a radially homogeneous RF plasma in the vessel, proper wave propagation or at least a large decay length of the evanescent RF field is required, allowing to sustain the plasma also at the HFS. It is proposed that the vertical inhomogeneity, showing systematically a higher density at the top of the vessel than at the bottom, is due to the combined gradient and curvature drift of the electrons and the polarization drift velocity of the ions. A review of the plasma confinement properties shows that due to these drifts, at discharge initiation the plasma moves as a whole to the top of the vessel (for clockwise toroidal magnetic field). By applying a small vertical magnetic field that stretches the plasma in the vertical direction, the vertical homogeneity can be improved. During D_2-ICWC experiments on JET, the largest present device, the ITER full field conditions with on axis location of the fundamental D^+-ICR layer could be simulated (ITER: $B_T = 5.3\,\mathrm{T}$, $f_{\mathrm{RF}} = 40\,\mathrm{MHz}$; JET: $B_T = 3.3\,\mathrm{T}$, $f_{\mathrm{RF}} = 25\,\mathrm{MHz}$), while operating the antenna in monopole antenna strap phasing. The experiments evidenced the feasibility of filling the entire JET vacuum vessel with plasma. On application of a small vertical field of 30 mT, bright recycling radiation was observed both at the central column on the HFS and in the divertor area.

A formula is derived for the charged particle confinement time, taking into account charged particle drifts, diffusion and losses along the tilted magnetic field lines. It is found that for partially ionized plasmas the confinement time is only weakly dependent on the applied small vertical magnetic field.

Chapter 4: Wall conditioning efficiency

In chapter 4 an overview was given of the experimental results on the efficiency of ICWC, obtained on TORE SUPRA, TEXTOR, JET and ASDEX Upgrade. Firstly the isotopic exchange efficiency of H_2 and H_2/He discharges was studied, and secondly the efficiency for wall desaturation and recovery of normal tokamak operation after disruptions using helium dis-

charges was studied. In these experiments, the ability of ICWC to change the surface state was shown, the wall fluxes were characterized, particle desorption and retention rates are calculated and the dependencies of the conditioning efficiency on RF power, discharge pressure, magnetic fields, etc. are treated. Finally also, the ICWC efficiency for impurity and codeposited layer removal is discussed.

It was shown that hydrogen ICWC is able to change the surface state within short time scales (removal of hydrogenic monolayers within minutes), both on carbon machines TORE SUPRA, TEXTOR and JET as on tungsten device ASDEX Upgrade. The removal of wall isotopes can go at the price of an up to 10 times higher retention of the discharge gas. It was shown experimentally that the ratio of retained over recovered atoms can be significantly lowered by optimizing the RF duty cycle. The ideal ratio of 1 is been achieved both on TORE SUPRA and on TEXTOR.

The cause of the retention was investigated. Firstly, no 'long term' saturation effects of the retention could be evidenced. Even after 15 min. of cumulated RF discharge time on TORE SUPRA, still extra hydrogen storage was observed. From this it was concluded that mechanisms such as retention in deeper layers, retention by codeposition and retention in remote areas might play an important role in ICWC discharges. From experiments on the tungsten machine ASDEX Upgrade, where the high retention rates were also observed, it was concluded that mechanisms other than codeposition with carbon have to be considered to explain the retention. By comparing the integrated total energetic CX atom flux on JET with the amount of retained isotopes it was concluded that direct implantation of these energetic particles is not the determining mechanism of the hydrogen retention. Additionally it was found that the fast CX atoms have also a limited contribution to the wall release. Both findings were confirmed by the particle balances for two TEXTOR isotopic exchange discharges, resp. with and without fast particle population (high and low B_T). On ASDEX Upgrade it was found that 11% of the retained hydrogen could be recovered by He-GDC illustrating that a significant part of the retained hydrogen is stored in layers accessible by GDC. As it was concluded that hydrogen retention is probably not due to codeposition, nor solely due to the fast particle fluxes, the remaining retained hydrogen (89%) must be stored differently. The hypothesis was made that ICWC discharges reach surface areas that are not accessible by glow discharges. Also the existence of a substantial non-resonant ion wall flux component with energies above the typical GDC flux, causing retention in deeper layers, can at this point not be excluded. Both points require further investigation.

It was found that the measured high retention during the ICWC dis-

charges can be understood as an effect of the high reionization probability: the probability that a neutral molecule will be ionized or dissociated instead of removed by the machine pumps. An extensive comparison of the isotope exchange efficiencies of ICWC and GDC on TORE SUPRA and TEXTOR learned that GDC can achieve 5 to 10 times higher removal rates of wall desorbed species by the machine pumps than ICWC, although the wall release rate of particles during ICWC is about 10 times higher than in GDC. These both points are due to the higher electron density of ICWC discharges compared to GDC, which makes the reionization probability in ICWC discharges ($\sim$ 99.8%) is much higher than in GDC ($\sim$ 86%). Consequently the removal efficiency of wall desorbed species by the machine pumps is less efficient in ICWC than in GDC. Even if the fraction of the wall flux that will be permanently retained is identical in GDC and in ICWC (e.g. 0.2%), the 10 times higher wall fluxes and the lower pumping probability in ICWC makes that the permanent retention rate in ICWC can be problematic (if not optimizing the RF duty cycle), whereas the extra retention in GDC is negligible.

Since reionization and wall flux retention only occurs during the plasma discharge, and since it was shown that most of the wall desorbed gas is recovered after the RF pulse, the use of shorter RF pulses ($\sim 1\,\mathrm{s}$) separated by sufficient time between pulses to recover the wall desorbed particles by the machine pumps ($\sim 20\,\mathrm{s}$ on TORE SUPRA) significantly reduces the retention, without severely lowering the total amount of removed particles.

It was found that the absolute removal efficiency of wall desorbed particles is higher at higher feedback pressures (TEXTOR: $1 \cdot 10^{-4}\,\mathrm{mbar}$ vs. $5 \cdot 10^{-4}\,\mathrm{mbar}$). Regarding the RF power it was found that the efficiency increases on increasing power (although the pulse length has to be decreased at higher RF powers, since retention is more important at higher powers), but that the gain is limited. The ideal RF power is the power at which the discharge can be established most reliably from point of view of antenna operation, and at which the discharge is most homogeneous. Whereas the toroidal field strength has a limited effect on the conditioning efficiency (at fixed coupled power), the ICWC conditioning efficiency can be improved by applying a vertical magnetic field. As charged particles are transported along the magnetic field lines, tilting the field lines can slightly increase or change conditioned areas.

He-ICWC discharges were successfully applied on TORE SUPRA to desaturate the wall from hydrogenic particles. In three discharges consisting each of $15 \times 2\,\mathrm{s}$ RF pulses with 18 s PT between pulses ($p_{\mathrm{He}} = 2 \cdot 10^{-4}\,\mathrm{mbar}$ and $P_{\mathrm{RF,gen}} = 200\,\mathrm{kW}$), 1 monolayer, or 5 to 10% of the short term retention accessible by plasma operation, could be removed illustrating the effective-

ness of He-ICWC. The hydrogen is mostly recovered after the RF pulse which indicates that including pumping time in the conditioning procedure increases the removal efficiency of wall desorbed particles. The removal efficiency is also a clear function of the coupled power: for a same discharge length, the hydrogen removal efficiency increases with a factor 2 on increasing the coupled power form 50 kW to 150 kW. It is expected that redeposition of wall desorbed particles is as in the case of H_2-ICWC also important in He-ICWC. Therefore, although it was found that the amount of removed hydrogen from the wall improves on increasing pulse length, it is recommended to also limit the RF pulse length in He-ICWC.

On TORE SUPRA, He-ICWC was successfully applied to recover normal tokamak operation after plasma disruption events (3/3 attempts successful). It is found that the removal efficiency of He-ICWC is at least as efficient as that of the routinely operated TDC technique, both for hydrogen removal as for removal of H_2O, indicating that the optimized He-ICWC discharges can be used for inter-pulse conditioning during experimental campaigns on TORE SUPRA.

Both on JET and ASDEX Upgrade is was found that during helium containing ICWC discharges, a significant amount of the injected helium was consumed by the wall, resp. 80% and 60%. The beryllium elements on the ICRF antennas are thought to be responsible for this on JET. The helium losses are also reported for He-GDC on ASDEX Upgrade. Since ITER will have as main plasma facing components tungsten and beryllium it is important to investigate this effect further in future, e.g. on JET which is presently equipped with an ITER like wall. The pulse cycle optimization criteria in terms of the ratio of retained discharge gas over recovered wall desorbed particles, used for hydrogen ICWC, might be adopted for He-ICWC as well. The ideal ratio for He-ICWC, and moreover for any He-based conditioning discharge, equals 'zero'. In case the (eventual) helium retention rates in beryllium and/or tungsten PFC's during helium discharge conditioning are unacceptable for ITER operation, conditioning discharges in other (noble) gases may need to be developed to substitute helium discharge conditioning.

During JET D_2-ICWC experiments (8×9 s long RF pulses) where the wall was preloaded by H_2-GDC, 0.13 monolayers of carbon were removed from the vessel. This relatively high removal efficiency can however not be extrapolated to the removal efficiency of codeposited layers since the carbon source is not known. The exposure of samples to TEXTOR ICWC plasmas to evidence carbon erosion or deposition remained inconclusive. On JET it was found that the impurity removal efficiency improves on increasing the discharge power, and finally it was evidenced that there is no clear influence of the present energetic CX flux on the removal of impurities (TEXTOR

experiments at high and low B_T).

The removal efficiency of the marker gas argon was tested on TEXTOR. In only seven 5 s H_2-ICWC pulses ($P_{RF,gen} = 2{\times}50$ kW, $p_{H_2} = 5{\cdot}10^{-4}$ mbar), 25% of the introduced argon by H_2/Ar-GDC could be removed. This illustrates that ICWC reaches a large part of the wall area affected by GDC.

Finally it was illustrated both on TEXTOR (H_2-ICWC) and TORE SUPRA (He-ICWC) that ICWC can reduce the oxygen content in the vacuum vessel. Whether this removal efficiency is sufficient to ensure tokamak operation could not be tested in the course of this PhD. For this ICWC has to be tested as routine conditioning technique during experimental campaigns. Promising results on this subject were reported by the KSTAR-team [130]. The superconducting tokamak KSTAR employs He-ICWC routinely for inter-pulse and lunchtime conditioning, in order to keep the vessel H_2O pressure below the operational limit.

Chapter 5: 0D modeling of hydrogen-helium ICWC plasmas

In chapter 5 the 0D kinetic description of magnetized toroidal hydrogen-helium RF discharges was outlined. The model is developed to obtain insight on ICRF plasma parameters, particle fluxes to the walls and the main collisional processes, the latter being the fundamental mechanism for the build-up of a plasma. This is of particular importance since most standard tokamak plasma diagnostics are not adapted to diagnose the typical low temperature and low density RF plasmas.

The 0D plasma description is based on the energy and particle balance equations for nine principal species: H, H^+, H_2, H_2^+, H_3^+, He, He^+, He^{++} and e^-. It takes into account (1) elementary atomic and molecular collision processes, such as excitation/radiation, ionization, dissociation, recombination, charge exchange, etc. and elastic collisions, (2) particle losses due to the finite dimensions of the plasma volume and confinement properties of the magnetic configuration, and particle recycling, (3) active pumping and gas injection, (4) RF heating of electrons (and protons) and (5) a qualitative description of plasma impurities.

On inclusion of plasma impurities the model reproduces experimental plasma density dependencies on discharge pressure and coupled RF power, both for hydrogen RF discharges ($n_e \approx (1-5)\cdot 10^{10}\,\mathrm{cm}^{-3}$) as for helium discharges ($n_e \approx (1-5)\cdot 10^{11}\,\mathrm{cm}^{-3}$). The modeled wall fluxes of hydrogen discharges are in the range of what is estimated experimentally: $\sim 10^{19} - 10^{20}$ /m^{2}s for H-atoms, and $\sim 10^{17}{-}10^{18}$ /m^{2}s for H^+-ions. In case of helium RF discharges it is found that the wall desorbed particles contribute largely

to the wall flux. The main wall bombarding flux are hydrogen neutrals. The helium and hydrogen ion flux are approximately of the same order of magnitude although the hydrogen neutral pressure, stemming from wall desorption, is in accordance to mass spectrometry data less than 5% of the helium neutral pressure.

The presented 0D ICWC plasma model allowed to reproduce experimental pressure, density and coupled power temporal dependencies of a TORE SUPRA H_2-ICWC discharge from discharge initiation to steady state plasma, and gave insight into the particle wall fluxes and retention rates. The wall interaction, represented in the model by a particle recycling coefficient, has a major influence on the neutral pressure and plasma density in H_2-ICWC discharges (in case of constant injection). During the breakdown phase, particles are transiently stored in the wall causing a steep pressure drop while during the plasma phase an equilibrium pressure is formed where the permanent hydrogen retention rate approximately equals the gas injection rate. This modeling result reconfirms that employing shorter RF pulses ($\sim$ 1 to 2 s) instead of long or continuous discharges is favored to limit retention, while maximizing the recovery of transiently stored particles.

It is estimated that a reconsideration of the inclusion of plasma impurities is required to reproduce the on TEXTOR evidenced sudden plasma density increase on increasing the discharge helium concentration in He/H_2-ICWC discharges, while keeping the total pressure constant. Since the coupled power, and thus the coupling efficiency does not show a similar discontinuity it is expected that collisional processes lie at the basis of this effect. To better understand the role of the RF power coupling aspects on this effect an upgrade of the 0D model to 1D, including a self consistent description of the coupled RF power is required.

Chapter 6: Modeling of the wall interaction

In chapter 6 a minimum structure for a 0D reservoir model of the TORE SUPRA (carbon) wall was determined to obtain more insight in experimental isotopic exchange particle balances. The hypothesis used to build up the model is that the same model structure should be able to describe the wall behavior during normal plasmas and conditioning procedures. The model consists of a reduced plasma model based on the 0D model described above, coupled (via wall fluxes and wall release rates) to the wall description. The wall description is based on four reservoirs: an accessible reservoir in which trapping, detrapping and exchange of particles is possible, a permanent reservoir in which only retention is possible, a transient reservoir representing diffusing particles in the wall and an additional reservoir accounting for effects that become important on high filling degrees of the

accessible reservoir. The formulated balance equations are able to describe the time evolution of retention rates in long TORE SUPRA discharges, to reproduce the slow change-over of the wall isotopic ratio, to illustrate the dependency of the maximum concentration of accessible particles in the wall on discharge power and to simulate natural plasma density, i.e. a plasma that is solely fueled by the wall.

Using the same wall parameters, the model also allows to simulate the H_2, HD and D_2 partial pressures during ICWC isotope exchange discharges. It is found that there is a strong interaction with the typical accessible hydrogen reservoir in carbon and that hydrogen removal from the permanent reservoir is not needed to be included in the model to reproduce the experimental ICWC data. At the same time, the fraction of the wall flux that enters into the permanent reservoir and that is thus permanently lost in the walls is significant ($\sim 1.5\%$). Moreover, the model illustrates also that the wall flux consists both of injected hydrogen isotopes and wall desorbed hydrogen isotopes, stemming from the accessible reservoir. If not optimizing the RF duty cycle, this recycling process will make that a large part of the desorbed wall isotopes will be retained in the permanent reservoir. At this point it is not clear whether the permanently stored particles can be retrieved, and thus whether hydrogen ICWC can be effectively applied for mitigating the tritium inventory build-up in ITER. Additional experimentation will be required to study this further.

The model is used to study the isotopic exchange efficiency as a function of the discharge timing (RF pulse length and interval between subsequent RF pulses) and the machine pumping speed. It is possible from the wall model to identify the ideal RF pulse length and pumping time between subsequent pulses to maximize the amount of recovered particles from the wall, while minimizing firstly the retention of injected gas, and secondly the implantation of wall desorbed particles into the permanent retention reservoir. The optimal discharge timing depends on the wall parameters (materials) and discharge parameters, and additionally to allow for achieving high conditioning efficiencies it is very important that the vacuum pumping speed is high. For a TORE SUPRA H_2-ICWC discharge with $p_{H_2} = 1.75{\cdot}10^{-4}$ mbar, $P_{RF,gen} = 60$ kW and pumping speed of $\tau_S = 6$ s, the ideal discharge timing consists of 2 s RF pulses every 20 s, i.e. respecting three characteristic pumping times ($3\tau_S$) between 2 discharge pulses.

General conclusion

ICWC discharge and plasma parameters

ICWC, operated in presence of the toroidal magnetic field, makes use of four main tokamak systems: the ICRF antennas to initiate and sustain the conditioning discharge, the gas injection valves to provide the discharge gas, the machine pumps to remove the wall desorbed particles, and the poloidal magnetic field system to optimize the discharge homogeneity. Additionally neutral gas and plasma diagnostics are required to monitor the discharge and the conditioning efficiency. The typical ICWC discharge pressures range from $2 \cdot 10^{-5}$ to $5 \cdot 10^{-4}$ mbar, with applied ICRF powers between 50 and 400 kW (on present devices), resulting in partially ionized low temperature plasmas ($T_e = 3-5$ eV) with densities in the order of $n_e \approx (1-5) \cdot 10^{10}$ cm^{-3} for hydrogen RF discharges and $n_e \approx (1-5) \cdot 10^{11}$ cm^{-3} for helium discharges. The conditioning efficiency increases on increasing pressure and power. Pressures higher than 10^{-3} mbar have to be avoided for antenna safety considerations. The ideal RF power is the power at which the discharge can be established most reliably from point of view of antenna operation, and at which the discharge is most homogeneous. For an optimal radial plasma homogeneity, antenna coupling efficiency and plasma breakdown time, the antennas are operated in monopole phasing on present devices. The recommended vertical magnetic field to increase the vertical homogeneity is of the order of $1 - 1.5\%$ of the toroidal field. ICWC discharges are operated preferably in pulsed mode, with RF pulse lengths of the order of ~ 1 s, dependent on the coupled RF power, and respecting three characteristic vacuum pumping times between subsequent pulses. This allows for an optimal removal of wall desorbed particles between RF pulses, and limits the permanent retention of discharge gas and wall desorbed particles. For an optimal removal efficiency, the pumping speed needs to be as high as possible.

ICWC discharges (like other discharge conditioning discharges) are initiated to produce a controlled flux of particles to the plasma facing components (PFC's). The interaction between this flux and the wall surfaces aims at removing impurities and fuel particles from the first wall (see further for specific conditioning aims). In section 2.5 an overview of the characterized wall flux during ICWC discharges was given, which we will repeat here briefly. Hydrogen ICWC:

- Neutral particles: $10^{19} - 10^{20}$ /m^{2}s (homogeneous over wall area), $3 - 5$ eV (chemical erosion), stemming predominantly from the dissociation of neutral hydrogen molecules.

- Energetic neutral particles: $10^{15} - 10^{17}\,/\mathrm{m}^2\mathrm{s}$ (also homogeneous), $1-10\,\mathrm{keV}$ (physical sputtering), stemming from CX collisions between low energy neutrals and high energy ions, produced by resonant absorption of RF power at the resonance layers. The contribution of this energetic CX flux to the conditioning effect is limited.

- Ions: $10^{17}-10^{18}\,/\mathrm{m}^2\mathrm{s}$ consisting mainly of H^+-ions, inhomogeneous on present devices: since ions are transported along the magnetic field lines, the highest flux will be on first limiting surfaces (due to the shaped ITER wall, the ion wall flux is expected to be homogeneous on ITER). The energy of the impinging ions is presently unknown (plasma ions of $\sim 3\,\mathrm{eV}$ which energy might increase due to sheath effects).

Helium ICWC:

- Ions: $5\cdot10^{16}-5\cdot10^{17}\,/\mathrm{m}^2\mathrm{s}$ consisting mainly of He^+-ions, the highest flux will be on limiting surfaces. An additional large ion flux contribution from wall desorbed hydrogen was evidenced.

- Neutrals: stemming from wall desorbed hydrogen, $10^{18} - 10^{19}\,/\mathrm{m}^2\mathrm{s}$, $3-5\,\mathrm{eV}$.

Feasible conditioning aims of ICWC on ITER

The aims for conditioning techniques during the ITER operational cycles, namely when the toroidal magnetic field is present, are controlling the in-vessel impurity content, controlling the recycling of hydrogenic fluxes and reducing the tritium inventory (as part of the good household approach proposed by Roth et al. [34] to keep the in-vessel tritium level below the administrative limit of 640 g).

The envisaged conditioning gases are presently hydrogen and helium. He-ICWC discharges are found to be efficient for desaturating the walls on TORE SUPRA, have been successfully employed to recover tokamak operation after plasma disruption events on TORE SUPRA, are found to be at least as efficient as the routinely employed TDC technique on TORE SUPRA, and were mentioned to be efficient for reducing the H_2O vacuum base pressure in the KSTAR device. He-ICWC is concluded to be a high potential candidate technique for inter-pulse conditioning on ITER. It is concluded that from operational point of view the conditioning aims for He-ICWC can be summarized as:

- recovering plasma start-up after disruptions,

- desaturating the wall from hydrogen isotopes to ensure plasma start-up, and
- improving the plasma performance by impurity removal.

Helium retention in beryllium and tungsten might however be severe, and requires further study (required for all helium based conditioning techniques).

H_2-ICWC is shown to be able to change the surface state within short time scales (removal of hydrogenic monolayers within minutes), both on carbon machines TORE SUPRA, TEXTOR and JET as on tungsten device ASDEX Upgrade. Most of the removed hydrogen is thought to stem from the typical accessible wall surface reservoirs responsible for the short term retention during tokamak discharges. During JET D_2-ICWC experiments (8×9 s long RF pulses) that were able to remove 6 monolayers of hydrogen atoms from the wall, at the same time 0.13 monolayers of carbon were removed from the vessel. This relatively high removal efficiency could however not be extrapolated to the removal efficiency of codeposited layers. It is nevertheless expected that the removal rate of codeposited layers occurs at much lower speeds than the exchange of hydrogen isotopes with the accessible surface reservoir. For significant removal of tritium-rich codeposited layers on ITER employing the optimized D_2-ICWC technique, long conditioning procedures are likely required. The conditioning aims for H_2-ICWC (or D_2-ICWC) are:

- changing the wall isotopic ratio to control the plasma isotopic ratio,
- improving the plasma performance by impurity removal, and
- removing tritium, for which long procedures are required.

On ITER, hydrogen ICWC could thus be adopted for overnight conditioning, followed by He-ICWC to ensure low recycling in the subsequent tokamak plasma.

Application of ICWC on ITER

On ITER the ICWC mode of operation of the tokamak systems needs to be preparable in a reliable and time efficient manner, with a minimum of manual interventions. A 435 s long He-ICWC procedure is proposed for ITER inter-pulse conditioning, extrapolated from optimized discharge results obtained on present tokamaks. The procedure consists of 15×2 s RF pulses, respecting three characteristic vacuum pumping times between two subsequent RF pulses ($3\tau_S = 27$ s), $p_{\mathrm{He}} = 2 \cdot 10^{-4}$ mbar and a coupled power between 4 and 5 MW. The proposed pulsed mode of operation

allows optimal removal of wall desorbed particles and will limit eventual helium retention in the PFC's. Extrapolated from TORE SUPRA results, the procedure allows to remove 0.3 monolayers of hydrogen isotopes from the first wall. The required helium gas injection for this procedure corresponds to less than 1% of the cryopump capacity. Also a 435 s long H_2 or D_2-ICWC procedure is proposed for ITER (that needs to be prolonged in case of overnight conditioning), extrapolated from optimized discharge results on present tokamaks. The procedure consists of 15×2 s RF pulses, respecting three characteristic vacuum pumping times between two subsequent RF pulses ($3\tau_S = 27$ s), $p_{H_2/D_2} = 2 \cdot 10^{-4}$ mbar and a coupled power between 1.5 and 2 MW. Also for hydrogen ICWC, the proposed pulsed mode of operation optimizes the removal of wall desorbed particles and limits its discharge gas retention. Extrapolated from TORE SUPRA results, the procedure allows to remove 1.7 monolayers of hydrogen isotopes from the first wall, corresponding to 68 mg of tritium in case of a 50:50 D:T wall isotopic ratio. To ensure optimal discharge homogeneity for both conditioning procedures, a vertical magnetic field is proposed of the order of $1 - 1.5\%$ of the toroidal field, and the expected ideal antenna strap phasing is monopole phasing.

References

[1] *International Energy Outlook 2010.* Electronic publication, U.S. Energy Information Administration, Office of Integrated Analysis and Forecasting, U.S. Department of Energy, Washington, DC 20585, July 2010.

[2] *Supply of Uranium.* Electronic publication, World Nuclear Association, 22a St James's Square, London SW1Y 4JH, United Kingdom, December 2010.

[3] *Three Mile Island, Chernobyl, and Tokaimura.* Electronic publication. Website of the Health Physics Society.

[4] H. Nifenecker. *Superphénix en chiffres.* Electronic publication, ISN Grenoble, February 1998.

[5] W. Marth. *The Story of the European Fast Reactor Cooperation.* Technical report, Kernforschungszentrum Karlsruhe GmbH, Postfach 3640, 76021 Karlsruhe, 1993.

[6] J. Ongena and G. Van Oost. *Energy for future centuries, Prospects for fusion power as a future energy source.* Trans. Fus. Sci. Tech., 49, 2006.

[7] O. Edenhofer et al. *Summary for Policymakers*, pages 1–25. Cambridge University Press, Cambridge, United Kingdom and New York (NY), USA, May 2011. In IPCC Special Report on Renewable Energy Sources and Climate Change Mitigation [O. Edenhofer, R. Pichs-Madruga, Y. Sokona, K. Seyboth, P. Matschoss, S. Kadner, T. Zwickel, P. Eickemeier, G. Hansen, S. Schlömer, C. v. Stechow (eds)].

[8] W. Nuttall. *Fusion as an Energy Source: Challenges and Opportunities.* Technical report, Institute of Physics, 76 Portland Place, London W1B 1NT, UK, September 2008.

[9] M. Vanderhaegen and G. Janssens-Maenhout. *Considerations on safety and proliferation-resistant aspects for the MSBR design.* Nuclear Engineering and Design, 240(3):482 – 488, 2010.

[10] M. Vanderhaegen, G. Janssens-Maenhout, P. Peerani, and A. Poucet. *On the proliferation issues of a fusion fission fuel factory using a molten salt.* Nuclear Engineering and Design, 240(10):2988 – 2993, 2010. 4th International Topical Meeting on High Temperature Reactor Technology (HTR 2008), with Regular Papers.

[11] H. A. Bethe. *The fusion hybrid.* Physics Today, 32(5):44–51, 1979.

[12] M. B. Kalinowski and L. Colschen. *International Control of Tritium to Prevent Horizontal Proliferation and to Foster Nuclear Disarmament.* Science & Global Security, 5:131–203, 1995.

[13] C. Nave. *Fission and fusion can yield energy.* Electronic publication, July 2011. HyperPhysics, Department of Physics and Astronomy, Georgia State University, Atlanta.

[14] A. Bradshaw, T. Hamacher, and U. Fischer. *Is nuclear fusion a sustainable energy form?* Fusion Eng. & Design, DOI: 10.1016/j.fusengdes.2010.11.040:–, 2011.

[15] J. Wesson. *Tokamaks.* Oxford Science Publications, Clarenden Press, Oxford, 2^{nh} edition edition, 1997.

[16] Electronic publication. FOM Institute for Plasma Physics, Rijnhuizen.

[17] Electronic publication. A website from the Institute of Physics, IOP.

[18] N. Fecorczak. *Etude Expérimentale du Transport Turbulent au Bord d'un Plasma de Tokamak.* PhD thesis, l'Université de Provence (France), Septembre 2010. Service Intégration Plasma Paroi, Institut de Recherche pour la Fusion Magnétique, CEA Cadarache.

[19] B. Schweer et al. *Limiter Lock Systems at TEXTOR: Flexible Tools for Plasma-Wall Investigation.* Fus. Sci. Tech., 47:171 –181, 2005.

[20] Electronic publication. JET-EFDA website.

[21] F. Durodié et al. *Main design features and challenges of the ITER-like ICRF antenna for JET.* Fusion Eng. & Design, 74(1-4):223 – 228, 2005. Proceedings of the 23rd Symposium of Fusion Technology - SOFT 23.

[22] J. Paméla et al. *The JET Programme in Support of ITER.* Technical Report EFDA-JET-CP(06)04-19, EFDA, Culham Science Centre, Abingdon, Oxon, OX14 3DB, UK., September 2006. Preprint of Paper to be submitted for publication in Proceedings of the SOFT Conference.

[23] J. Noterdaeme et al. *First results of ion cyclotron resonance heating on ASDEX upgrade.* In AIP Confer. Series, volume 289, pages 12–23, October 1994. The tenth topical conference on radio frequency power in plasmas.

[24] Electronic publication. ITER website.

[25] Electronic publication. EFDA website.

[26] M. Shimada et al. *Chapter 1: Overview and summary.* Nucl. Fusion, 47(6):S1, 2007.

[27] R. Pitts et al. *Physics basis and design of the ITER plasma-facing components.* J. Nucl. Mat., DOI: 10.1016/j.jnucmat.2011.01.114:–, 2011.

[28] B. Beaumont. *SRD-51 (ICH&CD) from doors.* Technical report, ITER Organization, 13115, St. Paul-lez-Durance , France, October 2009.

[29] A. Messiaen et al. *Performance of the ITER ICRH system as expected from TOPICA and ANTITER II modelling.* Nucl. Fusion, 50(2):025026, 2010.

[30] J. Winter. *Wall conditioning in fusion devices and its influence on plasma performance.* Plasma Phys. & Controlled Fusion, 38(9):1503, 1996.

[31] R. A. Pitts et al. *Material erosion and migration in tokamaks.* Plasma Phys. & Controlled Fusion, 47(12B):B303, 2005.

[32] A. Kirschner, V. Philipps, J. Winter, and U. Kögler. *Simulation of the plasma-wall interaction in a tokamak with the Monte Carlo code ERO-TEXTOR.* Nucl. Fusion, 40(5):989, 2000.

[33] A. Ekedahl et al. *Operational limits during high power long pulses with radiofrequency heating in Tore Supra.* Nucl. Fusion, 49(9):095010, 2009.

[34] J. Roth et al. *Tritium inventory in ITER plasma-facing materials and tritium removal procedures.* Plasma Phys. & Controlled Fusion, 50(10):103001, 2008.

[35] G. McCracken and P. Stott. *Plasma-surface interactions in tokamaks.* Nucl. Fusion, 19(7):889, 1979.

[36] E. Tsitrone, C. Brosset, J. Bucalossi, and et al. *Deuterium retention in Tore Supra long discharges.* IAEA Conference Proceedings, 2004. Proceedings of 20th IAEA Fusion Energy Conference.

[37] J. Davis and A. Haasz. *Reemission and thermal desorption of D0, D2 and CD4 from graphite.* J. Nucl. Mat., 220-222:832 – 835, 1995. Plasma-Surface Interactions in Controlled Fusion Devices.

[38] C. Grisolia, L. Horton, and J. Ehrenberg. *Modelling of hydrogen conditioning, retention and release in Tore Supra.* J. Nucl. Mat., 220-222:516 – 520, 1995. Plasma-Surface Interactions in Controlled Fusion Devices.

[39] K. Dimoff, C. Boucher, K. J. Parbhakar, and A. K. Vijh. *Modeling of impurity release rates during wall conditioning of a vacuum vessel by electric discharge.* Journal of Vacuum Science & Technology A: Vacuum, Surfaces, and Films, 6(5):2876–2882, 1988.

[40] B. Pégourié et al. *Overview of the deuterium inventory campaign in Tore Supra: Operational conditions and particle balance.* J. Nucl. Mat., 390-391:550 – 555, 2009. Proceedings of the 18th International Conference on Plasma-Surface Interactions in Controlled Fusion Device, Proceedings of the 18th International Conference on Plasma-Surface Interactions in Controlled Fusion Device.

[41] B. Pégourié and T. S. TEAM. *Particle balance and fuel retention in TORE SUPRA.* Fus. Sci. Tech., 56:1334 – 1352, 2009.

[42] M. Shimada and R. A. Pitts. *Wall conditioning on ITER.* J. Nucl. Mat., DOI: 10.1016/j.jnucmat.2010.11.085:–, 2010.

[43] S.-H. Hong and et al. *On the Spherical Dusts in Fusion Devices.* IAEA Conference Proceedings, October 2010. Proceedings of 23th IAEA Fusion Energy Conference, Deajeon.

[44] A. Peacock et al. *Dust and flakes in the JET MkIIa divertor, analysis and results.* J. Nucl. Mat., 266-269:423 – 428, 1999.

[45] R. Smirnov et al. *Modeling of dust impact on tokamak edge plasmas.* J. Nucl. Mat., DOI: 10.1016/j.jnucmat.2011.01.004:–, 2011.

[46] J. Winter. *Dust in fusion devices: a multi-faceted problem connecting high- and low-temperature plasma physics.* Plasma Phys. & Controlled Fusion, 46(12B):B583, 2004.

[47] S. Rosanvallon et al. *Dust in ITER: Diagnostics and removal techniques.* J. Nucl. Mat., 386-388:882 – 883, 2009. Fusion Reactor Materials, Proceedings of the Thirteenth International Conference on Fusion Reactor Materials.

[48] C. Grisolia. *Conditionnement TS.* Technical report, Association EUR-CEA / DRFC, TORE SUPRA, 1990. private communication.

[49] V. Philipps. *Wall conditioning on TEXTOR.* Fus. Sci. Tech., 47:119 – 125, 2005.

[50] V. Philipps et al. *Removal of redeposited layers and hydrogen release by oxygen ventilation of TEXTOR-94.* J. Nucl. Mat., 266-269:386 – 391, 1999.

[51] E. de la Cal and E. Gauthier. *First-wall cleaning and isotope control studies by D_2 ICRF conditioning in Tore Supra with a permanent magnetic field.* Plasma Phys. & Controlled Fusion, 39(7):1083, 1997.

[52] H. F. Dylla. *Glow discharge techniques for conditioning high-vacuum systems.* Journal of Vacuum Science & Technology A: Vacuum, Surfaces, and Films, 6(3):1276–1287, 1988.

[53] V. Philipps et al. *Development of wall conditioning and tritium removal techniques in TEXTOR for ITER and future fusion devices.* IAEA publication, FT/4-2Ra, 2008. Proceedings of the 22nd IAEA Fusion Energy Conference.

[54] V. Philipps et al. *Removal of carbon layers by oxygen glow discharges in TEXTOR.* J. Nucl. Mat., 363-365:929 – 932, 2007. Plasma-Surface Interactions-17.

[55] G. Sergienko et al. *Ion cyclotron wall conditioning in reactive gases on TEXTOR.* J. Nucl. Mat., 390-391:979 – 982, 2009. Proceedings of the 18th International Conference on Plasma-Surface Interactions in Controlled Fusion Device, Proceedings of the 18th International Conference on Plasma-Surface Interactions in Controlled Fusion Device.

[56] E. de la Cal and E. Gauthier. *Review of radio frequency conditioning discharges with magnetic fields in superconducting fusion reactors.* Plasma Phys. & Controlled Fusion, 47(2):197, 2005.

[57] J. Li et al. *Wall conditioning towards the utilization in ITER.* J. Nucl. Mat., DOI: 10.1016/j.jnucmat.2010.10.048:–, 2010.

[58] H. Amemiya and et al. *Analysis Of ICRF Plasma Production in Large Scale Tokamaks.* Japanese Journal of Applied Physics, 26:1534–1543, 1987.

[59] J. Bucalossi et al. *The conditioning procedures in Tore Supra after CIEL implementation.* J. Nucl. Mat., 313-316:263 – 268, 2003. Plasma-Surface Interactions in Controlled Fusion Devices 15.

[60] S.-H. Hong, K.-P. Kim, and et al. *Initial phase wall conditioning in KSTAR.* IAEA Conference Proceedings, October 2010. Proceedings of 23th IAEA Fusion Energy Conference, Deajeon.

[61] C. Schulz. *Figure inhomogeneity of glow discharges in the presence of magnetic fields.* private communications, December 2009. Tomas result in frame of PhD work of Christian Schulz.

[62] M. Merola et al. *ITER plasma-facing components.* Fusion Eng. & Design, 85(10-12):2312 – 2322, 2010. Proceedings of the Ninth International Symposium on Fusion Nuclear Technology.

[63] L. Oren and R. Taylor. *Trapping and removal of oxygen in tokamaks.* Nucl. Fusion, 17(6):1143, 1977.

[64] F. Schuller. *Report on Applications of ICWC on ITER.* Technical Report IO/2009/ADM-014, ITER - IO, 13115, St. Paul-lez-Durance , France, November 2009. report version 3.

[65] D. Whyte and J. Davis. *Tritium recovery in ITER by radiative plasma terminations.* J. Nucl. Mat., 337-339:560 – 564, 2005. PSI-16.

[66] A. Lyssoivan et al. *ICRF/ECR plasma production for wall conditioning in TEXTOR-94.* In AIP Confer. Series, volume 595, pages 146–149, October 2001.

[67] M. Shimada. *Wall conditioning on ITER.* Poster presentation slides on the 19th International Conference on Plasma Surface interaction, May 2010.

[68] S. Chiocchio. *Project requirements (PR).* Technical report, ITER Organization, 13115, St. Paul-lez-Durance , France, October 2009.

[69] X. Gao et al. *ICRF wall conditioning and plasma performance on EAST.* J. Nucl. Mat., 390-391:864 – 868, 2009. Proceedings of the 18th International Conference on Plasma-Surface Interactions in Controlled Fusion Device, Proceedings of the 18th International Conference on Plasma-Surface Interactions in Controlled Fusion Device.

[70] V. Bakaev et al. *Currentless plasma production and heating in the torsatron Uragan-3 by RF waves.* Plasma Physics and Controlled Nuclear Fusion Research, 2, 1984.

[71] N. Nazarov, V. Plyusnin, and et al. *Use of plasma to clean the surfaces in the Uragon-3 torsatron.* Sov. J. Plasma Phys., 13(12):871–873, 1987.

[72] A. Lyssoivan et al. *ICRF preionization and plasma production in TEXTOR.* In Europhysics Conference Abstracts 19C, pages Part III, 341, Bournemouth (UK), July 1995. 22nd European Physical Society Conference on Controlled Fusion and Plasma Physics.

[73] E. Gauthier et al. *Wall conditioning technique development in Tore Supra with permanent magnetic field by ICRF wave injection.* J. Nucl. Mat., 241-243:553 – 558, 1997.

[74] H. Esser et al. *ICRF wall conditioning at TEXTOR-94 in the presence of a 2.25 T magnetic field.* J. Nucl. Mat., 241-243:861 – 866, 1997.

[75] Z. Yan-ping et al. *A New Wall Conditioning Technique Developed on the HT-7 Superconducting Tokamak with a Permanent Magnetic Field.* Chinese Physics Letters, 14(12):916, 1997.

[76] J. Li et al. *ICRF boronization - A new technique towards high efficiency wall coating for superconducting tokamak reactors.* Nucl. Fusion, 39(8):973, 1999.

[77] J. Xie et al. *RF wall conditioning - a new technique for future large superconducting tokamak.* J. Nucl. Mat., 290-293:1155–1159, 2001. 14th Int. Conf. on Plasma-Surface Interactions in Controlled Fusion D evices.

[78] X. Gong et al. *ICRF siliconization in HT-7 superconducting tokamak.* J. Nucl. Mat., 290-293:1171 – 1175, 2001. 14th Int. Conf. on Plasma-Surface Interactions in Controlled Fusion D evices.

[79] R. Brakel, D. Hartmann, and P. Grigull. *ICRF wall conditioning experiments in the W7-AS stellarator.* J. Nucl. Mat., 290-293:1160–1164, 2001. 14th Int. Conf. on Plasma-Surface Interactions in Controlled Fusion Devices.

[80] A. Lyssoivan et al. *Studies of ICRF Discharge Conditioning (ICRF-DC) on ASDEX Upgrade, JET and TEXTOR.* AIP Conference Proceedings, 787(1):445–448, 2005.

[81] A. Lyssoivan et al. *Development of ICRF wall conditioning technique on divertor-type tokamaks ASDEX Upgrade and JET.* J. Nucl. Mat., 337-339:456 – 460, 2005. PSI-16.

[82] A. Lyssoivan et al. *New scenarios of ICRF wall conditioning in TEXTOR and ASDEX Upgrade.* J. Nucl. Mat., 363-365:1358 – 1363, 2007. Plasma-Surface Interactions-17.

[83] N. Ashikawa et al. *Ion cyclotron conditioning with strong magnetic field in LHD.* Fusion Eng. & Design, 81(23-24):2831–2836, 2006. Proceedings of the Fifteenth International toki Conference on Fusion and Advanced Technology - ITC-15 SI.

[84] A. Lyssoivan and et al. *Analysis of ICRF plasma production in large scale tokamaks.* Nucl. Fusion, 32:1361–1372, 1992.

[85] E. de la Cal. *Theoretical modelling of deuterium ICRF wall conditioning discharges.* Plasma Phys. & Controlled Fusion, 48(10):1455, 2006.

[86] A. Lyssoivan. *Development of ITER relevant ICRF wall conditioning technique on European tokamaks.* In Probl. At. Sci. Tech., volume 1 of *Plasma Physics*, pages 44–48, 2005. issue $N^0$10.

[87] A. Lyssoivan et al. *ICRF Plasma Production in Tore Supra: Analysis of Antenna Coupling and Plasma Properties.* In Europhysics Conference Abstracts of the 26th EPS Conference on Controlled Fusion and Plasma Physics, Maastricht (The Netherlands) - 14/18 June 1999, volume 23J, pages 737–740, 1999.

[88] V. Rohde. *Comparison of wall cleaning using HeGD and ICGD.* Technical Report AUG shots 22612-22174, Max Planck Institut für Plasmaphysik, Garching, Germany, March 2008. Internal report with unpublished data, Use of data for publication requires permission by the author.

[89] D. V. Eester and R. Koch. *A variational principle for studying fast-wave mode conversion.* Plasma Phys. & Controlled Fusion, 40(11):1949, 1998.

[90] J. Hu, J. Li, and Y. Zhao. *Oxygen removal with D2-ICR cleanings after oxidation experiment in HT-7.* Fusion Eng. & Design, 82(2):133 – 139, 2007.

[91] J. Buermans and T. Matthys. *0-D Transport Modeling of the RF Plasma Production in a Fusion Reactor.* Master's thesis, Royal Military Academy (Brussels), July 2006.

[92] A. Lyssoivan. *ICRF plasma production and application to start-up and wall conditioning.* Technical report, Laboratory for Plasma Physics - Royal Military Academy, 1000 Brussels, Belgium, October 1998. Final Report on ITER Design Task D350.2, Laboratory Report nř 114.

[93] A. Lyssoivan. *ICRF plasmas for fusion reactor applications.* In Probl. At. Sci. Tech., volume 1 of *Plasma Physics*, pages 30–34, 2007. issue $N^0$13.

[94] A. Lyssoivan et al. *ICRF physics aspects of wall conditioning with conventional antennas in large-size tokamaks.* J. Nucl. Mat., DOI: 10.1016/j.jnucmat.2010.11.059:–, 2010.

[95] A. Lyssoivan et al. *ICRF Wall Conditioning: Present Status and Developments for Future Superconducting Fusion Machines.* In V. Bobkov & J.-M. Noterdaeme, editor, AIP Confer. Series, volume 1187, pages 165–172, November 2009.

[96] A. Lyssoivan et al. *Low Voltage Start-up Assisted by ICRF in TEXTOR-94.* In Europhysics Conference Abstracts of the 24th EPS Conference on Controlled Fusion and Plasma Physics, Berchtesgaden (Belgium) - June 1997, volume 21A, pages 1741–1744, 1997.

[97] A. Lyssoivan et al. *Influence of toroidal and vertical magnetic fields on Ion Cyclotron Wall Conditioning in tokamaks.* J. Nucl. Mat., 390-391:907 – 910, 2009. Proceedings of the 18th International Conference on Plasma-Surface Interactions in Controlled Fusion Device, Proceedings of the 18th International Conference on Plasma-Surface Interactions in Controlled Fusion Device.

[98] V. Bobkov. *Studies of high voltage breakdown phenomena on ICRF (Ion Cyclotron Range of Frequencies) antennas.* PhD thesis, Technische Universität München (Germany), Fakultät für Physik, May 2003.

[99] M. A. Rothman, R. M. Sinclair, and S. Yoshikawa. *'Non-resonant' coupling of R.F. power to a plasma.* JNEC, 8(3):241, 1966.

[100] G. Agarici et al. *Tore Supra ICRH antennas for long pulse operation.* In Fusion Engineering, 1997. 17th IEEE/NPSS Symposium, volume 1, pages 429 –432 vol.1, October 1997.

[101] M. Graham. *JET Ion Cyclotron Wall Conditioning.* CCIC-09 Meeting, Cadarache, 09 July 2011, July 2011.

[102] A. Argouarch. *Ion Cyclotron Wall Conditioning (ICWC) on Tore Supra, RF operation.* CCIC-09 Meeting, Cadarache, 09 July 2011, July 2011.

[103] V. Bobkov. *Operation of ICWC in ASDEX Upgrade.* CCIC-09 Meeting, Cadarache, 09 July 2011, July 2011.

[104] M. Verviers. *ICWC in TEXTOR.* CCIC-09 Meeting, Cadarache, 09 July 2011, July 2011.

[105] A. Lyssoivan. *RF Aspects of Ion Cyclotron Wall Conditioning.* CCIC-08 Meeting, Torino, 08 March 2011.

[106] M. Carter et al. *Plasma production using radiofrequency fields near or below the ion cyclotron range of frequencies.* Nucl. Fusion, 30(4):723, 1990.

[107] A. Lyssoivan. *ICWC in Tore Supra: Numerical Analysis and Scenario Proposal.* private communications, November 2008. Calculation of neutral gas RF breakdown zone for TS-CIEL ICRF antenna.

[108] D. Reiter. *The data file HYDHEL: Atomic and Molecular Data for EIRENE.* Technical report, Forschungszentrum Juelich GmbH, 52425 Juelich, December 2002. Based upon: Janev, Langer, Evans, Post, Elementary Processes in Hydrogen-Helium Plasmas, Springer 1987.

[109] W. Umrath. *Fundamentals of Vacuum Technology.* Oerlikon Leybold Vacuum, Cologne, Germany, June 2007.

[110] C. Day. *Basics and applications of cryopumps.* CERN Document Server, page 34 p, 2007.

[111] T. Chou and H. Halama. *Cryopumping of deuterium hydrogen and helium mixtures on smooth 4.2 K surfaces.* Technical report, Brookhaven National Laboratory, Upton, New York 11973, January 1977. Conference: 7. international Vac. congress and 3. international conference on solid surfaces, Vienna, Austria, 12 Sep 1977.

[112] B. Unterberg. *Transport Processes in the Plasma Edge.* Trans. Fus. Sci. Tech., 57, 2010. Number 2T, FUSTE8 (2) 1-504.

[113] R. Laengner et al. *Electron density and temperature measurements in TEXTOR ion cyclotron wall conditioning plasmas by thermal Li beam*

spectroscopy. J. Nucl. Mat., DOI: 10.1016/j.jnucmat.2011.01.133:–, 2011.

[114] E. de la Luna et al. *Electron cyclotron emission radiometer upgrade on the Joint European Torus (JET) tokamak.* Rev. Sci. Instr., 75(10):3831–3833, 2004.

[115] I. Monakov, P. Jacquet, and M. Graham. private communications, July 2011. Culham Centre for Fusion Energy, Culham Science Centre, Abingdon, Oxfordshire, OX14 3DB, UK.

[116] J. Gunn. private communications, July 2011. Responsible diagnostician RFA TORE SUPRA.

[117] S. Mueller et al. *Effects of a vertical magnetic field on particle confinement in a magnetized plasma torus.* Phys. Rev. Lett., 93(16), 2004.

[118] P. C. T. van der Laan. *Drift of a plasma in a curved magnetic field.* J. Nucl. Energy, C: Plasma Phys., Accelerators, Thermonucl. Res., 6(6):559, 1964.

[119] S. Nakao, K. Ogura, Y. Terumichi, and S. Tanaka. *Particle loss from an electron cyclotron resonance discharge plasma in the WT-2 device.* Phys. Lett. A, 96(8):405 – 408, 1983.

[120] A. Komori, N. Sato, and Y. Hatta. *Drift motion of a plasma in a curved magnetic field with rotational transform.* Journal of the Physical Society of Japan, 47:990–997, September 1979.

[121] T. Loarer, J. Bucalossi, G. Matthew, and V. Philipps. *Tritium particle balance and retention during DT discharges in JET.* J. Nucl. Mat., 337-339:624 – 628, 2005. PSI-16.

[122] W. Eckstein. *Calculated Sputtering, Reflection and Range Values.* Technical report, Max Planck Society - eDocument Server, Germany, 2002.

[123] B. Pégourié. private communications, November 2010. IRFM, CEA Cadarache.

[124] V. Philipps and J. Ehrenberg. *Analysis of outgassing after Joint European Torus discharges under beryllium first wall conditions.* Journal of Vacuum Science Technology A: Vacuum, Surfaces, and Films, 11(2):437 –445, March 1993.

[125] R. Mitteau et al. *A shaped First Wall for ITER.* J. Nucl. Mat., DOI: 10.1016/j.jnucmat.2010.10.070:–, 2010.

[126] D. Douai et al. *Ion Cyclotron discharges for Tokamak wall conditioning in presence of a magnetic field: recent experimental results on Tore Supra.* In Europhysics Conference Abstracts of the 36th EPS Conference on Controlled Fusion and Plasma Physics, Sofia, (Bulgaria) - July 2009, 2009.

[127] D. Douai et al. *Recent results on Ion Cyclotron Wall Conditioning in mid and large size tokamaks.* J. Nucl. Mat., DOI: 10.1016/j.jnucmat.2010.11.083:–, 2010.

[128] K. Morishita, T. Inoue, and N. Yoshida. *Microstructural evolution in beryllium by fusion-relevant low energy helium ion irradiation.* Journal of Nuclear Materials, 266-269:997 – 1002, 1999.

[129] K. Schmid, T. Schwarz-Selinger, W. Jacob, R. Dux, and the ASDEX Upgrade Team. *The implications of high- Z first-wall materials on noble gas wall recycling.* Nuclear Fusion, 47(8):984, 2007.

[130] S. Hong and et al. *ICRF conditioning on KSTAR.* In 12$^{\text{th}}$ ITPA SOL'/Divertor Physics Meeting, Amsterdam, 2009. 5-8 May.

[131] K. Sungwoo et al. *Long term behavior of water molecules and their removal by inter-shot Ion Cyclotron Wall Conditioning.* J. Nucl. Mat., 2011. Under review.

[132] V. E. Moiseenko, A. I. Lysoivan, S. V. Kasilov, and V. V. Plyusnin. *Dynamics of r.f. production of Stellarator plasmas in the ion cyclotron range of frequency.* Fusion Eng. & Design, 26(1-4):203 – 207, 1995.

[133] B. Lloyd, P. G. Carolan, and C. D. Warrick. *ECRH-assisted start-up in ITER.* Plasma Phys. & Controlled Fusion, 38(9):1627, 1996.

[134] S. I. Braginskii. *Transport Processes in a Plasma.* In M. A. Leontovivh, editor, Reviews of Plasma Physics 1, New York, 1965. Consultants Bureau.

[135] D. Wünderlich, S. Dietrich, and U. Fantz. *Application of a collisional radiative model to atomic hydrogen for diagnostic purposes.* J. Quant. Spectrosc. Radiat. Transfer, 110(1-2):62 – 71, 2009.

[136] Y. V. Ralchenko and Y. Maron. *Accelerated recombination due to resonant deexcitation of metastable states.* J. Quant. Spectrosc. Radiat. Transfer, 71(2-6):609 – 621, 2001.

[137] I. I. Sobelman, L. A. Vainshtein, and E. A. IUkov. *Excitation of atoms and broadening of spectral lines / I.I. Sobelman, L.A. Vainshtein, E.A. Yukov.* Springer-Verlag, Berlin ; New York :, 1981.

[138] I. Bray and Y. Ralchenko. *CCC-database.* http://atom.curtin.edu.au/CCC-WWW/.

[139] V. Shevelko et al. *One-electron Capture and Target Ionization in He+-neutral-atom Collisions.* Technical report, NIFS, December 2009.

[140] R. Janev and J. J. Smith. *Recommended Cross Sections for Collision Processes of Hydrogen Ground-State and Excited Atoms with Electrons, Protons and Multiply Charged Atoms.* Atomic and Plasma-Material Data for Fusion, a supplement to the journal Nuclear Fusion, 4, 1993.

[141] M. B. Shah, P. McCallion, and H. B. Gilbody. *Electron capture and ionization in collisions of slow H + and He 2+ ions with helium.* J. Phys. B-At. Mol., 22(19):3037, 1989.

[142] Y. Ralchenko et al. *Electron-impact excitation and ionization cross sections for ground state and excited helium atoms.* Atomic Data and Nuclear Data Tables, 94(4):603–622, July 2008.

[143] R. Marchand, C. Illescas, X. Bonnin, and J. Botero. *Radiative Losses and Electron Cooling Rates of Hydrogen, Helium, Carbon and Oxygen.* Technical report, International Nuclear Data Committee, IAEA Nuclear Data Section, Wagramerstrasse 5, 1400 Vienna, Austria, July 1995.

[144] O. Marchuk et al. *Recombination mechanisms in He-like argon spectra measured in low-density plasmas.* J. Phys. B-At. Mol., 40(23):4403, 2007.

[145] D. V. Sivukhin. *Coulomb Collisions in a Fully Ionized Plasma.* In M. A. Leontovivh, editor, Reviews of Plasma Physics 4, New York, 1966. Consultants Bureau.

[146] H. H. Abou-Gabal and G. A. Emmert. *Helium transport in vented divertors and limiters.* Nucl. Fusion, 31:407–416, 1991.

[147] D. Reiter, P. Bachmann, and A. K. Prinja. *Influence of Elastic Collisions on Neutral Gas Transport in Boundary Plasmas.* Contrib. Plasma Phys., 32:261–267, 1992.

[148] P. Bachmann and D. Reiter. *Kinetic Description of Elastic Processes in Hydrogen-Helium Plasmas.* Contrib. Plasma Phys., 35:45–100, 1995.

[149] R. K. Janev. *Atomic and Molecular Processes in SOL/Divertor Plasmas.* Contrib. Plasma Phys., 38:307–318, 1998.

[150] R. K. Janev, editor. *Atomic and Molecular Processes in Fusion Edge Plasmas*, 1995.

[151] D. Reiter. *The data file AMJUEL: Additional Atomic and Molecular Data for EIRENE.* Technical report, Forschungszentrum Juelich GmbH, 52425 Juelich, May 2010.

[152] A. V. Phelps. *Cross Sections and Swarm Coefficients for H+, H2+, H3+, H, H2, and H- in H2 for Energies from 0.1 eV to 10 keV.* J. Phys. Chem. Ref. Data, 19(3):653–675, 1990.

[153] A. Lyssoivan. *Energy and Particle Balance Equations for RF Plasmas in Fusion Machines.* Document for internal use, version 3, 2007.

[154] T. Wauters et al. *Isotope exchange experiments on TEXTOR and TORE SUPRA using Ion Cyclotron Wall Conditioning and Glow Discharge Conditioning.* J. Nucl. Mat., DOI: 10.1016/j.jnucmat.2010.11.072, 2010.

[155] M. Rutigliano and M. Cacciatore. *Isotope and Surface Temperature Effects for Hydrogen Recombination on a Graphite Surface.* ChemPhysChem, 9(1):171 –181, 2008.

[156] E. Vietzke. *Reflection and adsorption of deuterium atoms and molecules on graphite.* J. Nucl. Mat., 266:324–329, 1999.

[157] A. Lyssoivan et al. *A study of RF power absorption mechanisms in JET ICWC plasmas.* In Europhysics Conference Abstracts of the 38th EPS Conference on Controlled Fusion and Plasma Physics, Strasbourg (France) - June 2011, 2011.

[158] R. Papoular. *The genesis of toroidal discharges.* Nucl. Fusion, 16(1):37, 1976.

[159] P. Linstrom and W. Mallard, editors. *NIST Chemistry WebBook.* National Institute of Standards and Technology, Gaithersburg MD, 20899, USA, nist standard reference database number 69 edition, 2011. récupérée 4 Mai 2011, http://webbook.nist.gov.

[160] R. K. Janev, W. D. Langer, D. E. Post, Jr., and K. Evans, Jr. *Elementary processes in hydrogen-helium plasmas: Cross sections and reaction rate coefficients*, volume 4 of *Atoms+Plasmas.* Springer-Verlag, 1987.

[161] M. Arnaud and R. Rothenflug. *Ionic fraction data.* Astronomy and Astrophysics Supplement Series, 60:425–457, 1985.

[162] T. Loarer et al. *Gas balance and fuel retention in fusion devices.* Nucl. Fusion, 47(9):1112, 2007.

[163] C. Grisolia, P. Ghendrih, B. Pégourié, and A. Grosman. *Plasma wall particle balance in Tore Supra.* J. Nucl. Mat., 196-198:281 – 284, 1992. Plasma-Surface Interactions in Controlled Fusion Devices, Proceedings of the Tenth International Conference on Plasma-Surface Interactions in Controlled Fusion Devices.

[164] P. Andrew et al. *Experiments on the release of tritium from the first wall of JET.* Nucl. Fusion, 33(9):1389, 1993.

[165] C. Sang et al. *Modeling of hydrogen reactive-diffusive transport and inventory in porous media with mixed materials deposited layers.* In Europhysics Conference Abstracts of the 38th EPS Conference on Controlled Fusion and Plasma Physics, Strasbourg (France) - 27 June/1 July 2011, 2011.

[166] A. Lyssoivan. *SIMULATION OF ITER ICWC SCENARIOS IN JET.* In Probl. At. Sci. Tech., volume 16 of *Plasma Physics*, pages 46–50, 2010. issue $N^0$6.

[167] A. Costley and D. Johnson, editors. *Special issue on plasma diagnostics for magnetic fusion research*, volume 53, No 2. Fus. Sci. Tech., 2^{nh} edition edition, February 2008.

[168] P. H. Dawson. *Quadrupole Mass Spectrometry and its Applications.* Elsevier Scientific Publishing Company, 1976. ISBN 10: 0444413456 / 0-444-41345-6, ISBN 13: 9780444413451.

[169] R. Botter and G. Bouchoux. *Spectrométrie de masse.* Techniques de l'ingénieur. Analyse et caractérisation, P3(P2615):P2615.1–P2615.39, 1995. Paris, FRANCE (Revue).

[170] C. C. Klepper, D. L. Hillis, M. R. Wade, R. Maingi, and G. R. McKee. *Application of a species-selective Penning gauge to the measurement of neon and hydrogen-isotope partial pressures in the plasma boundary.* Rev. Sci. Instr., 68(1):400–403, 1997.

[171] K. H. Finken, K. H. Dippel, W. Y. Baek, and A. Hardtke. *Measurement of helium gas in a deuterium environment.* Rev. Sci. Instr., 63(1):1–7, 1992.

[172] G. Sergienko. private communications, July 2009. Responsible diagnostician.

[173] R. Lässer et al. *The gas-chromatographic analysis system in the JET active gas handling plant.* Rev. Sci. Instr., 64:2449–2458, September 1993.

[174] W. Suttrop. *Electron Cyclotron Emission Plasma Diagnostics.* Technical report, Max-Planck-Institut für Plasmaphysik, D-85748 Garching, April 2004. From Emanuele Poli, Für die Studenten der Universität Ulm.

[175] R. L. Merlino. *Understanding Langmuir probe current-voltage characteristics.* Am. J. Phys., 75:1078–1085, December 2007.

[176] N. Hershkowitz, M. H. Cho, C. H. Nam, and T. Intrator. *Langmuir probe characteristics in RF glow discharges.* Plasma Chemistry and Plasma Processing, 8:35–52, 1988. 10.1007/BF01016929.

[177] G. Sergienko. private communications, March 2011. Responsible diagnostician.

[178] M. Kočan et al. *On the reliability of scrape-off layer ion temperature measurements by retarding field analyzers.* Rev. Sci. Instr., 79(7):073502, July 2008.

[179] R. A. Pitts. *Retarding Field Energy Analysis for Ion Temperature Measurement in the Tokamak Edge.* Contrib. Plasma Phys., 36:87–93, 1996.

[180] V. Moiseenko, Y. Stadnik, A. Lyssoivan, and D. M. *SELF-CONSISTENT MODEL OF THE RF PLASMA PRODUCTION IN STELLARATOR.* In Probl. At. Sci. Tech., volume 1 of *Plasma Physics*, pages 21–23, 2010. issue $N^0$6.

[181] T. Wauters et al. *Ion Cyclotron Wall Conditioning Experiments on Tore Supra in Presence of the Toroidal Magnetic Field.* In V. Bobkov and J.-M. Noterdaeme, editors, AIP Confer. Series, volume 1187, pages 173–176. AIP, 2009.

[182] M. K. Paul. *Plasma and antenna coupling characterization in ICRF-Wall Conditioning experiments.* Plasma Phys. & Controlled Fusion, 2010. Submitted.

A

Schemes of tokamak main systems

A.1 TORE SUPRA

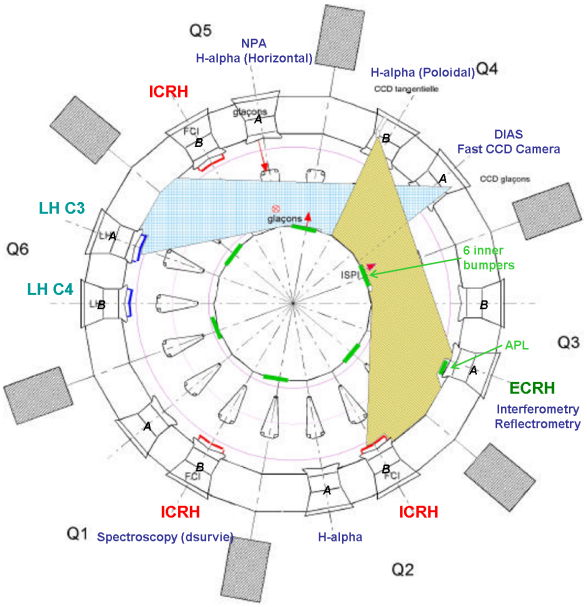

Figure A.1: TORE SUPRA: Toroidal cut

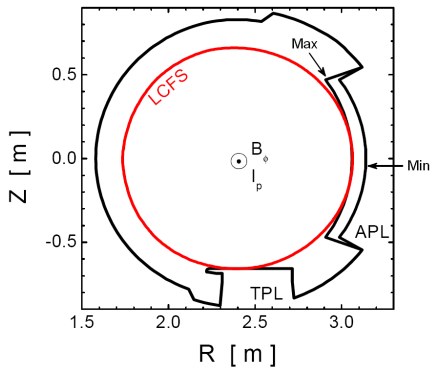

Figure A.2: TORE SUPRA: Poloidal cut

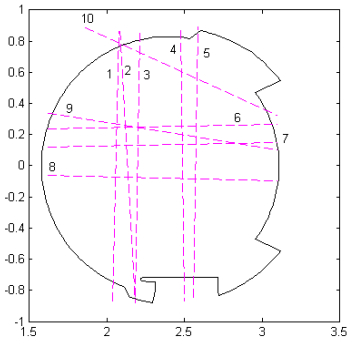

Figure A.3: TORE SUPRA: DCN interferometry viewing lines cut

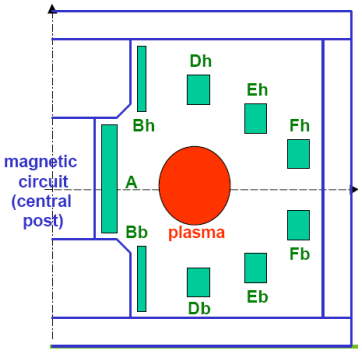

Figure A.4: The poloidal field system on TORE SUPRA to induce (central solenoid: A) and control (8 outer poloidal field coils: Bh, Bb, Dh, Db, Eh, Eb, Fh and Fb) the equilibrium of the plasma current, consisting of 9 copper coils associated with 9 power supplies.

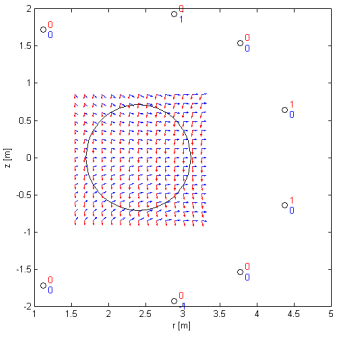

Figure A.5: Illustration of the poloidal magnetic field in TORE SUPRA calculated by Biot-Savart law from currents (A.U.) in the outer poloidal field coils (poloidal location given by black dots). On properly selecting the currents homogeneous vertical (red) or radial (blue) fields can be attained.

A.2 TEXTOR

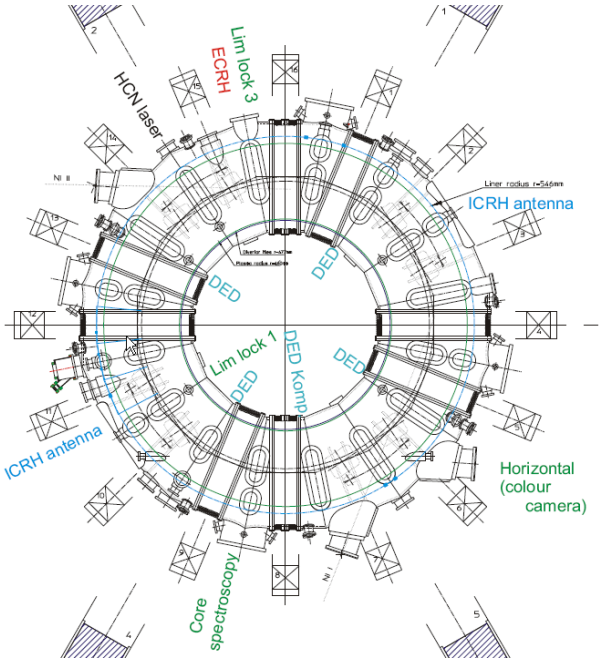

Figure A.6: TEXTOR: Toroidal cut

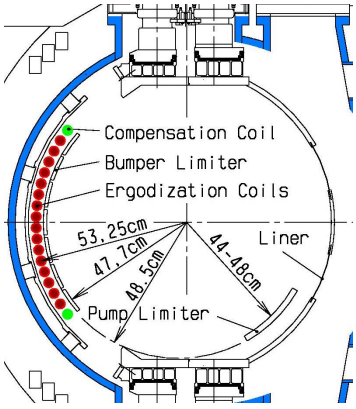

Figure A.7: TEXTOR: Poloidal cut

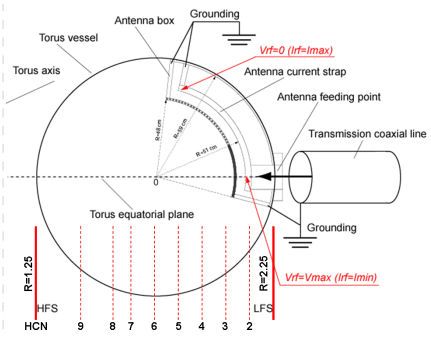

Figure A.8: TEXTOR: HCN interferometry viewing lines

A.3 JET

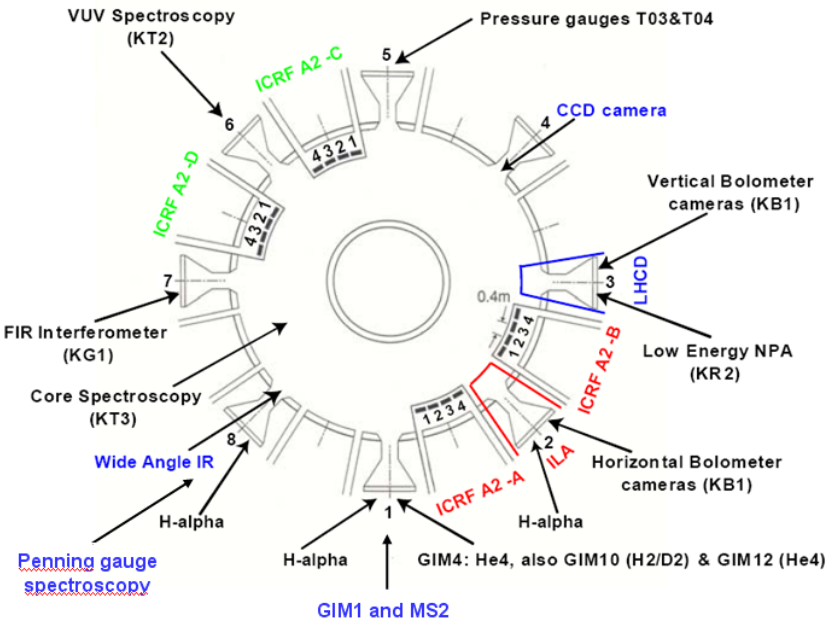

Figure A.9: JET: Toroidal cut

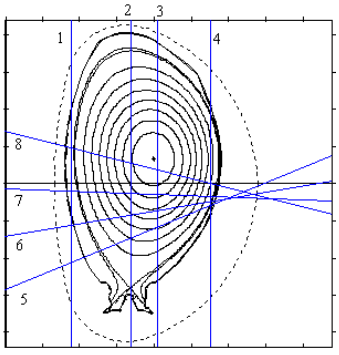

Figure A.10: JET: Poloidal cut, including HCN interferometry viewing lines

A.4 ASDEX Upgrade

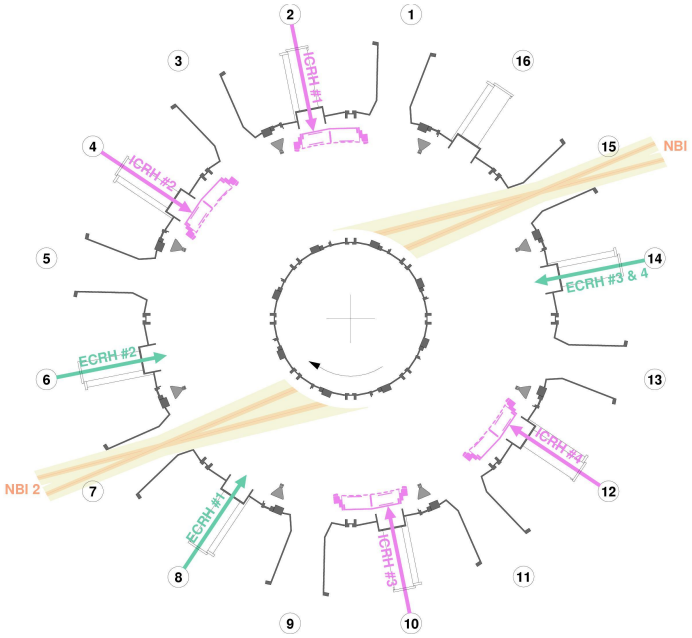

Figure A.11: ASDEX Upgrade: Toroidal cut

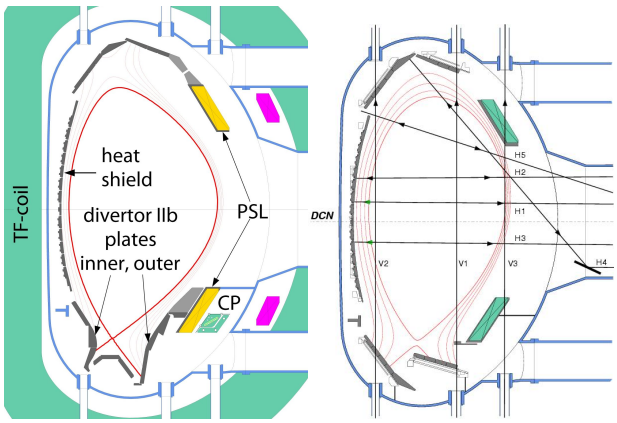

Figure A.12: ASDEX Upgrade: Poloidal cut. Left: present ASDEX Upgrade wall configuration, right: the DCN interferometry viewing lines on the old wall configuration.

B
ICWC diagnostics

B.1 Neutral gas diagnostics

Tokamak devices are equipped with a many measurement systems to examine firstly the performance of the tokamak systems (magnetic field system, heating systems, monitoring wall elements, etc...) to control and ensure safe operation, and secondly to study the properties of the produced plasma (plasma diagnostics). An extensive overview of these diagnostics can be found in [167]. Below we will give a brief summary of the diagnostic systems that are used during ICWC discharges. It includes the measurement tools to analyze the neutral gas in the vessel (pressure and gas composition), and the principle plasma diagnostics. Since present tokamaks are experimental facilities designed and exploited to support magnetic fusion research, the plasma diagnostic systems are designed to study high temperature ($\sim$ keV) and high density ($\sim 10^{19}\,\mathrm{m}^{-3}$) plasmas. Conditioning discharges operate at much lower temperatures ($\sim$ eV) and densities (ICWC: $10^{16} - 10^{18}\,\mathrm{m}^{-3}$) and therefore the standard diagnostics will be operated outside their normal operation range. This brings along some inconveniences, of which the gravest is that the standard diagnostics can not be used or that the accuracy of the measurements is very low. Often dedicated processing of the produced raw data is required.

B.1.1 Pressure measurements

Devices to measure pressure below atmospheric pressure are usually referred to as vacuum gauges. We will shortly describe the three most employed systems in tokamak vacuum vessels: baratron gauges, Penning gauges and Pirani gauges. The gauges are not in direct contact with the plasma. The few gauges in the vacuum vessel itself are located in plasma shadowed areas (e.g. behind divertor plates) while most of the gauges are located along the various pumping ducts.

The **baratron gauge** relies on capacitance changes due to the pressure force exerted on a membrane of a plate capacitor. The advantage of baratron gauges over ionization and Pirani gauges is that the calibration is independent of the gas. The accuracy dependents on the specific type of the baratron gauge, but generally the measurement uncertainty rises strongly for pressure below 10^{-4} mbar [109]. Below these pressures one can rely on the Penning gauge. The **Penning gauge** is an ionization vacuum gauge with cold electrodes. The neutral gas entering the gauge is partly ionized in the high electric field between 2 coaxially arranged electrodes (kV). Due to a small magnetic field the electrons spiral around the central electrode to increase the ionization probability. The current collected at the electrodes is proportional to the particle density, which is in turn proportional to the pressure. The upper pressure limit below which the proportionality of the ion current is conserved is 10^{-2} mbar [109]. The pressure reading is dependent on the discharge gas via the ionization cross section. The gauges are mostly calibrated for nitrogen N_2. Correction factors for other gases are often given in the device documentation, but it is strongly recommended to check them by a dedicated calibration. Table B.1 list typical conversion factors for some gases of interest in this manuscript. Penning gauges are,

Table B.1: Nominal Penning pressure reading correction factors for common gases relative to the calibration gas N_2 ($p_g = p_{N_2}/R_g$).

	He	D_2	H_2	N_2
R_g	0.18	0.35	0.46	1

next to baratron gauges, used to monitor the vacuum vessel pressure and are in this matter of particular importance since their lower measurement limit is orders below the limit for baratrons. Furthermore they are also often employed to monitor the neutral pressure in tokamak systems as for example the pressure in the vacuum RF transmission lines of the JET ICRH antennas. The **Pirani gauge** is a thermal conductivity gauge measuring pressure via the electrical resistivity of a heated thin wire. The thermal conductivity of the neutral gas will cause a heat loss of the wire propor-

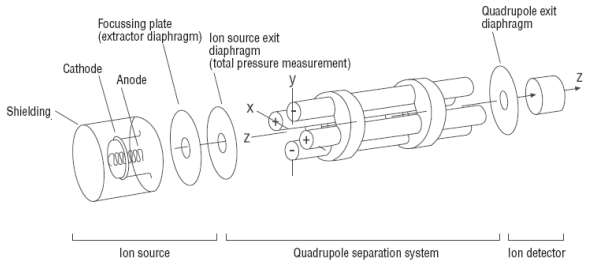

Figure B.1: Schematic of a quadrupole mass spectrometer showing the ion source, the quadrupole separation system and the ion detector [109].

tional to the neutral pressure in a range of 10^{-4} mbar to 10^{-1} mbar. The calibration of Pirani gauges is also gas dependent [109].

B.1.2 Mass spectrometry

B.1.2.1 Principle of quadrupole mass spectrometry

The assessment of the wall conditioning efficiency of ICWC discharges in this manuscript is mostly done by mass spectrometry. It allows to analyze quantitatively the composition of the neutral gas. In a mass spectrometer the neutral gas is ionized, whereafter the ion current is collected selectively according to the mass to charge ratio of the ions. Fig. B.1 shows a schematic of a quadrupole mass spectrometer where its three main sections are indicated: the ion source, the quadrupole separation system and the ion detector [109]. In the **ion source** the incoming neutral gas is cracked (molecules) and ionized by impact of electrons, originating from a constant electron source and having a constant energy distribution ($\sim 100\,\mathrm{V}$). The probability of these elementary collisions is proportional to the cross section of the reaction. To illustrate the operation of a quadrupole mass spectrometer, (and to illustrate its calibration in the next paragraph) we will use as example the detection of deuterium gas. Table B.2 gives the cross sections

Table B.2: Relevant elementary reactions for mass spectrometry measurements of deuterium, cross section taken from [160].

Reaction	m/e	cross section, σ
$D_2 + e^- \rightarrow D^* + D^+ + 2e^-$	2	$\sigma_2(100\,\mathrm{eV}) = 6 \cdot 10^{-18}\,\mathrm{cm}^{-2}$
$D_2 + e^- \rightarrow D_2^+ + 2e^-$	4	$\sigma_4(100\,\mathrm{eV}) = 1 \cdot 10^{-16}\,\mathrm{cm}^{-2}$
$D_2 + D_2^+ \rightarrow D_3^+ + D$	5	$\sigma_6(\sim 1\,\mathrm{eV}) > 1 \cdot 10^{-15}\,\mathrm{cm}^{-2}$

for the relevant elementary reactions in case of deuterium, namely dissocia-

tive ionization of the deuterium molecule, direct ionization and production of D_3^+. The latter reaction is a secondary reaction that does not involve electrons. Due to the small dimensions of the ion source and the low pressures, the electron flux can be considered constant over the interaction length between electrons and neutrals. In this case the total number of produced D^+ and D_2^+ ions is proportional to the electron current I_e from the electron source, the neutral particle density and the reaction cross section. We can thus write for the number of produced ions

$$N_{D^+} \propto I_e n_{D_2} \sigma_2 \tag{B.1}$$

$$N_{D_2^+} \propto I_e n_{D_2} \sigma_4 \tag{B.2}$$

$$N_{D_3^+} \propto n_{D_2^+} n_{D_2} \sigma_6 \propto I_e n_{D_2}^2 \sigma_4 \sigma_6 \tag{B.3}$$

where N_{D^+} and $N_{D_2^+}$ are linearly proportional to the deuterium pressure, and $N_{D_3^+}$ to the square of the pressure. The presence of $N_{D_3^+}$ at higher pressures is not negligible. Whereas the electron impact reactions only take place in the small electron beam, the interaction area for producing $N_{D_3^+}$ is larger. We will compare these dependencies, obtained from table B.2, with measurements later in this section.

The produced ions are extracted from the ion source and sent in the direction of the ion collector. In order the quantify the different ion fractions at the ion detector the **quadrupole section** will separate the ions according to their mass to charge ratio. It consists of 4 parallel rods as shown in Fig. B.1 to which a superposition of a constant and oscillating voltage is applied: $-\phi_0/2$ to the rods in the xz-plane, and $+\phi_0/2$ to the rods in the yz-plane, with $\phi_0 = U - V\cos(\omega t)$. The potential field in the xy-plane is thus given by

$$\phi = \phi_0 \frac{x^2 - y^2}{2r_0^2} \tag{B.4}$$

with r_0 the radius of the axial cylinder inside the rods. The equations of motion of the ions,

$$\frac{\mathrm{d}^2 x}{\mathrm{d}t^2} = -\frac{Z_i e}{m_i r_0^2}(U - V\cos(\omega t))x \tag{B.5}$$

$$\frac{\mathrm{d}^2 y}{\mathrm{d}t^2} = \frac{Z_i e}{m_i r_0^2}(U - V\cos(\omega t))y \tag{B.6}$$

with m_i and Z_i the ion mass and charge number, are of the form of the Mathieu differential equation, describing the phenomenon of an oscillator with periodically varying frequency [168]. The trajectory of the ions thus depends on the ion charge Z and mass unit M, the voltages U and V, and the RF frequency ω. The solution of the Mathieu equation is either

purely oscillatory, which means that an ion with certain M/Z-ratio has a stable oscillatory trajectory through the quadrupole section, or either the solution contains real exponential terms, due to which the ion will experience an exponential increase of the oscillation amplitude. The latter results in an unstable trajectory, leading to the loss of the ion due to the finite xy-dimensions of the quadrupole section. One explains the operation of the quadrupole often as a band pass filter for ions in a certain M/Z range determined by the RF voltage V [109,169]. The xz-plane provides a low pass filter, and likewise the yz-plane provides a high pass filter. The ratio U/V sets the width of the accepted M/Z range, which should be set small enough to avoid for example a current contribution from $M/Z = 4$ ions during the measurement of $M/Z = 3$. The resolution of the quadrupole is also important in this respect, and can be adjusted via the RF frequency, where the frequency has to be sufficiently high to impose several ion oscillations while the ion transverses the quadrupole length. A lower value for the frequency is derived in [168].

The spectrometer quadrupole section mostly works at fixed frequency, and either effectuates continuous scans of the ratio of U/V to obtain M/Z-spectra (e.g. Fig. B.2), or will alternate several fixed U/V-values to collect the ion current for a limited number of predefined M/Z-values (called peak mode). The **ion collector** at the final stage of the spectrometer collects the ion current, in the simplest case by a Faraday cup [109]. The collector circuit includes a variable current amplifier to allow for measurements ranging over more than 6 orders of magnitude. In 'fast' mass spectrometers the signal magnification needs to be set in advance. The fixed magnification allows measurements in a range which is about 3 orders of magnitude. These ranges are usually numbered according to their magnification:

$$\begin{aligned}
&\text{Ran } 0: \quad I_m = 10^{-0} I_{\text{QMS}}, \quad I_{\text{QMS}} = [10^{-8} - 10^{-5}] \\
&\text{Ran } 1: \quad I_m = 10^{-1} I_{\text{QMS}}, \quad I_{\text{QMS}} = [10^{-9} - 10^{-6}] \\
&\text{Ran } 2: \quad I_m = 10^{-2} I_{\text{QMS}}, \quad I_{\text{QMS}} = [10^{-10} - 10^{-7}] \quad \ldots
\end{aligned}$$

where I_{QMS} is the measured signal and I_m the correct(ed) ion current intensity. Slower mass spectrometers detect the required magnification automatically, and are therefore much slower. Each tokamak is equipped with the latter type of slow mass spectrometers, often called machine mass spectrometers, which are employed to monitor the gas content in the vacuum vessel during experimental programs. They continuously scan a wide range of M/Z values (1 to > 50) which takes about 30 s to a few minutes per scan. The machine mass spectrometers are important do determine the origin of eventual leaks in the vacuum vessel (air, water), or to detect for example the release of metallic impurities from antennas surfaces.

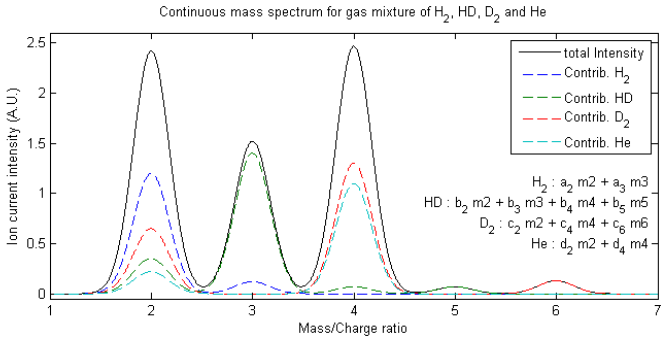

Figure B.2: Example of a continuous mass spectrum for a gas mixture of H_2, HD, D_2 and He

B.1.2.2 Calibration of a quadrupole mass spectrometer

Utilization of the mass spectrometer in peak mode requires both the accurate determination of the U/V-values localizing the requested M/Z values along the continuous M/Z spectrum, and the calibration of the measured ion current intensity to the neutral pressure of the gas. Fig. B.2 shows an arbitrary continuous mass spectrum for a typical conditioning gas mixture of H_2, HD, D_2 and He. For illustration, the separate contributions to the measured total ion current intensity for each gas are also given in dashed lines. These lines are often called the cracking patterns of the molecules. The peak measurement point for each mass to charge ratio has to be aligned with the maximum of the corresponding peak for optimal accuracy. The ratio of the measured peak values together with the calibrated cracking patterns of the gas components, allow to determine the gas composition. For the given gas mixture of 4 components one measures often 4 mass to charge ratios: 2, 3, 4 and 6. The measured intensities relate to the pressure the different components as (the quadratic pressure dependencies are ignored, see further):

$$\begin{pmatrix} I_2 \\ I_3 \\ I_4 \\ I_6 \end{pmatrix} = \begin{pmatrix} a_2 & b_2 & c_2 & d_2 \\ a_3 & b_3 & 0 & 0 \\ 0 & b_4 & c_4 & d_4 \\ 0 & 0 & c_6 & 0 \end{pmatrix} \begin{pmatrix} p_{\mathrm{H_2}} \\ p_{\mathrm{HD}} \\ p_{\mathrm{D_2}} \\ p_{\mathrm{He}} \end{pmatrix} \tag{B.7}$$

The decomposition of the intensities into pressure requires thus the inversion of the calibration matrix. However this simple operation often leads to problems. The coefficients in the 4x4 matrix can vary over 3 orders of magnitude, and separately the constituent partial pressures can also range over several orders of magnitude. The measurement accuracy and the accuracy of the calibration thus have to be extremely high if one wants to obtain partial

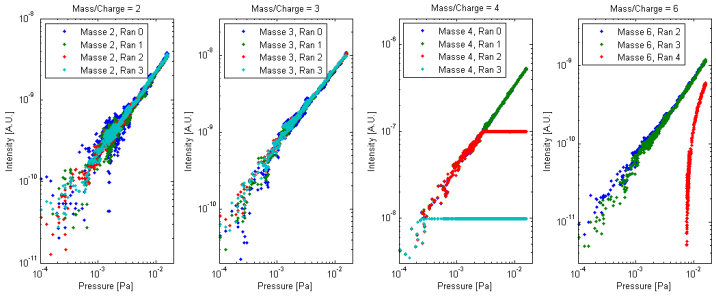

Figure B.3: Example of quadrupole mass spectrometer calibration plots for deuterium (TORE SUPRA, Q6B). The fits for the different mass to charge ratios are: $I_2 = 2.23 \cdot 10^{-7} p_{D_2}$, $I_3 = 6.56 \cdot 10^{-7} p_{D_2}$, $I_4 = 3.31 \cdot 10^{-5} p_{D_2}$ and $I_6 = 7.4 \cdot 10^{-8} p_{D_2}$.

pressures from this method. For practical cases one will choose to strongly simplify the matrix, with respect to the present gas mixture. Examples of terms that can be neglected in case of He/H_2 conditioning discharges to remove deuterium from the wall are colored gray in the matrix. For the analysis in this manuscript most efforts were put in the correct decomposition of the discussed H_2, HD, D_2 and He mixtures, but also measurements were carried out for heavier molecules such as water, carbon oxides, carbon hydrates, etc,...

In the following we will briefly discuss a calibration example. Fig. B.3 shows measured ion current intensities as a function of the neutral deuterium pressure in the vessel. The background values on both the baratron pressure measurement as on the QMS measurements were subtracted to obtain nice calibration curves for this example. One needs to note that these subtracted offset values can originate from incorrect setting of the measurement zero value or from a real pressure in the vessel. In the latter case one must take the background pressure into account in the mass spectrometric data analysis. A 10 point smoothing filter was applied to the baratron data (sampling interval of 2 ms), and likewise a 3 point smoothing filter on the sampled QMS data (sampling interval of 65 ms). The calibration for deuterium is interesting in that it shows both the strength and the difficulties of mass spectrometry in one example. We will discus first the effect of the measurement ranges on the measurement accuracy, and secondly the obtained pressure dependencies.

Ranges: First of all we see that the data collected using different ranges lines up very nicely. In case of mass to charge ratio 2, from now on shortly called ‘mass 2’, the ideal range to measure the ion current intensity is ran

3 $\sim [10^{-11} - 10^{-8}]$. The large spread of mass 2 ran 0 data points around pressures of $2 \cdot 10^{-3}$ Pa shows that the measurement accuracy decreases below the lower range limit. Additionally, the offset subtracted from mass 2 ran 0 and 1 is larger than the signal itself (resp. $1.4 \cdot 10^{-8}$ and $8.7 \cdot 10^{-9}$). For mass spectrometric measurements it is thus important to measure in the appropriate range so that the real signal intensity is larger than any background or uncertainty. Practically this means that the measured intensity minus the expected background intensity must not be lower than the lower limit of the measurement range. The effect of the upper range limit is clearly visible for mass 4. Ranges 2 and 3 saturate for higher intensities than respectively 10^{-7} and 10^{-8}. Logically one must avoid to measure above the upper range limit. The ideal measurement range for mass 4 in a pressure range of $[5 \cdot 10^{-4} - 1 \cdot 10^{-2}$ Pa] is ran 1 $\sim [10^{-9} - 10^{-6}]$. The figure of mass 6 shows another interesting effect. Ran 2 and 3 line up nicely and in principle we would expect this for ran 4 as well. However it appears that the offset value for ran 4 is negative and that these negative values are recorded as zeros. The slope of the linear fit of mass 6 ran 4 data at higher pressures ($\sim 1 \cdot 10^{-2}$ Pa) is identical to the ran 2 and 3 slopes.

Pressure dependencies: According to the relevant elementary collisions (table B.2) we would expect a linear dependency on the masses 2 and 4, and a quadratic dependency for mass 6, as shown in eq. (B.3). The linear dependencies are found back for masses 2 and 4. However, the mass 2 intensity is about 100 times weaker than mass 4, and not ~ 17 times as would be expected from the reaction cross sections. In these calibration measurements, the correlation for mass 6 is in good approximation linear instead of quadratic. This linear dependency means that the second step in the two step reaction leading to formation of D_3^+ does not depend on the pressure. The second step is thus clearly not the dissociative attachment reaction given in table B.2. At this point there is no clear understanding of this effect, but it is expected that the slowly varying concentration of deuterium atoms sticking on the spectrometer walls lies at its origin. The D_3^+ intensity is known to vary in time (which can be explained by the variation of the concentration of sticking atoms), and therefore it is recommended to calibrate its intensity regularly. Experience learns that it is difficult to rely on the mass 6 signal to quantify the D_2 pressure, especially when the pressure is low ($\sim 10^{-4}$ Pa). In this manuscript mass 6 is used to indicate the presence of deuterium qualitatively, but it is not used for qualitative analyses.

Finally mass 3 should, according to the above, be zero. As can be clearly seen on the figure, the linear dependency of mass 3 is not negligible, the

intensity is even the double of that for mass 2. This signal for mass 3 can originate from several things, which we will list here to conclude this section on mass spectrometry:

- either the quadrupole U/V-ratio is not optimal causing a too wide passing M/Z band,
- either the quadrupole RF frequency is too low resulting in bad resolution,
- either the spectral location for measuring mass 3 is not correctly set; e.g. slightly shifted to the side of mass 4, (for example at mass 3.3) so that a part of the peak tail of mass 4 ions is measured (see Fig. B.2),
- either the signal originates from HD molecules that can be formed inside the spectrometer itself from recombination of present deuterium atoms and residual hydrogen sticking on the spectrometer walls. The spectrometer can be cleaned from this residual gas by heating it up, inducing thermal desorption.

The above problems, if not too severe, can be overcome (the last if one can assume that the sticking hydrogen concentration varies only slowly in time) by carrying out a good calibration of the measured mass signals for different gases, and strongly simplifying the calibration matrix according to the expected gas mixture.

B.1.3 Other residual gas analysis systems

B.1.3.1 Penning gauge spectroscopy

As already indicated in the section on mass spectrometry, experience learns that the quantization of low deuterium partial pressures ($\sim 10^{-4}$ Pa) in a helium environment ($\sim 10^{-2}$ Pa) using mass spectrometry is not evident. Both helium and deuterium have their most important peak in the M/Z-spectrum at mass 4, more accurately at respectively 4.003 and 4.027. To separate the partial pressures of deuterium and helium one can employ the standard Penning vacuum gauges described above and analyze the characteristic light emitted by the Penning discharge. This is called Penning gauge spectroscopy. Optic fibers are connected to the gauge, transporting discharge light to a measurement bench. This allows to quantify the intensity of the emitted Balmer-α lines for hydrogen isotopes (H_α at 6562.8 Å and D_α at 6561.0 Å) [170], and the helium singlet 3s-2p transition at 5016 Å or triplet 3d-2p transition at 5875 Å [171]. The optic fibers can be connected to a spectrometer, or as is mostly the case via an interferential optical filter ($\Delta\lambda \sim 0.5$ nm) to a photomultiplier and photodetector. The detected

characteristic light intensities are proportional to the partial pressure p, the electron density n_e and excitation rate k^{exc} (de-excitation occurs immediately after excitation):

$$I_{\text{He}} = a\, n_e p_{\text{He}} k^{\text{exc}}_{\text{He}} + b\, n_e p_{\text{D}} k^{\text{exc}}_{D} \quad \text{(B.8)}$$

$$I_{\text{D}} = c\, n_e p_{\text{D}} k^{\text{exc}}_{\text{D}} + d\, n_e p_{\text{He}} k^{\text{exc}}_{\text{He}} \quad \text{(B.9)}$$

Penning gauge spectroscopy was used to decompose the partial pressures during JET ICWC experiments, and to obtain qualitative information on the neutral gas content on ASDEX Upgrade. However care has to be taken in the data analysis. The equation above shows two important disadvantageous features. First of all, the light intensity is clearly dependent on the electron density. In turn, the electron density is dependent on the total pressure. This makes that the D_α line intensity in case of a constant deuterium partial pressure can increase on adding a helium pressure. Although this fact is in principle true, it is not be observed in measurements (e.g. [170]). Secondly the employed filters are not perfect. The grey factors in eq. (B.8-B.9) account for the concomitant contributions ($b, d \neq 0$). Finally, it is not possible to determine with Penning gauge spectroscopy the origin of the hydrogen isotopes that emit the measured H_α and D_α lines. Mostly H_α are D_α not measured separately due to the too wide filter band, and even if they can be separated (e.g. by slightly tilting the filter and thus changing its thickness and was done on JET [172]), additional measurements are required to relate the lines to H_2, HD, D_2, CH_4, ... molecules. The measurement accuracy of Penning gauge spectroscopy is strongly dependent on the amount of light that can be guided to the measurement bench, the quality of the employed filters, the characteristics of the photomultipliers and the suppression of background light.

B.1.3.2 Gas chromatography

The residual gas analysis technique 'gas chromatography' is used during ICWC experiments on JET. During the regeneration of the cryopumps, the neutral gas adsorbed on the cryopanels is collected and passed through a chromatography system. The employed gas-chromatograph consists of a compression/injection stage and two parallel analytical stages, one for the detection of helium, hydrogen isotopes, oxygen, nitrogen, methane and carbon monoxide by means of a thermal conductivity detector and one for the detection of carbon monoxide, methane, carbon dioxide, and higher hydrocarbons by means of a flame ionization detector [173]. Gas chromatography was used during the JET experimental session on ICWC. It enabled the independent verification of the total number of removed wall desorbed particles, obtained by mass spectrometry and Penning gauge spectroscopy.

B.2 Plasma diagnostics

In this section we will discuss the employed plasma diagnostics during ICWC experiments on different tokamaks, namely interferometry, reflectometry, Langmuir probes and retarding field analyzers, spectroscopy, lithium beam spectroscopy and electron cyclotron emission. These measurement systems, which are installed on the tokamak devices, are as already mentioned designed to measure on high density and high temperature fusion plasmas. Obtaining data from low density and low temperature conditioning plasmas was thus not always evident. One relied much on the extra efforts of the responsible diagnosticians.

B.2.1 Interferometry

Via interferometry measurements one obtains the integrated electron density along a line of sight. The interferometer measures the phase shift between 2 electromagnetic waves from which 1 passes through the plasma, perpendicular to the magnetic field. The phase shift of the latter depends on the electron density profile along the line of sight [167]:

$$\Delta\phi = -\frac{\omega}{2cn_c}\int n_e(r)\mathrm{d}r \tag{B.10}$$

where c is the speed of light and $n_c = \omega^2 m_e \epsilon_0 / e^2$ is the critical density above which the wave cannot propagate, with ω the wave frequency. One distinguishes in this manuscript DCN and HCN interferometers according to the employed lasers: respectively $\sim 195\,\mu$m and $337\,\mu$m. Furthermore one can use homodyne detection of the phase shift by measuring the resulting light intensity after mixing of the plasma and reference bundles, and heterodyne detection where one of the beams is slightly modulated in frequency and the phase shift is measured from the changes in beat frequency of the two mixed bundles. In most experimental setups, especially for measuring radial lines of sight, the laser beams pass two times through the plasma. For radial lines of sight, the laser beam is injected from the low field side, reflected on a mirror at the high field side, and collected again on the low field side. The phase shift can be influenced by mechanical vibrations of the involved systems, or displacements of the mirrors due thermal effects.

Appendix A shows for tokamak TORE SUPRA, TEXTOR, ASDEX Upgrade and JET, the lines of sight of the installed interferometry systems on a poloidal plane, and the location of the diagnostic on the toroidal plane.

B.2.2 Reflectometry

Reflectometry is similar to interferometry. It employs the cut off density n_c above which the wave is no longer propagative ($f < 100\,\mathrm{GHz}$), and thus will be partially reflected, to obtain a 1D density profile of the plasma. The reflectometer will scan through a range of frequencies and detect the phase shift of the reflected wave. From this phase shift the location of the reflection point along the line of sight can be determined, to which the cut off density can be assigned.

B.2.3 Electron cyclotron emission (ECE)

Electrons gyrate around the magnetic field lines with cyclotron frequency

$$\omega_c = \frac{e}{Bm_e}$$

Because of this accelerated motion the electrons emit electromagnetic radiation with the same cyclotron frequency. The inhomogeneous toroidal magnetic field in the vessel makes that each of the emitted frequencies is related to a specific radial position. In case the plasma is optically thick (it absorbs its own electron cyclotron emission) the plasma will radiate as a black body, in which case the intensity is only related to the electron temperature. For tokamak plasmas with temperatures $> 10\,\mathrm{eV}$ the Rayleigh-Jeans approximation for black body radiators holds [174]:

$$I_{\mathrm{BB}} = \frac{\omega^2}{4\pi^2 c^3} kT_e$$

The lower detection limit, i.e. the lowest detectable electron temperature, is determined by the receiver noise level which appears in practice to be in the range of ICWC conditioning plasma temperatures. Interesting results were obtained from ECE, however the responsible diagnosticians do not have much confidence of the accuracy of their devices for ICWC plasma parameters.

B.2.4 Langmuir probes

A Langmuir probe consist of one or more electrodes inserted into a plasma to which a time-varying voltage, the sweeping voltage, is applied. By analyzing the obtained I-V characteristic information can be obtained on the local density and temperature of electrons and ions, and on the plasma potential. All kinds of probe configurations exist. We will discuss here the two most important, namely the single and double probe configuration. Fig. B.4

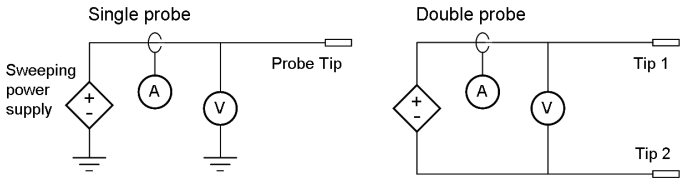

Figure B.4: Left: Schematic of a single-probe circuit including the sweeping power supply, the voltage measurement and the current measurement. Right: Schematic of a double probe circuit. Notice that the sweeping power supply and voltage measurement float. Drawing based on [167].

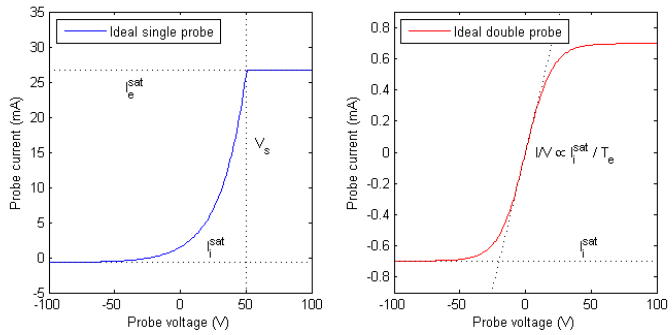

Figure B.5: Ideal single and double probe I-V characteristic for a hydrogen plasma with $T_e = 20\,\mathrm{eV}$, $T_i = 20\,\mathrm{eV}$, $n_e = 10^{16}\,\mathrm{m}^{-3}$ and $V_s = 50\,\mathrm{V}$ according to equation (B.11) and (B.12).

shows the electric scheme of a single and double probe where the measurement location for current and voltage are indicated. The ideal single probe I-V characteristic assuming Maxwellian populations is given by [167]:

$$I_{\mathrm{pr}} = I^{+} - I^{-}\exp[e(V_{\mathrm{pr}} - V_s)/kT_e] \tag{B.11}$$

where I_{pr} and V_{pr} are the probe current and voltage, V_s is the plasma potential, $I^{+} = 0.5en_eSc_s$ is the ion saturation current and $I^{-} = -0.25en_eSc_e$ the electron saturation current, with $c_s = [k(T_e + Z\gamma_i T_i)/m_i]^{1/2}$ the sound velocity, $c_e = [8kT_e/m_e]^{1/2}$ the thermal electron velocity, S the effective current collection area, n_e the electron density, T_e and T_i the Maxwellian electron and ion temperature, m_i the ion mass, Z the ion charge state and finally $\gamma \approx 1.5$ the ion adiabatic constant, which is a measure for the plasma compressibility. Fig. B.5 shows the ideal probe characteristic for the single probe configuration in case of a hydrogen plasma with $T_e = T_i = 20\,\mathrm{eV}$, $n_e = 10^{16}\,\mathrm{m}^{-3}$ and $V_s = 50\,\mathrm{V}$; on the figure the ion and electron saturation current, and the plasma potential are indicated by dotted lines. It is

clear that the sweeping voltage amplitude has to be higher than the plasma potential to be able to determine the electron saturation current. If the complete characteristic is obtained, one can derive the electron temperature and density, the ion temperature and the plasma potential. However, the sharp knee at the plasma potential in the I-V characteristic and the flat electron and ion saturation currents are ideal probe features that are rarely seen in practice. The current can in reality continue to increase beyond the saturation currents due to sheath expansion [175].

An alternative scheme for the single probe that allows obtaining the electron temperature, electron density and ion temperature, independently from the plasma potential is the double probe configuration. In the double probe configuration the time-varying potential is applied between two probe electrodes. This has as additional advantage that the measured characteristic will be less affected by RF effects such as rectifier current in RF plasmas [176]. The double probe I-V characteristic assuming Maxwellian populations is given by [167]:

$$I_{\mathrm{pr}} = I^{+}\tanh(eV_{\mathrm{pr}}/kT_e) \tag{B.12}$$

Fig. B.5 shows also the ideal probe characteristics for a double probe, for the same plasma. Both at higher negative and positive voltages the current is limited by the ion saturation current. The slope of the characteristic at $V_{\mathrm{pr}} = 0$ is inversely proportional to the electron energy. In case of high electron temperatures larger sweeping voltage ranges will thus be required.

On TORE SUPRA, several attempts are carried out to employ the installed Langmuir probes with limited success. On TEXTOR it was possible to obtain values for plasma density, temperature and potential. The results were obtained with a dedicated double probe shown in Fig. B.6 powered by a sinusoidal sweeping voltage with a period of 20 ms and amplitude of 75 V.

B.2.5 Retarding field analyzer

The retarding field analyzer (RFA) belongs to the same family of electrostatic probe techniques as Langmuir probes. It is the most widely accepted diagnostic for SOL T_i measurements [178], and is used during TORE SUPRA ICWC experiments to determine the parallel ion flow (no values for T_i could be retrieved). An RFA consists of a thin aperture aligned normal to the total magnetic field, a pair of retarding (= to which a voltage is applied) grids and a collecting element [179]. The plasma ions are transmitted through the aperture into the analyzer where their parallel velocity distribution is analyzed by means of a retarding electric field applied to a grid.

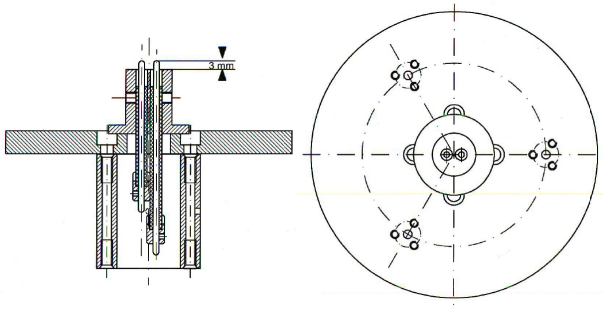

Figure B.6: Double Langmuir probe designed for ICWC plasma characterization at TEXTOR [177] (Left: side view, right: top view): Plate diameter 10 cm, probe height 3 mm, probe electrode height 3 mm and probe electrode diameter 1.96 mm.

The RFA probe on TORE SUPRA consists in fact of two a RFA analyzers respectively collecting ions from both direction along the magnetic field, respectively the electron current side and ion current side [178].

B.2.6 Visual imaging

The vacuum vessels of all tokamaks are monitored by CCD cameras, recording 2D visual light images with sampling time in the order of 0.1 s. These monitoring systems are of importance to evidence the presence of a plasma during experimental programs and to get a first idea on plasma performance by visual inspection. The light intensity and distribution can deliver information on instabilities such as RF trips or on plasma homogeneity. In general the intensity from ICWC plasmas is much lower than in regular tokamak plasmas, which can be solved by increasing the sensitivity of the acquisition system.

B.2.7 Spectroscopy

Plasma spectroscopy, namely the detection and quantification of radiation emitted by plasma, can deliver important information on plasma content and the electron temperature of the plasma. The employed spectroscopic systems during ICWC discharges are mostly based on the emission of Balmer-α lines of hydrogen isotopes, which can be used to evidence hydrogen plasma breakdown, determine the isotopic ratio of the plasma (if H_α and D_α can be separated), to obtain information on plasma distribution (if multiple lines of sight are available) and to quantify fast particle energies from the broadening of the spectral line (if high resolution spectra can be obtained). For the latter one specifically employed lines of sight

of the charge exchange spectroscope without fast particle injection (TEXTOR). Characteristic radiation of impurities are monitored to evidence the presence of impurities, of which the most important is carbon (except for ASDEX Upgrade which has solely tungsten plasma facing components).

The integral over the emitted spectrum for different lines of sight, representing the total radiated power along these lines of sight, is measured directly by bolometry on most tokamaks (although the integral is often not complete: e.g. 2 to 2000 Å on TORE SUPRA). An Abel inversion of multiple viewing lines (48 on TORE SUPRA) allows reconstructing a radiated power profile, which could give important information on plasma distribution. However the total radiated power in ICWC discharges is too low to obtain an accurate reconstruction.

B.2.8 Lithium beam spectroscopy

On TEXTOR a beam spectroscopic system was set up to determine the electron density and temperature via characteristic radiation emitted by thermal lithium atoms (LiI) [113]. A collisional radiative model for lithium atoms was developed including spontaneous emission after excitation, electron collisional excitation, de-excitation and ionization, where the electron energy distribution is assumed to be Maxwellian. The parametric dependencies (n_e, T_e) for ratios of characteristic line intensities, $I(610\,\mathrm{nm})/I(670\,\mathrm{nm})$ and $I(460\,\mathrm{nm})/I(610\,\mathrm{nm})$, obtained from the model allowed to evaluate the electron density and temperature in ICWC plasmas. Lithium beam spectroscopy on TEXTOR provided valuable information allowing to evidence the extension of the RF plasma towards the bottom of the vessel on application of a small vertical magnetic field [113] which will be discussed further in chapter 3.

B.2.9 Neutral particle analyser

A neutral particle analyzer (NPA) will analyze the flux of neutral particles to the wall. This flux originates from plasma ions undergoing charge exchange reactions with neutral particles or recombination with electrons. In ICWC plasmas also dissociation of neutral molecules or of molecular ions contributes to the total neutral wall flux, however the energy of these neutrals ($\sim$ Franck Condon energy) is out of the measurement range of the installed NPA's. The flux of hydrogen or deuterium atoms with energy (E) emerging from a unit volume of the plasma is given by [167]:

$$F_{\mathrm{H,D}}(E) = n_{\mathrm{H^+,D^+}} f_{\mathrm{H^+,D^+}} (n_0 \langle \sigma v \rangle_{\mathrm{CX}}) \tag{B.13}$$

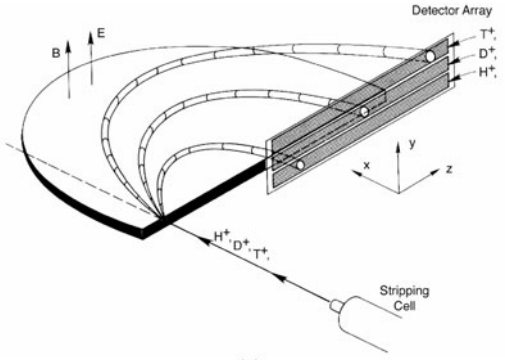

Figure B.7: Illustration of the mass and charge separation principle of a NPA. After reionization of the CX neutrals in the stripping cell, the ions enter into a semicircular region containing a magnetic and parallel electric field, both perpendicular to the initial ion path, making that the impact location on the detector plane is both energy and mass resolved. [167]

with $n_{\mathrm{H}^+,\mathrm{D}^+}$ the density of hydrogen and deuterium ions, $f_{\mathrm{H}^+,\mathrm{D}^+}$ their distribution function, n_0 the density of neutral hydrogen isotopes and $\langle\sigma v\rangle_{\mathrm{CX}}$ the rate coefficient for CX, where we neglect recombination. In the NPA the neutrals are ionized and separated according to their mass and charge by an electric and magnetic field (see Fig. B.7). The detection plane resolves the ion mass, in the figure, along the y-axis and the ion energy, via the gyration radius of the ions in the magnetic field, along the z-axis.

The employed NPA's in this manuscript resolve hydrogen and deuterium fluxes for a limited number of energy values in the range of 0.5 to 50 keV and deliver line integrated CX fluxes along a viewing line with certain solid angle. The Maxwellian temperature of the energetic particle flux can be derived by fitting a Maxwellian distribution to the signals of the different energy channels. The measured data is given with unit $[(\mathrm{dE\ dt\ m^2\ sr})^{-1}]$. To obtain the total time resolved wall flux, assuming that the plasma parameters are homogeneous and that the flux from each unit volume is isotrope, one has to multiply by 4π to obtain the complete solid angle, divide by the length of the line of sight, multiply by the plasma volume and integrate over the energy.

The energetic ions in ICWC plasmas are produced by resonant absorption of RF power at the resonance layers. From this it is expected that the CX flux originates from the resonance layer as well, and thus the assumption of homogeneous plasma parameters in the above is in principle not correct. Thus to obtain the total wall flux it is not correct to divide the data by the length of the line of sight and multiplying with the plasma volume. One

has to divide by the width of the resonance layer δr, and multiply by the volume of the resonance layer $V_r = 4\pi r_{ic} a \delta r$, with r_{ic} the radial location of the resonance layer and a the minor radius. This consideration will give only a small correction to the total flux, but on the other hand it makes that the wall flux can not be assumed homogeneous. Due to the vertical resonance layers, the vertical fluxes will be more important than the fluxes in the horizontal plane.

C

Appendix to chapter 5

C.1 Benefits and limitations of a 0D approach

C.1.1 Homogeneity

To justify the relevancy of a 0D approach to study the plasma parameters in RF plasmas, a proper consideration of the homogeneity of RF plasmas is required. In chapter 3 this point was thoroughly discussed. In the toroidal direction the plasma parameters are considered uniform [73, 92, 93]. In the poloidal plane the measured densities appear to be systematically higher on the low field side than on the high field side [127] and, dependent on the discharge pressure and coupled RF power, is sometimes peaked along the radius. The poloidal inhomogeneity is thought to have two main causes. The vertical inhomogeneity is due to collective plasma drifts in the toroidal magnetic field, and the radial inhomogeneity is due to inhomogeneous power deposition. TOMCAT [89] simulations show that in proper selected regimes, depending on the plasma composition and the choice of RF frequency and magnetic field, the RF power is mainly coupled to the electrons and that the power can be deposited over the whole radial extension of the vessel [97].

To describe self consistently the drifts and RF coupling properties of the plasma, a 2D model would be required. In case the model only needs to describe the RF power deposition profiles without detailing out vertical inhomogeneities, a 1D model along the radial dimension is sufficient. Recently Moiseenko [180] developed such a self consistent model for RF plasma

production in stellarators. Whereas Moiseenko upgraded his original model for atomic hydrogen [132] to 1D, on our side we have upgraded the balance equations to molecular hydrogen and helium. This complementary choice is especially justified for the description of plasmas with low ionization degree, such as wall conditioning plasmas. The simple structure of a 0D code allows to study within reasonable calculation times (2 min cpu time for 1 s of plasma) a complete set of plasma species, including their most important elementary processes. The information on the plasma parameters and their relative concentrations as a function of the pressure, gas mixture and coupled power can for example be used in an iteration with RF coupling codes (e.g. TOMCAT) to complete our understanding on the power absorption [93]. To conclude: in this stage of the development of the RF wall conditioning technique a 0D model including edge conditions at the wall is sufficient. Later the elements of this 0D model can be used in an upgrade to a 1D code, using an RF-power deposition profile as input, or to a self consistent 1D code. For this matter a coupling with the TOMCAT code, or the code of Moiseenko can be an option.

C.1.2 Fast particles

A limitation of the presented code is the absence of the population of fast ions that are produced by resonant absorption of RF power at the IC resonance layer [73]. Resonant absorption by ions is however a local effect[1], unlike the coupling of RF power to the electrons which takes place over the whole plasma volume. It is thus not straightforward to implement the population in a 0D code. From neutral particle fluxes measured on JET [127] compared to TOMATOR-0D simulations (see chapter 4) it is found that the density of fast particles ($T_{\text{fast}} \sim 10\,\text{keV}$) is very low ($n_{\text{fast}} \approx 10^{-4} n_e$) and might be safely neglected. (TOMCAT simulations show that also outside the IC layer power can be coupled to the ions by non-resonant ion-neutral, ion-ion and ion-electron collisional absorption. The latter will likely not give rise to fast particles and is included in the model assuming the power deposition is homogeneous.) The local character of the resonant coupling can in a 1D model easily be implemented by varying the coupled power to the electrons and ions along the radial direction. A meaningful implementation of the fast ion population around the resonance layer appears not to be straightforward in a 0D model. When keeping the assumption of Maxwellian temperatures, it implies the addition of an extra particle

[1] More precisely: a local effect in radial direction and non-local in toroidal direction, depending on area of FW propagation. It means that IC absorption may happens everywhere along the torus if FW reaches the ICR layer with high enough amplitude of RF field.

specie that represents the fast ions. This leads to two problems that, on introducing sufficient simplifications, can be overcome. The first is related to the particles that interact with the fast ions, the second with source terms for the fast particle population. However it is decided not to include the fast particle population since a study of related effects should be done preferentially in a 1D context.

Nevertheless, the two mentioned 'problems' that need to be solved in this respect are discussed here shortly to illustrate the interesting driving mechanisms that could motivate a future model expansion to 1D. The first is related to the particles that interact with the fast ions, the second with source terms for the fast particle population. (1) For each particle that interacts with the fast ion population a specie, representing its local density, has to be added. The same is true for the resulting species. It is clear that by definition the model will be no longer 0D. The model can regain its 0D character by drastically limiting the elementary processes of the fast ion population. For example by regarding (a) the fact that in a H_2 plasma, the fast H^+ ions have as most probable interaction charge exchange with H for which the density distribution might be considered homogeneous and (b) the fact that the produced fast H neutrals are most probably lost to the walls before they can collide with an other particle. The energy balance of the fast ions can in this way be calculated self consistently; the coupling of power to the fast ion population is balanced by charge exchange with neutrals. (2) In the calculation of the particle balance however we encounter the second problem: the population of fast ions needs a source term. The main H^+-ion source is ionization of H-atoms and dissociative ionization of H_2. In a simple approach, the produced ions could be divided into the fast and slow population according to the ratio of their radial extent in the vessel. Then again this would appear too simple; if the only accounted loss mechanism is charge exchange, in which a fast ion is replaced by an other ion that also must be counted to the fast ion population due to its radial position, the ion concentration in the resonance layer can only grow in this approach. In the limit this leads to the unphysical situation where the resonance layer continuously milks the hydrogen from slow populations until there is no hydrogen left in the vessel, all will be in the resonance layer. This problem could be solved in turn, by considering that the fast ions radially drift or diffuse out of the resonance layer, or by including losses of fast particles along field lines on inclusion of a vertical magnetic field.

Experimentally, from NPA measurements, there is no clear evidence of a continuous increase of the fast particle population. A study of the described effects, e.g. on the involved time scales, might however be interesting and should be done preferentially in a 1D context. It is as such considered out

of the scope of this 0D model.

C.1.3 Plasma breakdown phase

In the 0D approach the total coupled RF power is normalized to the plasma volume. This is meaningful only when the plasma density is uniform over the vessel and in the approximation that the RF power deposition is homogeneous over the whole vessel volume. The first point is important to consider if the model needs to be used to study the breakdown of the plasma, namely the build up of plasma from zero density to the steady state value. According to the present understanding, and in present devices, the plasma breakdown occurs in front of the antenna, in the near antenna electric field [94]. In the equilibrium state the plasma is sustained by excited waves. A complete description of the breakdown should include the conversion from the first regime to final: namely from ionization by accelerated electrons in the near antenna electric field to a plasma extended over the whole vessel sustained by excited waves as described in [95]. Even though the 0D model simplifies the involved RF-physics to a maximum (see section 5.1.5), it allows to simulate plasma breakdown. The reason for this is that the plasma build up is dominated by particle collisions, which are very well described in the model. The 0D model describes the time evolution of the plasma parameters through the breakdown phase automatically if the electron coupled power is enough to achieve ionization in the given volume. How power coupling and plasma breakdown is handled in the model is described in section 5.1.5. From wave theory it is known that on increasing plasma density different waves can be excited. The model is in principle also able to determine the moment at which wave propagation becomes possible ($\omega = \omega_{pe}$), from the calculated plasma density.

Experimentally the breakdown moment goes accompanied with a sudden drop in the antenna voltage and a sudden increase of the emitted H-alpha light [181]. The breakdown time is dependent on the strength of the near antenna electric field, its shape (defined by the geometry and the number of straps and their phasing), the RF frequency and the pressure in the vessel [81, 86]. The strength of the initial electric field is determined by the initial antenna voltage, which is in turn dependent on the generator power. The final antenna voltage is determined by the generator power and the coupling efficiency [182]. The 0D model can reproduce the dependency of the breakdown time on the pressure and power, but is not able to reproduce the dependency on RF frequency and electric field. Efforts to include dependencies on RF frequency and electric field in the model have been carried out, without satisfactory results at this point.

In the initial phase of the numerical simulation the coupled RF power

is set proportional to the electron density, which might be expected to be a realistic assumption. By adapting the proportionality, the experimental breakdown time can be reproduced. This point is further discussed in section 5.1.5.

C.1.4 Wall conditioning efficiency

Wall conditioning aims at removing impurities, fuel particles or codeposited layers from the plasma facing components. The efficiency of the wall conditioning techniques is measured by the rate Q at which it removes wall desorbed particles from the vessel. For the removal of the produced gas one uses the machine pumps. The removal rate is proportional to their pumping speed S and the gas pressure $Q = pS$. A correct description of the wall conditioning effect requires the implementation of (1) gas injection and pumping by the machine pumps (see section 5.1.4), and (2) dynamics of the exchange of particles between plasma and wall. The first point is easy to implement into the balance equations of the neutrals (H_2 and He) by adding a term for the removal rate Q and an injection rate of gas into the vessel. As will be explained in section 5.1.3.4 the model can be run with or without the dynamic gas throughput. In relation to the second point, the model allows to set a recycling coefficient representing the wall interaction leaving the possibility to study the effect of wall recycling on the plasma (see modeling result in section 5.2.4). Experimentally the recycling is found to be very close to 1 [154]. The exchange of particles between plasma and wall will depend on the wall materials and particle flux properties like their energy, fluency, chemical activeness, etc... A complete mathematical description of the wall behavior is a complicated matter and requires a study on its own, as will be presented in the next chapter (6).

C.2 Figures reaction rates

This subsection gathers the reaction rate figures for the collisional processes relevant to hydrogen-helium conditioning discharges, presented in section 5.1.2.

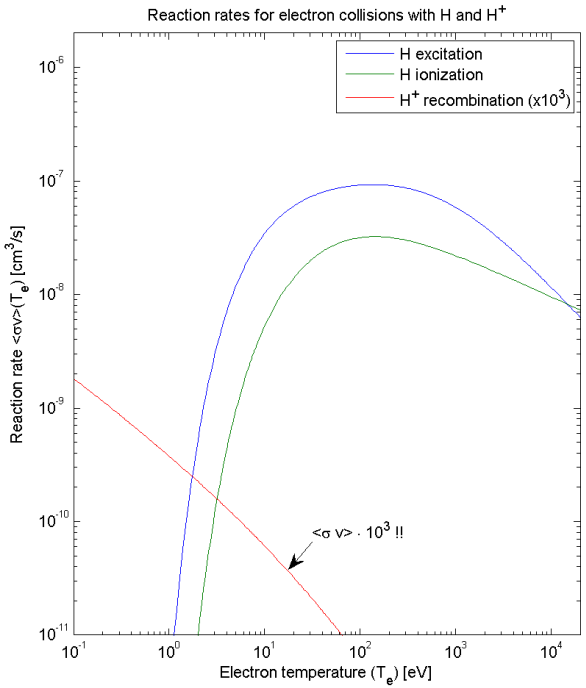

Figure C.1: Reaction rates ($\langle\sigma v\rangle$) for H excitation, H ionization and H^+ recombination on electron impact as a function of the electron temperature (T_e).

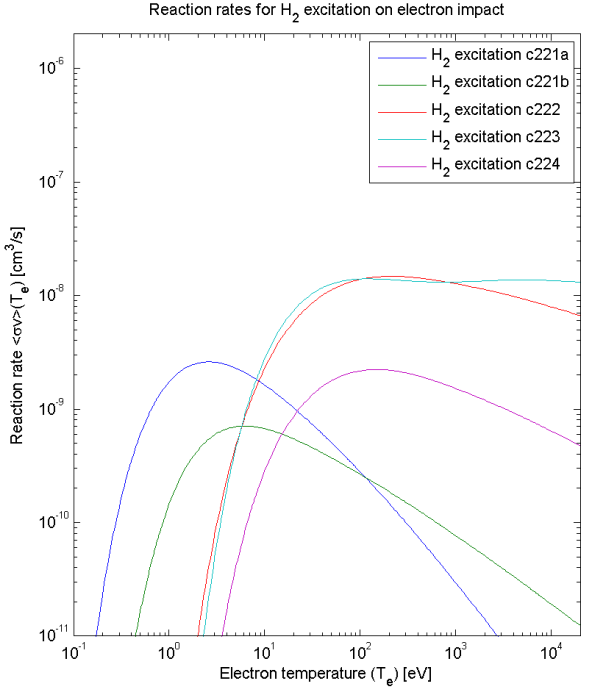

Figure C.2: Reaction rates ($\langle\sigma v\rangle$) for H_2 excitation on electron impact as a function of the electron temperature (T_e).

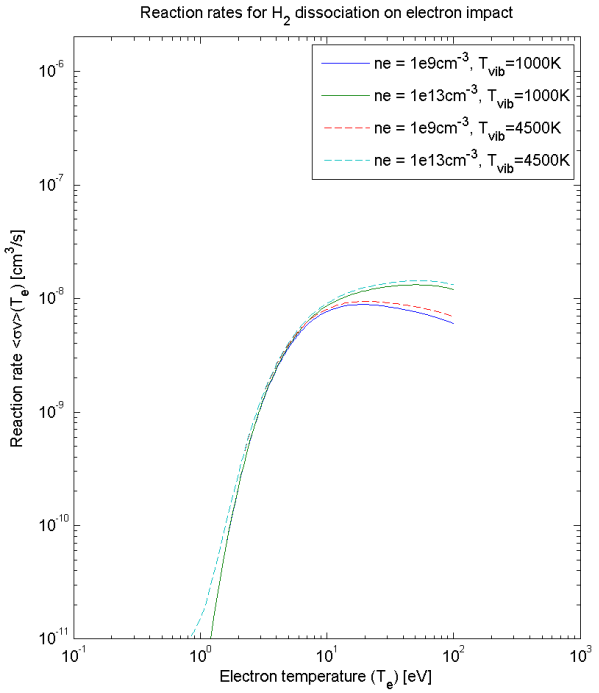

Figure C.3: Reaction rates ($\langle \sigma v \rangle$) for H_2 dissociation on electron impact as a function of the electron temperature (T_e), the H_2 vibrational temperature (T_{vib}) and the electron density (n_e).

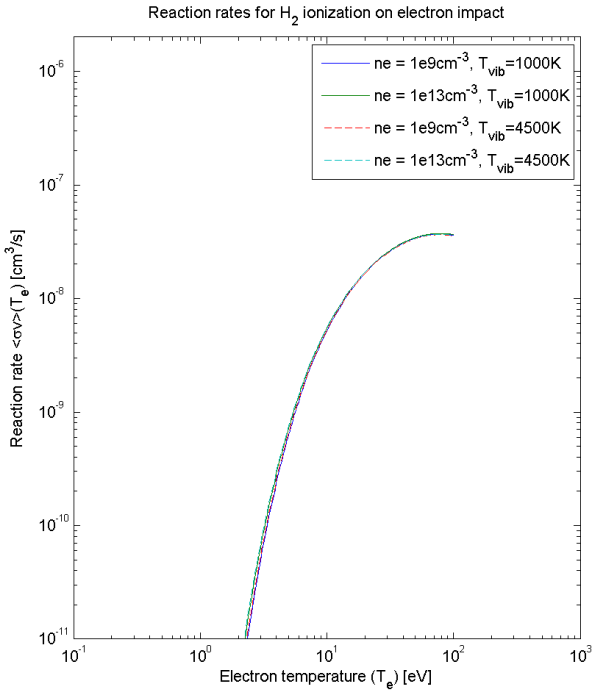

Figure C.4: Reaction rates ($\langle \sigma v \rangle$) for H_2 ionization on electron impact as a function of the electron temperature (T_e), the H_2 vibrational temperature (T_{vib}) and the electron density (n_e).

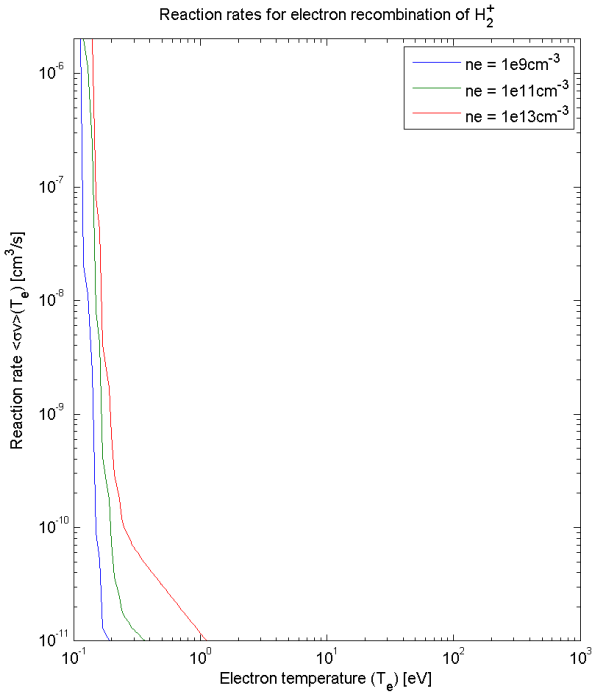

Figure C.5: Reaction rates ($\langle \sigma v \rangle$) for electron-H_2^+ recombination as a function of the electron temperature (T_e) and the electron density (n_e).

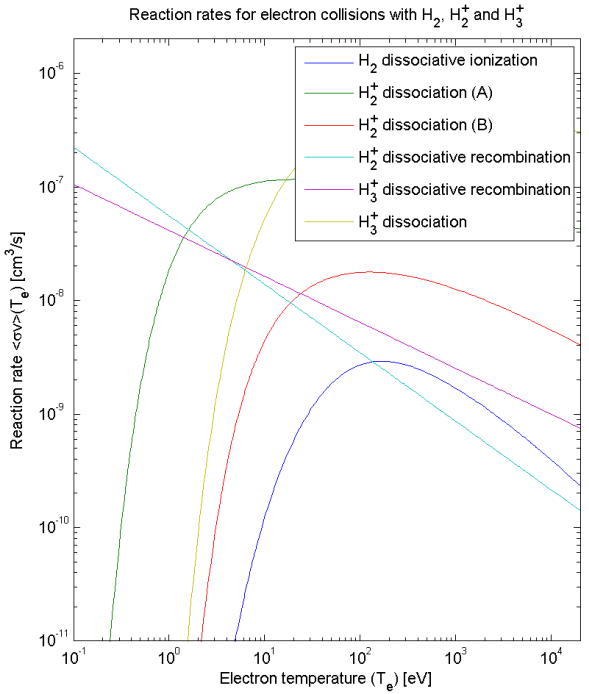

Figure C.6: Reaction rates ($\langle \sigma v \rangle$) for additional electron impact reactions with H_2, H_2^+ and H_3^+ as a function of the electron temperature (T_e).

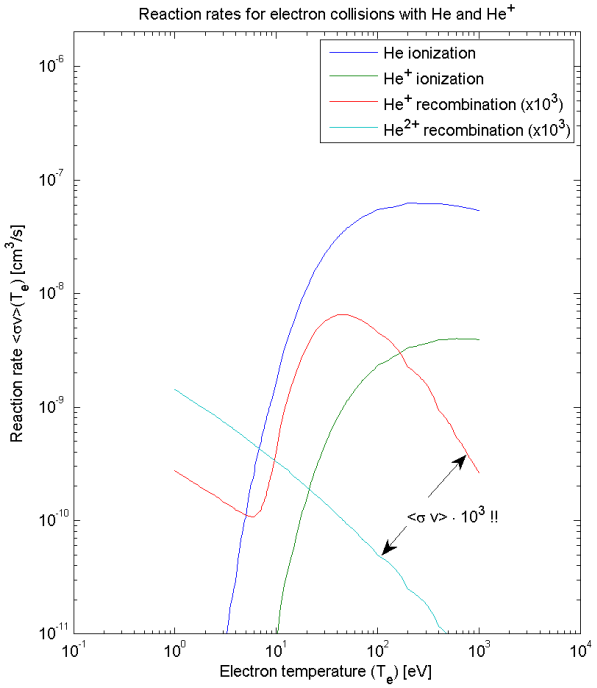

Figure C.7: Reaction rates ($\langle \sigma v \rangle$) for He and He^+ ionization and He^+ and He^{2+} recombination on electron impact as a function of the electron temperature (T_e).

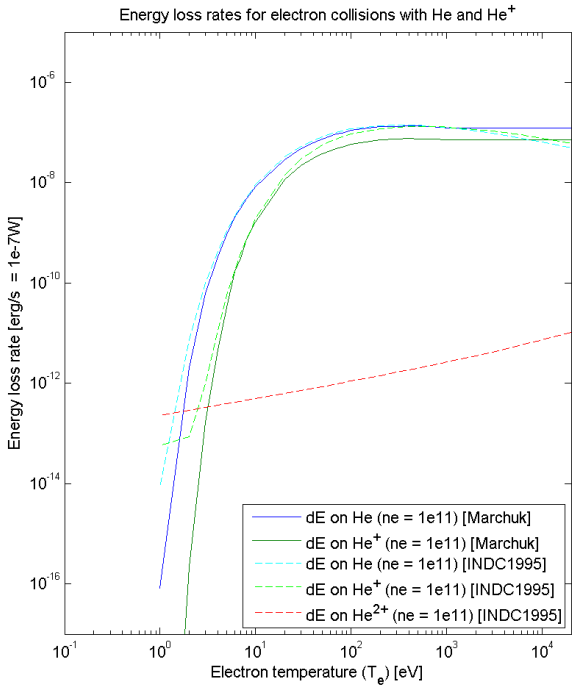

Figure C.8: Total cooling rate of the electrons for collisions with He, He^+ and He^{+2} as a function of the electron temperature (T_e) and the electron density (n_e). ([143] = [INDC1995])

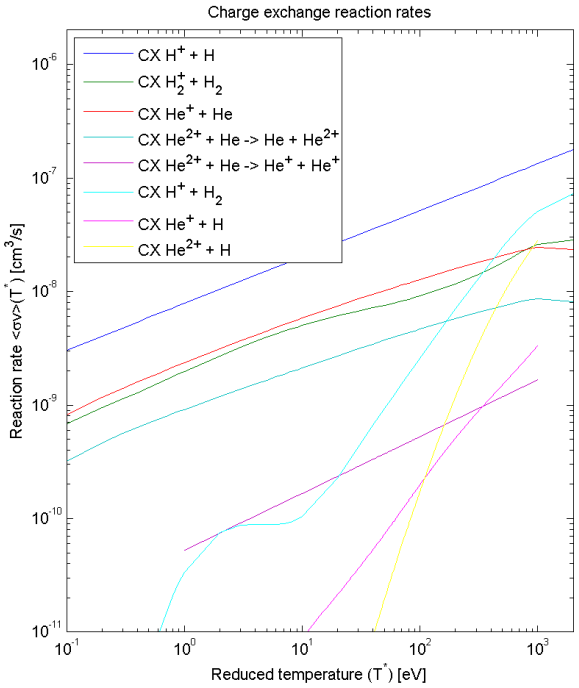

Figure C.9: Charge exchange reaction rates ($\langle \sigma v \rangle$) as a function of the reduced temperature (T^*) of the involved particles.

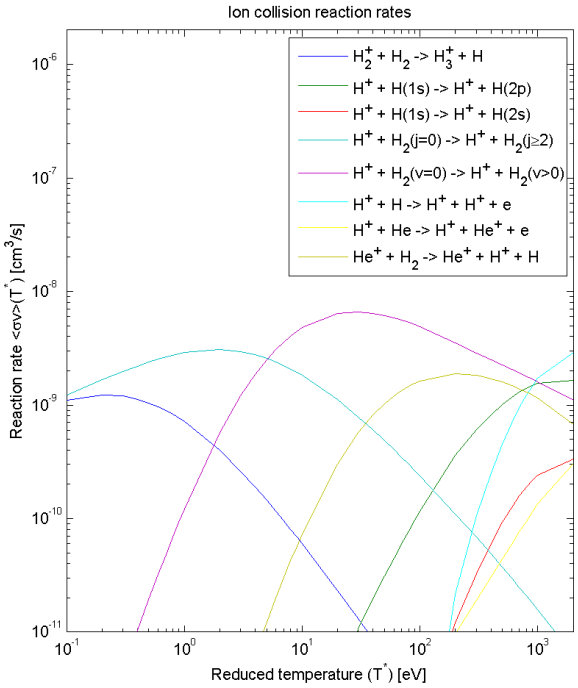

Figure C.10: Additional heavy particle collision reaction rates ($\langle \sigma v \rangle$) as a function of the reduced temperature (T^*) of the involved particles.

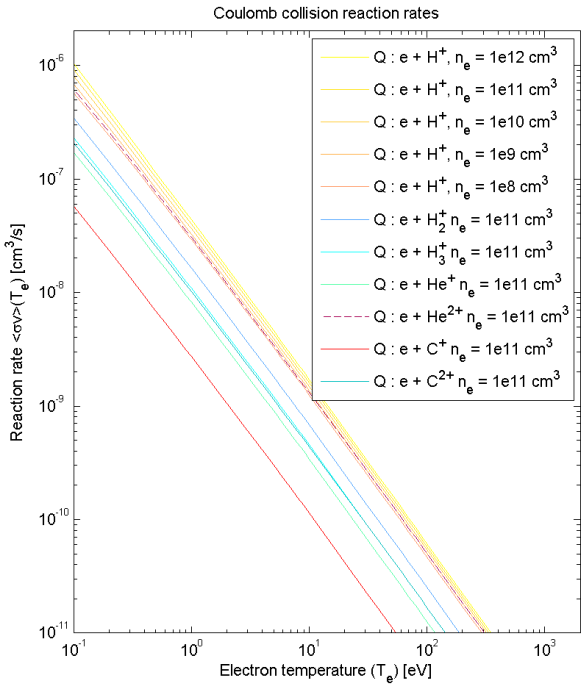

Figure C.11: Reaction rates ($\langle \sigma v \rangle$) for electron-ion Coulomb collisions as a function of the electron temperature (T_e) and density (n_e).

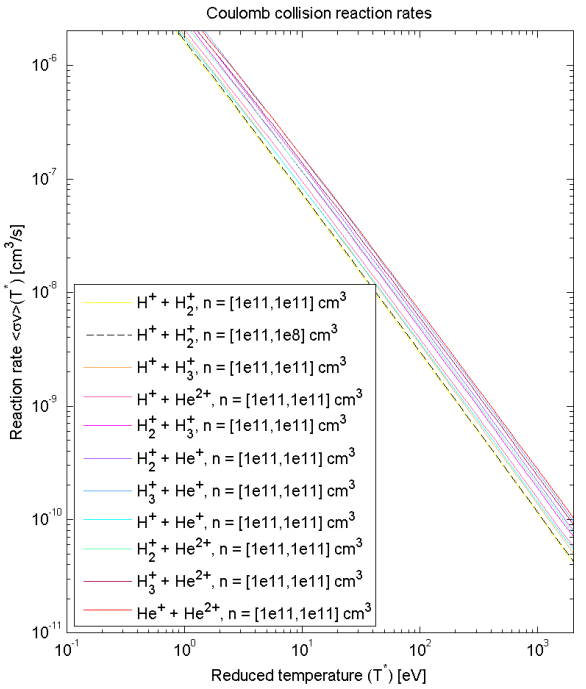

Figure C.12: Reaction rates ($\langle \sigma v \rangle$) for ion-ion Coulomb collisions as a function of the reduced temperature (T^*) and density (n) of the involved particles.

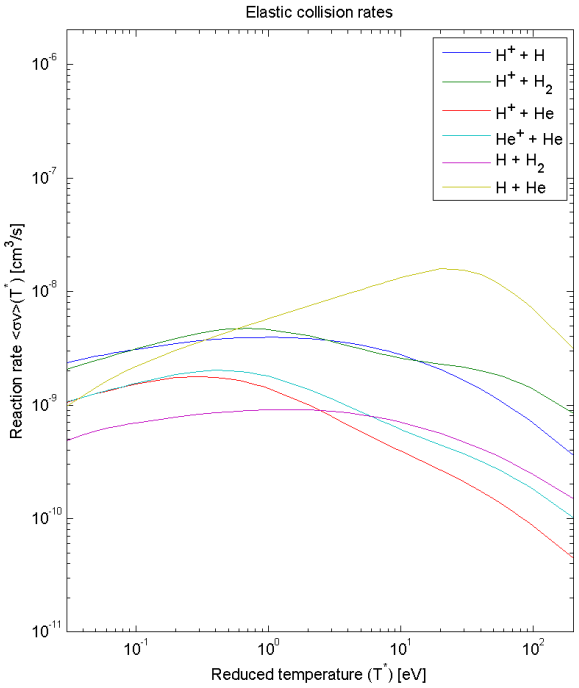

Figure C.13: Elastic collision rates ($\langle \sigma v \rangle$) as a function of the reduced temperature (T^*) of the involved particles.

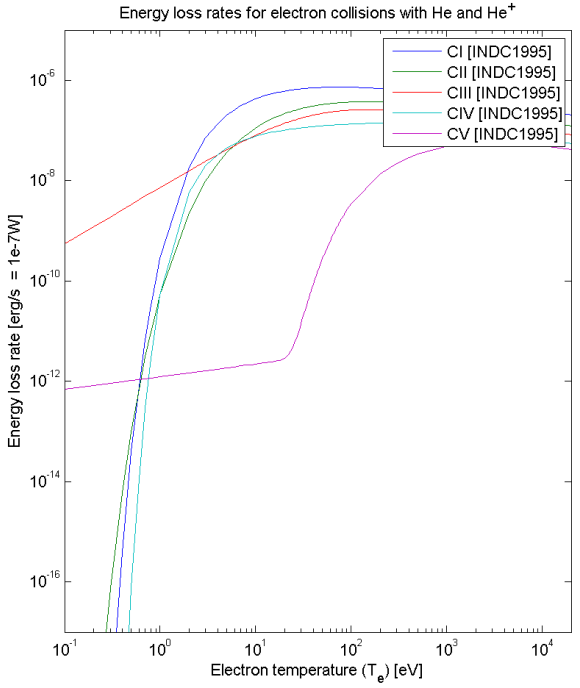

Figure C.14: Total cooling rate of the electrons for collisions with C, C^+, C^{2+}, C^{3+} and C^{4+}, as a function of the electron temperature (T_e) and the electron density (n_e). ([143] = [INDC1995])

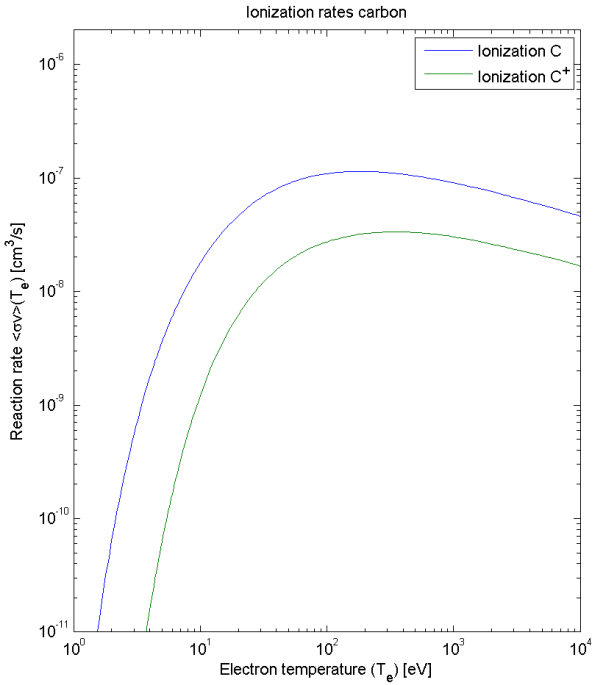

Figure C.15: Reaction rates ($\langle \sigma v \rangle$) for C and C^+ ionization on electron impact as a function of the electron temperature (T_e). [151]

C.3 Relation particle confinement and energy confinement

The confinement time of a particle can be expressed as a function of the dimensions of the vessel and the particle velocity towards the vessel walls. This velocity will depend on the considered physical mechanism, discussed into detail in chapter 3. In the 0D model we consider for each specie a Maxwellian velocity distribution. Particles from the high energy tail of the distribution generally have a smaller confinement time than lower energy particles. These particles will thus be lost faster than less energetic ones, which will in turn affect the particle velocity distribution, and likewise the average energy of the distribution. As was done for the reaction rates, it is possible to obtain effective confinement times by taking into account the particle velocity distribution. Using effective confinement times instead of confinement times where the energy distribution is not specifically taken into account, appeared not to significantly influence the modeling results. An additional complication results from the weighting of the wall flux by the energy dependent mean free path of the particles, which appeared e.g. important to describe correctly the neutral wall flux in section 5.9. Therefore it was chosen not to include the effective confinement times in the final model. And also for the same reason it was chosen to use the same confinement time for the particle and energy confinement time. Nevertheless, if we disregard the dependency on the mean free path for the moment, it is easy to calculate the effective confinement times. We will have a closer look to this in the following short analysis: the effective particle confinement time and energy confinement time for the vertical '$\vec{B} \times \nabla B$' drift of the ions in the magnetic field, the radial '$\vec{E} \times \vec{B}$' drift and the losses along the magnetic field lines are calculated.

With $\tau(v)$ the velocity dependent particle confinement time we can write the change of the velocity distribution as:

$$\frac{\mathrm{d}f(\vec{v})}{\mathrm{d}t} = -\frac{f(\vec{v})}{\tau(v)} \tag{C.1}$$

For a singly charged particle, the confinement time related to the vertical '$\vec{B} \times \nabla B$' drift is defined as ($\tau = a/v$ with a the minor radius):

$$\tau(v) = \frac{qaR_0B_T}{2k_BT} = \frac{3}{2}\frac{qaR_0B_T}{mv^2} \tag{C.2}$$

with R_0 the major radius, q, m, T and v the particle charge, mass, temperature (K) and velocity, B_T the toroidal magnetic field, k_B the Boltzmann

constant, and $\langle 1/2mv^2 \rangle = 3/2k_BT$. We obtain

$$\frac{\mathrm{d}f(\vec{v})}{\mathrm{d}t} = -\left(\frac{m}{2\pi k_B T}\right)^{3/2} \frac{2}{3} \frac{mv^2}{qaR_0B_T} e^{-\frac{mv^2}{2k_BT}} \tag{C.3}$$

with T the Maxwellian temperature. The following integrals gives respectively the time evolution of the total number of particles and the time evolution of the total energy:

$$\int_{-\infty}^{\infty} \frac{\mathrm{d}f(\vec{v})}{\mathrm{d}t} \mathrm{d}^3\vec{v} = \frac{\mathrm{d}N}{\mathrm{d}t} \tag{C.4}$$

$$\int_{-\infty}^{\infty} \frac{1}{2}mv^2 \frac{\mathrm{d}f(\vec{v})}{\mathrm{d}t} \mathrm{d}^3\vec{v} = \frac{\mathrm{d}E}{\mathrm{d}t} \tag{C.5}$$

Using equation (C.3) and the integral identities

$$\int_0^{\infty} x^{2n} e^{-ax^2} \mathrm{d}x = \frac{(2n)!}{n!2^{2n+1}} \sqrt{\frac{\pi}{a^{2n+1}}}, \quad \int_0^{\infty} x^{2n+1} e^{-ax^2} \mathrm{d}x = \frac{n!}{2a^{2n+1}}$$

where $a > 0$ and $n = 0, 1, 2, ...$, we find

$$\frac{\mathrm{d}N}{\mathrm{d}t} = -\frac{2k_BT}{aR_0qB_T} = -\frac{1}{\tau(T)} \tag{C.6}$$

$$\frac{\mathrm{d}E}{\mathrm{d}t} = -\frac{5}{2} \frac{k_BT}{aR_0qB_T} k_BT = -\frac{5}{6} \frac{\frac{3}{2}k_BT}{\tau(T)} \tag{C.7}$$

For the vertical drift we can express the effective particle confinement time of the Maxwellian distribution as the confinement time of their Maxwellian temperature. As the particles from the energetic tail are lost more rapidly, eq. (C.7) shows that the Maxwellian temperature decreases in time.

In case of the outward radial '$\vec{E} \times \vec{B}$' drift, where the drift velocity does not depend on the energy of the charged particles, the drift doesn't cause a change in energy distribution. For losses along the magnetic field lines the confinement time of a particle will be inversely proportional to its parallel velocity $v_\parallel$. A similar integration as for the vertical drift leads to an effective confinement time inversely proportional to the thermal velocity: $\tau_p(T) \propto \sqrt{\pi/2} v_T^{-1}$. The effect on the Maxwellian energy is more pronounced $\tau_E(T) \propto 6\sqrt{\pi/2}\, v_T^{-1}$.